Modèle de facteur de structure pour l'estimation ultrasonore des structures cellulaires

Emilie Franceschini

AIX-MARSEILLE UNIVERSITÉ
Laboratoire de Mécanique et d'Acoustique LMA CNRS UPR 7051

Mémoire présenté pour l'obtention de
L'HABILITATION A DIRIGER DES RECHERCHES

par

Emilie FRANCESCHINI

Modèle de facteur de structure pour l'estimation ultrasonore des structures cellulaires

Date de soutenance : 1er octobre 2015

Membres du jury :

Prof. Olivier Basset Examinateur
Dr. Lori B. Bridal Rapporteur
Prof. Joseph Moysan Examinateur
Prof. William D. O'Brien Rapporteur
Dr. Frédéric Ossant Examinateur
Dr. Frédéric Padilla Rapporteur

Table des matières

Introduction

Ce mémoire d'habilitation présente un résumé des travaux de recherche que j'ai menés après ma thèse, comme post-doc à l'université de Montréal (Canada) en 2007-2008, puis comme chargée de recherche au CNRS depuis octobre 2008 au sein de l'équipe Ondes et Imagerie au Laboratoire de Mécanique et d'Acoustique LMA à Marseille.

Après ma thèse portant sur les méthodes de tomographie ultrasonore pour l'imagerie du sein, j'ai étendu mes activités aux techniques d'estimation ultrasonore des structures cellulaires. Ces techniques sont utilisées dans le domaine de la caractérisation tissulaire pour différencier des tissus sains et pathologiques, détecter un cancer ou faire le suivi d'une thérapie. Je me suis principalement intéressée à l'estimation ultrasonore des microstructures pour deux applications principales : le sang et les tumeurs. Les deux applications ont en commun une modélisation acoustique des milieux en terme de fluides hétérogènes, qu'il s'agisse d'écoulements chargés (suspensions d'agrégats de globules rouges) ou des tissus biologiques (les tissus mous sont assimilés à des fluides aux fréquences ultrasonores).

Le chapitre 1 porte sur la caractérisation ultrasonore de l'agrégation érythrocytaire pour la détection ou le suivi de l'hyperagrégation associée à des pathologies impliquant des désordres rhéologiques sanguins. J'ai démarré cette activité à Montréal entre 2007 et 2008, à l'occasion de mon post-doctorat qui portait sur l'application *in vivo* des techniques d'estimation de taille. Lors de mon retour à Marseille, j'ai poursuivi ces activités en me concentrant sur le développement et l'évaluation d'un nouveau modèle de diffusion ultrasonore pour l'estimation de la structure des agrégats érythrocytaires. Les difficultés majeures pour modéliser la rétrodiffusion par le sang est de considérer une forte concentration de particules ($\approx 40\%$) et des agrégats de particules. Nous présentons notre contribution, en particulier la proposition d'une théorie de milieu effectif combinée au modèle de facteur de structure. Nous comparons la précision de cette théorie avec des modèles classiques pour estimer la structure des agrégats sur la base de simulations numériques (où tous les paramètres sont contrôlés) et sur des données expérimentales de sang cisaillé en écoulement.

Le chapitre 2 concerne la compréhension de la rétrodiffusion ultrasonore par les tumeurs. Les tumeurs cancéreuses résultent souvent d'une prolifération de cellules anormales formant une masse qui grossit. Les modèles classiques de diffusion ultrasonore utilisés par les techniques d'estimation des structures cellulaires supposent que les diffuseurs sont distribués de façon aléatoire (i.e. des milieux dilués), alors que les tumeurs sont des milieux à fortes concentrations cellulaires. L'enjeu scientifique est de répondre aux questions suivantes : quels sont les modèles de diffusion adaptés à un amas dense de cellules ? Quelles sont les principales structures responsables de la diffusion ultrasonore au sein des tumeurs ? Les problèmes que nous étudions pour l'agrégation érythrocytaire peuvent donc aider à mieux comprendre la diffusion ultrasonore par les tumeurs cancéreuses. Nous comparons

différents modèles de diffusion et discutons de leurs limites à travers des expériences sur des biofantômes de cellules modélisant des tumeurs cancéreuses.

Ce mémoire se termine par des perspectives (chapitre 3), où je présente les orientations que je souhaite donner à mes activités de recherche. Il est complété par un curriculum vitae à l'annexe A présentant notamment ma liste complète de publications ainsi que le détail de mes activités d'enseignement et d'encadrement. Enfin, l'annexe B reproduit une sélection de mes publications post-thèse. A noter que, pour chaque étude présentée dans le manuscrit, le lecteur trouvera en tête de section la liste des personnes avec qui j'ai collaboré pour ces travaux.

Chapitre 1

Diffusion ultrasonore par des suspensions concentrées d'agrégats érythrocytaires

C'est au cours de mon post-doctorat au Laboratoire de Biorhéologie et d'Ultrasonographie Médicale (LBUM) à Montréal que je me suis familiarisée aux techniques de caractérisation ultrasonore de l'agrégation érythrocytaire, et plus généralement aux méthodes d'estimation des microstructures tissulaires. Ce chapitre est consacré aux travaux que j'ai développés au LMA depuis mon recrutement au CNRS en 2008 sur le développement et l'évaluation d'un modèle de diffusion ultrasonore pour l'agrégation érythrocytaire, ainsi qu'aux travaux que j'ai menés lors de mon post-doctorat au LBUM en 2007-2008 sur l'application *in vivo* des techniques d'estimation des structures d'agrégats.

Le sang est une suspension d'érythrocytes, de leucocytes et de plaquettes dans un liquide newtonien, le plasma ; l'ensemble constituant un liquide non newtonien. La diffusion ultrasonore par le sang est principalement attribuée aux érythrocytes, appelés aussi globules rouges, car ils constituent la majorité (97%) du contenu cellulaire dans le sang. Dans le sang normal, la fraction volumique des globules rouges (appelée hématocrite) est comprise entre 35 et 45%. En écoulement dans des vaisseaux sanguins, les globules rouges s'agrègent et se désagrègent, formant un processus réversible. Les agrégats prennent la forme de rouleaux ou de structures tridimensionnelles enchevêtrées. Les mécanismes de formation ou de dissociation d'agrégats sont complexes et dépendent principalement du cisaillement auxquels les globules rouges sont soumis, de la concentration de macromolécules plasmatiques (telles que le fibrinogène) (Chien 1975 ; Meiselman 1993 ; Armstrong *et al.* 2004) et de l'agrégabilité des globules rouges (Rampling *et al.* 2004). Le phénomène d'agrégation est normal ; cependant l'augmentation anormale de l'agrégation, l'hyperagrégation, est associée à plusieurs pathologies impliquant des désordres rhéologiques sanguins (thrombose, diabète, athérosclérose,...). Les méthodes actuellement utilisées en clinique pour caractériser l'agrégation des globules rouges sont effectuées à partir d'un prélèvement sanguin et ne permettent qu'une mesure globale du niveau d'agrégation. Or les pathologies provoquent des désordres circulatoires sanguins en des sites bien particuliers (par exemple le pied pour le diabète, les membres inférieurs pour la thrombose). L'objectif est de développer un outil ultrasonore de diagnostic permettant de mesurer quantitative-

ment l'agrégation *in situ* et *in vivo*. Cet outil permettra de quantifier l'hyperagrégation des globules rouges en des sites bien particuliers, donc localement, là où les méthodes utilisées en clinique n'autorisent que des mesures globales.

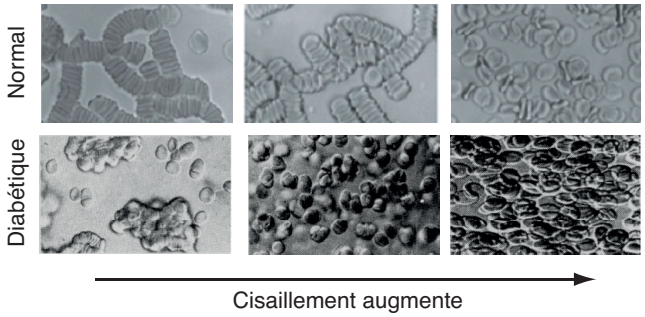

Figure 1.1 – Images au microscope optique de l'agrégation érythrocytaire pour du sang normal et pathologique dans un rhéomètre transparent. Dans le cas sain, les agrégats prennent la forme de rouleaux alors que dans le cas pathologique, les agrégats forment des structures tridimensionnelles isotropes. Les images pour le sang pathologique sont issues de (Schmid-Schönbein *et al.*1990).

Les méthodes adaptées à ce problème sont les *techniques ultrasonores d'estimation des microstructures tissulaires* basées sur l'analyse fréquentielle des signaux rétrodiffusés. Ces signaux contiennent des informations sur l'arrangement spatial, la taille, la concentration et les propriétés mécaniques des diffuseurs (i.e. des cellules). La technique consiste à mesurer expérimentalement le coefficient de rétrodiffusion (en anglais *BackScatter Coefficient - BSC*) par le tissu à caractériser, puis à utiliser une approche par problème inverse qui consiste à minimiser l'écart entre le coefficient de rétrodiffusion mesuré et le coefficient de rétrodiffusion théorique calculé à l'aide d'un modèle de diffusion approprié. Pour le sang agrégeant, l'enjeu est de développer et de valider expérimentalement un modèle de diffusion ultrasonore pour l'estimation de la structure des agrégats prenant en compte une forte hématocrite (40%) et des agrégats de globules rouges possédant parfois des structures complexes (polydisperse, anisotrope). En effet, la structure et l'organisation spatiale des agrégats de globules rouges sont des paramètres quantitatifs pertinents pour la caractérisation du sang puisque la structure des agrégats diffère entre des cas sains et pathologiques. Schmid-Schönbein *et al.* (1990) ont observé avec un microscope optique couplé à un rhéomètre transparent des échantillons de sang de patients normaux et diabétiques (voir Fig. 1.1). Les agrégats de globules rouges ont tendance à former des structures isotropes pour du sang humain pathologique comme le diabète, alors que les structures sont des rouleaux anisotropes pour du sang normal.

Le chapitre s'ouvre sur la présentation du modèle de facteur de structure utilisé de façon classique pour modéliser la diffusion ultrasonore par des globules rouges agrégés (Savéry & Cloutier 2001, Fontaine *et al.* 2002). Des simulations numériques de la rétrodiffusion ultrasonore par le sang sont ensuite présentées, basées sur le modèle de facteur de structure. Ces simulations ont permis d'isoler et d'étudier les effets de la taille des agrégats et de l'arrangement spatial des globules rouges sur l'allure du coefficient de rétrodiffusion. Cette étude numérique a aussi permis de développer un nouveau modèle de diffusion ultrasonore par des agrégats érythrocytaires. La précision de ce nouveau modèle pour estimer la structure des agrégats a été comparée à des modèles classiques sur la base de simulations numériques où la structure des agrégats est contrôlée. Le chapitre se ter-

mine sur des expériences *in vitro* sur du sang cisaillé en écoulement contrôlé, ainsi que sur des expériences *in vivo*.

1.1 Théorie de la rétrodiffusion ultrasonore

Afin de modéliser la rétrodiffusion ultrasonore par le sang, certaines hypothèses simplificatrices (mais acoustiquement réalistes) sont nécessaires. Premièrement, on suppose que les ondes de cisaillement et la conversion de mode sont négligeables, de telle sorte que seuls les ondes de compression sont prises en compte. Deuxièmement, l'atténuation du sang étant faible (<0.05 dB/mm/MHz), l'absorption est aussi négligée. Par conséquent, les globules rouges et le plasma sont décrits acoustiquement comme des milieux fluides non-visqueux. Par ailleurs, contrairement à la majorité des tissus biologiques, la rétrodiffusion par les agrégats érythrocytaires en écoulement dans le sang est aussi dépendante du temps. Cependant, on peut considérer que le mouvement du sang est beaucoup plus lent que la vitesse de propagation (environ 1540 m/s dans le sang). Le sang insonifié est donc considéré comme quasi-stationnaire (Mo & Cobbold 1993).

Sous ces conditions, les difficultés majeures pour modéliser la rétrodiffusion ultrasonore par le sang sont la fraction volumique des globules rouges élevée (i.e. l'hématocrite) et les agrégats de globules rouges. Dans cette partie, on rappelle comment ces difficultés ont été surmontées dans la littérature en présentant successivement la diffusion ultrasonore par un globule rouge isolé, un ensemble de globules rouges désagrégés et des globules rouges agrégés.

1.1.1 Rétrodiffusion ultrasonore par un globule rouge isolé

La description du phénomène de diffusion des ultrasons par une particule isolée fait habituellement intervenir la section efficace différentielle de diffusion définie comme la puissance ultrasonore totale diffusée par la particule par unité d'intensité incidente et par unité d'angle solide.

L'hémoglobine encapsulée par la membrane érythrocytaire est acoustiquement décrite comme un milieu fluide non-visqueux, caractérisé par une compressibilité κ_1=3.41×10^{-10} Pa^{-1} et une densité ρ_1=1.092 (ou de façon équivalente une impédance z_1=1.766 MRayl et une célérité c_1=1617 m/s) (Shung 1982 ; Savéry & Cloutier 2007). L'effet de la membrane érythrocytaire sur la rétrodiffusion acoustique est négligeable car la membrane est extrêmement fine d'environ 10 nm (en comparaison de la taille caractéristique du globule rouge d'environ 2.2 µm). Le plasma est acoustiquement décrit comme un milieu fluide non-visqueux, caractérisé par une compressibilité κ_2=4.09×10^{-10} Pa^{-1} et une densité ρ_2=1.021(ou de façon équivalente une impédance z_2=1.580 MRayl et une célérité c_1=1547 m/s) (Shung 1982 ; Savéry & Cloutier 2007). Un érythrocyte est donc considéré comme un milieu faiblement diffusant avec un contraste d'impédance acoustique entre le globule rouge et le plasma égal à $\gamma_z = (z_1 - z_2)/z_2 = 0.13$.

Un érythrocyte se présente comme un disque biconcave ayant un diamètre d'environ 8 µm et une épaisseur de 2.2 µm. Dans la plupart des expériences, on travaille à des fréquences f allant de 5 à 30 MHz, soit des longueurs d'onde allant de 50 à 300 µm. Puisque la longueur d'onde est grande par rapport à la taille d'un globule rouge, un érythrocyte peut être considéré comme un diffuseur de Rayleigh. En régime de diffusion Rayleigh, l'intensité ultrasonore rétrodiffusée est proportionnelle au carré du volume de la particule diffusante et varie comme la puissance 4^e de la fréquence des ultrasons ; un comportement qui ne dépend pas de la forme du diffuseur. La section efficace différentielle

de rétrodiffusion σ_b d'un érythrocyte faiblement diffusant est donné par (Mo & Cobbold 1993 ; Insana & Brown 1993) :

$$\sigma_b(k) = \frac{k^4 V_s^2}{4\pi^2}\gamma_z^2. \tag{1.1}$$

où k et le nombre d'onde et V_s est le volume d'un érythrocyte.

Un érythrocyte est souvent modélisé comme un diffuseur de forme simple, tel qu'une sphère de volume équivalent. Le volume d'un érythrocyte étant environ 94 μm^3, un érythrocyte peut être approché par une sphère de rayon a=2.82 μm. Afin de prendre en compte une forme sphérique, un facteur de forme sphérique F peut être ajouté dans l'expression de σ_b permettant de s'écarter des conditions de Rayleigh (Insana & Brown 1993 ; Savéry & Cloutier 2007) :

$$\sigma_b(k) = \frac{k^4 V_s^2 \gamma_z^2}{4\pi^2} F(k) = \frac{k^4 V_s^2 \gamma_z^2}{4\pi^2}\left(3\frac{sin(2ka) - 2ka\ cos(2ka)}{(2ka)^3}\right)^2. \tag{1.2}$$

Savery & Cloutier (2007) ont comparé la section efficace différentielle d'un érythrocyte biconcave de forme réaliste avec des formes géométriques simples (sphère, cylindre, ellipse) modélisant un globule rouge. Cette étude montre que pour des fréquences inférieures à 21 MHz (i.e. $ka < 0.21$), un érythrocyte peut être considéré comme une sphère de volume équivalent comme décrit à l'Eq. (1.2). Pour des fréquences plus hautes, la forme et l'orientation d'un érythrocyte peut modifier le comportement de la section efficace différentielle. Cependant, en pratique, pour un ensemble de globules rouges orientés aléatoirement, le comportement de la section efficace différentielle devrait dépendre d'un facteur de forme moyen permettant de repousser cette limite fréquentielle de 21 MHz pour l'expression de σ_b avec un facteur de forme sphérique. C'est pourquoi un ensemble de globules rouges désagrégés à des hématocrites de 0.06 à 0.3 montre expérimentalement une dépendance fréquentielle en f^4, i.e. de type Rayleigh, pour l'intensité rétrodiffusée jusqu'à 30 MHz (Wang & Shung 1997).

1.1.2 Rétrodiffusion ultrasonore par des globules rouges désagrégés

Considérons dans un premier temps le cas d'un ensemble de particules identiques distribuées de façon homogène et aléatoire dans l'espace lorsque la fraction volumique de particules est faible. L'onde incidente diffusée par chaque particule est indépendante de la présence des autres particules. L'intensité ultrasonore incohérente rétrodiffusée est la somme algébrique des intensités rétrodiffusées par les particules individuelles. Le coefficient de rétrodiffusion (noté par la suite BSC), défini comme la puissance rétrodiffusée par unité d'angle solide et par unité de volume pour une onde plane incidente d'amplitude unité, est proportionnel au nombre de diffuseurs par unité de volume n (lié à l'hématocrite ϕ par $n = \phi/V_s$) :

$$BSC(k) = n\sigma_b(k) \tag{1.3}$$

où σ_b est la section efficace différentielle d'un diffuseur isolé obtenu à l'Eq. (1.2). Cependant, même en l'absence d'agrégation, le sang humain à un hématocrite physiologique est une suspension concentrée de globules rouges ($\phi \approx$0.4). Les diffuseurs (i.e. les globules rouges) ne peuvent pas être traités de façon indépendante du fait des effets de proximité et des effets de corrélation qui contribuent à diminuer la puissance ultrasonore rétrodiffusée. En l'absence d'agrégation, plusieurs modèles ont été proposés (Mo & Cobbold 1986 ; Twersky 1987 ; Angelsen 1980 ; Mo & Cobbold 1992 ; Fontaine *et al.* 1999) et sont décrits

en détail dans l'article de revue de Mo & Cobbold (1993). Je présenterai içi en détail le modèle particulaire.

L'approche classique, appelée Modèle Particulaire (MP), consiste à sommer les contributions par les particules individuelles (plus petites que la longueur d'onde) et à modéliser leur interaction par un facteur d'entassement W (Mo and Cobbold 1986 ; Twersky 1987). Basé sur cette approche, le BSC est donné par :

$$BSC_{MP}(k) = n\sigma_b(k)W. \tag{1.4}$$

Le facteur d'entassement W décrit l'arrangement spatial des particules et peut être estimé par la fonction de corrélation de paire $g(\mathbf{r})$, qui est la probabilité de trouver deux particules séparées par une distance $\mathbf{r}$:

$$W = 1 + n \int (g(\mathbf{r}) - 1)\, d\mathbf{r}. \tag{1.5}$$

Pour des hématocrites faibles, quand la distribution spatiale des globules rouges est aléatoire et indépendante, [1] $(g(\mathbf{r})-1)$ est égal à 0 et W est égal à l'unité ; le BSC est simplement la somme des sections efficaces différentielles σ_b des globules rouges. Lorsque l'hématocrite augmente, W diminue graduellement vers 0 puisque le rapprochement spatial des particules produit un arrangement spatial plus ordonné. L'expression la plus utilisée pour le facteur d'entassement est basée sur l'approximation de Percus-Yevick pour des particules identiques, impénétrables et radicalement symétriques dans la dimension m (plans, cylindres et sphères respectivement pour m =1, 2 et 3) (Twersky 1987). Le facteur d'entassement de Percus-Yevick W_{PY} dépend uniquement de l'hématocrite et s'écrit pour des sphères en 3D (Twersky 1987) :

$$W_{PY} = \frac{(1-\phi)^4}{(1+2\phi)^2}. \tag{1.6}$$

Plusieurs études ont comparé des mesures expérimentales avec les prédictions théoriques du modèle particulaire BSC_{PM} en fonction de l'hématocrite (Shung 1982 ; Lucas & Twersky 1987 ; Yuan & Shung 1988). Pour des échantillons de globules rouges mis en suspension dans une solution saline qui ne présente pas d'agrégation, le modèle particulaire a permis d'expliquer la relation non-linéaire entre l'amplitude de l'intensité rétrodiffusée et l'hématocrite comme montrée à la Fig. 1.2 (Yuan & Shung 1988).

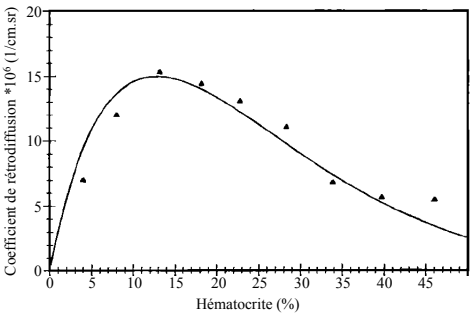

Figure 1.2 – Coefficients de rétrodiffusion mesurés sur des suspensions de globules rouges à des hématocrites variables. La courbe continue représente le modèle théorique du modèle particulaire calculé avec l'Eq. (1.4) en utilisant le facteur d'entassement de Percus-Yevick W_{PY}. Les points représentent les résultats expérimentaux. (Figure modifiée extraite de (Yuan & Shung 1988))

1. Deux variables aléatoires sont *indépendantes* si la probabilité pour que la valeur de l'une d'elle tombe dans un intervalle donné, ne dépend pas de la valeur prise par l'autre.

1.1.3 Rétrodiffusion ultrasonore par des globules agrégés : le Modèle de Facteur de Structure (MFS)

Une difficulté majeure pour modéliser la rétrodiffusion par le sang est de considérer des agrégats de particules. Les approches mentionnées ci-dessus ont échoué à prédire l'amplitude et la dépendance fréquentielle des signaux rétrodiffusés observés sur des expériences *in vitro* sur du sang agrégé (Yuan & Shung 1988). En effet, le sang agrégé ne présente pas une dépendance fréquentielle en f^4 contrairement au sang désagrégé (Yuan & Shung 1988, Savéry & Cloutier 2001). C'est pourquoi Savéry & Cloutier (2001) ont proposé le modèle de facteur de structure pour prédire la rétrodiffusion par des érythrocytes agrégés. Pour des particules identiques, le modèle de facteur de structure consiste à sommer la contribution des particules individuelles et à modéliser leur interaction par un facteur de structure (Savéry & Cloutier 2001, Fontaine *et al* 2002) :

$$BSC_{\mathrm{MFS}}(k) = n\sigma_b(k)S(k) = \frac{\phi}{V_s}\sigma_b(k)S(k). \tag{1.7}$$

Le phénomène d'agrégation se traduit par le facteur de structure S puisque les propriétés des globules rouges (i.e. σ_b et V_s) et l'hématocrite restent constante dans la région d'intérêt modélisée. Le facteur de structure permet de prendre en compte n'importe quel arrangement spatial des globules rouges. Il est par définition lié à la transformée de Fourier de la fonction de corrélation totale $(g(\mathbf{r}) - 1)$:

$$S(k) = 1 + n\int (g(\mathbf{r}) - 1)\, e^{-2j\mathbf{kr}} d\mathbf{r}. \tag{1.8}$$

La limite basse fréquence de S est par définition le facteur d'entassement W utilisé en régime de diffusion Rayleigh. Pour des globules rouges désagrégés en régime de diffusion Raygleigh, l'Eq. (1.7) se réduit directement à l'Eq. (1.4). Il est important de noter que le facteur de structure ne peut pas être calculé analytiquement contrairement au facteur d'entassement (Twersky 1987).

Le modèle de facteur de structure a été largement utilisé pour réaliser des études de simulations numériques sur l'agrégation érythrocytaire comme présenté dans le paragraphe suivant 1.2.

1.2 Simulations numériques de la diffusion ultrasonore par des globules rouges agrégés

1 article dans IEEE Trans Ultras Ferroelectr Freq Control (A7), en collaboration avec Bloen Metzger (IUSTI) et Guy Cloutier (LBUM, Canada)

Des simulations numériques ont été menées par le groupe de Cloutier pour prédire la dépendance fréquentielle du BSC pour différentes distributions spatiales de globules rouges en se basant sur le modèle de facteur de structure. La plupart de ces simulations ont été réalisés en 2D à cause du temps de calcul pour réaliser des distributions de particules à de fortes hématocrites (Savéry & Cloutier 2001 ; Fontaine *et al.* 2002 ; Fontaine & Cloutier 2003 ; Savéry & Cloutier 2005 ; Saha & Cloutier 2008). Les méthodes de distribution ont fait appel à des techniques basées sur la mécanique statistique et avaient pour objectif de simuler le comportement rhéologique du sang. Les distributions de globules rouges obtenues présentaient des agrégats avec une forme anisotrope et/ou une polydispersité en terme de taille ou de forme d'agrégats.

Pour les travaux présentés dans cette partie, nous avons utilisé une méthode simple et rapide pour distribuer aléatoirement des agrégats isotropes de tailles identiques. Bien que cette méthode ne permette pas de considérer des interactions réalistes entre les globules rouges, elle a permis d'isoler les effets de l'hématocrite, de la taille et de la compacité des agrégats sur la réponse ultrasonore (Franceschini *et al.* 2011 ; Saha *et al.* 2011).

1.2.1 Calcul du coefficient de rétrodiffusion avec le Modèle de Facteur de Structure (MFS)

Le calcul du BSC_{MFS} avec le modèle de facteur de structure nécessite de calculer le facteur de structure S, comme décrit à l'Eq. (1.7). Ce paragraphe décrit le calcul pratique du facteur de structure S obtenu à partir des distributions spatiales connues de particules.

Pour chaque distribution de globules rouges, une matrice M est calculée en divisant le domaine de simulation L^2 en N_p^2 pixels pour une simulation 2D (ou L^3 en N_p^3 pixels pour une simulation 3D) et en comptant le nombre de globules rouges présent dans chaque pixel. Cette matrice représente une distribution de densité définie par

$$M(\mathbf{r}) = \sum_{i=1}^{N} \delta(\mathbf{r} - \mathbf{r}_i) \tag{1.9}$$

où $\mathbf{r}_i$ désignent les vecteurs positions du centre du $i^{\text{ème}}$ globule rouge, N le nombre total de globules rouges et δ la fonction Dirac. Une expression équivalente de l'Eq. (1.8) pour le facteur de structure S peut être donnée en utilisant la distribution de densité M :

$$S(\mathbf{k}) = E\left[\frac{1}{N}\left|\int M(\mathbf{r}) e^{-i2\mathbf{kr}} d\mathbf{r}\right|^2\right] \tag{1.10}$$

où E est l'espérance mathématique. Le facteur de structure est alors calculé comme la moyenne des transformées de Fourier 2D pour les simulations numériques 2D (ou des transformées de Fourier 3D pour les simulations numériques 3D) de plusieurs distributions de densité pour un moyennage. La transformée de Fourier permet d'obtenir le facteur de structure $S(-2\mathbf{k})$ sur une grille de vecteurs d'onde entre $\pm\pi N_p/2L$ avec un pas de $\Delta k = \pi/L$. .

1.2.2 Influence de la taille et de la compacité des agrégats sur l'amplitude et la dépendance fréquentielle du coefficient de rétrodiffusion

Les simulations numériques 2D présentées ici ont permis d'isoler pour la première fois les effets de la compacité des agrégats ϕ_i (i.e. la concentration de globules rouges à l'intérieur des agrégats) sur la dépendance fréquentielle du BSC (Franceschini *et al.* 2011). L'algorithme de simulation a permis de générer des agrégats isotropes et impénétrables. Le positionnement des globules rouges à l'intérieur des agrégats est généré aléatoirement afin d'obtenir la compacité désirée, de façon à ce que l'arrangement spatial des globules rouges à l'intérieur des agrégats est différente pour chaque agrégat (section III.A, Franceschini *et al.* 2011).

Effet de la compacité des agrégats sur le BSC. La caractéristique de ces simulations 2D était la possibilité d'obtenir une compacité d'agrégats différente pour une taille d'agrégats identique. La figure 1.3 montre des arrangements spatiaux de globules rouges

pour une taille d'agrégat fixée $r_{ag} = 6.32a = 17.32$ µm et un hématocrite fixé ϕ=0.2 pour deux compacités d'agrégats différentes de 0.4 et 0.6. Les coefficients de rétrodiffusion correspondants BSC_{MFS} ont été calculés avec le modèle de facteur de structure pour différentes valeurs de compacités d'agrégats de 0.4, 0.5 et 0.6 pour un hématocrite de 0.2 (Fig. 1.3c). Lorsque la compacité des agrégats ϕ_i augmente, l'amplitude du BSC_{MFS} augmente en basses fréquences (<23 MHz). La position fréquentielle du premier pic est quasiment identique (entre 18.0 et 20.6 MHz) pour toutes les conditions simulées.

Effet de la taille des agrégats sur le BSC. La figure 1.4 illustre des BSC_{MFS} en fonction de la fréquence pour un cas désagrégé (r_{ag}/a=1) et pour des cas agrégés avec des rayons d'agrégats r_{ag}/a=3.16, 5.0 et 7.07, à différents hématocrites. Dans ces simulations, la compacité des agrégats est fixée à ϕ_i=0.6. Pour les fréquences inférieures à 20 MHz, l'amplitude des BSC_{MFS} augmente avec la taille des agrégats. Lorsque la taille des agrégats augmente, la position fréquentielle des pics des BSC_{MFS} se déplace vers les basses fréquences.

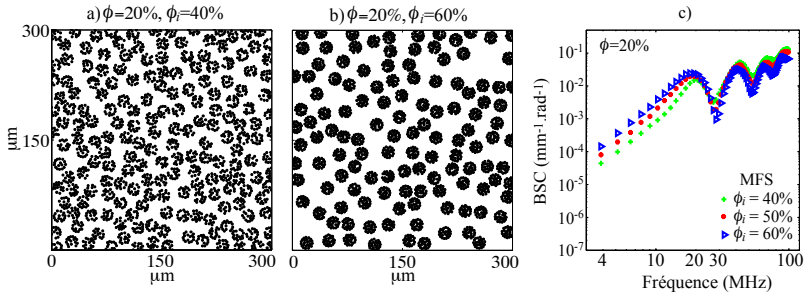

Figure 1.3 – (a) et (b) Distributions d'agrégats de globules rouges pour une taille d'agrégat fixée $r_{ag} = 6.32a = 17.32$ µm et un hématocrite fixé ϕ=0.2 pour deux compacités d'agrégats différentes (a) ϕ_i=0.4 et (b) ϕ_i=0.6. (c) Coefficients de rétrodiffusion BSC_{MFS} en fonction de la fréquence pour différentes compacités d'agrégats étudiées. Configurations d'agrégation : r_{ag}/a = 6.32 et ϕ=0.2

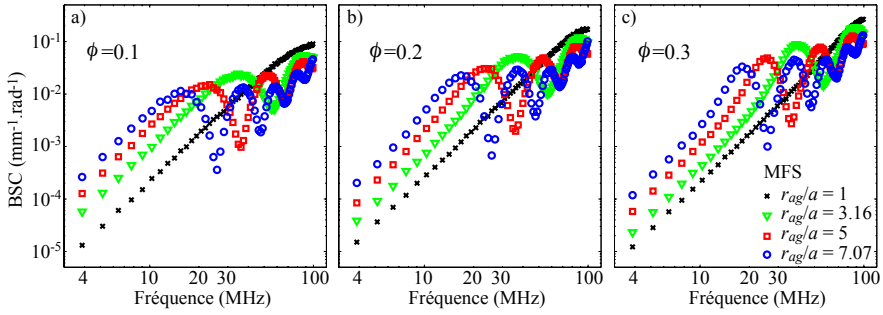

Figure 1.4 – Coefficients de rétrodiffusion BSC_{MFS} en fonction de la fréquence pour différentes tailles d'agrégats et une compacité fixée ϕ_i=0.6 à différents hématocrites de 0.1, 0.2 et 0.3.

Cette étude montre l'influence de la taille et de la compacité des agrégats sur le comportement du BSC. La taille ainsi que la compacité des agrégats ont une grande influence

sur l'amplitude du BSC. La position fréquentielle du premier pic du BSC est principalement affecté par les modifications de taille des agrégats (mais pas par des modifications de compacité). Des simulations numériques 3D en collaboration avec Ratan K. Saha (Saha Institute of Nuclear Physics, Inde) ont aussi été réalisées montrant des comportements similaires. Les simulations numériques 3D utilisent une structure hexagonale compacte pour l'arrangement spatial des globules rouges à l'intérieur des agrégats et se limitent donc à une compacité fixée élevée ($\phi_i = 0.74$) (Saha *et al* 2011), contrairement à l'étude 2D présentée içi.

1.3 Modèle de rétrodiffusion ultrasonore pour l'estimations des paramètres de structure des agrégats

Comme vu précédemment, le modèle de facteur de structure permet de simuler le coefficient de rétrodiffusion par des globules rouges quelle que soit la distribution spatiale des globules rouges (i.e. désagrégés ou agrégés avec une forme isotrope ou anisotrope et/ou avec différentes tailles, formes et compacités d'agrégats). Néanmoins, résoudre le problème inverse avec ce modèle est lourd en terme de calcul à cause de l'infinité des possibilités pour l'arrangement spatial des globules rouges. C'est pourquoi deux modèles de diffusion ultrasonore, à savoir l'estimateur de taille basé sur le facteur de structure (en anglais *Structure Factor Size Estimator* - SFSE) et la Théorie de Milieu Effectif combinée au Modèle de Facteur de Structure (TMEMFS), ont été récemment développées afin d'approcher le modèle de facteur de structure et d'estimer la structure des agrégats dans le cadre d'un problème inverse. Ces deux modèles sont basés sur des hypothèse simplificatrices concernant les distributions spatiales de globules rouges :

- Premièrement, les agrégats sont supposés de forme sphérique. Pour le sang humain, les cisaillements faibles favorisent la formation d'agrégats avec des structures anisotropes (i.e. rouleaux) ou isotropes (i.e. blocs sphériques) (Fig. 1.1). Les structures anisotropes en rouleaux sont plutôt associées au sang normal, alors que les agrégats sphériques sont caractéristiques du sang pathologique comme pour le diabète (Schmid-Schönbein *et al.*1990). L'hypothèse d'agrégats isotropes est donc valide pour l'étude des cas pathologiques.
- Deuxièmement, la polydispersité en terme de taille d'agrégats est supposée négligeable. Pour des mesures ultrasonores *in vivo* sur du sang en écoulement dans un vaisseau sanguin, le cisaillement varie avec la position radiale, et par conséquent, la distribution de la taille des agrégats varie aussi. C'est pourquoi les signaux rétrodiffusés par le sang sont généralement analysés sur une fenêtre rectangulaire ou une fenêtre de hamming glissante le long du signal temporel afin de pouvoir examiner le vaisseau entier à différentes profondeurs (Yu & Cloutier 2007, Yu *et al.* 2009). Par exemple, pour une fréquence centrale de 25 MHz, la longueur de la fenêtre est typiquement de 400 µm. Les agrégats de globules rouges sont donc considérés localement identiques, mais des variations peuvent être considérées dans une image ultrasonore en déplaçant une fenêtre d'analyse.

Cette partie présente les deux modèles de diffusion ainsi que leur évaluation par des simulations numériques.

1.3.1 Structure Factor Size Estimator (SFSE)

1 article dans J Acoust Soc Am (A9) en collaboration avec Ratan K. Saha (Saha Institute of Nuclear Physics, Inde) et Guy Cloutier (LBUM, Canada)

Yu & Cloutier (2007) ont développé le modèle SFSE basé sur le développement de Taylor au second ordre du facteur de structure.

$$\begin{aligned} S(-2k) &\approx C_0 + (-2k)C_1 + (-2k)^2 C_2 \\ &\approx W - 4R_g^2 k^2 \\ &\approx W - \frac{12}{5}(kD)^2 \end{aligned} \tag{1.11}$$

où C_0, C_1 et C_2 sont les coefficients de la série de Taylor. Dans l'Eq. 1.11 (comme dans l'article de Yu & Cloutier 2007), la dépendance de S en $(-2k)$ indique la configuration en rétrodiffusion quand le vecteur d'onde est opposé au vecteur d'onde incident **k**. Le coefficient C_0 est la limite basse fréquence du facteur de structure, appelée facteur d'entassement W, ici pour des globules rouges agrégés (Yu & Cloutier 2007). En considérant des agrégats isotropes, le coefficient C_1 est nul puisque le sang présente les mêmes structures dans les directions de propagation opposées **k** et **-k** (i.e. $S(-2k) = S(2k)$). Par une analyse dimensionnelle, le coefficient C_2 est une surface en m^2 et est supposé être lié au carré du rayon de giration R_g^2 (Yu & Cloutier 2007 ; Guinier 1964). Le diamètre de l'agrégat (normalisé par le rayon d'un globule rouge) peut aussi être lié au rayon de giration par $D = \sqrt{5/3}R_g/a$ (Yu & Cloutier 2007 ; Guinier 1964).

En résumé, le modèle SFSE permet de paramétrer le BSC en fonction de deux paramètres : le facteur d'entassement W et le rayon de giration des agrégats R_g.

$$\begin{aligned} BSC_{\mathrm{SFSE}}(k) &= n\sigma_b(k)\left(W - 4R_g^2 k^2\right) \\ &= \frac{\phi}{V_s}\frac{k^4 V_s^2 \gamma_z^2}{4\pi^2}\left(3\frac{\sin(2ka) - 2ka\cos(2ka)}{(2ka)^3}\right)^2\left(W - 4R_g^2 k^2\right). \end{aligned} \tag{1.12}$$

En supposant que l'hématocrite ϕ, le rayon de la sphère équivalente pour un globule rouge a et le contraste d'impédance γ_z sont connus *a priori*, les paramètres d'agrégation W et R_g sont évalués en minimisant l'écart entre le BSC mesuré et le BSC_{SFSE} théorique donné par l'Eq. (1.12).

La précision de la méthode SFSE pour l'estimation de la taille des agrégats a été évaluée par des simulations numériques 3D en collaboration avec Ratan K. Saha (Saha Institute of Nuclear Physics SINP, Inde) et Guy Cloutier (LBUM, Canada) (Saha *et al* 2011). L'algorithme de simulation a permis de générer aléatoirement (grâce à un générateur de nombres aléatoires) des agrégats sphériques, impénétrables et identiques. Les globules rouges à l'intérieur des agrégats possèdent un arrangement hexagonal compact permettant d'obtenir une compacité de 0.74. Le BSC pour les distributions 3D de globules rouges est calculé avec le modèle de facteur de structure supposé donner le coefficient de rétrodiffusion exact. Les calculs ont été réalisés dans la bande de fréquence de 1 à 50 MHz pour des tailles d'agrégats variant de 10 à 18 µm à des hématocrites de 0.2, 0.3 et 0.4. Pour chaque simulation, le facteur d'entassement W et le rayon de giration des agrégats R_g ont été évalués. Une très bonne corrélation avec des coefficients de corrélation supérieurs à 0.94 a été obtenue entre la taille réelle R_{sim} et la taille estimée R_g avec la méthode SFSE

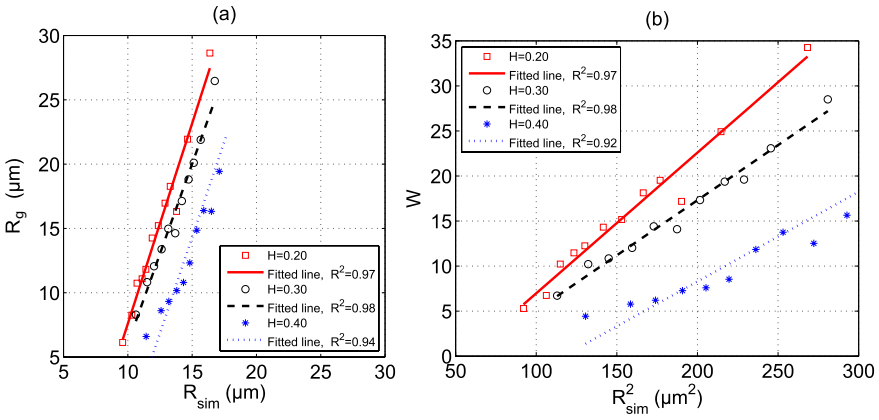

FIGURE 1.5 – (a) Taille des agrégats R_g estimée avec le modèle SFSE en fonction de la taille réelle de agrégats de globules rouges simulées R_{sim}. (b) Relation quadratique entre le facteur d'entassement W et la taille des agrégats R_g obtenus avec le modèle SFSE.

pour les trois hématocrites (Fig. 1.5a). Néanmoins, il est important de noter que les deux paramètres caractérisant l'agrégation (W et R_g) sont liés par une relation quadratique, comme on peut le voir sur la figure 1.5b. La méthode ne donnant pas les mêmes relations linéaires entre R_{sim} et R_g (Fig. 1.5a), et les paramètres W et R_g étant liés (Fig. 1.5b), on peut conclure que dans sa forme actuelle, le modèle SFSE est encore empirique.

1.3.2 Théorie de Milieu Effectif combinée au Modèle de Facteur de Structure (TMEMFS)

1 article dans IEEE Trans Ultras Ferroelectr Freq Control (A7) en collaboration avec Bloen Metzger (IUSTI) et Guy Cloutier (LBUM, Canada)
1 lettre en préparation pour IEEE Trans Ultras Ferroelectr Freq Control (A1) en collaboration avec Romain de Monchy (doctorant LMA), Ratan K. Saha (SINP, Inde), François Destrempes et Guy Cloutier (LBUM, Canada)

Le modèle SFSE ne permettant pas d'expliquer pleinement l'allure du coefficient de rétrodiffusion en fonction de la fréquence (Saha *et al* 2011), nous avons développé un nouveau modèle de diffusion basé sur la Théorie de Milieu Effectif combinée au Modèle de Facteur de Structure (TMEMFS). Le modèle TMEMFS considère les agrégats de globules rouges comme des particules homogènes individuelles, dont les propriétés effectives sont déterminées par la compacité des agrégats ϕ_i et les propriétés acoustiques du plasma et des globules rouges. L'approche de milieu effectif est combinée avec le modèle de facteur de structure pour considérer des milieux denses. L'interaction entre les particules effectives est donc modélisée par un facteur de structure. Le modèle TMEMFS permet de paramétrer le BSC en fonction de trois paramètres : la taille des agrégats r_{ag}, la concentration des globules rouges à l'intérieur des agrégats ϕ_i (appelée aussi la compacité des agrégats) et l'hématocrite ϕ. Une description complète du modèle TMEMFS est donnée ici.

En première approximation, on suppose que tous les globules rouges sont agrégés dans le sang, que les agrégats sont identiques et sphériques, et que les globules rouges à l'intérieur des agrégats sont distribués de façon équivalente. Le modèle TMEMFS suppose

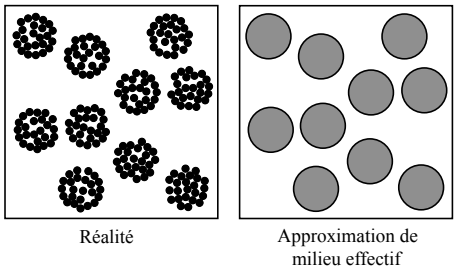

Figure 1.6 – Représentation schématique des agrégats traités comme des particules individuelles. Les agrégats de globules rouges dans le sang (à gauche) sont supposés être des particules homogènes (à droite) avec des propriétés effectives dépendant de la compacité des agrégats et de la densité et compressibilité des globules rouges.

que les agrégats de globules rouges peuvent être traités comme des particules homogènes individuelles (Fig. 1.6). Chaque agrégat est donc approché par une particule effective. La densité ρ_{ag} et la compressibilité κ_{ag} de la particule effective sont déterminées par la théorie de milieu effectif (Kuster & Toksoz 1974), i.e. ρ_{ag} et κ_{ag} dépendent des propriétés acoustiques des deux fluides constituant l'agrégat (i.e. ρ_1, ρ_2, κ_1 et κ_2, où l'indice 1 indique les propriétés des globules rouges et l'indice 2 les propriétés du plasma) et de la compacité ϕ_i :

$$\begin{aligned} \rho_{ag} &= \phi_i \rho_1 + (1-\phi_i)\rho_2 \\ \frac{1}{\kappa_{ag}} &= \frac{\phi_i}{\kappa_1} + \frac{1-\phi_i}{\kappa_2} \end{aligned} \tag{1.13}$$

Le BSC est obtenu en sommant les contributions par les particules individuelles de rayon r_{ag} et en modélisant l'interaction entre les particules effectives par un facteur de structure S_{ag}. L'expression du BSC équivalent est donnée par :

$$BSC_{\mathrm{TMEMFS}}(k) = n_{ag}\sigma_{ag}(k)S_{ag}(k), \tag{1.14}$$

où n_{ag} est le nombre moyen d'agrégats par unité de volume. La fraction volumique de particules effectives est égale au rapport entre la fraction volumique de globules rouges dans le sang ϕ et de la compacité des agrégats ϕ_i : $\phi_{ag} = \phi/\phi_i$. La section efficace différentielle de rétrodiffusion σ_{ag} d'une particule effective peut être déterminée par un modèle de sphère fluide (Insana & Brown 1993) :

$$\sigma_{ag}(k) = \frac{4k^4 r_{ag}^6 \gamma_{z_{ag}}^2}{9}\left(3\frac{\sin(2kr_{ag}) - 2kr_{ag}\cos(2kr_{ag})}{(2kr_{ag})^3}\right)^2 \tag{1.15}$$

où z_{ag} est l'impédance de la particle équivalente et $\gamma_{z_{ag}}$ le contraste d'impédance entre la particule effective et le plasma ($\gamma_{z_{ag}} = (z_{ag} - z_2)/z_2$). Le facteur de structure S_{ag} est calculé pour la distribution homogène et aléatoire de N_{ag} particules identiques de rayon r_{ag} grâce à la formule analytique de Wertheim en 3D (Wertheim 1963).

A noter que nous avons poursuivi le développement du modèle TMEMFS dans le cadre de la thèse de Romain de Monchy en collaboration avec François Destrempes et Guy Cloutier (LBUM, Canada). La théorie de milieu effectif a été modifiée pour décomposer la section efficace différentielle de rétrodiffusion σ_{ag} d'une particules effective en deux termes cohérent et incohérent ($\sigma_{\mathrm{ag}} = \sigma_{\mathrm{ag,coh}} + \sigma_{\mathrm{ag,incoh}}$) comme proposé par (Morse & Ingard 1968). Le terme cohérent $\sigma_{\mathrm{ag,coh}}$ correspond à l'onde moyenne émergeant du diffuseur effectif (i.e. l'agrégat), et le terme incohérent $\sigma_{\mathrm{ag,incoh}}$ correspond aux fluctuations de l'onde diffusée autour de sa moyenne. Cette amélioration permet d'améliorer la modélisation du BSC en hautes fréquences (de Monchy *et al* 2015). Seul le terme cohérent

donné à l'Eq. 1.15 est pris en compte dans (Franceschini *et al.* 2011, 2013) et dans la suite du manuscrit.

En supposant que l'hématocrite ϕ, le rayon de la sphère équivalente pour un globule rouge a et les propriétés acoustiques du plasma et des globules rouges sont connus *a priori*, les paramètres d'agrégation r_{ag} et ϕ_i sont évalués en minimisant l'écart entre le BSC mesuré et le BSC_{TMEMFS} théorique donné par l'Eq. (1.14).

1.3.3 Comparaison des modèles de diffusion ultrasonore pour déterminer la structure des agrégats

1 article dans IEEE Trans Ultras Ferroelectr Freq Control (A4) en collaboration avec Ratan K. Saha (SINP, Inde) et Guy Cloutier (LBUM, Canada)

A notre connaissance, il n'y a pas de moyens expérimentaux permettant d'évaluer la structure des agrégats à un hématocrite physiologique de 40% puisque le sang à cet hématocrite est opaque à la lumière visible. L'évaluation expérimentale de la précision de la méthode SFSE a été seulement réalisée pour un hématocrite faible de 6% en comparant des mesures optique et ultrasonore de taille d'agrégats de globules rouges statiques (Yu & Cloutier 2007). C'est pourquoi des simulations numériques 3D prédisant des BSC pour des globules rouges agrégés ont été réalisées pour évaluer la précision du modèle SFSE (Saha *et al.* 2011). Dans la présente étude, nous déterminons la précision du modèle TMEMFS pour évaluer les paramètres de structure des agrégats à partir de BSC_{MFS} simulés et nous le comparons au modèle SFSE. Cette comparaison est basée sur les simulations numériques 2D utilisant le modèle de facteur de structure présentées au paragraphe 1.2.2. A noter que la configuration d'agrégation lorsque la compacité des agrégats varie et le rayon des agrégats est fixé est facilement réalisable en 2D mais difficile à réaliser en 3D à cause du long temps de calcul pour générer des distributions de globules rouges avec des compacités variables (nécessaire pour le modèle de facteur de structure).

Les modèles SFSE et TMEMFS ont été premièrement examinés lorsque la taille des agrégats est fixe r_{ag}/a=6.32 et que la compacité varie de 0.4 à 0.6. A noter que, par la suite, les symboles $*$ désignent les estimations. La figure 1.7a représente les courbes d'ajustement obtenues avec les modèles SFSE et TMEMFS pour les BSC_{MFS} simulées déjà présentées à la Fig. 1.3. Les courbes d'ajustement obtenues avec le modèle SFSE surestiment l'amplitude des BSC_{MFS} simulés en basses fréquences, alors que le modèle TMEMFS permet d'obtenir des courbes d'ajustement satisfaisantes. Les valeurs des tailles d'agrégats R_g^* estimées avec le modèle SFSE et des paramètres r_{ag}^*/a et ϕ_i^* obtenues avec le modèle TMEMFS sont données respectivement dans les figures 1.7b et 1.8a. Bien que le rayon réel des agrégats soit fixé, les tailles d'agrégat R_g^* estimées par le modèle SFSE augmentent avec la compacité (Fig. 1.7b). On peut noter la relation linéaire entre les paramètres W^* and R_g^* quand la compacité des agrégats ϕ_i varie (Fig. 1.7c), comme observé précédemment par Yu & Cloutier (2007) et Saha *et al.* (2011). Par conséquent, le modèle SFSE ne montre pas de corrélation significative entre les rayons des agrégats réels et estimés (r^2 <0.06). Le modèle SFSE ne peut pas prendre en compte une variation de compacité des agrégats puisque une variation de compacité est interprétée comme une modification de la taille des agrégats. Alors que le modèle TMEMFS permet d'obtenir des résultats quantitatifs satisfaisants avec des erreurs relatives inférieures à 12% (Fig. 1.8b).

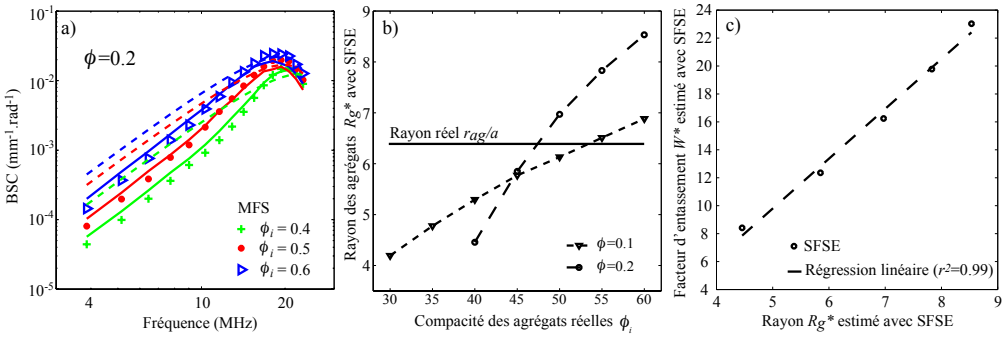

FIGURE 1.7 – (a) Coefficients de rétrodiffusion calculés avec le modèle MFS pour différentes compacités et un rayon d'agrégat fixe r_{ag}/a=6.32 à un hématocrite de 0.2 ; et courbes d'ajustement correspondantes avec le modèle SFSE (courbes en pointillés) et avec le modèle TMEMFS (courbes continues). (b) Rayons des agrégats R_g^* estimés avec le modèle SFSE en fonction de la compacité réelle des agrégats. (c) Relation linéaire entre les paramètres W^* et R_g^* obtenus avec le modèle SFSE.

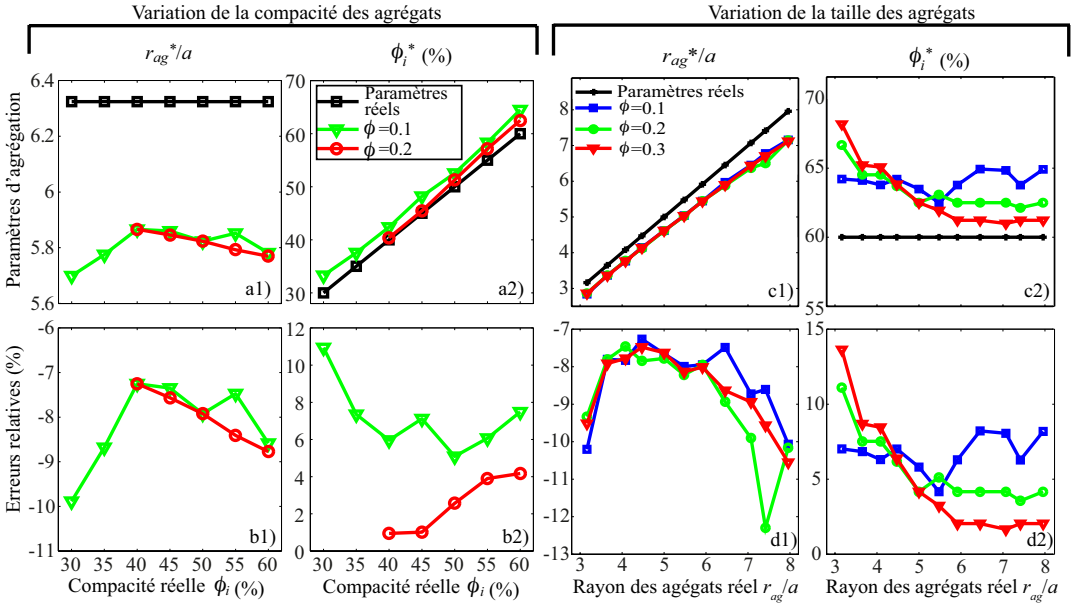

FIGURE 1.8 – Valeurs des paramètres d'agrégation estimées par la Théorie de Milieu Effectif combinée au Modèle de Facteur de Structure (TMEMFS) (a) en fonction de la compacité réelle des agrégats lorsque la taille des agrégats est fixe r_{ag}/a=6.32 et (c) en fonction de la taille réelle des agrégats lorsque la compacité des agrégats est fixe ϕ_i=0.6. (b) et (d) Erreurs relatives correspondantes.

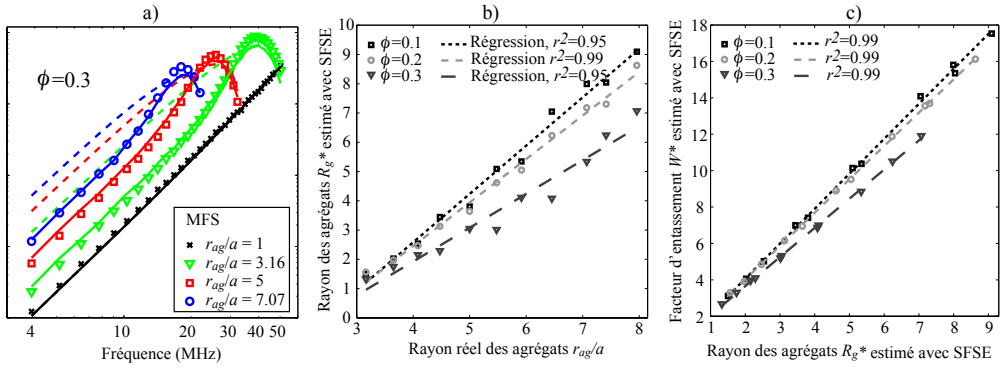

Figure 1.9 – (a) Coefficients de rétrodiffusion calculés avec le modèle de facteur de structure pour différentes tailles d'agrégats et une compacité fixe ϕ_i=0.6 pour un hématocrite de 0.3. Les lignes en pointillés représentent les courbes d'ajustement avec la méthode SFSE tandis que les lignes continues les courbes d'ajustement pour le modèle TMEMFS. (b) Comparaison entre les rayons d'agrégats estimés avec SFSE et la taille réelle r_{ag}/a pour les hématocrites de 0.1, 0.2 et 0.3. (c) Relation linéaire entre W^* and R_g^*.

Les modèles SFSE et TMEMFS ont aussi été évalués lorsque la taille des agrégats varie et que la compacité est fixe $\phi_i = 0.6$. La figure 1.9a présente les courbes d'ajustement avec les modèles SFSE et TMEMFS pour les BSC_{MFS} simulés à un hématocrite de 0.3. Le modèle TMEMFS permet d'obtenir des courbes d'ajustement satisfaisantes alors que le modèle SFSE surestime l'amplitude des BSC_{MFS} simulés en basses fréquences. Pour le modèle SFSE, des corrélations significatives (r^2 $\geq$0.95) ont été obtenues entre les tailles réelle et estimée pour tous les hématocrites (Fig. 1.9b). Les erreurs relatives obtenues avec le modèle TMEMFS pour les tailles et les compacités des agrégats sont inférieures à 13% et 14%, respectivement, pour tous les hématocrites étudiés (Fig. 1.8c et d) ; alors que les erreurs relatives sur la taille des agrégats estimée avec le modèle SFSE sont comprises entre 24 et 62% pour des hématocrites élevés.

Pour conclure, bien que la méthode SFSE ne produise pas des courbes d'ajustement satisfaisantes, des corrélations significatives ont été obtenues entre les tailles des agrégats réelles et estimées (r^2 $\geq$0.95) lorsque la compacité des agrégats est fixe. Cependant, le modèle SFSE ne montre pas de corrélation significative entre la taille des agrégats fixe et celle estimée lorsque la compacité varie, et les paramètres W^* et R_g^* sont liés par une relation linéaire. La méthode SFSE est donc réduite à un modèle à un seul paramètre. Le modèle TMEMFS donne des estimations des paramètres d'agrégation satisfaisantes lorsque la taille et la compacité des agrégats varie pour tous les hématocrites étudiés. Ces résultats montrent la supériorité du modèle TMEMFS par rapport au modèle SFSE. Pour le moment, le modèle SFSE est largement utilisé car son temps de calcul pour remonter aux paramètres d'agrégation à partir de la mesure d'un BSC est dix fois plus rapide que le temps de calcul du modèle TMEMFS. Par ailleurs, la méthode SFSE a été développée pour considérer l'atténuation dans les mesures *in vivo* (Franceschini *et al.* 2008, 2010), alors que ce travail n'a toujours pas été effectué avec le modèle TMEMFS.

1.4 Expériences *in vitro* sur du sang en écoulement

1 brevet (B2) en collaboration avec Guy Cloutier (LBUM, Canada)

Par la suite, nous avons aussi confronté les modèles SFSE et TMEMFS sur des données expérimentales. Il est difficile de contrôler les paramètres de structure des agrégats même dans des conditions expérimentales *in vitro*. L'expérience *in vitro* la plus simple consiste à cisailler le sang dans un dispositif de Couette (Fig. 1.10) permettant de créer un écoulement avec un profil de vitesse $v(z)$ linéaire et un cisaillement constant en fonction de la profondeur z. L'écoulement contient donc des agrégats de globules rouges qui ont une taille caractéristique dépendant du taux de cisaillement auquel ils sont soumis. La figure 1.10 montre le comportement typique des BSC_{mes} en fonction de la fréquence pour du sang de porc à un hématocrite ϕ de 0.3 cisaillé à différents taux de cisaillement dans le dispositif de Couette. Ces mesures ont été réalisées au LBUM à Montréal (lors de mes séjours effectués entre 2009 et 2011) avec un échographe Visualsonics Vevo 770 (Toronto, Canada) équipé d'une sonde ultrasonore de fréquence centrale 25 MHz (RMV 710). Les BSC_{mes} mesurés indiquent içi les mesures expérimentales du coefficient de rétrodiffusion. Les BSC_{mes} ont été calculés par une technique de fantôme de référence. Cette technique consiste à utiliser un milieu diffusant de référence dont le BSC est connu, afin de compenser les spectres de puissance des signaux rétrodiffusés pour la fonction d'instrumentation et pour les effets de focalisation et de diffraction du transducteur ultrasonore. Comme observé à la Fig. 1.10, l'amplitude du BSC_{mes} augmente et la position fréquentielle du premier pic se déplace vers les basses fréquences lorsque le cisaillement décroit (i.e. lorsque le niveau d'agrégation augmente). Nous avons aussi représenté les courbes d'ajustement obtenues avec les modèles SFSE et TMEMFS, ainsi que les paramètres de structure correspondants. Le modèle SFSE permet d'obtenir des courbes d'ajustements satisfaisantes (sauf pour le niveau d'agrégation le plus élevé avec le cisaillement 2 s^{-1}), et les paramètres de structure W^* et D^* estimés augmentent lorsque le cisaillement décroit. Le modèle TMEMFS donne des courbes d'ajustements médiocres. La taille des agrégats r_{ag}/a estimée avec le modèle TMEMFS augmente lorsque le cisaillement décroit, comme attendu. On peut noter que la compacité des agrégats ϕ_i reste quasiment constante avec des valeurs comprises entre 0.73 et 0.89.

La simplicité du modèle SFSE permet d'obtenir des bonnes courbes d'ajustement alors que les simulations numériques ont montré que le modèle SFSE est empirique et n'est pas basé sur une théorie physique. Il est important de noter que le modèle SFSE ne produit pas de bonnes courbes d'ajustement pour des tailles d'agrégats importantes : typiquement $D \geq 14$ (Yu *et al.* 2009). Le modèle TMEMFS n'est pas suffisant pour expliquer l'allure des BSC_{mes} expérimentaux car il est probable que les approximations réalisées sur la structure des agrégats ne sont pas réalistes. L'une des approximations majeures est l'hypothèse d'une taille d'agrégats monodisperse. Pour un modèle monodisperse, les pics des BSC sont d'autant plus prononcés que l'hématocrite est élevé, comme on peut le voir à la Fig. 1.4. Les BSC_{mes} expérimentaux ne présentent pas de pics de BSC prononcés (sauf pour les niveaux d'agrégation très élevés). La prise en compte de la polydispersité en terme de taille des agrégats devrait permettre de se rapprocher de la distribution de taille réelle des agrégats et d'améliorer l'allure des BSCs. Nous avons réalisé un premier test préliminaire pour explorer cette voie en considérant une distribution d'agrégats bidisperse.

Dans le sang, seulement une fraction de globules rouges est agrégée. Dans cette partie, nous supposons qu'une fraction de globules rouges Φ est agrégée, alors que le reste $(1 - \Phi)$ reste désagrégé, et que tous les agrégats sont identiques et isotropes. L'expression du

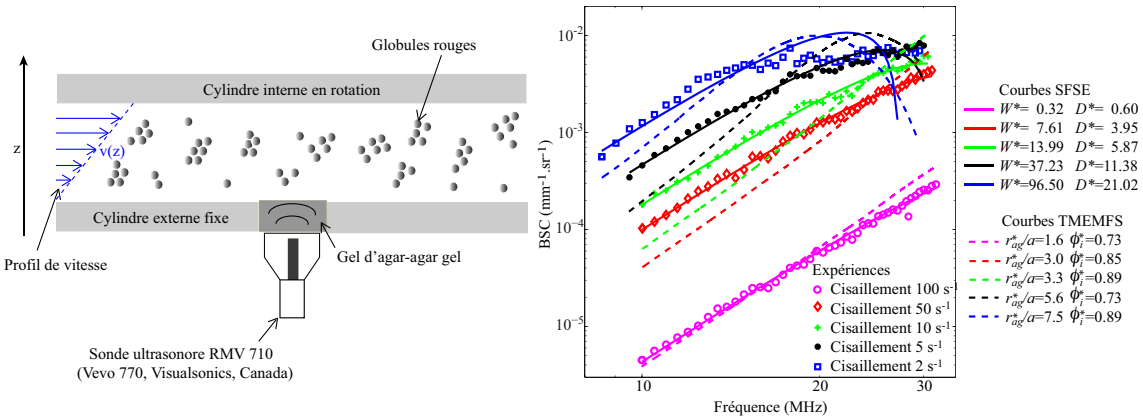

Figure 1.10 – (A gauche) Schéma du dispositif de Couette couplé à une sonde ultrasonore. (A droite) Coefficients de rétrodiffusion mesurés BSC_{mes} sur du sang de porc cisaillé dans un dispositif de Couette (dans la bande de fréquence à -20 dB) et courbes d'ajustement obtenues avec les modèles SFSE et TMEMFS.

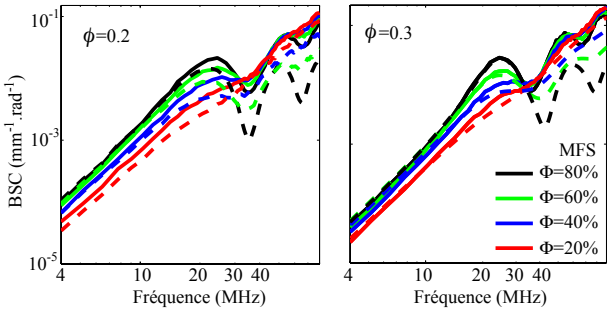

Figure 1.11 – Coefficients de rétrodiffusion calculés avec le modèle exact de facteur de structure (traits continus) et le modèle TMEMFS bidisperse (traits en pointillés) à des hématocrites ϕ de 0.2 et 0.3 pour différentes valeurs de Φ. Pour les globules rouges agrégés, la configuration d'agrégation est la suivante : r_{ag}/a=5 et ϕ_i=0.6.

BSC équivalent pour des agrégats bidisperses peut être approchée par une simple loi de mélange :

$$BSC_{\text{TMEMFS}_B}(k) = \Phi BSC_{\text{TMEMFS}}(k; r_{ag}, \phi'_{ag}) + (1-\Phi)BSC_{\text{PM}}(k; a, \phi'), \qquad (1.16)$$

où le BSC_{TMEMFS} correspond au BSC pour des globules rouges agrégés de rayon r_{ag} avec une concentration d'agrégats $\phi'_{ag} = \phi\Phi/\phi_i$ donnée par le modèle TMEMFS monodisperse (Eq. 1.14), et le BSC_{PM} correspond au BSC pour des globules rouges désagrégés avec une concentration $\phi' = \phi(1-\Phi)$ donné par le modèle particulaire (Eq. 1.4 et Eq. 1.6). Le modèle TMEMFS bidisperse permet donc de paramétrer le BSC en fonction de trois paramètres : la taille r_{ag} et la compacité ϕ_i des agrégats et la fraction de globules rouges agrégés Φ (au lieu de deux paramètres avec le modèle TMEMFS monodisperse). Nous avons comparé les BSC_{MFS} simulés (calculés avec le modèle de facteur de structure) et les BSC_{TMEMFS_B} calculés avec le modèle TMEMFS bidisperse lorsque tous les paramètres d'agrégation sont connus. Le modèle TMEMFS bidisperse basé sur une simple loi de mélange donne une bonne correspondance entre les BSC simulés et théoriques, comme on peut le voir à la Fig. 1.11. Comme attendu, les pics du BSC deviennent de moins en moins prononcés lorsque la fraction de globules rouges agrégés diminue. Nous avons aussi mené une étude numérique pour déterminer les paramètres de structure avec le modèle TMEMFS bidisperse à partir des BSC_{MFS} simulés avec le modèle de facteur de structure. Nous avons pu montrer que

les erreurs relatives obtenues sur la taille et la compacité des agrégats étaient inférieures à 28% et 7%, respectivement, quels que soient les hématocrites et les fractions de globules rouges agrégés étudiés (Franceschini & Cloutier 2014).

Reprenons à présent les mesures expérimentales de BSC_{mes} sur du sang de porc cisaillé dans le dispositif de Couette présenté à la Fig. 1.10. La figure 1.12 montre les courbes d'ajustements avec le modèle TMEMFS bidisperse (traits en pointillés) ainsi que les paramètres de structure estimés pour les différents cisaillements. Le rayon des agrégats r_{ag}^*/a et la fraction de globules rouges agrégés Φ^* estimés avec le modèle TMEMFS bidisperse augmentent lorsque le cisaillement décroit (i.e. lorsque le niveau d'agrégation augmente). La compacité des agrégats estimée ϕ_i^* est quasiment identique et comprise entre 0.86 et 0.89 quel que soit le niveau d'agrégation étudié. On peut noter que les valeurs des rayons et des compacités estimées avec les modèles TMEMFS monodisperse et bidisperse sont similaires. Cependant le modèle bidisperse permet d'obtenir de meilleures courbes d'ajustement, excepté pour le niveau d'agrégation le plus élevé avec le cisaillement 2 s^{-1} (comme observé précédemment avec le modèle SFSE). On peut observer la présence de deux pics sur la courbe expérimentale BSC_{mes} au cisaillement 2 s^{-1} qui pourraient correspondre à la contribution de deux tailles d'agrégats. Le modèle TMEMFS bidisperse peut être légèrement modifié pour considérer deux tailles d'agrégats r_{ag1} et r_{ag2} (au lieu des deux tailles r_{ag} et a). Un exemple de courbe d'ajustement obtenu pour deux tailles d'agrégats r_{ag1}/a=8.7 et r_{ag2}/a=4.8 (et des compacités fixées à 0.89) est donné en trait continu sur la Fig. 1.12. La correspondance avec la courbe expérimentale est bien meilleure mais le nombre de paramètres à considérer est considérablement augmenté (5 paramètres au lieu de 3).

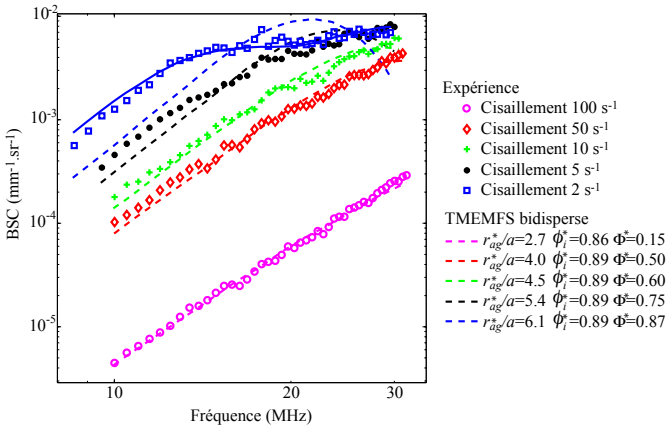

Figure 1.12 – Coefficients de rétrodiffusion mesurés BSC_{mes} identiques à la Fig. 1.10 et courbes d'ajustement obtenues avec le modèle TMEMFS bidisperse. Les traits en pointillés représentent le modèle bidisperse considérant une taille d'agrégat r_{ag}/a et des globules rouges désagrégés de rayon a. La courbe en trait plein représente la courbe d'ajustement pour le cisaillement 2 s^{-1} avec le modèle TMEMFS bidisperse considérant deux tailles d'agrégat r_{ag1}/a et r_{ag2}/a.

Pour conclure, ces premiers développements préliminaires considèrent un modèle TMEMFS bidisperse basé sur une simple loi de mélange permettant de produire de bonne courbes d'ajustement aux mesures expérimentales *in vitro*. Notons qu'il est possible de construire des modèles de diffusion ultrasonore bidisperse ou polydisperse de façon plus rigoureuse. Ce travail fait l'objet de la thèse de Romain de Monchy qui a débuté sa thèse en Octobre 2013. Le modèle est basé sur un facteur de structure analytique polydisperse basé sur l'approximation de Percus-Yevick (Griffith *et al.* 1987) considérant une fonction de distribution de taille, type loi Gamma-Schulz.

1.5 Estimation simultanée de la structure des agrégats et de l'atténuation : vers les applications *in vivo*

1 brevet (B1), 1 article dans J Acoust Soc Amer (A10) et 1 lettre dans J Acoust Soc Amer Express Letter (A12) en collaboration avec François T. H. Yu (doctorant, LBUM), François Destrempes et Guy Cloutier (LBUM)

Lors de mon post-doctorat au LBUM de l'Université de Montréal, mes travaux de recherche ont principalement porté sur le développement de la méthode SFSE pour les applications *in vivo*. Pour exploiter des mesures *in vivo*, la principale difficulté est de prendre en compte les effets d'atténuation des tissus intermédiaires (tels que la peau) situés entre la sonde ultrasonore et le vaisseau sanguin. En effet, l'absorption et la diffraction des tissus intermédiaires affectent le contenu fréquentiel des signaux rétrodiffusés par le sang provoquant une estimation erronée des paramètres ultrasonores de structure. Des groupes de recherche comme He & Greenleaf (1986), Oosterveld *et al.* (1991) ont développé des techniques de mesures *in vivo* pour évaluer l'atténuation et compenser *a posteriori* les coefficients de rétrodiffusion. Plus récemment, Bigelow *et al.* (2005) ont proposé une méthode pour estimer simultanément la taille effective des diffuseurs et l'atténuation totale. Ces deux paramètres sont déterminés par une méthode d'optimisation permettant de faire correspondre le spectre des signaux rétrodiffusés par la région d'intérêt avec un spectre estimé par un modèle théorique approprié. Nous avons adapté cette dernière stratégie pour l'estimation de la taille des agrégats érythrocytaires en modifiant légèrement le modèle SFSE pour le modèle *Structure Factor Size and Attenuation Estimator* SFSAE (Franceschini *et al.* 2008). La méthode SFSAE permet de déterminer simultanément les paramètres de structure du sang (i.e. W et D) et l'atténuation totale des tissus intermédiaires en modélisant le BSC comme (Franceschini *et al.* 2008) :

$$\begin{aligned} BSC_{\text{SFSAE}}(k) &= n\sigma_b(k)\left(W - \frac{12}{5}(kaD)^2\right)A(k) \\ &\approx n\sigma_b(k)\left(W - \frac{12}{5}(kaD)^2\right)e^{\frac{-4\alpha_0 k}{8.68}\frac{c}{2\pi}} \end{aligned} \tag{1.17}$$

où A est la fonction d'atténuation totale, c est la vitesse moyenne dans les tissus intermédiaires et α_0 est le coefficient d'atténuation (en dB/MHz) défini par : $\alpha_0 = \sum_i \alpha_i e_i$, où α_i et e_i sont respectivement les atténuations des tissus intermédiaires et leurs épaisseurs. Le coefficient 8.68 dans l'Eq. (1.17) exprime la conversion des dB au Neper : α_0[Neper/MHz]= α_0[dB/MHz]/8.68. On fait donc l'hypothèse usuelle pour les tissus mous que l'atténuation augmente linéairement avec la fréquence f : $\alpha(f) = \alpha_0 f/8.68$. Le facteur d'entassement W^*, le diamètre des agrégats D^* et l'atténuation totale sur le trajet de propagation α_0^* sont déterminés en faisant correspondre le BSC mesuré et le BSC_{SFSAE} théorique donné par l'Eq. (1.17).

Notons que la méthode SFSAE permet d'estimer l'atténuation totale, incluant les tissus intermédiaires situés entre la sonde et le vaisseau sanguin, mais aussi l'atténuation du sang lui-même. La peau est la couche de tissu la plus atténuante. L'atténuation du derme humain est égale à environ 0.21 dB/mm/MHz à 14-50 MHz (Raju and Srinivasan 2001). Alors que l'atténuation du sang est plus faible variant de 0.015 dB/mm/MHz pour du sang désagrégé à 0.053 dB/mm/MHZ pour des niveaux d'agrégation élevés (Franceschini *et al.* 2010).

Le premier objectif était d'isoler et de mettre en évidence les effets de l'absorption sur la détermination ultrasonore des paramètres quantitatifs de structure des agrégats. L'expérience réalisée est la suivante : un écoulement sanguin est réalisé dans un dispositif de Couette, cet écoulement contient des agrégats de globules rouges avec une taille caractéristique (dépendant du taux de cisaillement auquel ils sont soumis). Une couche d'agar-agar chargée de microsphères de cellulose (Sigmacell) est placée entre le transducteur et l'écoulement, et permet de modéliser une couche de tissu absorbant (appelée fantôme acoustique de peau). Cette couche ayant une impédance proche de celle du sang et ces interfaces étant parallèles aux fronts d'onde, les effets de la diffraction sont négligeables : seul le phénomène d'absorption a lieu. La figure 1.13 représente les BSC mesurés avec différents fantômes de peau d'atténuations variables pour les cisaillements 5, 10 et 50 s^{-1}. Pour tous les cisaillements, l'augmentation de l'atténuation provoque une diminution de l'amplitude des BSC à toutes les fréquences, ainsi qu'un décalage du pic du BSC vers les basses fréquences. Il est intéressant d'observer l'influence de l'atténuation sur l'allure du BSC en régime quasi-Rayleigh pour des globules rouges désagrégés, i.e. au cisaillement 50 s^{-1}. En effet, pour le cisaillement 50 s^{-1} combiné à la mesure de référence sans Sigmacell, la dépendance fréquentielle du BSC est proche de f^4 et est quasi-linéaire sur une échelle logarithmique. En présence d'atténuation, les dépendances fréquentielles sont fortement modifiées.

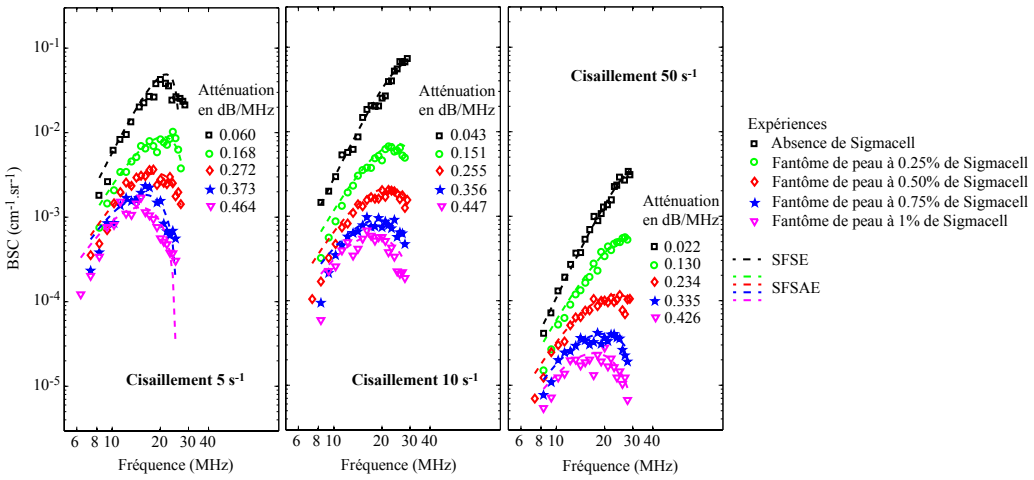

Figure 1.13 – Coefficients de rétrodiffusion mesurés pour du sang cisaillé à 5, 10 et 50 s^{-1} avec différents fantômes acoustiques de peau. Les courbes en noir représentent les expériences sans fantôme acoustique de peau (absence de Sigmacell) et constituent donc les mesures de référence. Les valeurs d'atténuation données içi correspondent à la somme des atténuations du fantôme de peau et du sang mesurées par une méthode classique de substitution.

Ce dispositif expérimental a aussi permis de valider la méthode d'optimisation que nous avons proposée afin d'évaluer simultanément l'atténuation totale des tissus intermédiaires α_0 et les paramètres quantitatifs de structure W et D. La figure 1.14 montre les images quantitatives pour du sang cisaillé à 10 s^{-1} dans le dispositif de Couette en l'absence de couche absorbante (mesure de référence) et avec deux fantômes acoustiques de peau. Une distinction claire peut être observée pour les images d'atténuation, alors que les images paramétriques des paramètres de structure W^* et D^* sont similaires pour tous les fantômes de peau étudiés, comme attendu. Notons que les images des paramètres

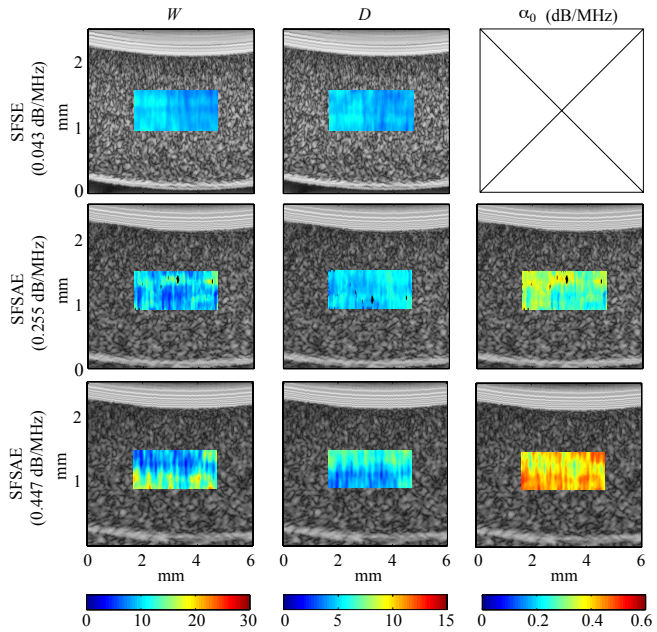

Figure 1.14 – Images quantitatives de sang cisaillé à 10 s^{-1} dans un dispositif de Couette superposées aux images en mode B. Les paramètres de structure sont estimés avec le modèle classique SFSE pour l'expérience sans couche absorbante (en haut) et avec le modèle SFSAE pour les expériences avec les fantômes acoustiques de peau.

W^* et D^* sont homogènes puisque le niveau d'agrégation est identique quelle que soit la profondeur explorée dans un dispositif de Couette. Cette étude a permis de montrer que la méthode SFSAE donne des estimations précises des paramètres W^*, D^* et α_0^* pour des atténuation totales comprises entre 0.115 et 0.411 dB/MHz et pour des tailles d'agrégats D_{ref} inférieures à 10.11 (correspondant à un produit $kr_{ag} < 2.08$ à f_c=25 MHz).

Des mesures ultrasonores ont aussi été réalisées *in vivo* sur les veines d'un bras d'un sujet sain avec l'échographe Visualsonics Vevo 770 (Toronto, Canada) équipé avec une sonde de fréquence centrale 25 MHz. Trois conditions d'écoulement sanguin sont étudiées : un écoulement normal, un écoulement bloqué en effectuant une constriction autour de la veine, et finalement un écoulement complexe sur une zone contenant deux valves veineuses fermées présentant des zones de stagnation et de circulation. Pour chaque écoulement, les paramètres W^*, D^* et α_0^* sont évalués (Fig. 1.15) et résumés dans le tableau 1.1. A noter que les pixels en noir sur les images quantitatives correspondent aux solutions rejetées lorsque l'un des paramètres W^* ou D^* estimé est nul, ce qui est irréaliste (section V.D. dans Franceschini *et al.* 2010). Pour les deux paramètres de structure W^* et D^*, des différences statistiquement significatives sont observées entre les conditions d'écoulement normal et bloqué, ainsi qu'entre les zones de stagnation et de circulation dans le cas des deux valves veineuses (Franceschini *et al.* 2009). Cette étude a montré la capacité du modèle SFSAE à estimer les paramètres de structure des agrégats *in vivo* et *in situ*.

Table 1.1 – Estimation moyenne du facteur d'entassement W^*, du diamètre des agrégats D^* et de l'atténuation totale α^* en dB/cm/MHz pour trois conditions d'écoulement.

	Ecoulement sanguin normal	Ecoulement sanguin bloqué	Ecoulement complexe	
			Circulation	Stagnation
W^*	0.91 ± 0.70	2.17 ± 1.82	0.86 ± 0.46	4.20 ± 1.34
D^*	1.61 ± 0.59	2.42 ± 1.13	1.09 ± 0.66	3.69 ± 0.81
α_0^*	0.221 ± 0.106	0.246 ± 0.105	0.342 ± 0.067	0.318 ± 0.036

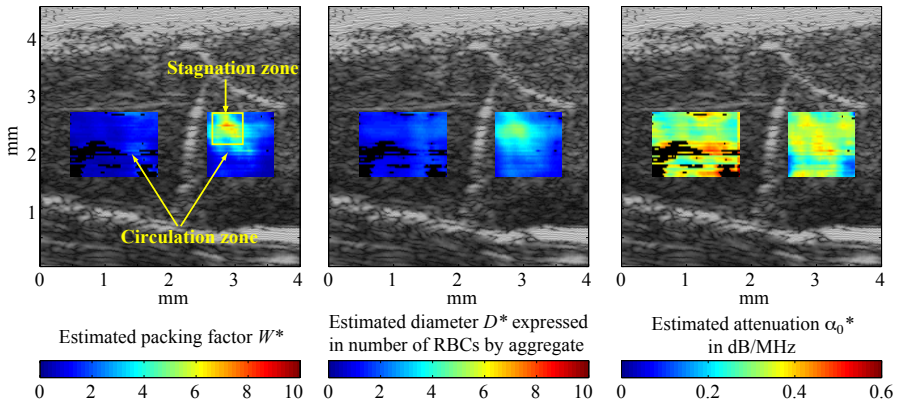

Figure 1.15 – Images quantitatives des trois paramètres (facteur d'entassement W^*, diamètre des agrégats D^* et absorption totale α_0^*) estimés par la méthode SFSAE. Les images quantitatives sont superposées à l'image B-mode représentant deux valves fermées dans une veine du bras d'un sujet normal. Comme attendu, la région où le sang stagne (région située en dessous de la valve du haut) présente des valeurs de W^* et D^* plus importantes puisque la stagnation favorise l'agrégation.

1.6 Conclusion

Ce chapitre s'est focalisé sur des simulations numériques afin de comprendre l'influence de la structure des agrégats sur la dépendance fréquentielle du BSC et sur deux modèles théoriques approchés, le SFSE (ou SFSAE) et le TMEMFS, permettant d'évaluer les paramètres de structure des agrégats érythrocytaires. La méthode SFSAE que nous avons proposée est capable d'évaluer simultanément la structure des agrégats et l'atténuation totale des tissus intermédiaires entre la sonde et le vaisseau sanguin *in vivo* et *in situ*. Les futures études *in vivo* seront menées pour montrer que les paramètres quantitatifs ultrasonores de structure des agrégats sont des biomarqueurs pertinents d'inflammation (voir par exemple le suivi de la réponse inflammatoire avant et après un pontage cardio-pulmonaire - Tripette *et al.* 2013).

La théorie TMEMFS récemment proposée est un modèle de diffusion prometteur pour la caractérisation des agrégats. Des simulations numériques ont pu montrer la supériorité du modèle TMEMFS pour estimer la taille et la compacité des agrégats en comparaison de la méthode SFSE. La contribution importante de ce nouveau modèle est la paramétrisation du BSC avec la compacité des agrégats, qui est un nouveau paramètre de structure dans le domaine de l'imagerie ultrasonore quantitative basée sur le BSC. Néanmoins, le modèle

TMEMFS nécessite d'être développé afin de prendre en compte (1) la polydispersité en terme de taille des agrégats, (2) l'anisotropie des agrégats et (3) la possibilité d'estimer simultanément l'atténuation comme pour la méthode SFSAE.

Chapitre 2

Diffusion ultrasonore par des fantômes de tumeurs denses - Compréhension des phénomènes

Le deuxième thème de mes activités de recherche concerne la caractérisation ultrasonore par des tumeurs par des techniques d'estimation de microstructures (i.e. taille et concentration des diffuseurs) basées sur l'analyse fréquentielle des signaux rétrodiffusés. Une approche classique consiste à faire correspondre le coefficient de rétrodiffusion (en anglais *BackScatter Coefficient* BSC) mesuré expérimentalement avec un BSC estimé par un modèle théorique approprié. Le modèle de diffusion couramment utilisé est le modèle continu Gaussien développé par Lizzi *et al.* (1983, 1986) qui décrit le tissu comme un milieu hétérogène aléatoire avec des fluctuations d'impédance continues. Le modèle continu Gaussien permet de remonter à deux paramètres : la taille moyenne des diffuseurs et la concentration acoustique définie comme le produit du nombre de diffuseurs par unité de volume et du carré du contraste d'impédance (Lizzi *et al.* 1986, Oelze & O'Brien 2006). Cette approche a été utilisée pour faire le suivi de la réponse tumorale aux thérapies (Kolios *et al.* 2002), pour différencier des tissus sains et pathologiques et pour détecter des tumeurs cancéreuses pour l'oeil (Feleppa *et al.* 1986), la prostate (Feleppa *et al.* 1997) et le sein (Oelze *et al.* 2002, 2004). Une autre classe de modèle théorique décrit le milieu comme des diffuseurs discrets aléatoirement distribués utilisant (1) un modèle discret de sphères fluides, une sphère modélisant une cellule isolée ou un noyau isolé (Anderson 1950, Oelze & O'Brien 2006, Han *et al.* 2013) ou (2) un modèle discret de sphères concentriques, deux sphères concentriques modélisant le noyau et le cytoplasme (Oelze & O'Brien 2006, McNew *et al.* 2009, Teisseire *et al.* 2010, Han *et al.* 2011). Dans les modèles mentionnés ci-dessus (modèle Gaussien, modèle discret de sphères fluides ou modèle discret de sphères concentriques), les diffuseurs sont supposés être distribués de façon aléatoire et indépendante[1], et la diffusion multiple est négligée. Sous ses hypothèses, l'intensité rétrodiffusée augmente linéairement avec la concentration des diffuseurs et dépend de la taille et des propriétés acoustiques des structures diffusantes. Cette relation linéaire a été utilisée pour remonter à la taille et à la concentration acoustique. Cependant, des expériences ultrasonores menées sur des transplantations de greffons (xénogreffes) de tumeurs simples

1. On rappelle que deux variables aléatoires sont *indépendantes* si la probabilité pour que la valeur de l'une d'elle tombe dans un intervalle donné, ne dépend pas de la valeur prise par l'autre.

(carcinome et sarcome) ont montré qu'il était difficile d'établir un lien entre les tailles des diffuseurs évaluées par ultrasons et estimées par histologie quel que soit le modèle utilisé (Oelze & O'Brien 2006). Dans cette étude, Oelze & O'Brien (2006) attribuent l'insuccès des techniques d'estimation de taille au fait que les modèles de diffusion (pour une cellule isolée ou pour un ensemble de cellules) ne sont pas adaptés, les structures responsables de la diffusion au sein des tumeurs n'étant pas connues.

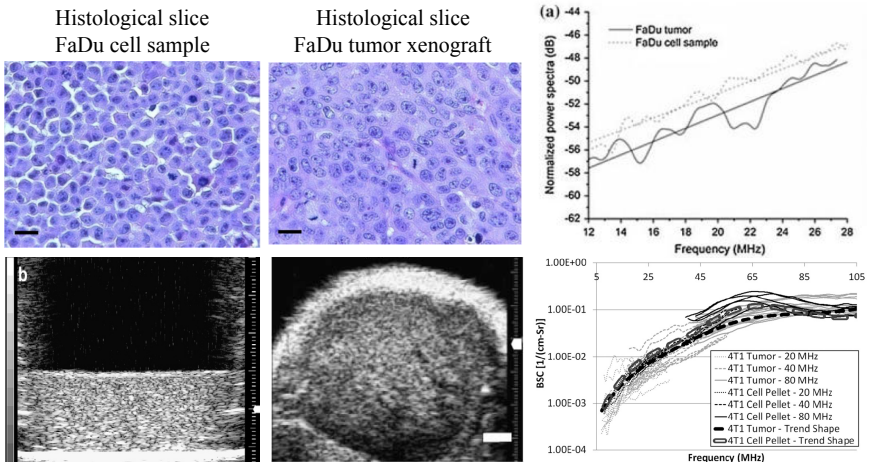

Figure 2.1 – Comparaison des coefficients de rétrodiffusion mesurés sur des cellules centrifugées (appelées culots de cellules) et des xénogreffes de tumeurs dont les cellules sont issues de la même lignée cellulaire (Falou *et al.* 2013, Han *et al.* 2013). On peut observer que les allures des coefficients de rétrodiffusion sur les culots et les xénogreffes sont similaires. Les culots de cellules centrifugées constituent donc des versions simplifiées de tumeurs puisqu'une seule lignée cellulaire est considérée. Les images sont extraites des articles (Falou *et al.* 2013) et (Han *et al.* 2013).

Ainsi, en parallèle de ces travaux sur l'estimation ultrasonore des microstructures, des études expérimentales sont aussi menées pour mieux comprendre et identifier les sources de diffusion. Identifier les structures responsables de la diffusion ultrasonore permettra d'améliorer les modèles de diffusion théoriques et donc d'augmenter la spécificité des techniques d'estimation de microstructure. Baddour *et al.* (2005, 2007) et Falou *et al.* (2010) ont réalisé différentes études pour mesurer la réponse ultrasonore (fréquences de 12 à 57 MHz) par des cellules isolées et ont modélisé la cellule comme une sphère unique possédant des propriétés acoustiques uniformes. Ces mesures expérimentales ont été comparées avec des prédictions théoriques d'un modèle de sphère fluide (Anderson 1950) ou d'un modèle de sphère élastique (Faran 1951). Falou *et al.* ont ainsi pu montrer qu'un modèle de sphère fluide possédant la taille de la cellule entière pouvait correctement modéliser la réponse d'une cellule isolée. Taggart *et al* (2007) ont conduit des mesures hautes fréquences sur des culots de cellules centrifugées composés de cellules mono- ou multi-nucléées ou de noyaux isolés. Cette étude suggère que les mesures de BSC sont corrélées à la taille des noyaux. Teisseire *et al.* (2010) et Han *et al.* (2011) ont récemment développé des bio-fantômes de tissus (i.e. des culots de cellules) avec différentes concentrations cellulaires allant de 0.0017 à 0.63. Les fortes concentrations représentent des cellules entassées et donc un milieu très compact proche de la disposition spatiale des cellules dans une tumeur (Fig. 2.1). Les mesures du BSC sur les bio-fantômes ont été comparées avec le modèle discret de deux sphères concentriques (McNew *et al.* 2009) dans la bande de fréquence allant de

26 à 105 MHz. Pour des faibles concentrations cellulaires ($\leq$0.026), les tailles des cellules estimées par ultrasons correspondent aux tailles réelles des cellules entières, mais pas pour des fortes concentrations cellulaires (>0.096) (Han *et al.* 2011). Une relation non-linéaire a aussi été observée entre l'amplitude du BSC et la concentration cellulaire pour des fréquences inférieures à 50 MHz, qui peut être causé par la diffusion cohérente (Han *et al.* 2011). Cette étude sur les bio-fantômes de cellules suggère que le modèle discret de deux sphères concentriques devient moins fiable lorsque la concentration cellulaire augmente.

L'enjeu scientifique est donc de répondre aux deux questions suivantes : quels sont les modèles de diffusion adaptés à un amas dense de cellules ? Quelles sont les principales structures responsables de la diffusion ultrasonore au sein des tumeurs ? L'hypothèse simplificatrice de diffuseurs disposés de façon indépendante et aléatoire n'est pas adaptée pour des cellules étroitement entassées dans une tumeur (Vlad *et al.* 2010). Un modèle adapté au milieu dense est le modèle de facteur de structure utilisé pour la caractérisation ultrasonore du sang (Savéry & Cloutier 2001, Fontaine *et al.* 2002). Dans ce chapitre, je présente la comparaison des modèles classiques (modèle continu Gaussien et/ou modèle discret) avec le modèle de facteur de structure avec deux études expérimentales sur des fantômes de tissus biologiques (des suspensions denses de microsphères de polyamide) et sur des bio-fantômes de cellules. Nous verrons que les modèles classiques sont mis en défaut pour décrire la diffusion par des milieux concentrés. Nous discutons les sources de diffusion au sein des bio-fantômes de cellules à l'aide du modèle de facteur de structure.

2.1 Evaluation expérimentale de quatre modèles de diffusion pour caractériser des fantômes de tissus biologiques concentrés

Un article (A5) dans J Acoust Soc Amer en collaboration avec Régine Guillermin (LMA)

2.1.1 Etude du problème direct : comparaison des résultats théoriques et expérimentaux

Des expériences ultrasonores ont été réalisées avec deux transducteurs focalisés de fréquences centrales 10 et 17.5 MHz sur des fantômes de tissus biologiques (Franceschini & Guillermin 2012). Ces fantômes sont constitués de microsphères de polyamide (Orgasol, Arkema) de rayon moyen 6 µm modélisant des noyaux de cellules (rayon compris entre 4 et 7 µm) en suspension dans de l'eau. Les microsphères de polyamide sont caractérisées par une célérité $c = 2300$ m/s, une densité $\rho = 1.03$ et un coefficient de Poisson $\nu = 0.42$. Ces fantômes ont une taille de particules identiques avec un contraste d'impédance de 48% (contre 32% pour les noyaux de cellules) mais ont différentes concentrations volumiques allant de 1 à 25%. Les fantômes à fortes concentrations simulent des cellules entassées dans une tumeur.

Les modèles théoriques (modèle discret de sphères élastiques, modèle particulaire de Percus-Yevick et modèle de facteur de structure) ont été comparés avec les mesures expérimentales dans le cadre du problème direct. Les BSC théoriques ont donc été calculés à partir des paramètres (acoustiques et structurels) connus des microsphères et comparés avec les BSC expérimentaux. Le modèle discret de sphères élastiques s'applique seulement aux milieux aléatoires (i.e. milieux à faibles concentrations). Les modèles particulaire de

Percus Yevick et de facteur de structure ont été utilisés dans le domaine de la caractérisation ultrasonore de l'agrégation érythrocytaire (Savéry & Cloutier 2001, Fontaine *et al.* 2002). Le modèle de facteur de structure est basé sur l'hypothèse qu'à fortes concentrations de diffuseurs, les interférences sont principalement causés par les corrélations entre les positions spatiales des diffuseurs. Le modèle de facteur de structure somme les contributions des cellules individuelles et modélise leur interaction par un facteur de structure (voir section 1.1.3 au chapitre 1). Dans cette étude, la distribution des microsphères est considérée homogène et le facteur de structure est calculé de façon analytique pour des sphères distribuées de façon aléatoire (Wertheim 1963). Comme vu précédemment dans la section 1.1.2 au chapitre 1, le modèle particulaire de Percus Yevick est la limite basse fréquence du modèle de facteur de structure. Ces deux derniers modèles sont donc adaptés à des milieux fortement concentrés.

Dans l'expérience proposée, l'amplitude et la dépendance fréquentielle des BSCs sont bien prédites par les modèles particulaire de Percus-Yevick et de facteur de structure (Fig. 2.2b). Le modèle de sphères élastiques et le modèle particulaire de Percus-Yevick surestiment l'amplitude du BSC pour des concentrations supérieures à 2.5% et 12.5%, respectivement (Fig. 2.2c). Le modèle de facteur de structure donne la meilleure correspondance entre les prédictions théoriques de BSC et les données expérimentales en comparaison des deux autres modèles (Fig. 2.2c).

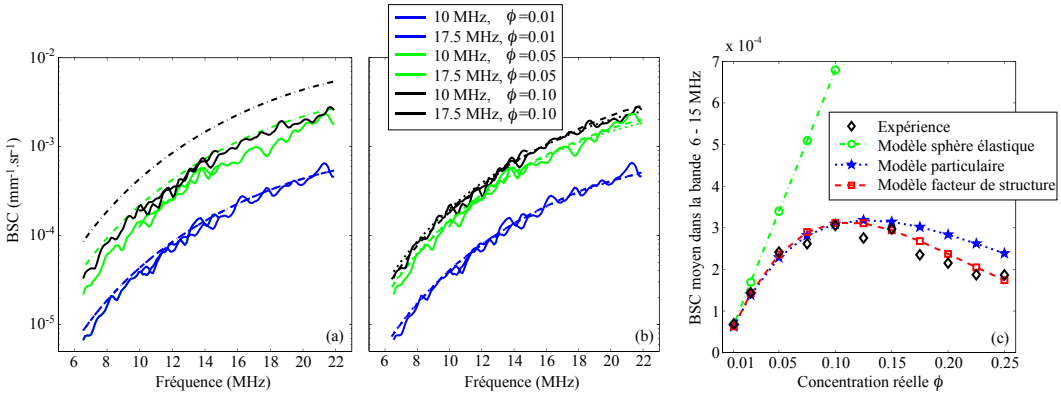

Figure 2.2 – (a) Comparaison des BSC théoriques calculés avec le modèle discret de sphères élastiques (traits en pointillé) et les BSC expérimentaux pour les concentrations de 0.01, 0.05 et 0.10. (b) Même figure que (a) pour les modèles particulaire de Percus-Yevick et de facteur de structure, les deux modèles donnant des courbes de BSC quasiment identiques pour ces concentrations. (c) Comparaison des BSC théoriques et expérimentaux moyennés dans la bande de fréquence de 6 à 15 MHz en fonction de la concentration réelle des microsphères.

2.1.2 Etude du problème inverse : estimation des paramètres de structure

Sur la base de ces expériences, nous nous sommes aussi intéressées au problème inverse, i.e. à l'estimation des paramètres de structure (taille et concentration) à partir de la mesure expérimentale du BSC (Franceschini & Guillermin 2012). Les modèles classiques (continu Gaussien et de sphères élastiques) ne permettent pas d'estimer correctement les paramètres

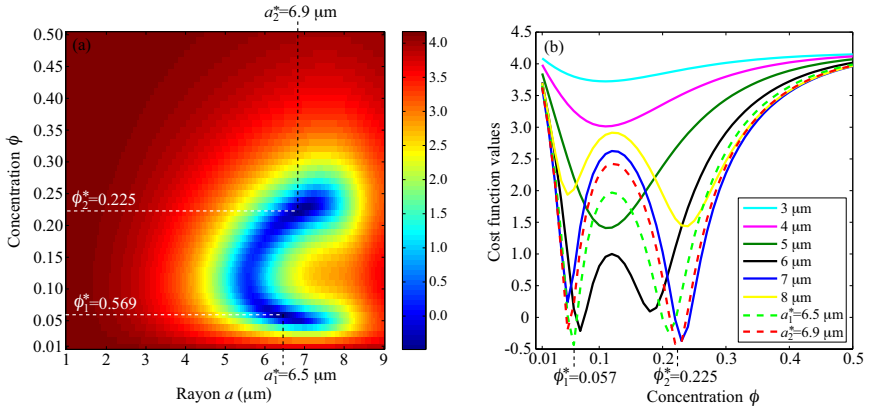

FIGURE 2.3 – (a) Exemple du logarithme de la fonction coût $\log(F_{MFS}(a,\phi))$ obtenue pour une mesure sur les microphères de rayon 6 µm et de concentration réelle 0.2. Cette fonction coût présente deux minima locaux (a_1^*,ϕ_1^*) et (a_2^*,ϕ_2^*). (b) Exemple de fonctions $\log(F_{MFS}(a,\phi))$ obtenue pour différentes valeurs fixées de a. Ces fonctions coûts présentent un ou deux minima.

de structure : le modèle Gaussien surestime la taille et sous-estime la concentration, alors que le modèle de sphères élastiques donne une taille de diffuseurs satisfaisante mais surestime la concentration pour des concentrations réelles supérieures à 12.5%. L'inversion des modèles particulaire de Percus-Yevick et de facteur de structure s'est révélée difficile car les fonctions coûts peuvent présenter deux minima locaux : l'un correspondant à une faible concentration, l'autre à une forte concentration (Fig. 2.3). En effet, comme on peut le voir dans l'étude du BSC moyen en fonction de la concentration (Fig. 2.2c), l'amplitude des BSC peut être identique pour des faibles et fortes concentrations (par exemple 5% et 20%). Pour l'estimation des paramètres a et ϕ, la méthode consiste à évaluer deux couples de solutions (a_1^*,ϕ_1^*) et (a_2^*,ϕ_2^*), correspondant respectivement à une faible valeur initiale et une forte valeur initiale de la concentration au début de la procédure d'optimisation. La solution finale (a^*,ϕ^*) est la valeur minimale entre les deux fonctions coûts $F(a_1^*,\phi_1^*)$ et $F(a_2^*,\phi_2^*)$ (i.e. le minimum global). La figure 2.4 présente les résultats de l'inversion pour le modèle de facteur de structure. Des résultats similaires ont été obtenus avec le modèle particulaire de Percus-Yevick. Comme on peut l'observer sur la Fig. 2.4, le minimum global ne correspond pas à chaque fois à la solution attendue, alors que l'un des deux minima locaux est toujours proche de la solution attendue. Afin de résoudre ce problème, deux possibilités ont été envisagées : (1) travailler à des fréquences plus élevées, et (2) combiner le modèle de facteur de structure avec d'autres paramètres quantitatifs permettant de différencier les faible et forte concentrations (atténuation, paramètres d'enveloppes statistiques). Dans ce cas, le modèle de facteur de structure donne des estimations de taille et de concentration satisfaisantes : les erreurs relatives sont inférieures à 20% pour la taille et inférieures à 38% pour la concentration. Le modèle particulaire de Percus-Yevick est moins performant, pouvant atteindre des erreurs relatives de l'ordre de 100% pour estimer la concentration, alors que le produit ka est relativement faible (i.e. compris entre 0.15 et 0.55 pour les fréquences de 6 à 22 MHz).

Pour conclure, cette étude expérimentale a permis (1) de déterminer les limites des modèles classiques (continu gaussien et discret de sphères élastiques) pour caractériser des

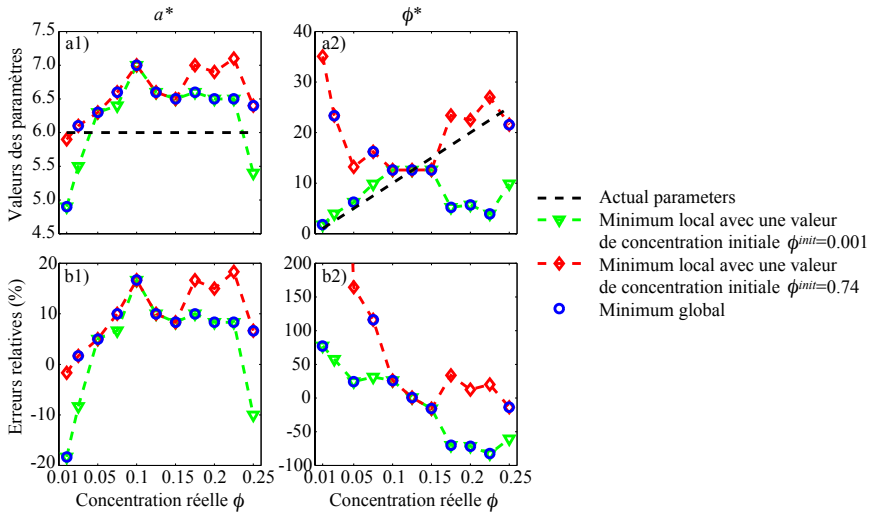

Figure 2.4 – Paramètres estimés avec le modèle de facteur de structure pour les différentes concentrations de microsphères. Les courbes verte et rouge représentent les deux couples de solutions (a_1^*,ϕ_1^*) et (a_2^*,ϕ_2^*), correspondant respectivement à une faible valeur initiale et une forte valeur initiale de la concentration au début de la procédure d'optimisation. Les symboles circulaires bleus représentent le minimum global.

milieux concentrés et (2) de montrer la supériorité du modèle de facteur de structure en comparaison des modèles classiques et du modèle basse fréquence de Percus Yevick. A ma connaissance, le modèle de facteur de structure n'a jamais été utilisé dans le cadre de la caractérisation ultrasonore des tumeurs cancéreuses alors que la concentration cellulaire peut être importante au sein d'une tumeur. Je poursuis ces travaux en collaboration avec Olivier Basset du laboratoire CREATIS-LRMN (Lyon) dans le cadre de l'ANR BBMUT afin de confronter cette méthode d'analyse fréquentielle avec une technique de statistiques des niveaux de gris de l'image enveloppe (thèse de Anca Cristea à CREATIS) pour différencier des milieux dilués et concentrés.

2.2 Modèle de facteur de structure pour la caractérisation ultrasonore de bio-fantômes de cellules

2.2.1 Identification des structures responsables de la diffusion au sein de bio-fantômes de cellules

Un article [A3] dans J. Acoust. Soc. Amer., en collaboration avec Franck Tourniaire (LMA), Régine Guillermin (LMA) et Jean-François Landrier (UMR INSERM 1062/INRA 1260)

Après avoir démontré la supériorité du modèle de facteur de structure pour caractériser des milieux concentrés avec des microsphères solides de polyamide, nous nous sommes intéressés à une expérience similaire sur des fantômes de tissus biologiques plus proches de la réalité en développant des bio-fantômes de cellules K562 (lignée cellulaire de leucémie

humaine). Ce travail a été réalisé en collaboration avec des biologistes, Franck Tourniaire (CDD IR LMA) et Jean-François Landrier (UMR INSERM 1062/INRA 1260, Marseille), et des anatomo-pathologistes, Edouard Lamy et Sandrine Roffino (faculté de pharmacie de la Timone, Marseille).

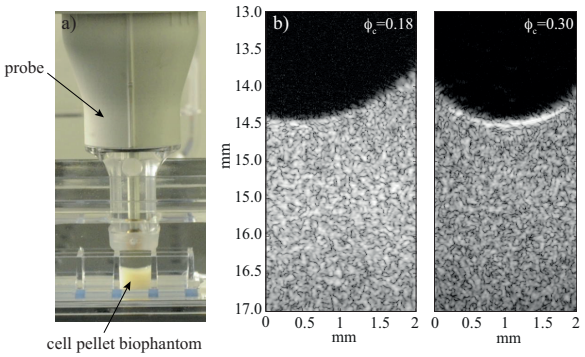

Figure 2.5 – (a) Sonde ultrasonore et bio-fantôme de cellule immergé dans une solution saline. (b) Images B-mode de bio-fantômes de cellules pour des concentrations de 0.18 et 0.30 avec une sonde de fréquence centrale 20 MHz.

Les bio-fantômes consistent en des cellules mises en suspension puis figées dans un mélange coagulé de plasma et de thrombine à fortes fractions volumiques de cellules variant de 0.006 à 0.30. La concentration de 0.30 représente des cellules entassées et donc un milieu très compact proche de la disposition spatiale des cellules dans une tumeur. Les culots de cellules sont ensuite examinés par voie ultrasonore avec un échographe de recherche (Visualsonics Vevo 770, sondes de 20 et 35 MHz, échographe de recherche acquis dans le cadre de ce projet) durant l'heure suivant la préparation du culot (Fig. 2.5). L'objectif de cette étude était de comparer trois modèles (modèle de sphères fluides, modèle particulaire de Percus Yevick et modèle de facteur de structure) pour comprendre la diffusion ultrasonore par un ensemble de cellules. Même si une seule lignée cellulaire est utilisée pour l'élaboration des bio-fantômes, les cellules ne possèdent pas la même taille, et l'allure des BSC est affectée par la distribution de taille des diffuseurs (surtout en hautes fréquences). Nous présentons dans un premier temps la modification apportée sur ces trois modèles pour prendre en compte un ensemble de sphères de tailles variables (et de propriétés acoustiques identiques).

Pour un milieu polydisperse, l'expression du modèle de facteur de structure implique le calcul complexe de facteur de structure partiel et peut-être simplifiée par l'utilisation d'une *approximation locale monodisperse* (Pederson 1994, 1997). Cette approximation suppose qu'un diffuseur avec une taille donnée est entouré par des diffuseurs de tailles identiques. Sous cette hypothèse, le système polydisperse est approché par plusieurs sous-systèmes où les particules sont monodisperses. La diffusion par un milieu polydisperse est calculée comme la somme des diffusions de sous-systèmes monodisperses pondérée par la fonction de distribution de taille (i.e. la probabilité que le rayon de la sphère prenne la valeur r) $p(r)$. Le BSC théorique s'exprime alors de la façon suivante :

$$BSC_{MFS}^{polyd}(k) = n \int_0^\infty p(r)\sigma_b(k,r)S(k,r,\phi)dr, \quad \text{Modèle de Facteur de Structure MFS} \tag{2.1}$$

où $\sigma_b(k,r)$ est la section efficace différentielle de rétrodiffusion par une sphère de rayon r calculée par l'Eq. 1.2, $S(k,r,\phi)$ est le facteur de structure monodisperse pour un système équivalent, constitué seulement de particules de rayon r avec une concentration totale fixée ϕ, et n est le nombre total de diffuseurs par unité de volume lié à la concentration totale ϕ de sphères par $m = \dfrac{\phi}{(4/3)\pi \int_0^\infty p(r) r^3 dr}$. A partir de l'Eq. 2.1, on peut déduire l'expression des BSC pour les deux autres modèles :

$$\begin{aligned} BSC_{MP}^{polyd}(k) &= n\frac{(1-\phi)^4}{(1+2\phi)^2}\int_0^\infty p(r)\sigma_b(k,r)dr, && \text{modèle particulaire Percus-Yevick} \\ BSC_{MDSF}^{polyd}(k) &= n\int_0^\infty p(r)\sigma_b(k,r)dr, && \text{modèle discret de sphères fluides} \end{aligned} \tag{2.2}$$

La figure 2.6 montre des exemples de BSCs théoriques calculés avec les trois modèles dans des cas monodisperse et polydisperse. On peut noter que la polydispersité en taille a pour effet de lisser l'amplitude du premier creux du BSC autour de la fréquence 87 MHz pour les trois modèles. La dépendance fréquentielle des courbes de BSC est identique pour les concentrations de 0.006, 0.06 et 0.3 avec le modèle discret de sphères fluides et le modèle particulaire Percus-Yevick alors que la dépendance fréquentielle du BSC diffère selon les concentrations dans la bande de fréquence 10-45 MHz avec le modèle de facteur de structure.

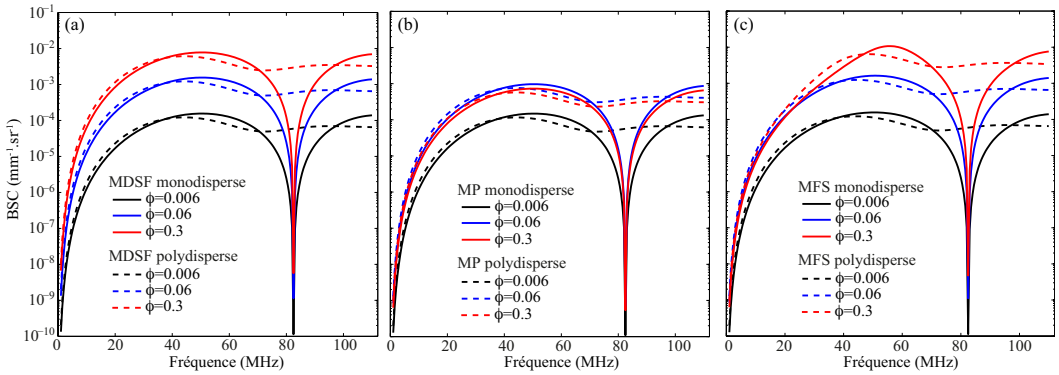

Figure 2.6 – Coefficients de rétrodiffusion calculés avec les trois modèles étudiés, (a) modèle discret de sphères fluides - MDSF, (b) modèle particulaire de Percus-Yevick - MP et (c) modèle de facteur de structure MFS, en considérant une distribution monodisperse de sphères de rayon 6.5 µm ou une distribution de taille suivant une loi gaussienne de 6.5±1.5 µm avec un contraste d'impédance γ_z=0.05, pour des concentrations de 0.006, 0.06 et 0.3.

Si un seul modèle de diffusion permet d'expliquer l'amplitude et la dépendance fréquentielle des BSCs mesurés pour toutes les concentrations cellulaires étudiées, on peut espérer identifier les structures diffusantes. Notre objectif est donc d'estimer la taille et le contraste d'impédance de diffuseurs effectifs permettant d'expliquer les allures des BSC mesurés pour toutes les concentrations étudiées. Nous supposons que la taille moyenne réelle des cellules r_c ainsi que les différentes concentrations cellulaires ϕ_c sont connues *a priori*. La taille $\overline{r}$ et l'écart type μ des diffuseurs effectifs (suivant une distribution gaussienne $p(r)$) ainsi que le contraste d'impédance γ_z sont estimés simultanément grâce à une

procédure d'optimisation. Cette procédure consiste à minimiser une fonction coût F, qui mesure l'écart entre les BSCs mesurés et théoriques et qui synthétise toutes les données expérimentales, i.e. les BSC par les bio-fantômes des concentrations diluées à concentrées ϕ_{c_i} $(i = 1 \cdots N)$, pour tous les nombres d'ondes k_j $(j = 1 \cdots M)$ dans la bande de fréquence étudiée :

$$F = \frac{1}{N} \sum_{i=1}^{N} \frac{\sum_j ||BSC_{meas}(k_j, \phi_{c_i}) - BSC_{theo}(k_j, \phi_{c_i})||^2}{\sum_j ||BSC_{meas}(k_j, \phi_{c_i})||^2}, \tag{2.3}$$

où N est le nombre de concentrations étudiés. A chaque itération du processus d'optimisation, les concentrations des diffuseurs effectifs sont calculées comme $\phi = \phi_c \frac{\int p(r) r^3 dr}{{r_c}^3}$.
Cette procédure a été appliquée sur :

- des mesures ultrasonores sur des bio-fantômes de cellules K562 (r_c=6.48 µm) réalisées au LMA dans la bande de fréquence 10 - 42 MHz (correspondant à $0.26 \leq kr_c \leq 1.11$). Les concentrations étudiées sont égales à ϕ_c= (0.006, 0.03, 0.06, 0.12, 0.18, 0.24, 0.3).
- des mesures ultrasonores sur des bio-fantômes de cellules CHO (lignée cellulaire d'ovaires de hamster, r_c=6.71 µm) réalisées par Han *et al* (2011) dans la bande de fréquence 26-105 MHz (correspondant à $0.73 \leq kr_c \leq 2.95$). Les concentrations étudiées sont égales à ϕ_c=(0.0017, 0.0066, 0.026, 0.096, 0.3, 0.63). A noter que les courbes de BSC ont été extraites des figures 9 et 10 de l'article de Han *et al* (2011) en utilisant le logiciel DataThief III.

Les tailles de diffuseurs effectifs obtenues avec notre procédure ont été comparées aux tailles cellulaires (cellule entière et noyau) pour identifier les structures diffusantes.

Table 2.1 – Estimation des paramètres avec les trois modèles de diffusion (modèle discret de sphères fluides - MDSF, modèle particulaire de Percus-Yevick - MP et modèle de facteur de structure MFS). Pour l'étude sur les bio-fantômes de cellules CHO, une étude supplémentaire a été réalisée sur une bande de fréquence réduite de 26-56 MHz (correspondant à $0.73 \leq kr_c \leq 1.5$) puisque le modèle de sphère fluide ne permet pas d'approcher correctement la forme/structure d'une cellule isolée en hautes fréquences.

	Lignée cellulaire	Bande de fréquence	Modèle	$\overline{r}^* \pm \mu^*$ (µm)	$\lvert\gamma_z^*\rvert$	Erreurs normalisées
1	K562	10-42 MHz	MDSF	4.48 ± 0.00	0.112	0.116
2	K562	10-42 MHz	MP	4.03 ± 1.15	0.137	0.053
3	K562	10-42 MHz	MFS	6.40 ± 1.44	0.051	0.029
4	CHO	26-105 MHz	MDSF	5.04 ± 1.18	0.073	0.108
5	CHO	26-105 MHz	MP	4.02 ± 1.67	0.101	0.183
6	CHO	26-105 MHz	MFS	5.47 ± 1.07	0.068	0.077
7	CHO	26-56 MHz	MDSF	3.83 ± 1.39	0.094	0.196
8	CHO	26-56 MHz	MP	3.67 ± 1.56	0.124	0.069
9	CHO	26-56 MHz	MFS	6.04 ± 1.11	0.057	0.054

Le tableau 2.1 donne la taille $\overline{r}^* \pm \mu^*$ et le contraste d'impédance γ_z^* estimés avec les trois modèles grâce à la procédure d'optimisation proposée, ainsi que l'erreur normalisée correspondante (i.e. l'évaluation de la fonction coût au minimum global pour les valeurs $\overline{r}^*$, μ^* et γ_z^*). L'erreur normalisée permet d'évaluer la qualité des courbes de correspondance. On peut noter que les erreurs normalisées sont nettement plus petites avec le modèle de

facteur de structure polydisperse. Les résultats obtenus avec les cellules K562 et CHO montrent que les modèles de sphères fluides et particulaire sont insuffisants pour expliquer l'allure complexe des BSC (figures 2.7 et 2.8). On peut noter que l'expérience sur les cellules CHO présente une relation non linéaire entre les BSCs mesurés et la concentration cellulaire en basses fréquences (Fig. 2.8b) et une relation linéaire en hautes fréquences (Fig. 2.8c). Seul le modèle de facteur de structure polydisperse permet de rendre compte du comportement des BSCs, quelle que soit la bande de fréquence ou la lignée cellulaire étudiée. Les paramètres d'impédance et de taille estimés avec le modèle de facteur de structure polydisperse sont satisfaisants : l'estimation du contraste d'impédance est de l'ordre de 0.06 proche des valeurs de la littérature, et le rayon du diffuseur effectif correspond aux rayons des cellules entières pour les deux lignées cellulaires K562 et CHO (avec une erreur relative de 18% dans la bande de fréquence 26-105 MHz et avec une erreur relative de 10% dans la bande de fréquence 26-56 MHz pour les CHO).

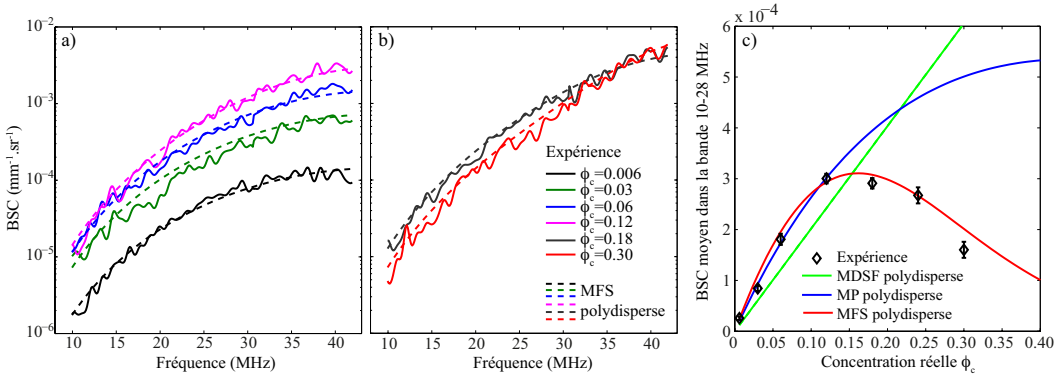

Figure 2.7 – (a) Coefficients de rétrodiffusion mesurés sur les bio-fantômes de cellules K562 (traits pleins) et calculés avec le modèle de facteur de structure polydisperse (traits en pointillés) en utilisant les valeurs du rayon moyen estimé $\overline{r}^* \pm \mu^*$ et du contraste d'impédance γ_z^* (voir tableau 2.1 ligne 3). (b) et (c) Comparaison des coefficients de rétrodiffusion moyens mesurés et prédits par les trois modèles de diffusion (modèle discret de sphères fluides - MDSF, modèle particulaire de Percus-Yevick - MP et modèle de facteur de structure MFS) en fonction de la concentration de cellules. Pour les courbes théoriques, les paramètres $\overline{r}^* \pm \mu^*$ et γ_z^* sont issus de la procédure d'optimisation (voir tableau 2.1 lignes 1-3).

Cette étude montre que la cellule entière joue un rôle important dans le comportement du BSC (amplitude et dépendance en fréquence) pour les deux lignées cellulaires K562 et CHO. Ce résultat est de première importance puisque de nombreuses études dans la littérature font l'hypothèse que le noyau est la principale structure responsable de la diffusion, alors que notre étude sur les deux lignées cellulaires K562 et CHO démontre le contraire. D'autres expériences sur des cellules de tailles variables (taille cellule entière, rapport de taille entre le noyau et le cellule entière) sont nécessaires pour confirmer notre résultat.

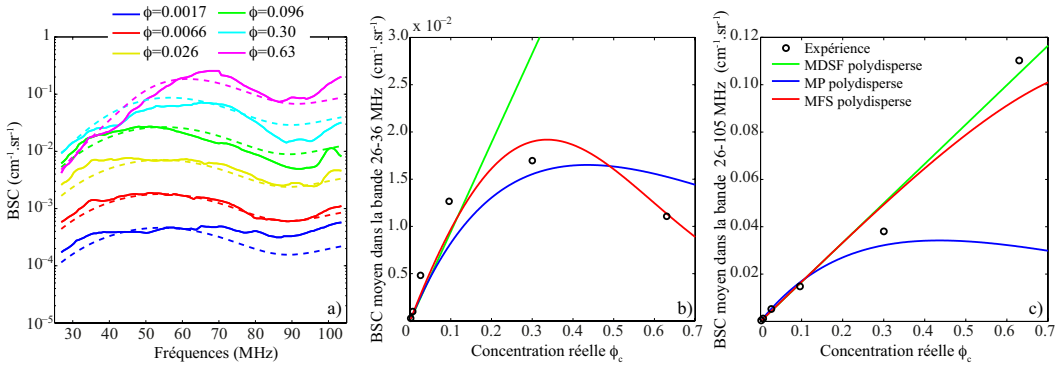

Figure 2.8 – (a) Coefficients de rétrodiffusion mesurés sur les bio-fantômes de cellules CHO (traits pleins) et calculés avec le modèle SFM polydisperse (traits en pointillés) en utilisant les valeurs du rayon moyen estimé $\overline{r}^* \pm \mu^*$ et du contraste d'impédance γ_z^* (voir tableau 2.1 ligne 6). (b) et (c) Comparaison des coefficients de rétrodiffusion moyens mesurés et prédits par les trois modèles de diffusion (MDSF, PM et MFS) en fonction de la concentration de cellules. Les calculs théoriques utilisent les paramètres $\overline{r}^* \pm \mu^*$ et γ_z^* issus de la procédure d'optimisation (voir tableau 2.1 lignes 4-6).

2.2.2 Etude du problème inverse : estimation des paramètres de structure

Un article en préparation avec Jonathan Mamou (Lizzi Center for Biomedical Engineering, Riverside Research Institute)

Une procédure d'estimation plus classique a aussi été appliquée sur les données expérimentales de BSC sur les bio-fantômes de cellules K562 : au lieu d'effectuer une procédure d'optimisation synthétisant toutes les données expérimentales (des concentrations diluées à concentrées) basée sur la fonction coût présentée à l'Eq. (2.3), nous avons réalisé une procédure d'inversion sur les données de BSC pour chaque concentration étudiée basée sur une fonction coût classique (du type de celle présentée à l'Eq. (2.4) ou l'Eq. (2.5)).

L'une des particularités du modèle de facteur de structure est la possibilité d'estimer simultanément trois paramètres : le rayon r, la concentration ϕ et le contraste d'impédance γ_z. En effet, pour le modèle de facteur de structure, le comportement du BSC en fonction de la fréquence dépend du produit $\sigma_b(k,r)S(k,r,\phi)$ alors que pour les modèles classiques, il dépend seulement de $\sigma_b(k,r)$. Pour des milieux concentrés, le facteur de structure diffère de la valeur unité et a une grande influence sur la dépendance fréquentielle du BSC, permettant d'estimer la concentration. L'estimation simultanée de ces trois paramètres est effectuée en minimisant une fonction coût. Deux fonctions coûts F_1 et F_2 ont été étudiées : l'une mesurant l'écart entre le BSC mesuré et le BSC théorique, et l'autre mesurant l'écart entre le logarithme du BSC mesuré et le logarithme du BSC théorique.

$$F_1 = \frac{\sum_j ||BSC_{mes}(k_j) - BSC_{MFS}(k_j)||^2}{\sum_j ||BSC_{meas}(k_j)||^2}, \tag{2.4}$$

$$F_2 = \frac{\sum_j ||\log\left(BSC_{mes}(k_j)\right) - \log\left(BSC_{MFS}(k_j)\right)||^2}{\sum_j ||\log\left(BSC_{meas}(k_j)\right)||^2}. \tag{2.5}$$

La fonction coût F_1 pénalise surtout les écarts importants en hautes fréquences alors que la fonction coût F_2 basée sur le logarithme du BSC donne quasiment le même poids à toutes les fréquences. La figure 2.9 représente l'estimation simultanée des trois paramètres r^*, ϕ^* et γ_z^* utilisant les deux fonctions coûts, ainsi que l'estimation des deux paramètres r^* et ϕ^* lorsque le contraste d'impédance est fixé $\gamma_z = 0.051$ (évalué au paragraphe 2.2.1 Tableau 2.1). Comme attendu, les rayons et les concentrations estimées sont quantitativement satisfaisantes pour toutes les concentrations étudiées lorsque le contraste d'impédance est fixé à $\gamma_z = 0.051$, quelle que soit la fonction coût utilisée. L'estimation simultanée des trois paramètres de structure est qualitativement satisfaisante pour des concentrations réelles $\phi_c \geq 0.12$ (avec des erreurs relatives inférieures à 50%) quelle que soit la fonction coût utilisée. Pour les concentrations les plus faibles de 0.006, 003 et 0.06, les estimations du contraste d'impédance et de la concentration cellulaire ne sont pas satisfaisantes. Pour les concentrations 0.03 et 0.06, les estimations obtenues avec les deux fonctions coût sont bien distinctes : le contraste d'impédance est légèrement sous-estimé et la concentration cellulaire est largement surestimée avec la fonction coût F_1, alors que le contraste d'impédance est largement surestimé allant de pair avec une sous-estimation de la concentration cellulaire avec la fonction coût F_2. L'estimation des paramètres de structure est donc plus robuste pour les bio-fantômes concentrés ($\phi_c \geq 0.12$), puisque la dépendance fréquentielle du BSC à forte concentration est fortement modifiée par le facteur de structure $S(k, r, \phi)$.

Par la suite, nous avons comparé le rayon r^* et la concentration acoustique $(n\gamma_z)^*$ estimés avec trois modèles de diffusion : modèle continu Gaussien, modèle discret de sphères fluides et modèle de facteur de structure (Fig. 2.10). Comme attendu, les modèles classiques (Gaussien et de sphères fluides) donnent des estimations satisfaisantes pour les faibles concentrations ($\phi_c \leq 0.12$) ; mais pour des concentrations élevées $\phi_c > 0.12$, ils sous-estiment la taille des cellules et surestiment la concentration acoustique, et ceci quelle que soit la fonction coût utilisée. On peut remarquer que le rayon estimé avec les modèles classiques décroit lorsque la concentration cellulaire augmente, alors que pour le modèle de facteur de structure, le rayon est généralement estimé autour de 8.82 µm quelle que soit la concentration étudiée (sauf pour les concentrations 0.03 et 0.06 avec la fonction coût F_2). **Seul le modèle de facteur de structure donne des estimations correctes pour les deux paramètres de structure (rayon et concentration acoustique) quelle que soit la concentration étudiée, avec une légère surestimation de la taille des cellules.**

Pour conclure, le modèle de facteur de structure a permis d'estimer correctement les trois paramètres r^*, ϕ^* et γ_z^* pour les culots de cellules concentrés mais pas pour les culots dilués. Pour les concentrations faibles, le facteur de structure est proche de l'unité, et le modèle de facteur de structure est alors équivalent au modèle discret de sphères fluides. C'est pourquoi il est difficile de dissocier le contraste d'impédance et la concentration pour les milieux dilués, seul l'estimation de la concentration acoustique peut être robuste dans ce cas particulier (comme montré à la Fig. 2.10).

2.3 Conclusion

Les résultats obtenus sur les suspensions denses de microsphères et sur les bio-fantômes de cellules montrent que le modèle de facteur de structure est un modèle approprié pour la caractérisation ultrasonore des tumeurs possédant une forte concentration cellulaire. Cependant, les bio-fantômes sont des versions simplifiées de tumeurs puisqu'une seule lignée cellulaire est considérée. Des études devront être menées *in vivo* pour confirmer

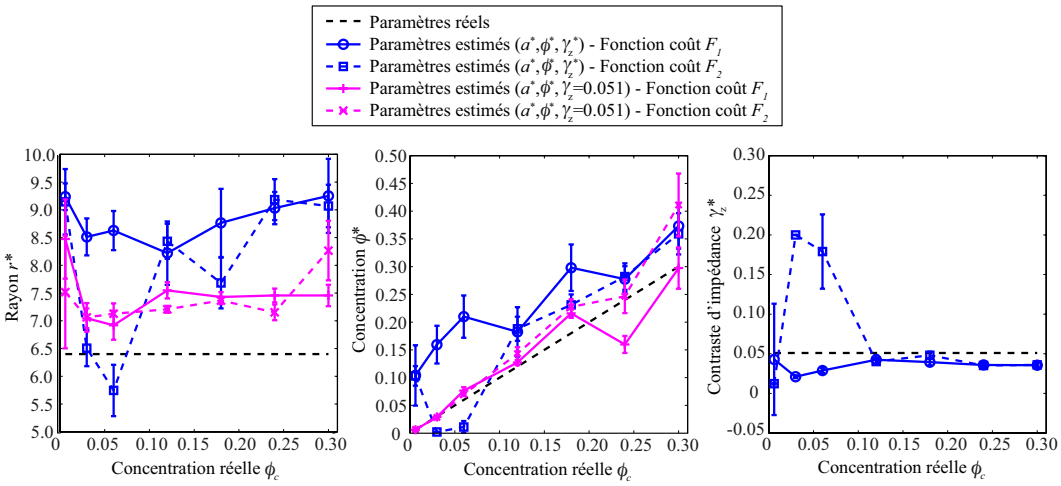

Figure 2.9 – Rayon r^*, concentration ϕ^* et contraste d'impédance γ_z^* estimés avec le modèle de facteur de structure en utilisant deux fonctions coûts (Eqs. 2.4 et 2.5). Les paramètres réels attendus sont ceux estimés dans l'étude précédente (voir paragraphe 2.2.1).

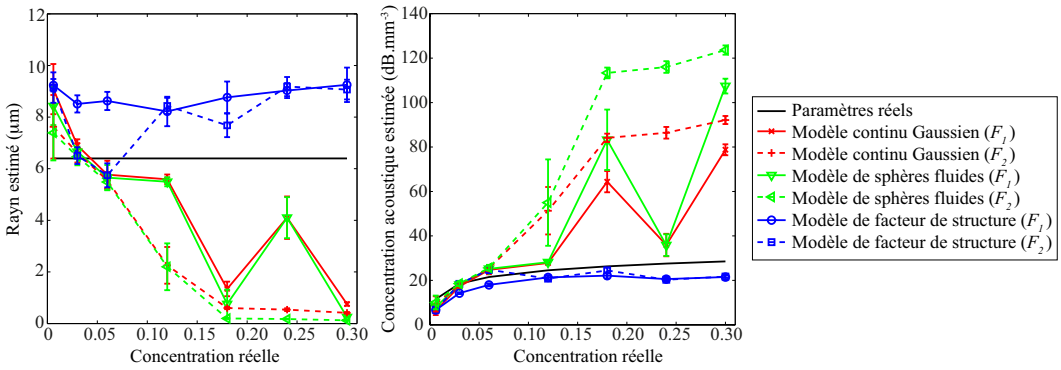

Figure 2.10 – Rayon r^* et concentration acoustique $(n\gamma_z)^*$ estimés avec trois modèles de diffusion (modèle continu Gaussien, modèle discret de sphères fluides et modèle de facteur de structure) en fonction de la concentration cellulaire réelle en utilisant deux fonctions coûts (Eqs. 2.4 et 2.5). Les paramètres réels attendus sont ceux estimés dans l'étude précédente (voir paragraphe 2.2.1).

l'apport de ce modèle. Les tumeurs ont des structures plus complexes que les bio-fantômes. La matrice extracellulaire, les microvaisseaux sanguins et l'hétérogénéité tumorale (avec des zones de cellules proliférantes et nécrotiques) peuvent jouer un rôle important sur la diffusion, comme montré par Han *et al.* (2013). Pour le moment, nous avons démontré la supériorité du modèle de facteur de structure en comparaison des modèles classiques (continu Gaussien ou discret de sphères fluides) pour modéliser des cellules entassées dans une tumeur simple composée d'une seule lignée cellulaire. Les travaux futurs se focaliseront sur la prise en compte de l'hétérogénéité tumorale (présence de plusieurs lignées cellulaires ou de microvaisseaux sanguins).

Chapitre 3

Perspectives

Ce mémoire d'habilitation se clôt sur les projets de recherche que je souhaite développer. Je poursuivrai mes travaux sur la caractérisation ultrasonore de l'agrégation érythrocytaire afin de considérer l'anisotropie des rouleaux de globules rouges et de valider la technique ultrasonore d'estimation de structures des agrégats grâce au développement d'un dispositif expérimental combinant des mesures ultrasonores et optiques. Par ailleurs, les travaux sur la compréhension de la diffusion ultrasonore par des cellules entassées dans une tumeur s'orientent à présent vers la détection ultrasonore de la mort cellulaire pour faire le suivi de la réponse tumorale aux thérapies anticancéreuses.

3.1 Caractérisation ultrasonore de suspensions denses

Dans le prolongement de mes travaux sur la caractérisation ultrasonore de l'agrégation des globules rouges, j'ai initié une collaboration avec Valérie Deplano et Yannick Knapp, des mécaniciens des fluides de l'Institut de Recherche sur les Phénomènes Hors Equilibre (IRPHE, Marseille) et Stéphane Veesler, Zoubida Hammadi et Nadine Candoni, chercheurs en nanotechnologie du Centre Interdisciplinaire de Nanoscience de Marseille (CINaM, Marseille). Le premier objectif de cette association acousticiens/ mécaniciens des fluides est de pouvoir valider la Théorie de Milieu Effectif combinée au Modèle de Facteur de Structure TMEMFS (voir section 1.4). La théorie a été validée par des expériences virtuelles, i.e. par des simulations numériques de la propagation des ondes ultrasonores à travers des agrégats de globules rouges de tailles variables. Il est nécessaire maintenant de la valider de façon expérimentale. L'expérience proposée est la suivante : un écoulement sanguin est réalisé dans un dispositif cône-plan couplé à un microscope optique et à des transducteurs ultrasonores, cet écoulement contient des agrégats de globules rouges micrométriques qui ont une taille caractéristique. Grâce à ce dispositif expérimental, pour différents hématocrites et différents régimes d'écoulement, des mesures ultrasonores hautes fréquences (8 à 35 MHz) seront confrontés à des mesures optiques (taille et compacité des agrégats, hématocrite et profils de vitesse) dans les limites d'application de ces métrologies (suspension diluée et/ou faible épaisseur). Le montage expérimental a été récemment finalisé fin 2014 (Fig. 3.1). Des expériences seront menées dans un premier temps sur des particules rigides de PMMA dans un fluide iso-densité (mélange monodisperse, bidisperse et polydisperse en taille), puis sur des microsphères transparentes en alginate possédant des propriétés d'agrégation (développées par le CINaM pour ce projet) imitant des globules rouges.

Une fois la méthode ultrasonore validée, l'expérience sera étendue pour réaliser le

second objectif de notre association : progresser dans la compréhension de certains mécanismes fondamentaux qui régissent les fluides complexes comme le sang. Des comparaisons des comportements en écoulement de particules déformables et/ou rigides permettront notamment d'analyser les effets induits sur l'écoulement par la présence de particules déformables. La variation du degré de confinement de l'écoulement permettra d'étudier les effets de ce dernier sur les particules. D'autres questions pourront également être investiguées : Quels sont les effets induits sur l'écoulement par la présence des particules ? Quels sont les liens entre la microstructure (forme, taille, agrégation des particules...) et les propriétés macroscopiques de l'écoulement (profils de vitesse, cisaillement...) ?

Au delà de ces questions de nature fondamentale, une meilleure compréhension des mécanismes mis en jeu apportera des éléments de réponse sur le comportement des globules rouges déformables lorsque ces derniers ne sont plus considérés comme des entités isolées et soumis à un écoulement dans une géométrie confinée. L'outil de mesure ultrasonore permettra d'aborder ces questions expérimentalement. Le savoir faire expérimental des mécaniciens des fluides couplé aux nouvelles techniques ultrasonores devrait donner lieu à des résultats particulièrement intéressants sur la caractérisation des fluides complexes.

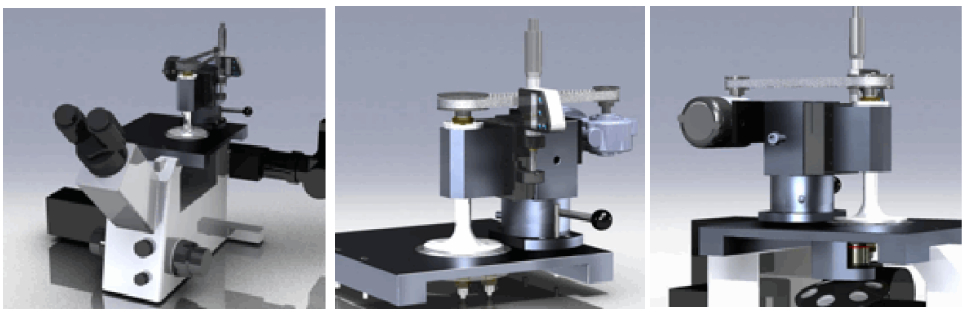

Figure 3.1 – A gauche : Vue d'ensemble du montage expérimental composé d'un dispositif de Couette, d'un microscope et de deux transducteurs ultrasonores. Au centre : Vue de détail montrant l'emplacement des transducteurs. A droite : Vue de détail montrant l'accès optique.

Concernant le modèle de diffusion ultrasonore, le modèle TMEMFS est actuellement amélioré par Romain de Monchy (doctorant LMA ayant débuté sa thèse en Octobre 2013) pour intégrer une fonction de structure analytique polydisperse (Griffith *et al.* 1987) permettant de prendre en compte une polydispersité en terme de taille de particules effectives/agrégats. Par ailleurs, un autre aspect à considérer est l'hypothèse d'agrégats isotropes dans le modèle TMEMFS. Les agrégats de globules rouges ont tendance à former des structures isotropes pour du sang humain pathologique comme le diabète, alors que les structures sont des rouleaux anisotropes pour du sang normal. La prise en compte de l'anisotropie pourrait donc permettre de différencier des sangs pathologique et normal. Dans ce but, nous inclurons dans le modèle TMEMFS l'expression analytique de la diffusion par un cylindre fini ou par une ellipsoïde afin de modéliser la réponse ultrasonore effective d'un rouleau de globules rouges isolé. La stratégie expérimentale sera d'estimer dans un premier temps l'orientation des rouleaux en réalisant des mesures ultrasonores en rétrodiffusion suivant différents angles d'incidence par rapport à l'écoulement, puis d'évaluer la taille moyenne des rouleaux en utilisant la nouvelle formulation théorique anisotrope de TMEMFS pour des mesures en diffraction. Des validations expérimentales seront menées

sur des particules sphériques modélisant des agrégats isotropes (cas pathologique rencontré chez les diabétiques) et des particules cylindriques qui ont tendance à s'orienter dans le sens de l'écoulement modélisant le comportement des rouleaux de globules rouges. Afin de préparer un passage vers des mesures *in vivo*, cette stratégie d'acquisition sera considérée en utilisant des sondes ultrasonores multi-élements utilisant une imagerie ultrarapide par ondes planes (collaboration avec Damien Garcia et Guy Cloutier à l'Université de Montréal).

3.2 Suivi ultrasonore de la mort cellulaire

La chimiothérapie permet de tuer les cellules cancéreuses par apoptose, un mode de mort cellulaire qui a été largement investigué ces dernières décennies. Durant l'apoptose, les cellules subissent d'importantes modifications morphologiques ; les noyaux se condensent puis se fragmentent et des protubérances membranaires se forment ("membrane blebbing"). Notre objectif est d'évaluer deux méthodes ultrasonores quantitatives de caractérisation tissulaire pour le suivi de l'apoptose :

- une technique d'estimation des microstructures cellulaires basée sur l'analyse fréquentielle des signaux échographiques rétrodiffusés (ref travaux précédents). Cette méthode est sensible aux modifications des structures cellulaires.
- une technique d'analyse de la non linéarité tissulaire basée sur l'étude comparative des signaux modulés en amplitude (en collaboration avec Cédric Payan au LMA, spécialiste de cette technique). Cette méthode est sensible aux micro-inhomogénéités des milieux, en particulier en présence de contacts ou de fragmentations.

Des expériences préliminaires ont été réalisées sur des culots des cellules K562 traitées avec un agent chimiothérapeutique (cisplatinum) provoquant l'apoptose des cellules. Au temps 0h, les cellules sont traitées avec cette drogue durant 6, 12, 24 et 48h. Avant l'acquisition ultrasonore, les cellules sont lavées au tampon phosphate salin (PBS) puis centrifugées pour former un agrégat compact de cellules, simulant l'entassement des cellules dans les tumeurs. Les mesures ultrasonores sont réalisées dans l'heure suivant la centrifugation. Les premiers résultats obtenus sont montrés à la figure 3.2. Le paramètre de non linéarité augmente de façon significative au temps 6 et 12 heures lors des phases de condensation et de fragmentation de l'ADN, puis le paramètre de non linéarité est à nouveau proche de sa valeur initiale au temps 24 et 48 heures (Fig. 3.2c). Cette dynamique est comparable à celle observée dans les milieux solides fissurés. L'amplitude du coefficient de rétrodiffusion augmente de façon significative lorsque les noyaux/cellules se fragmentent pour former des corps apoptotiques (Fig. 3.2d). Les deux techniques ultrasonores seraient donc complémentaires et permettraient de détecter les phases d'apoptose précoce (fragmentation de l'ADN) et tardive (formation de corps apoptotiques).

Ces résultats préliminaires m'ont permis d'obtenir un financement A*Midex interdisciplinarité PR2I 2014-2016 pour poursuivre ces expériences en collaboration avec Palma Rocchi du Centre de Recherche en Cancérologie de Marseille (CRCM INSERM UMR 1068/ CNRS UMR 7258, Marseille) spécialiste du traitement pour le cancer de la prostate, Benjamin Guillet de l'unité Endothelium, pathologies vasculaires et cibles thérapeutiques (UMR S1076, Marseille) spécialiste des mécanismes d'angiogénèse et Guillemette Chapuisat de l'Institut de Mathématiques de Marseille (I2M UMR 7373, Marseille) spécialiste des modèles mathématiques de croissance tumorale. Le projet a pour objectif d'évaluer le potentiel des paramètres ultrasonores quantitatifs (paramètres de microstructure et de non-linéarité) pour faire le suivi de la réponse tumorale à une thérapie. Dans ce but, nous

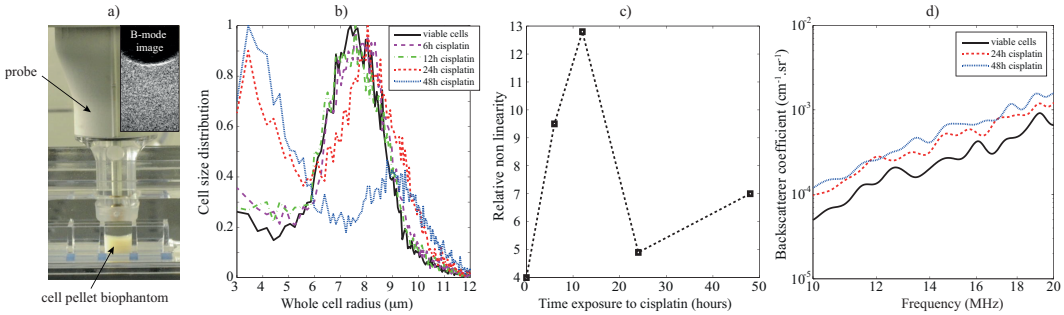

Figure 3.2 – (a) Culot de cellules examiné par une sonde ultrasonore. (b) Histogrammes de la distribution de taille des cellules entières durant le traitement (obtenus avec le compteur Scepter 2.0 Millipore basé sur le principe de la mesure de l'impédance électrique). Les structures cellulaires sont identiques durant les premières 12 heures (condensation et fragmentation de l'ADN). Les corps apostoliques apparaissent aux temps 24h et 48h. (c) Paramètres de non linéarité. (d) Mesures du coefficient de rétrodiffusion aux temps 0h, 24h et 48h.

caractérisons les processus d'apoptose, de nécrose et d'angiogénèse par les méthodes ultrasonores quantitatives en utilisant des modèles *in vitro* (i.e. culots de cellules) et *in vivo* (i.e. xénogreffes de tumeur chez la souris) de cancer de la prostate exposés à des thérapies anticancéreuses systémiques. Le second objectif de cette collaboration entre acousticiens et mathématiciens sera d'intégrer ces nouveaux biomarqueurs ultrasonores dans des modèles mathématiques de croissance tumorale pour prédire la réponse tumorale aux traitements sur le long terme.

En parallèle de ces travaux sur le suivi ultrasonore de la mort cellulaire, je poursuivrai mes études sur la compréhension de la diffusion par des tumeurs (en l'absence de thérapie). Des expériences ultrasonores seront menées sur différents modèles de tumeurs allant du plus simple (culots de cellules, xénogreffes de tumeur non vascularisée et matrigel contenant seulement des microvaisseaux sanguins) au plus complexe (tumeurs vascularisées). Cette étude expérimentale permettra d'isoler la diffusion par des microvaisseaux sanguins et/ou par des cellules entassées, et de progresser dans la compréhension de la diffusion ultrasonore par des tumeurs hétérogènes.

Bibliographie

Anderson VC (1950) Sound scattering from a fluid sphere, J Acoust Soc Am 22 :426-431

Angelsen BAJ (1980) Theoretical study of the scattering of ultrasound by blood. IEEE Trans Biomed Eng 27 :61-67

Armstrong JK, Wenby RB, Meiselman HJ and Fisher TC (2004) The hydrodynamic radii of macromolecules and their effect on red blood cell aggregation. Biophys J 87 :4259-4270

Baddour RE, Sherar MD, Hunt JW, Czarnota GJ and Kolios MC (2005) High-frequency ultrasound scattering from microspheres and single cells, J Acoust Soc Am 117 :934-943

Baddour RE and Kolios MC (2007) The fluid and elastic nature of nucleated cells : implications from the cellular backscatter response, J Acoust Soc Am 121 :EL16-22

Bigelow TA, Oelze ML and O'Brien WD (2005) Estimation of total attenuation and scatterer size from backscatter ultrasound waveforms. J Acoust Soc Am 117 :1431-1439

Bigelow TA and O'Brien WD (2005) Signal processing strategies that improve performance and understanding of the quantitative ultrasound SPECTRAL FIT algorithm. J Acoust Soc Am 118 :1808-1819

Chien S (1975) Biophysical behavior of red cells in suspensions, in : D.M. Surgenor (ed) The Red Blood Cell. Academic Press, New York.

de Monchy R, Destrempes F, Saha RK, Franceschini E and Cloutier G (2015) Effective medium model for ultrasound backscattering by aggregating cells, in preparation for correspondence IEEE Trans. on Ultrason., Ferroelect., Freq. Contr.

Falou O, Rui M, Kaffas AE, Kumaradas JC and Kolios MC (2010) The measurement of ultrasound scattering from individual micron-sized objects and its application in single cell scattering, J Acoust Soc Am 128 :894-902

Falou O, Sadeghi-Naini A, Al-Mahrouki A, Kolios MC and Czarnota GJ (2013) Quantitatiave ultrasound and cell death. In : Mamou J and Oelze ML (eds.), Quantitative ultrasound in soft tissues. Springer.

Faran JJ (1951) Sound Scattering by Solid Cylinders and Spheres, J Acoust Soc Amer 121 :405-418

Feleppa EJ, Lizzi FL, Coleman DJ and Yaremko MM (1986) Diagnostic spectrum

analysis in ophthalmology : a physical perspective, Ultrasound Med Biol 12 :623-631

Feleppa EJ, Liu T, Kalisz A, Shao MC, Fleshner N and Reuter V (1997) Ultrasonic spectral-parameter imaging of the prostate, Int J Imag Syst Technol 8 :11-25

Fontaine I, Bertrand M and Cloutier G (1999) A system-based approach to modeling the ultrasound signal backscattered by red blood cells. Biophysical Journal 77 :2387-2399

Fontaine I, Savery D and Cloutier G (2002) Simulation of ultrasound backscattering by red blood cell aggregates : effect of shear rate and anisotropy. Biophysical Journal 82 :1696-1710

Fontaine I and Cloutier G (2003) Modeling the frequency dependence (5-120 MHz) of ultrasound backscattering by red cell aggregates in shear flow at a normal hematocrit, J Acoust Soc Amer 113 :2893-2900

Franceschini E, Yu FTH, and Cloutier G (2008) Simultaneous estimation of attenuation and structure parameters of aggregated red blood cells from backscatter measurements. J Acoust Soc Amer 123 :EL85-91

Franceschini E, Yu FTH, Destrempes F and Cloutier G (2009) In vivo ultrasound characterization of red blood cell aggregation using the Structure Factor Size and Attenuation Estimator. Proceedings IEEE Ultrason Symp 301-304

Franceschini E, Yu FTH, Destrempes F, and Cloutier G (2010) Ultrasound characterization of red blood cell aggregation with intervening attenuating tissue-mimicking phantoms. J Acoust Soc Amer 127 :1104-1115

Franceschini E, Metzger B and Cloutier G (2011) Forward problem study of an effective medium model for ultrasound blood characterization. IEEE Trans Ultras Ferroelectr Freq Control 58 :2668-2679

Franceschini E and Guillermin R (2012) Experimental assessment of four ultrasound scattering models for characterizing concentrated tissue-mimicking phantoms. J Acoust Soc Amer 132 :3735-3747

Franceschini E, Saha RK and Cloutier G (2013) Comparison of three scattering models for ultrasound blood characterization. IEEE Trans Ultrason Ferroelect Freq Contr 60 :2321-2334

Franceschini E, Guillermin R, Tourniaire F, Roffino S, Lamy E and Landrier J-F (2014) Structure Factor Model for understanding the measured backscatter coefficients from concentrated cell pellet biophantoms. J Acoust Soc Amer 135 :3620-3631

Franceschini E and Cloutier G, brevet No. US 2014/0016438 A1 publié le 16 Janvier 2014 : System and method of ultrasound scatterer characterization

Griffith WL, Triolo R and Compere AL (1987) Analytical scattering function of a polydiperse Percus-Yevick fluid with Schulz-distributed diameters. Physical Review A 35 :2200-2206

Guinier A (1964) La diffusion des rayons X aux très petits angles. Dans : Théorie et technique de la radiocristallographie. Dunod, Paris.

Han A, Abuhabsah R, Blue JP, Sarwate S and O'Brien WD (2011) Ultrasonic backscatter coefficient quantitative estimates from high-concentration Chinese hamster

ovary cell pellet biophantoms, J Acoust Soc Am 130 :4139-4147

Han A, Abuhabsah R, Blue JP, Sarwate S and O'Brien WD (2013) The measurement of ultrasound backscattering from cell pellet biophantoms and tumors ex vivo, J Acoust Soc Am 134 :686-693

He P and Greenleaf JF (1986) Application of stochastic analysis to ultrasonic echoes - Estimation of attenuation and tissue heterogeneity from peaks of echo envelope. J Acoust Soc Am 79 :526-534

Insana MF and Brown DG (1993) Acoustic scattering theory applied to soft biological tissues. In : Shung KK and Thieme GA (ed) Ultrasonic Scattering in Biological Tissues. CRC, Boca Raton, FL

Kolios MC, Czarnota GJ, Lee M, Hunt JW and Sherar MD (2002) Ultrasonic spectral parameter characterization of apoptosis, Ultrasound Med Biol 28 :589-597

Kuc R and Schwartz M (1979) Estimating the acoustic attenuation coefficient slope for liver from reflected ultrasound signals. IEEE Trans Sonics Ultrason SU-26 :353–362

Kuster GT and Toksoz MN (1974) Velocity and attenuation of seismic waves in two-phase media : part I. Theoretical formulations, Geophysics 39 :587-606

Lizzi FL, Greenebaum M, Feleppa EJ, and Elbaum M (1983) Theoretical framework for spectrum analysis in ultrasonic tissue characterization. J Acoust Soc Amer 73 :1366-1373

Lizzi FL, Ostromogilsky M, Feleppa EJ, Rorke MC and Yaremko MM (1986) Relationship of ultrasonic spectral parameters to features of tissue microstructure, IEEE Trans Ultrason Ferroelect Freq Contr 33 :319-329

Lucas RJ and Twersky V (1987) Inversion of ultrasonic scattering data for red blood cell suspensions under different flow conditions. J Acoust Soc Am 82 :794-799

McNew J, Lavarello R and O'Brien WD (2009) Sound scattering from two concentric fluid spheres (L), J Acoust Soc Am 125 :1-4

Meiselman HJ (1993) Red blood cell role in RBC aggregation : 1963-1993 and beyond. Clin Hemorheol 13 :575-592

Mo LYL and Cobbold RSC (1986) A stochastic model of the backscattered Doppler ultrasound from blood. IEEE Trans Biomed Eng 33 :20-27

Mo LYL and Cobbold RSC (1992) A unified appraoch to modeling the backscattered Doppler ultrasound from blood. IEEE Trans Biomed Eng 39 :450-461

Mo LYL and Cobbold RSC (1993) Theoretical models of ultrasonic scattering in blood. In : Shung KK and Thieme GA (ed) Ultrasonic Scattering in Biological Tissues. CRC, Boca Raton, FL

Morse PM and Ingard KU (1968) Theoretical Acoustics. Princeton, NJ : Princeton University Press, ch. 8, pp. 400-466

Oelze ML, Zachary JF and O'Brien WD (2002) Characterization of tissue microstructure using ultrasonic backscatter : Theory and technique for optimization using a Gaussian form factor, J Acoust Soc Am 112 :1202-121

Oelze ML, O'Brien WD, Blue JP and Zachary JF (2004) Differentiation and charac-

terization of rat mammary fibroadenomas and 4T1 mouse carcinomas using quantitative ultrasound imaging, IEEE Trans Med Imaging 23 :764-771

Oelze ML and O'Brien WD (2006) Application of three scattering models to characterization of of solid tumors in mice, Ultrasonic Imaging 28 :83-96

Oosterveld BJ, Thijssen JM, Hartman PC, Romijn RL and Rosenbusch GJE (19991) Ultrasound attenuation and texture analysis of diffuse liver disease : methods and preliminary results. Phys Med Biol 36 :1039-1064

Pedersen JS (1994) Determination of size distributions from small-angle scattering data for systems with effective hard-sphere interactions. J. Appl. Cryt. 27 :595-608

Pedersen JS (1997) Analysis of small-angle scattering data from colloids and polymer solutions : modeling and lest-squares fitting", Advances in Colloid and Interface Science. 70 :171-210

Raju I and Srinivasan MA (2001) High-frequency ultrasonic attenuation and backscatter coefficients of in vivo normal human dermis and subcutaneous fat. Ultrasound Med Biol 27 :1543–1556

Rampling MW, Meiselman HJ, Neu B and Baskurt OK (2004) Influence of cell-specific factors on red blood cell aggregation. Biorheology 41 :91-112

Saha RK and Cloutier G (2008) Monte Carlo Study on ultrasound backscattering by three-dimensional distributions of red blood cells. Physical Review E 78 :061919

Saha RK, Franceschini E and Cloutier G (2011) Assessment of accuracy of the structure-factor-size-estimator method in determining red blood cell aggregate size from ultrasound spectrum backscattering coefficient. J Acoust Soc Am 129 :2269-2277

Savery D and Cloutier G (2001) A point process approach to assess the frequency dependence of ultrasound backscattering by aggregating red blood cells. J Acoust Soc Am 110 :3252-3262

Savery D and Cloutier G (2005) Effect of Red Cell Clustering and Anisotropy on Ultrasound Blood Backscatter : A Monte Carlo Study. IEEE Trans Ultras Ferroelectr Freq Control 52 :94-103

Savery D and Cloutier G (2007) High-frequency ultrasound backscattering by blood : Analytical and semi-analytical models of the erythrocyte cross section. J Acoust Soc Amer 23 :3963-3971

Schmid-Schönbein H, Malotta H and Striesow F (1990) Erythrocyte aggregation : causes, consequences and methods of assessment. Tijdschr NVKS 15 :88-97

Shung KK (1982) On the ultrasound scattering from blood as a function of hematocrit. IEEE Trans Sonics Ultrason SU-29 :327-331

Taggart LR, Baddour RE, Giles A, Czarnota GJ and Kolios MC (2007) Ultrasonic characterization of whole cells and isolated nuclei. Ultrasound Med Biol 33 :389-401

Teisseire M, Han A, Abuhabsah R, Blue JP, Sarwate S and O'Brien WD (2010) Ultrasonic backscatter coefficient quantitative estimates from chinese hamster ovary cell pellet biophantoms, J Acoust Soc Am 128 :3175-3180

Tripette J, Denault AY, Allard L, Chayer B, Perrault LP and Cloutier G (2013) Ultrasound monitoring of RBC aggregation as a real-time marker of the inflammatory response in a cardiopulmonary bypass swine model. Critical Care Med 41 :171-178

Twersky V (1987) Low-frequency scattering by correlated distributions of randomly oriented particles. J Acoust Soc Am 81 :1609-1618

Vlad RM, Saha RK, Alajez NM, Ranieari S, Czarnota GJ and Kolios MC (2010) An increase in cellular size variance contributes to the increase in ultrasound backscatter during cell death, Ultrasound in Medicine & Biology 9 :1546-1558

Wertheim MS (1963) Exact solution of the Percus-Yevick integral equation for hard spheres. Physical Review Letters 10(8) :321-323

Yu FTH and Cloutier G (2007) Experimental ultrasound characterization of red blood cell aggregation using the structure factor size estimator. J Acoust Soc Am 122 :645-656

Yu FTH, Franceschini E, Chayer B, Armstrong JK, Meiselman HJ and Cloutier G (2009) Ultrasonic parametric imaging of erythrocyte aggregation using the structure factor size estimator. Biorheology 46 :343–363

Yu FTH, Armstrong JK, Tripette J, Meiselman HJ and Cloutier G (2011) A local increase in red blood cell aggregation can trigger deep vein thrombosis : Evidence based on quantitative cellular ultrasound imaging. J. Thrombosis & Haemostasis 9 :481-488

Yuan YW and Shung KK (1988) Ultrasonic backscatter from flowing whole blood. I : Dependence on shear rate and hematocrit. J Acoust Soc Am 84 :52-58

Annexe A

Curriculum Vitæ

A.1 Situation actuelle

Franceschini Emilie
Née le 26 Juin 1980 à Montpellier

Chargée de Recherche (CR1 CNRS, section 9).
Laboratoire de Mécanique et d'Acoustique LMA CNRS UPR 705
31 chemin Joseph Aiguier, 13402 Marseille cedex 20
tel : 04 91 16 40 30, email : franceschini@lma.cnrs-mrs.fr

A.2 Cursus

1998 - 2000	Classe préparatoire "Physique et Sciences de l'Ingénieur". Lycée Joffre, Montpellier.
2000 - 2003	**Ingénieur généraliste, spécialisation en Mécanique et Matériaux**. Ecole Supérieure d'Ingénieurs de Marseille (Centrale Marseille).
2002 - 2003	**DEA d'acoustique** Université de la Méditerranée, Marseille. Stage au LMA. *Imagerie ultrasonore de la diaphyse osseuse* (dir : P. Lasaygues). Mention Très Bien, classement : $1^{\text{ère}}/25$.
2003 - 2006	**Doctorat de l'Université de Provence** au LMA, Marseille. *Tomographie ultrasonore dédiée à la détection du cancer du sein* (dir : J-P Lefebvre & S. Mensah). Mention très honorable.
Octobre 2006 -Janvier 2007	**ATER** à l'Université de Provence Aix-Marseille I. Recherche au LMA *Imagerie ultrasonore du bois*
2007 - 2008	**Post-doctorat** au Laboratoire de Biorhéologie et d'Ultrasonographie Médicale (LBUM, Montréal, Canada) *Estimation simultanée de l'atténuation et des paramètres de structures des agrégats érythrocytaires pour les mesures in vivo*
2008	**Admission au CNRS - Chargée de Recherche CR2 (section 9)**
2012	**Promue Chargée de Recherche CR1 (section 9)**

A.3 Collaborations scientifiques

- Guy Cloutier, Professeur & François Destrempes, Associé de Recherche, Laboratoire de Biorhéologie et d'Ultrasonographie Médicale, Montréal, Canada : *Caractérisation ultrasonore de l'agrégation des globules rouges.*
- Elisa Konofagou, Professeur et Directrice du laboratoire "Ultrasound and Elasticity Imaging", Université de Columbia, New York, Etats-Unis : *Suivi de la technique HIFU par une technique ultrasonore microscopique d'estimation de taille.*
- Olivier Basset, Professeur, Centre de Recherche en Imagerie Médicale, CREATIS, Lyon : *Confrontation des techniques ultrasonores d'estimation de taille et d'analyse statistique sur des fantômes de tissus biologiques.*
- Valérie Deplano, Directrice de Recherche CNRS & Yannick Knapp, Maître de Conférence, Institut de Recherche sur les Phénomènes Hors Equilibre IRPHE, Marseille : *Caractérisation ultrasonore et optique des suspensions denses de particules.*
- Jean-François Landrier, Chargé de Recherche INRA, Laboratoire Nutrition Humaine et Lipides, UMR 476 INSERM/1260 INRA, Marseille : *Compréhension de la diffusion ultrasonore par des biofantômes de cellules.*
- Thierry Pourcher, Chercheur CEA, Laboratoire Transporteur en Imagerie et Radiothérapie Oncologique (TIRO), Nice : *Suivi ultrasonore de la radiothérapie : étude in vivo.*
- Dominique Amy, sénologue, Université de médecine Montpellier - Nîmes : *Construction de fantômes de sein anatomiquement réaliste.*
- Société EUROSONIC, Marseille (2003-2006).

A.4 Contrats de recherche

Responsabilité scientifique de contrats de recherche

- A*Midex interdisciplinarité PR2I 2014-2016, *Novel ultrasonic biomarkers of tumor response to systemic anticancer therapies and their integration on mathematical predictive model*, avec G. Chapuisat (I2M), B. Guillet (UMR/S 1076) et P. Rocchi (CRCM) (279 000 €).
- Contrat PEPS INSIS CNRS 2014, *Modélisation ultrasonore de l'agrégation érythrocytaire*, avec B. Metzger (IUSTI) et G. Cloutier (LBUM) (14 000 €).
- Contrat Région PACA 2013, *Caractérisation UltraSonore et Optique de Suspensions denses d'agrégats érythrocytaires en écoulement*, avec G. Cloutier (LBUM) (27 000 €).
- Cancéropôle PACA 2013, *Etude combinée par imageries SPECT, ultrasonore et spectrométrie de masse des effets de la radiothérapie sur des tumeurs précliniques en fonction de leur hétérogénéité*, avec T. Pourcher (UMR E 4320), G. Chapuisat (I2M) et J.-P. Gérard (CAL) (29 060 €).
- Contrat EDF 2013, *Evaluation ultrasonore des effets d'irradiation forte dose lors d'un accident de contamination externe ou interne : étude in vivo sur le petit animal*, avec C. Payan, R. Guillermin et E. Debieu (15 000 €).
- ANR BBMUT 2012-2015, *Imagerie ultrasonore large bande à l'aide d'une sonde cMUT*, avec O. Basset (CREATIS - porteur du projet) (budget LMA 191 000 €,

budget total 772 000 €).
- Ville de Marseille 2012, *Caractérisation ultrasonore in vivo des tumeurs cancéreuses du sein à l'échelle cellulaire*, avec E. Charafe-Jauffret (IPC CRCM) (14 000 €).
- Fonds Incitatif Recherche aide au montage projet international de l'Université de Provence en 2010-2011, *Caractérisation ultrasonore de suspensions denses de particules*, avec V. Deplano (IRPHE) et G. Cloutier (LBUM) (31 396 €).

Autres contrats

- Cancéropôle PACA 2011-2012, *Echographie haute résolution en PACA*, avec S. Mensah (30 000 €).
- Participation au Labex MEC Mécanique et Complexité 2011-2021 (porteur : Alain Pocheau, IRPHE, Marseille). *Caractérisation ultrasonore de suspensions denses de particules*, collaboration LMA-IRPHE.

A.5 Transfert technologique et valorisation

A.5.1 Brevets déposés

Mes travaux sur la caractérisation ultrasonore de l'agrégation érythrocytaire ont permis de déposer deux brevets

- Brevet No. US 2011/0092817 A1 publié le 21 Avril 2011 : "Method and system of ultrasound scatterer characterization", Guy Cloutier, François Yu, Emilie Franceschini, David Savéry.
- Brevet No. US 2014/0016438 A1 publié le 16 Janvier 2014 : "System and method of ultrasound scatterer characterization", Emilie Franceschini, Guy Cloutier.

A.5.2 Collaboration industrielle

Je participe à une ANR TECSAN BBMUT "Imagerie ultrasonore large bande à l'aide d'une sonde CMUT", dont le porteur principal est Olivier Basset de CREATIS-LRMN à Lyon. Le projet BBMUT a pour objectif d'exploiter les propriétés prometteuses d'une nouvelle technologie de sondes échographiques, appelées CMUT (Capacitive Micromachined Ultrasonic Transducers) et développées par la société VERMON pour proposer de nouvelles techniques d'imagerie et de caractérisation des tissus hépatiques. Ce projet regroupe cinq partenaires de compétences complémentaires : VERMON pour la fabrication des sondes ultrasonores, Creatis et l'Unité U930 dans le domaine de l'imagerie harmonique, le LMA dans la caractérisation ultrasonore des tissus et les Hospices civils de Lyon pour l'expertise clinique.

A.6 Enseignement, Formation et Diffusion de la culture scientifique

A.6.1 Enseignement

- Depuis 2011 : Chargée de cours en Master Mécanique, Physique et Ingénierie spécialité Acoustique (12 heures/an).

Module Propagation des ondes dans les milieux naturels et biologiques.
Travaux pratiques/Mini-projet. *Caractérisation ultrasonore de fantômes de tissus biologiques.*

- 2010-2012 : Chargée de cours en Master recherche Interface Physique-Biologie 2ème année (4 heures/an). Module Marquage biomédicaux pour l'imagerie ultrasonore.

- Octobre 2006 - Janvier 2007 : **ATER, Université Aix-Marseille I**.
  Travaux dirigés en mécanique des solides en DEUG 2ème année (24 heures).
  Cours d'analyse numérique en master 1ère année (20 heures).
  Travaux dirigés en analyse numérique en master 1ère année (20 heures).

- 2003 - 2006 : **Vacations en écoles d'ingénieurs :** Ecole Supérieure d'Ingénieurs de Marseille (ESIM), Ecole Supérieure de Mécanique de Marseille (ESM2) (Ecole Centrale Marseille).
  Travaux dirigés : acoustique en 1ère année (56 heures).
  méthodes numériques en 1ère et 2^{ième} années (49 heures).
  mécanique des solides en 1ère année (8 heures).
  Cours de techniques d'innovation en 1ère année (12 heures).

A.6.2 Encadrement

Post-doctorats et Ingénieurs de recherche

- **LABELLE Pauline**, post-doctorat Mars 2015- Mars 2016, *Suivi ultrasonore de la mort cellulaire*
- **COLLIER Nicolas**, post-doctorat Juin 2014-Juin 2015, *Modèle de diffusion ultrasonore pour des milieux bidisperses*
- **TOURNIAIRE Franck**, ingénieur de recherche Octobre 2013-Mai 2014, *Compéhension de la diffusion ultrasonore par des biofantômes de cellules*

Thèses

- **DE MONCHY Romain**, Aix-Marseille Université, thèse débutée en Octobre 2013, *Caractérisation ultrasonore de l'agrégation érythrocytaire avec un modèle de milieu effectif combiné au modèle de facteur de structure*, Directeurs de thèse : Emilie Franceschini et Bruno Lombard
- **YU François T. H.**, Université de Montréal (soutenue en Décembre 2009), *Paramétrisation de la rétrodiffusion ultrasonore érythrocytaire haute fréquence et pertinence comme facteur de risque de thrombose veineuse*, Directeur de thèse : Guy Cloutier

Participation aux travaux de thèses

- **GARCIA Julian**, Université de Montréal, thèse débutée en Septembre 2012, *Caractérisation expérimentale de l'agrégation érythrocytaire à l'aide de sondes multi-éléments hautes fréquences*, Directeur de thèse : Guy Cloutier (LBUM, Montréal)

- **ROUYER Julien**, Aix-Marseille Université (soutenue le 15 Février 2012), *Tomographie Ultrasonore dédiée à l'imagerie anatomique du sein - Validation expérimentale du projet ANAIS*, Directeur de thèse : Serge Mensah

Encadrements de stages

- **TRAORE Ali**, Stage de Master, Université de Montréal (Septembre 2010/Septembre 2012), co-encadré avec Guy Cloutier (LBUM, Montréal), *De la modélisation à la quantification par ultrasons de l'agrégation érythrocytaire.*
- **AWAD Nesmah**, Stage de Master, Université Française d'Egypte (Février/Juillet 2011), *Comparaison de quatre modèles de diffusion ultrasonore pour la caractérisation de fantômes de tissus biologiques.*
- **POREE Jonathan**, Stage de Master, INSA Lyon (Février/Juillet 2010), co-encadré avec Olivier Basset (CREATIS, Lyon), *Caractérisation ultrasonore de la composition d'un tissu biologique à partir des signaux rétrodiffusés.*
- **SCHUELLER William**, Stage de Licence, ENS Lyon (2 mois, Juin/Juillet 2010), *Expérience à grande échelle pour la compréhension de la diffusion ultrasonore par des agrégats de globules rouges.*
- **PAUZIN Marie-Christine**, Stage de Master, Université de Provence (Février/Juillet 2005), co-encadré avec S. Mensah, *Tomographie ultrasonore d'atténuation des tissus biologiques.*

A.6.3 Participation à des jurys et comités de thèse

- Membre du jury de la thèse de Aiguo Han (University of Illinois at Urbana-Champaign, 3 Novembre 2014) *Ultrasonic characterization of cell pellet biophantoms and tumors using quantitative ultrasound models*
- Membre du comité de thèse (programme MEDITIS) de Julian Garcia (Université de Montréal, thèse débutée en Septembre 2012) *Caractérisation expérimentale de l'agrégation érythrocytaire à l'aide de sondes multi-éléments hautes fréquences*

A.6.4 Organisation de journées scientifiques

- Co-organisation du congrès ICU 2015 pour la session "Quantitative Ultrasound for Soft Tissues" les 10-15 Mai 2015
- Co-organisation du colloque de la Fédération Fabri de Peiresc "Mécanique et milieux vivants" le 30 Janvier 2014
- Co-organisation du congrès Acoustics 2012 pour la session "Biomedical and Biological Ultrasounds" les 23-27 Avril 2012
- Co-organisation des journées de laboratoire du LMA les 28-29 Juin 2010, le 25 Juin 2012, le 28 Janvier 2013 et le 14 Novembre 2013

A.6.5 Travaux d'expertise

- Expertise des articles soumis à des revues scientifiques internationales : IEEE Trans. on Ultrason., Ferroelect., Freq. Contr., IEEE Transactions on Medical Imaging, J. Acoust. Soc. Am., Ultrasound in Medecine and Biology, WSEAS Transaction on Signal Processing Journal
- Expertise de projets scientifiques pour ANR (France) et Terry Fox Research Institute (Canada)

A.7 Activités administratives

- 2014 - : Elue au Conseil Scientifique de l'INSIS.

- 2012 - 2013 : Elue au Conseil de Laboratoire LMA.
- 2011 - 2014 : Elue aux Commissions Administratives Paritaires CAP CR2.
- 2004 - 2005 : Représentante des étudiants et des doctorants au Conseil de Laboratoire dont l'organisation de la journée des doctorants du LMA (le 27 Octobre 2005).
- 2000 - 2002 : Responsable du groupe financement pour le groupe local "Ingénieurs Sans Frontière" (ISF) de Provence, une association de solidarité internationale à but non lucratif : coordination financière pour le groupe local, et recherche de bailleurs de fonds publics et privés (budget 300KF) pour les journées nationales d'ISF 2001 - Prix du Trophée étudiant 2001.

A.8 Publications et communications scientifiques

Brevets

B1 Brevet No. US 2011/0092817 A1 publié le Apr. 21, 2011 : “Method and system of ultrasound scatterer characterization", Guy Cloutier, François Yu, Emilie Franceschini, David Savéry.

B2 Brevet No. US 2014/0016438 A1 publié le Jan. 16, 2014 : “System and method of ultrasound scatterer characterization", Emilie Franceschini, Guy Cloutier.

Chapitre de livre

CL1 FRANCESCHINI E. & CLOUTIER G.
“Modeling of ultrasound backscattering by aggregating red blood cells", Chapter 6, pp. 117-145, in *Quantitative Ultrasound in Soft Tissues* edited by J. Mamou and M. Oelze (Springer, 2013).

Revues avec comité de lecture

A1 FRANCESCHINI E. & MAMOU J.
2015 Ultrasound estimation of tissue microstructure on K562 cell pellet biophantoms, in preparation for **IEEE Trans. on Ultrason., Ferroelect., Freq. Contr.**

A2 DE MONCHY R., DESTREMPES F., SAHA R. K., FRANCESCHINI E. & CLOUTIER G.
2015 Effective medium model for ultrasound backscattering by aggregating cells, in preparation for **J. Acoust. Soc. Amer.**

A3 DESTREMPES F., FRANCESCHINI E., YU F. T. H. & CLOUTIER G.
2015 Unifying concepts of statistical and spectral quantitative ultrasound techniques, submitted to **IEEE Trans. on Medical Imaging**

A4 FRANCESCHINI E., GUILLERMIN R., TOURNIAIRE F., ROFFINO S., LAMY E.,& LANDRIER J.-F.
2014 Structure Factor Model for understanding the measured backscatter coefficients from concentrated cell pellet biophantoms, **J. Acoust. Soc. Amer. 135**(6) 3620-3631.

A5 FRANCESCHINI E., SAHA R. K. & CLOUTIER G.
2013 Comparison of three scattering models for ultrasound blood characterization, **IEEE Trans. on Ultrason., Ferroelect., Freq. Contr. 60**(11) 2321-2334.

A6 FRANCESCHINI E. & GUILLERMIN R.
2012 Experimental assessment of four ultrasound scattering models for characterizing concentrated tissue-mimicking phantoms, **J. Acoust. Soc. Amer. 132**(6) 3735-3747.

A7 ROUYER J., MENSAH S., FRANCESCHINI E., LASAYGUES P. & LEFEBVRE, J.-P.
2012 Conformal ultrasound imaging system for anatomical breast inspection, **IEEE Trans. on Ultrason., Ferroelect., Freq. Contr.** special issue on Novel Embedded

Systems for Ultrasonic Imaging and Signal Processing, vol. 59, no. 7, pp. 1457-1469, 2012.

A8 FRANCESCHINI E., METZGER B. & CLOUTIER G.
2011 Forward problem study of an effective medium model for ultrasound blood characterization, **IEEE Trans. on Ultrason., Ferroelect., Freq. Contr. 58**(12) 2668-2679.

A9 ALESSANDRINI M., MAGGIO S., POREE J., DE MARCHI L., SPECIALE N., FRANCESCHINI E., BERNARD. O & BASSET O.
2011 A Restoration Framework for Ultrasonic Tissue Characterization, **IEEE Trans. on Ultrason., Ferroelect., Freq. Contr. 58**(11) 2344-2360.

A10 SAHA R. K., FRANCESCHINI E. & CLOUTIER G.
2011 Assessment of accuracy of the structure-factor-size-estimator method in determining red blood cell aggregate size from ultrasound spectral backscatter coefficient, **J. Acoust. Soc. Amer. 129**(4), 2269-2277.

A11 FRANCESCHINI E., YU F. T. H., DESTREMPES F., & CLOUTIER G.
2010 Ultrasound characterization of red blood cell aggregation with intervening attenuating tissue-mimicking phantoms, **J. Acoust. Soc. Amer. 127**(2) 1104-1115.

A12 YU F. T. H., FRANCESCHINI E., CHAYER B., ARMSTRONG J.K., MEISELMAN H. J., & CLOUTIER G.
2009 Ultrasonic parametric imaging of erythrocyte aggregation using the structure factor size estimator, **Biorheology 46** 343–363.

A13 FRANCESCHINI E., YU F. T. H., & CLOUTIER G.
2008 Simultaneous estimation of attenuation and structure parameters of aggregated red blood cells from backscatter measurements, **J. Acoust. Soc. Amer. 123** (4) EL85-EL91.

A14 FRANCESCHINI E., MENSAH S., LE MARREC L., & LASAYGUES P.
2007 An optimization method for quantitative impedance tomography, **IEEE Trans. on Ultrason., Ferroelect., Freq. Contr.** special issue on High Resolution Ultrasonic Imaging in Industrial, Material and Biomaterial Applications **54**(8) 1578-1588.

A15 MENSAH S. & FRANCESCHINI E.
2007 Near-field ultrasound tomography, **J. Acoust. Soc. Amer. 121**(3) 1423-1433.

A16 FRANCESCHINI E., MENSAH S., AMY D., & LEFEBVRE J.-P.
2006 A 2D anatomic breast ductal computer phantom for ultrasonic imaging, **IEEE Trans. on Ultrason., Ferroelect., Freq. Contr. 53**(7) 1281-1288.

A17 MENSAH S., FRANCESCHINI E., & LEFEBVRE J.-P.
2006 Mammographie ultrasonore en champ proche, **Traitement de Signal numéro spécial Cancérologie 23**(3) 259-275.

A18 FRANCESCHINI E., PAUZIN M.-C., MENSAH S., & GROBY J.-P.
2005 Soft tissue absorption tomography with correction for scattering aberrations, **Ultrasonic Imaging 27**(4) 221-236.

Actes de congrès

AC1 DE MONCHY R., DESTREMPES F., SAHA R. K., FRANCESCHINI E. & CLOUTIER G.
2014 Effective Medium Theory for Ultrasound Blood Characterization, **9th International Conference on Ultrasonic Biomedical Microscanning**, Peebles, Scotland, 28 Septembre-1 Octobre.

AC2 DESTREMPES F., FRANCESCHINI E. & CLOUTIER G.
2014 Statistical Modeling of the Echo Envelope and its Relation with Scatterers Spatial Organization in the Context of Ultrasound Blood Aggregation, **9th International Conference on Ultrasonic Biomedical Microscanning**, Peebles, Scotland, 28 Septembre-1 Octobre.

AC3 FRANCESCHINI E., GUILLERMIN R., TOURNIAIRE F. & LANDRIER J.-F.
2014 Structure Factor Model for understanding the ultrasonic scattering from concentrated cell pellet biophantoms, **9th International Conference on Ultrasonic Biomedical Microscanning**, Peebles, Scotland, 28 Septembre-1 Octobre.

AC4 FRANCESCHINI E., GUILLERMIN R., TOURNIAIRE F. & LANDRIER J.-F.
2014 Structure Factor Model for understanding the ultrasonic scattering from concentrated cell pellet biophantoms, **Proceedings of the 2014 IEEE International Ultrasonics Symposium**, pp. 628-631, doi :10.1109/ULTSYM.2014.0154, Chicago, 3-6 Septembre.

AC5 FRANCESCHINI E., GUILLERMIN R., TOURNIAIRE F., LAMY E., ROFFINO S. & LANDRIER J.-F.
2013 On the use of the Structure Factor Model to understand the measured backscatter coefficient from concentrated cell pellet biophantoms, **Proceedings of the 2013 IEEE International Ultrasonics Symposium**, pp.1220-1223, doi :10.1109/ULTSYM.2013.0312, Pragues, 22-25 Juillet.

AC6 FRANCESCHINI E. & GUILLERMIN R.
2012 Quantitative ultrasound estimates from tissue-mimicking phantoms with high scatterer volume fraction, **8th International Conference on Ultrasonic Biomedical Microscanning**, Saint-Paulin, Canada, 24-27 Septembre.

AC7 FRANCESCHINI E. & CLOUTIER G.
2012 Comparison of three scattering models for ultrasound blood characterization, **8th International Conference on Ultrasonic Biomedical Microscanning**, Saint-Paulin, Canada, 24-27 Septembre.

AC8 FRANCESCHINI E.
2012 Experimental ultrasound characterization of tissue-mimicking phantoms with high scatterer volume fractions, **Proceedings of the Joint meeting 11th Congrès Français d'Acoustique and IOA annual meeting**, Nantes, 23-27 Avril 2012.

AC9 FRANCESCHINI E. & AWAD N.
2011 Experimental validation of the structure factor model on tissue-mimicking phantoms, **Proceedings of the 2011 IEEE International Ultrasonics Symposium**, Orlando, 18-21 Octobre 2011.

AC10 FRANCESCHINI E., METZGER B. & CLOUTIER G.
2011 An effective medium model for ultrasound blood characterization, **Proceedings of the 2011 IEEE International Ultrasonics Symposium**, Orlando, 18-21 Octobre 2011.

AC11 ALESSANDRINI M., MAGGIO S., POREE J., DE MARCHI L., SPECIALE N., FRANCESCHINI E., BERNARD. O & BASSET O.
2011 An expectation maximization framework for an improved ultrasound-based tissue characterization, **SPIE Medical imaging conference**, Proc. SPIE 7968, 79680E doi :10.1117/12.877632, Orlando (USA), 12-17 Février.

AC12 FRANCESCHINI E., LOMBARD B., & PIRAUX J.
2011 Ultrasound characterization of red blood cells distribution : a wave scattering simulation study, Proceedings of the 6th conference of the GDR 2501 Research on Ultrasound Propagation for NDT jointly with the 10th Anglo-French Physical Acoustics Conference (AFPAC), **Journal of Physics : Conference Series 269** doi : 10.1088/1742-6596/269/1/012014

AC13 NGUYEN L.-C., TRIPETTE J., FRANCESCHINI E., CHIASSON J.-L., GIROUX M.-F., ROBILLARD P., SOULEZ G. & G. CLOUTIER
2010 In-situ characterization of red blood cell aggregation measured with high frequency ultrasound in type 2 diabetic patients, **Proceedings of the 2010 IEEE International Ultrasonics Symposium**, San Diego, 11-14 Octobre.

AC14 FRANCESCHINI E., LOMBARD B., & PIRAUX J.
2010 Caractérisation ultrasonore de la distribution de globules rouges : étude par simulation numérique, **Acte du 10ème Congrès Français d'Acoustique**, Lyon, 12-16 avril 2010.

AC15 FRANCESCHINI E., YU F. T. H., DESTREMPES F., & CLOUTIER G.
2009 *In vivo* ultrasound characterization of red blood cell aggregation using the Structure Factor Size and Attenuation Estimator, **Proceedings of the 2009 IEEE International Ultrasonics Symposium**, Rome, 20-23 September, pp. 301-304

AC16 FRANCESCHINI E., YU F. T. H., & CLOUTIER G.
2009 Ultrasound characterization of aggregated red blood cells : towards in vivo application, in **Springer Proceedings in Physics, Ultrasonic Wave Propagation in Non Homogeneous Media**, pp. 293-302

AC17 ROUYER J., MENSAH S., LASAYGUES P., FRANCESCHINI E., DEBIEU E., & LEFEBVRE J. P.
2009 Prototype ANAÏS : Tomographe ultrasonore pour l'imagerie anatomique du sein - Comparaison avec l'échographie, **19ème Congrès Français de Mécanique**, Marseille, 24-28 août.

AC18 CLOUTIER G., YU F. T. H., FRANCESCHINI E., NGUYEN L. C., & ZIMMER A.
2008 Ultrasound determination of structural indices of red blood cell aggregation for in vivo scanning, **13th International Congress of Biorheology and 6th International Conference on Clinical Hemorheology**, Penn State University, USA, July 9–13, in **Biorheology 45**, no.1-2, pp. 98.

AC19 YU F. T. H., FRANCESCHINI E., ARMSTRONG J. K., MEISELMAN H. J., & CLOUTIER G.

2008 Ultrasound parametrical imaging of RBC aggregation in Couette and tube flows and local viscosity extrapolations,**13th International Congress of Biorheology and 6th International Conference on Clinical Hemorheology**, Penn State University, USA, July 9–13, in **Biorheology 45**, no.1-2, pp. 117.

AC20 FRANCESCHINI E., YU F. T. H., FENECH M., & CLOUTIER G.
2007 Evaluation of the Structure Factor Size Estimator from Simulated Ultrasonic Backscattered Signals from Blood, **Proceedings of the 2007 IEEE International Ultrasonics Symposium**, New York, October 28-31, pp. 2503-2506, DOI 10.1109/ULTSYM.2007.630.

AC21 LASAYGUES P., FRANCESCHINI E., DEBIEU E., & BRANCHERIAU L.
2007 Non-destructive diagnostic of integrity of green wood using ultrasonic diffraction tomography, **Proceedings of the International Congress on Ultrasonics**, Vienna, April 9-13.

AC22 FRANCESCHINI E., MENSAH S., AMY D., & LEFEBVRE J.-P.
2007 Breast ductal computer phantoms, **Proceedings of the 28th International Symposium on Acoustical Imaging** (Ed. M.P. André, Springer) **28** 213-221.

AC23 MENSAH S. & FRANCESCHINI E.
2007 Parametric acoustic microscopy, **Proceedings of the International Congress on Ultrasonics**, Vienna, April 9-13.

AC24 LASAYGUES P., FRANCESCHINI E., GUILLERMIN R., LEFEBVRE J.-P., SALAUD N.& PETIT P.
2007 Two-dimensional ultrasonic computed tomography of growth bone, **Proceedings of the 2007 IEEE International Ultrasonics Symposium**, New York, October 28-31, pp. 1816-1819, DOI 10.1109/ULTSYM.2007.457.

AC25 MENSAH S., FRANCESCHINI E., & PAUZIN M.-C.
2007 Ultrasound mammography, **Proceedings of the 1st European Conference on Molecular Imaging Technology - EuroMedIm, Nuclear Instruments and Methods in Physics Research A 571**(1) 52-55.

AC26 FRANCESCHINI E., PAUZIN M.-C., & MENSAH S.
2006 Ultrasonic absorption tomography on soft tissues with correction for scattering effects, **Proceedings of the 2006 International Symposium on Biomedical Imaging : From Nano to Macro (ISBI)**, Vols 1-3, pp. 872-875, DOI 872 0-7803-9577-8/06/.

AC27 FRANCESCHINI E., LE MARREC L., & MENSAH S.
2006 Une méthode d'optimisation pour la tomographie quantitative d'impédance, **Acte du 8ème Congrès Français d'Acoustique**, Tours, 24-27 Avril.

AC28 PAUZIN M.-C., FRANCESCHINI E., & MENSAH S.
2006 Tomographie ultrasonore d'absorption des tissus mous avec correction des effets de diffraction, **Acte du 8ème Congrès Français d'Acoustique**, Tours, 24-27 Avril.

Séminaires invités

S1 4 Novembre 2014, Bioacoustics Research Laboratory, University of Illinois, Urbana-Champaign : "Structure factor model for the ultrasound estimation of tissue microstructure. Erythrocyte aggregation and cell pellet biophantoms".

S2 4 Avril 2014, au Laboratoire d'Imagerie Biomédicale, Paris : "Modèle de Facteur de Structure pour l'estimation ultrasonore des microstructures tissulaires".

S3 3 Novembre 2011, Ultrasound and Elasticity Imaging Laboratory, Department of Biomedical Engineering, University of Columbia, New York : "Ultrasound backscattering by aggregated red blood cells".

S4 3 Mai 2010, au Laboratoire de Spectrométrie Physique, Grenoble : "Caractérisation ultrasonore in vivo des tissus biologiques à l'échelle microscopique".

S5 5 juin 2009, au Laboratoire d'Imagerie Paramétrique, Paris : "Caractérisation ultrasonore in vivo des propriétés microscopiques des tissus biologiques".

S6 21 Mars 2008, au laboratoire Applications des ultrasons à la thérapie (INSERM unité 556), Lyon : "Caractérisation ultrasonore de l'agrégation des globules rouges : vers une application *in vivo*".

S7 16 Février 2007, au LBUM (Laboratoire de Biorhéologie et d'Ultrasonographie Médicale), Montréal, Canada : "Ultrasound tomography applied to breast cancer detection".

S8 23 Novembre 2006, au laboratoire Applications des ultrasons à la thérapie (INSERM unité 556), Lyon : "Tomographie ultrasonore dédiée à la détection du cancer du sein".

S9 20 Juillet 2006, au laboratoire ACULAB, Université de Roma Tre - Département d'in-génierie électrique, Rome, Italie : "Ultrasound tomography applied to breast cancer detection".

S10 1er Mars 2006, au Laboratoire Ondes et Acoustique, Paris : "Tomographie ultrasonore dédiée à la détection du cancer du sein".

S11 27 Février 2006, au Laboratoire d'Imagerie Paramétrique, Paris : "Tomographie ultrasonore dédiée à la détection du cancer du sein".

Communications à des journées scientifiques et des GDR

C1 24-25 Juin 2014, GDR Mécanique des matériaux et fluides biologiques (GDR 3570), Paris : "Structure Factor Model for understanding the ultrasonic scattering from concentrated cell pellet biophantoms".

C2 30 Janvier 2014, colloque Mécanique et Milieux Vivants, Fédération Fabri de Peiresc, Marseille : "Caractérisation ultrasonore et optique de suspensions denses de particules agrégeantes".

C3 3 Décembre 2013, Workshop sur l'écoulement et l'agrégation du sang du GDR Mécanique des matériaux et fluides biologiques (GDR 3570), Grenoble : "Modeling of ultrasound backscattering by aggregating red blood cells".

C4 3-4 Juillet 2013, GDR Mécanique des matériaux et fluides biologiques (GDR 3570), Autrans : "Caractérisation ultrasonore des tissus biologiques : Agrégation érythrocytaire et Os enfant".

C5 7 Juin 2012, Cancéropôle PACA, Marseille : "Suivi de la mort cellulaire par une méthode de caractérisation ultrasonore : étude sur des fantômes de tissus biologiques et sur des cultures de cellules".

C6 3 Juin 2010, GDR Interaction Fluide Structure Biologique, Compiègne : "Caractérisation ultrasonore des suspensions denses de particules".

C7 18-22 Janvier 2010, 10ième conférence acoustique physique franco-anglaise et GDR Ultrasons, Lake District, Royaume-Uni : "Ultrasound characterization of red blood cells distribution : a wave scattering simulation study".

C8 4 Décembre 2008, GDR Ultrasons, Institut Jean D'Alembert, Paris : "De la difficulté de prendre en compte l'atténuation des tissus intermédiaires pour la caractérisation ultrasonore de l'agrégation des globules rouges".

C9 2-5 Juin 2008, GDR Ultrasons, Biarritz : "Caractérisation ultrasonore de l'agrégation des globules rouges : vers une application *in vivo*".

C10 14-19 Mai 2006, GDR Ultrasons, Presqu'île de Giens : "Tomographie ultrasonore en champ proche pour un fantôme anatomique 2D de sein".

C11 21 Mars 2006, GDR ISIS/GDR Stic-Santé, ENST, Paris : "Tomographie ultrasonore en champ proche".

C12 2 Mars 2006, GDR Ondes/GDR Ultrasons, Supelec, Paris : "Tomographie ultrasonore d'absorption avec correction des effets de diffraction.

C13 18 Octobre 2005, Journée Bio-mécanique, LMA, Marseille : "Tomographie ultrasonore appliquée à la détection du cancer du sein".

C14 6-8 Avril 2005, IXièmes Journées d'Acoustique Physique, Sous-marine et Ultrasonore (JAPSUS), IUT d'Aix-en-Provence : "Fantôme numérique simulant les tissus du sein".

C15 21-22 Octobre 2004, GDR Ultrasons, INRIA : "Comparaison des reconstructions tomographique et échographique pour un fantôme simulant les tissus du sein".

Annexe B

Sélection d'articles post-thèse

B.1 Diffusion ultrasonore par des suspensions concentrées d'agrégats érythrocytaires

A11 YU F. T. H., FRANCESCHINI E., CHAYER B., ARMSTRONG J.K., MEISELMAN H. J., & CLOUTIER G.
2009 Ultrasonic parametric imaging of erythrocyte aggregation using the structure factor size estimator, **Biorheology 46** 343–363.

A9 SAHA R. K., FRANCESCHINI E. & CLOUTIER G.
2011 Assessment of accuracy of the structure-factor-size-estimator method in determining red blood cell aggregate size from ultrasound spectral backscatter coefficient, **J. Acoust. Soc. Amer. 129**(4), 2269-2277.

A7 FRANCESCHINI E., METZGER B. & CLOUTIER G.
2011 Forward problem study of an effective medium model for ultrasound blood characterization, **IEEE Trans. on Ultrason., Ferroelect., Freq. Contr. 58**(12) 2668-2679.

A4 FRANCESCHINI E., SAHA R. K. & CLOUTIER G.
2013 Comparison of three scattering models for ultrasound blood characterization, **IEEE Trans. on Ultrason., Ferroelect., Freq. Contr. 60**(11) 2321-2334.

A10 FRANCESCHINI E., YU F. T. H., DESTREMPES F., & CLOUTIER G.
2010 Ultrasound characterization of red blood cell aggregation with intervening attenuating tissue-mimicking phantoms, **J. Acoust. Soc. Amer. 127**(2) 1104-1115.

A12 FRANCESCHINI E., YU F. T. H., & CLOUTIER G.
2008 Simultaneous estimation of attenuation and structure parameters of aggregated red blood cells from backscatter measurements, **J. Acoust. Soc. Amer. 123** (4) EL85-EL91.

Biorheology 46 (2009) 343–363
DOI 10.3233/BIR-2009-0546
IOS Press

Ultrasonic parametric imaging of erythrocyte aggregation using the structure factor size estimator *

François T.H. Yu [a], Émilie Franceschini [a], Boris Chayer [a], Jonathan K. Armstrong [b], Herbert J. Meiselman [b] and Guy Cloutier [a,c,**]

[a] *Laboratory of Biorheology and Medical Ultrasonics, Centre de Recherche, Centre Hospitalier de l'Université de Montréal, Montréal, QC, Canada*

[b] *Department of Physiology and Biophysics, Keck School of Medicine, University of Southern California, Los Angeles, CA, USA*

[c] *Department of Radiology, Radio-Oncology and Nuclear Medicine and Institute of Biomedical Engineering, Université de Montréal, Montréal, QC, Canada*

Received 7 January 2009
Accepted in revised form 25 June 2009

Abstract. Ultrasound characterization of erythrocyte aggregation (EA) is attractive because it is a non-invasive imaging modality that can be applied *in vivo* and *in situ*. An experimental validation of the Structure Factor Size Estimator (SFSE), a non-Rayleigh scattering model adapted for dense suspensions, was performed on 4 erythrocyte preparations with different aggregation tendencies. Erythrocyte preparations were circulated in Couette and tube flows while acoustically imaged over a bandwidth of 9–28 MHz. Two acoustically derived parameters, the packing factor (W) and ensemble averaged aggregate size (D), predictably increased with increasing EA, a finding corroborated by bulk viscosity measurements. In tube flow, a "black hole" reflecting the absence of aggregates was observed in the center stream of some parametric images. The SFSE clearly allowed quantifying the EA spatial distribution with larger aggregates closer to the tube walls as the aggregation tendency was increased. In Couette flow, W and D were uniformly distributed across the shear field. Assuming that the viscosity increase at low shear is mainly determined by EA, viscosity maps were computed in tube flow. Interestingly, erythrocyte suspensions with high aggregabilities resulted in homogeneous viscosity distributions, whereas a "normal" aggregability promoted the formation of concentric rings with varying viscosities.

Keywords: Ultrasound backscattering coefficient, ultrasound tissue characterization, packing factor, Born approximation, non-Rayleigh scattering, hemorheology, local viscosity

1. Introduction

Blood is a shear thinning non-Newtonian fluid: in steady state, the viscosity increase at low shear is predominantly caused by reversible erythrocyte aggregation (EA) [8]. The level of EA is dependent

* This article is based on a paper given by Dr. Guy Cloutier in Symposium 31 at the 13th International Congress of Biorheology and 6th International Conference of Clinical Hemorheology at the Pennsylvania State University, State College, PA, USA, July 9–14, 2008.

** Address for correspondence: Guy Cloutier, Director LBUM-CRCHUM, 2099 Alexandre de Sève, Pavilion J.A. de Sève (room Y-1619), Montréal, QC, H2L 2W5, Canada. Tel.: +1 514 890 8000 (24703); Fax: +1 514 412 7505; E-mail: guy.cloutier@umontreal.ca; URL: http://lbum-crchum.com.

on the erythrocyte aggregability [43], on the concentration of aggregation-inducing macromolecules in plasma (primarily fibrinogen but also immunoglobulins and other inflammatory proteins) and on mechanical shearing forces [3,9]. Indices of aggregation can be measured *in vitro* on samples obtained by venipuncture using different techniques – including viscosimetry, erythrocyte sedimentation rate, electrical impedance, light and ultrasound scattering [54]. In humans, increased bulk blood viscosity and aggregation measured *in vitro* correlate with numerous cardiovascular diseases and complications including diabetes [27,33], deep venous thrombosis and its recurrence [10,30], and ischemic heart events [32,61]. The fact that these diseases and their complications generally occur in specific locations of the vascular system suggest a pathological micro- and/or macro-circulatory hemodynamic contribution to their etiologies.

Analytical [18,42,45] and numerical [4,26,65] models have been proposed to interpret the rheological behavior of blood. However, the complexity of the time dependent non-Newtonian behavior of blood and the computational loads required for transposing numerical models to real vascular and erythrocyte geometries remain important challenges for these approaches. Ultrasound (US) imaging, which utilizes non-invasive pressure wave propagation through biological tissues, is a tool that has the potential to measure EA for both *in vivo* and *in situ* flow conditions. This imaging modality could significantly contribute to hemorheology especially at high US frequencies, since it allows characterization of EA in space and in time, as demonstrated by its sensitivity to measure aggregate formation kinetics [11, 14] and its ability to follow cyclic aggregation and disaggregation states under pulsatile flows [17,39]. *In situ* quantification, etiological impacts and *in vivo* monitoring are potential applications of US EA characterization.

1.1. Ultrasound and EA

The increased B-mode blood echogenicity caused by EA during clinical scans, typically performed at 2–12 MHz, is well known [28,52]. The access to radio-frequency (RF) data from laboratory instruments and, increasingly, from clinical scanners allows application of a normalization procedure [34,53,58] to obtain a backscattering coefficient (BSC), defined as the power backscattered by a unit volume of scattering entities per unit incident intensity per unit solid angle [51]. The BSC is an acoustic signature of a tissue's microstructure and is therefore not dependent on the scanner and US probe sensitivity. This is a quantitative and reproducible absolute measure that is superior to B-mode echogenicity, which is only qualitative and relative.

It is now well established that the BSC for blood is modulated by the erythrocyte aggregation state that can be modified by flow or shear rate, plasma fibrinogen concentration and hematocrit H [12,37,50, 51]. By measuring blood BSC at different frequencies, it has been shown that the frequency dependence $BSC(f)$ for non-aggregated erythrocytes obeys the Rayleigh scattering theory and its 4th power (f^4) frequency dependence up to $f < 30$ MHz for $H < 30\%$ [63]. However, it has also been shown that beyond these limits, the presence of EA causes a deviation of the backscattered signal from that predicted by the Rayleigh scattering mode. By using a broadband transducer, this deviation can be quantified through the spectral analysis of $BSC(f)$. This approach has been extensively used in US tissue characterization to study cell apoptosis [49], for prostate cancer diagnosis [19] and to differentiate murine mammary fibroadenomas from carcinomas [40].

Our group recently introduced the Structure Factor Size Estimator (SFSE) [62], a data reduction model based on a structure factor $S(f)$, with the objective of solving the inverse problem, i.e., extracting blood microstructural properties from $BSC(f)$. This model, which assumes a known hematocrit, estimates two

physical parameters describing the microstructure of erythrocyte clusters: (1) the packing factor (W) that increases with erythrocyte clustering and is related to the Boltzmann compressibility state equation [44], and (2) the ensemble averaged aggregate isotropic diameter (D), a measure of the mean spatial extent of aggregates, expressed in terms of the number of erythrocytes.

1.2. Control of erythrocyte aggregation tendency

In order to control the aggregation tendency of erythrocytes while maintaining a consistent suspending phase, the covalent attachment of Pluronic copolymers F68 and F98 to the erythrocyte surface was employed as previously described [2]. Pluronics are block copolymers comprised of central poly(propylene glycol) chain flanked by two poly(ethylene glycol) chains. In aqueous solution, Pluronic copolymers micellize (self-aggregate) at a critical temperature dependent on the molecular weight of the poly(propylene glycol) core and copolymer concentration. By utilizing the known micellization behavior of Pluronic copolymers, following covalent attachment of derivatized Pluronic copolymers to the erythrocyte surface, it is possible to create erythrocytes with defined aggregation tendencies. Below the micellization temperature, erythrocyte aggregation is inhibited, and above the micellization temperature, erythrocyte aggregation is augmented [2].

1.3. Objectives

The first objective was to demonstrate that the SFSE allows characterization of EA in homogenous Couette shear flow under steady state conditions with blood at 40% hematocrit having different aggregation tendencies promoted by F68 and F98 Pluronics. The second objective was to circulate the same blood samples in the Couette instrument and a tube flow system in order to compare W and D and their dependence on the shear rate spatial pattern. The last objective was to establish the relationships between steady state bulk viscosity, measured with a low-shear viscometer, and steady state parameters W and D to extrapolate local viscosity maps in tube flow.

2. Material and methods

2.1. Blood samples

Fresh porcine blood from 4 animals was obtained from a local slaughter house. It was anticoagulated with 0.3% (w/w) EDTA. All blood samples were centrifuged (2500g for 10 min) to separate the plasma and erythrocytes. The buffy coat was carefully removed and discarded. Plasma was centrifuged at 20,000g for 20 min and platelet poor plasma (PPP) was kept to reconstitute blood with erythrocytes washed two times with phosphate buffered saline (PBS) and one more time with PPP. This high-speed centrifugation was necessary since we noted in preliminary experiments that platelet aggregates were echogenic in blood exposed to high shear (300 s^{-1}) in Couette flow. Hence, using PPP eliminated this confounding effect potentially affecting the interpretation of our results.

Four types of erythrocyte preparations at 40% hematocrit were then assembled: one non-aggregating erythrocytes suspended in PBS (PBS suspension), control reconstituted blood samples with erythrocytes suspended in PPP (*control*), and erythrocytes coated with tri-block copolymers termed Pluronic F68 or F98 and suspended in PPP. Briefly, the copolymer coating consisted of covalently binding a reactive succinimidyl carbonate derivative of Pluronic F68 and F98 to the primary amines on the erythrocyte

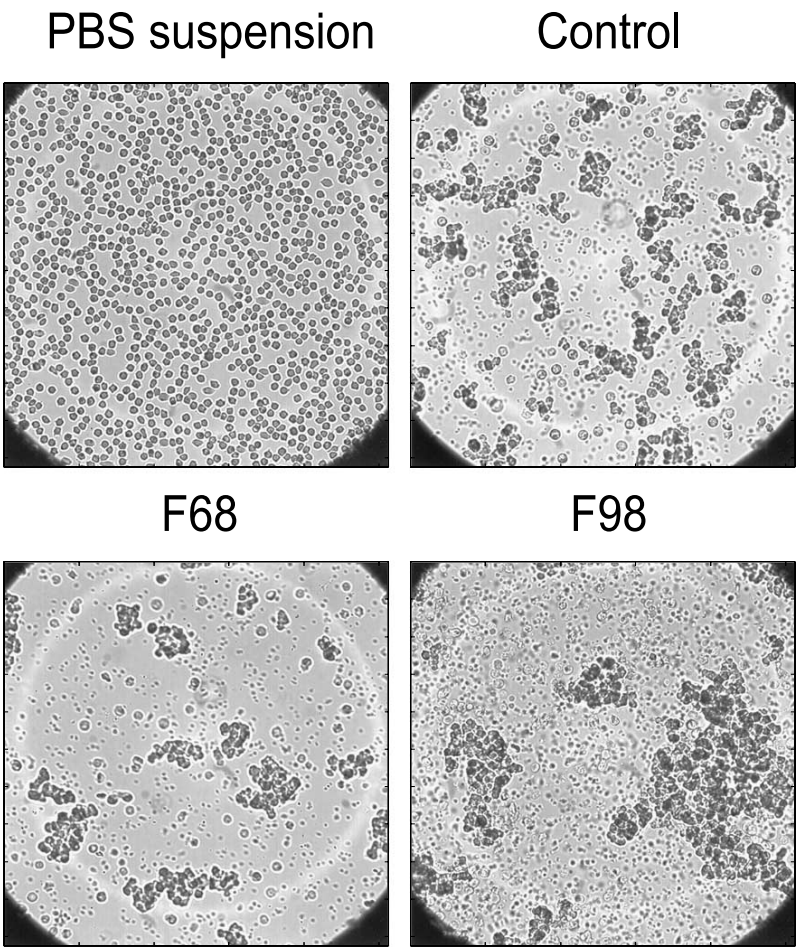

Fig. 1. Microscopic images (40×) of diluted (≈1% hematocrit) PBS suspension, *control* blood, F68 and F98 Pluronics coated erythrocytes at 25°C. F98 increases erythrocyte aggregation whereas F68 has a neutral effect on the clustering organization.

membrane; in the present study, the concentration of the activated Pluronic during the coating process was 0.25 mg/ml of suspension. These tri-block copolymers form temperature-dependent micelles that are determined mainly by the length of the poly(propylene glycol) block chain and its concentration. At room temperature, F98 coating increases EA and F68 coating has essentially no effect on plasma-induced aggregation [2]. Figure 1 shows typical images of uncoated cells, control cells in plasma, and F68 or F98 coated cells in plasma (≈1% hematocrit, stasis, 25°C). All measurements were performed at 25°C.

2.2. Experimental setup

Two flow geometries were investigated in this study (see Fig. 2). A Couette flow was created between two coaxially aligned cylinders with respective diameters of 160 and 164 mm. The inner cylinder's speed was controlled using a stepper motor (Zeta 6104, Parker Hannifin Corporation, Rohnert Park, CA,

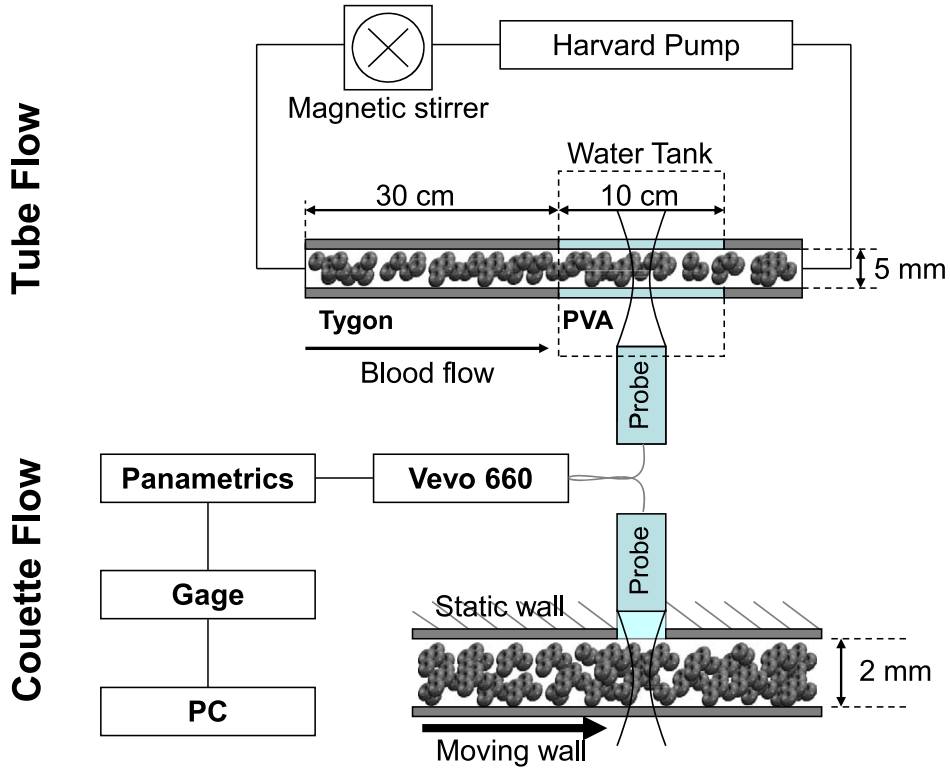

Fig. 2. Schematics of tube and Couette flow experimental setups.

USA). The ultrasound probe was positioned in the fixed outer wall of the Couette flow apparatus with its focal zone positioned at the center of the gap. The 2 mm gap was filled with 70 ml of blood, which was alternatively submitted to a disaggregating cycle of 30 s at a high-shear (300 s^{-1}) to initially disrupt all aggregates, and then to lower shear rates (SR) of 1, 2, 5, 10, 22, 47 and 100 s^{-1} for one minute to allow erythrocyte aggregate formation. At the one minute mark when aggregation was stabilized [62], eight ultrasound images were captured for subsequent analysis offline.

Prepared blood samples were also circulated in a horizontal straight tube submerged in degassed water at flow rates of 1, 2, 5 and 10 ml/min (5 mm inner tube diameter, 40 cm tube length). Measurements were made at 35 cm from the entrance, the required tube entry length for fully developed flow is 1.4 mm at the maximum flow rate of 10 ml/min [36], and shorter for lower flow rates. The last 10 cm section of the tube was composed of an acoustically compatible polyvinyl alcohol (PVA) cryogel tube made by applying 3 freeze-thaw cycles to the molded material [24]. A double syringe pump (model PHD2000, Harvard Apparatus, Holliston, MA, USA) was used to simultaneously push and pull blood to minimize deformation of the PVA tube. A reservoir with a magnetic stirrer was placed upstream of the tube to disaggregate erythrocyte clusters and prevent sedimentation before entering into the tube. Prior to acquiring US data, the 70 ml blood sample was moved back and forth with the Harvard pump for 10 minutes to evacuate air bubbles (which increase blood echogenicity). Blood was then flowed in the forward direction at the selected flow rate to allow aggregate formation. Twenty US images were acquired in the longitudinal

axis of the tube after one minute of steady flow to again stabilize the size of aggregates as performed for Couette flow experiments.

2.3. Ultrasound data acquisition and computation of the SFSE model

An ultrasound biomicroscope (Vevo 660, Visualsonics, Toronto, Canada) was used to insonify blood in B-mode with a RMV-710 probe (central frequency = 25 MHz, focal distance = 1.5 cm, F-number = 2.1), at frame rates of 5 (Couette flow) and 20 (tube flow) images/s. As the transducer was mechanically swept across the sample, sequences of RF data were amplified and filtered with a wideband acoustic receiver (model 5900 PR, Panametrics, Waltham, MA, USA), and digitized at 250 MHz with 8 bit resolution (model CS8500, Gagescope, Montreal, Canada). With these settings, one RF data block consisted of 8 or 20 images, with a pixel resolution of 21 μm (width) × 3 μm (depth). Each vertical line of an image was divided into overlapping segments of 400 μm with a step resolution of 30 μm (92.5% overlapping) for spectral estimation. This window length was determined as an acceptable compromise between image resolution and variance of power spectra.

BSC(f) was computed for every position, each 400 μm of data being Fourier transformed, averaged with corresponding segments from multiple frames and normalized across the −10 dB (9–28 MHz) spectral bandwidth of the system using a 6% hematocrit reference non-aggregating erythrocyte suspension. This normalization procedure for focused transducers is known as the modified substitution method [58]. For each *BSC*(f), W and D were then calculated using the SFSE method [62]. Briefly, this data reduction model is based on a second order polynomial approximation of the structure factor $S(f)$ that describes the weakly scattering tissue's microstructure in the spectral domain. $S(f)$ is directly related to the pair correlation function $g(r)$ describing spatial interactions between erythrocytes through a Fourier transform [57]. The SFSE is a minimization problem in which W and D are deduced from a polynomial fit of the measured frequency dependent *BSC*(f):

$$F(W, D) = \min \|\mathit{BSC}(f) - m\sigma_b(f)S(f)\|^2. \tag{1}$$

In this expression, m is the scatterer number density ($m = H/V$ with H the known hematocrit and V the volume of an erythrocyte), σ_b is the backscattering cross-section of an erythrocyte scatterer prototype of radius a (i.e., in the frequency range used in this study, the error on σ_b is about 5% when using a sphere with a volume V rather than a typical biconcave erythrocyte [47]) and S is the structure factor that is approximated by the polynomial expression [62]:

$$S(f) \approx W - \frac{12}{5}\left(\frac{2\pi}{c}\right)^2 (Da)^2 f^2. \tag{2}$$

This model considers that the increase in *BSC*(f) with aggregation is caused by a change in erythrocyte positions that has an effect on $S(f)$, both W and D increase when erythrocytes form clusters.

2.4. Velocity and shear rate assessments based on speckle tracking analysis

The positioning of the US probe in the longitudinal plane for both Couette and tube flow geometries allowed performing velocity speckle tracking analyses on sequences of B-mode images [56]. A cross correlation algorithm was used to find the translation of a prototype window in two successive frames across the region of interest. By measuring displacements of speckle and knowing the elapsed time

between two images, spatially varying velocities could be determined. For Couette flow, a homogeneous shear rate and a linear velocity profile were measured (data not shown), whereas for tube flow, the shear rate profile was estimated from the velocity profile determined by fitting the power law

$$v(r) = v_{\max}\left[1 - \left(\frac{r}{R}\right)^n\right], \tag{3}$$

where $v_{\max}$ is the maximum velocity, r is the radial position and R the tube radius. A power law with $n = 2$ describes a Poiseuille parabolic flow, whereas n greater than 2 indicates the blunting of the velocity profile caused by aggregation [13,48]. The shear rate *SR*(r) was calculated at the different radial positions using

$$SR(r) = \frac{\partial v(r)}{\partial r} = n v_{\max}\frac{r^{n-1}}{R^n}. \tag{4}$$

To simplify the data analysis of W and D as a function of the shear rate in tube flow, both indices were pooled over image areas covering different shear rate intervals. Namely, the label SR 1 was used to indicate regions with $SR \leqslant 1\ \mathrm{s}^{-1}$, SR 2 regions with $1\ \mathrm{s}^{-1} < SR \leqslant 2\ \mathrm{s}^{-1}$, SR 5 regions with $2\ \mathrm{s}^{-1} < SR \leqslant 5\ \mathrm{s}^{-1}$ and SR 10 regions with $5\ \mathrm{s}^{-1} < SR \leqslant 10\ \mathrm{s}^{-1}$.

2.5. Viscosity measurements

Viscosity measurements were performed with a low-shear viscometer (Contraves LS30, Zurich, Switzerland) at 25°C on similar pig blood samples prepared on site by Dr. J.K. Armstrong in Los Angeles. PBS suspensions, *control* blood, F68 and F98 coated erythrocytes were studied at shear rates varying from 1 to 100 s^{-1}.

3. Results

3.1. Ultrasound measures in Couette flow

3.1.1. BSC(f) and SFSE model

The SFSE model allowed extracting the erythrocyte aggregation parameters W and D from the spectral content of the backscattering coefficient *BSC*(f). Figure 3 illustrates typical *BSC*(f) for the 4 blood types at selected SR of 1, 2, 5, 22 and 100 s^{-1}. Experimental *BSC*(f) are represented by discrete points and SFSE fittings are traced in full lines. The respective values of W, D and the correlation coefficient r^2 of the fitted model are shown in the legend. In Fig. 3a for the PBS suspension, W and D were SR independent because of the absence of aggregation. With normal aggregating erythrocytes (*control* – panel b and F68 – panel c), decreasing the shear rate resulted in increases in W and D. For both types of blood, the SFSE performed very well with r^2 values higher than 0.94. However, for the hyperaggregating F98-coated erythrocytes (panel d), the SFSE could not follow the frequency dependence of *BSC*(f) at shear rates of 2 and 5 s^{-1} when D became larger than 13.7 (value at 22 s^{-1}), as reflected by drastically lower values of r^2. The frequency dependence of aggregated erythrocytes between 9 and 28 MHz could only be efficiently modeled with the SFSE when $D < 14$, i.e., for $kDa < 4.3$ at $f = 28$ MHz, where k is the acoustic wave vector defined as $k = \frac{2\pi f}{c}$ with c the speed of sound in biological tissues (≈1540 m/s).

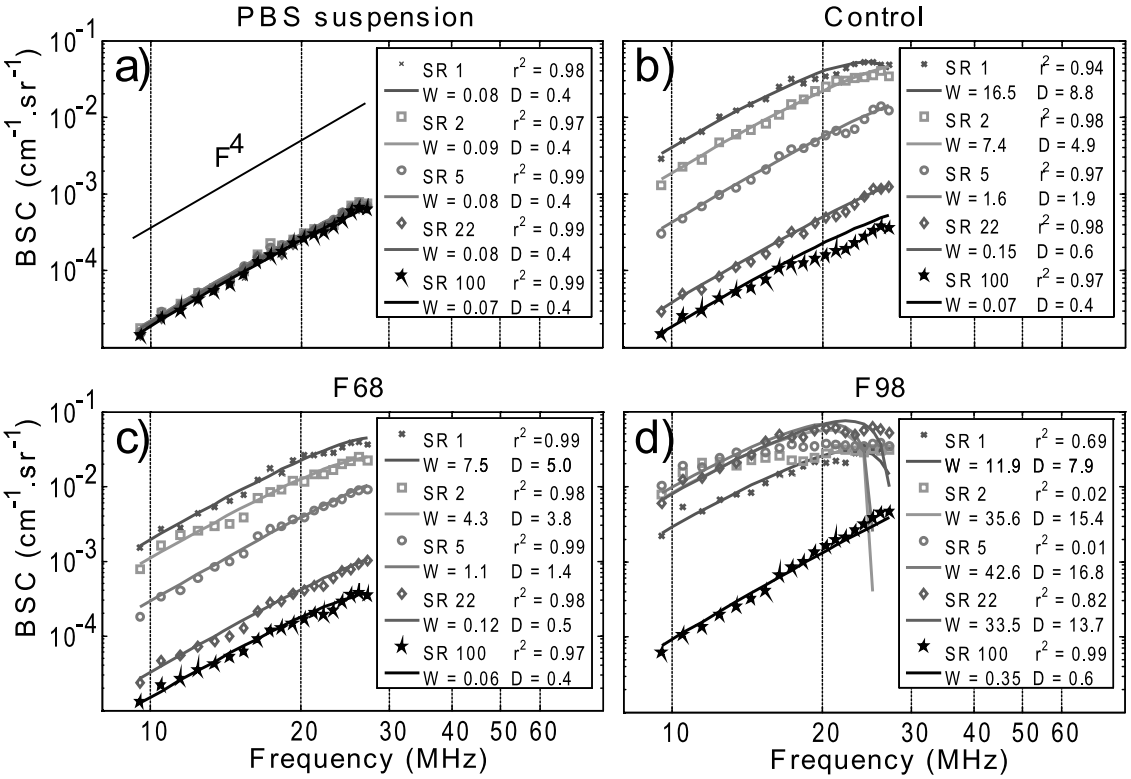

Fig. 3. Typical experimental backscatter coefficient BSC as a function of the ultrasound frequency for (a) erythrocytes suspended in PBS (no aggregation), (b) *control* blood samples, (c) F68 coated blood samples and (d) F98 hyperaggregating coated blood samples under Couette flow. Lines indicate the Structure Factor Size Estimator (SFSE) fitting of experimental data, SR is the shear rate, W and D are erythrocyte aggregation measurements, and r^2 is the correlation coefficient of the fitting.

3.1.2. SFSE reproducibility

The reproducibility of the SFSE measurements was evaluated in the Couette homogenous shear field. W and D were computed on one control sample using 5 repetitions of the protocol at SR of 1, 2, 5, 10, 22, 47 and 100 s^{-1}. Results are presented in Fig. 4 where both W and D are seen to decrease with increasing SR. At a SR of 100 s^{-1}, W was 0.08 ± 0.01 (mean $\pm$ SE) and D was smaller than 1 (0.51 ± 0.04), both values corresponding to disaggregated erythrocytes [62]. W and D standard errors increased with aggregation at the lower shear rates (logarithmic scale). Statistically different levels of W and D ($p < 0.05$) were found between all SR, except between 47 and 100 s^{-1} (Student–Newman–Keuls pair-wise comparisons of the mean ranks, Sigmastat 3.11, Systat Software, San Jose, CA, USA), where erythrocyte aggregation is very low or absent.

3.1.3. SFSE and viscosity shear rate dependencies

Shear rate dependencies of W (panel a), D (panel b) and apparent viscosity (panel c) for Couette flow are presented in Fig. 5. For the PBS suspension, these three parameters were SR independent between 1 and 100 s^{-1}. For the *control* and F68 samples, each index showed a gradual decrease with increasing SR, at any SR, values of W, D and viscosity were similar for both types of blood. For F98, only data for $SR \geqslant 47\ s^{-1}$ are presented because of the limit of the SFSE model, i.e. that it was unable to fit $BSC(f)$ at

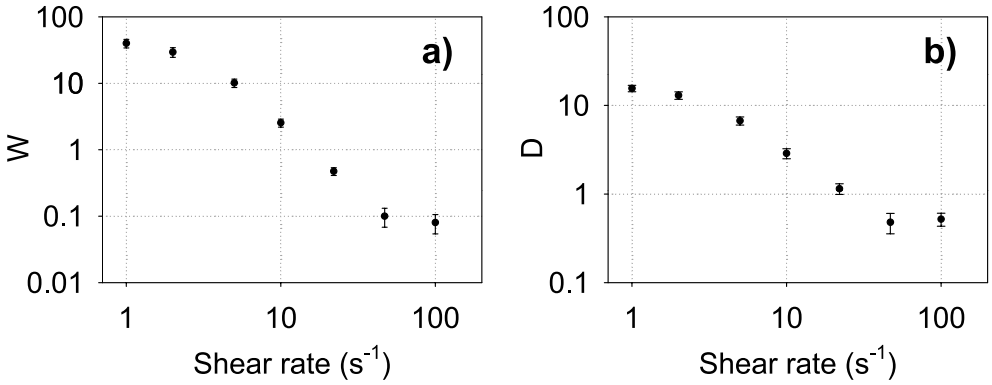

Fig. 4. (a) W and (b) D in Couette flow as a function of the shear rate for 5 measurements realized with a control blood sample. Results are mean $\pm$ SE. Statistically different levels ($p < 0.05$) of W and D were found between all SR, except between 47 and 100 s^{-1}.

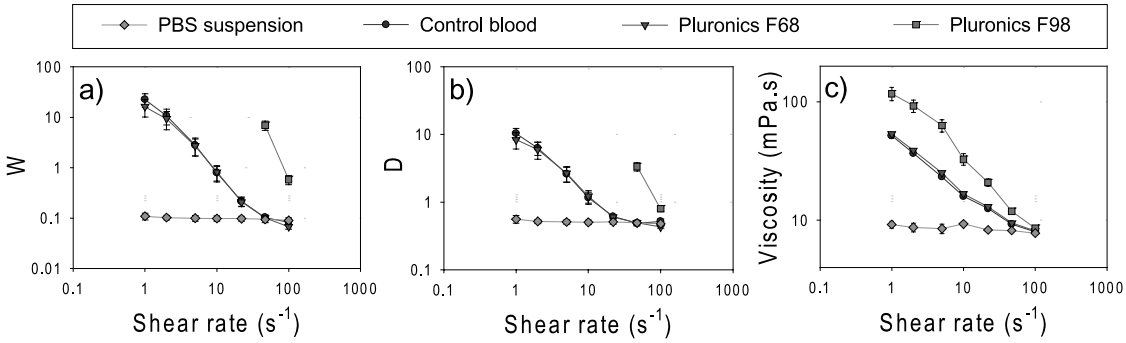

Fig. 5. Shear rate dependencies of (a) W, (b) D and (c) bulk viscosity (measured with a low shear viscometer) for the 4 blood samples (PBS suspension, *control* blood, F68 and F98 coated erythrocytes) collected from 4 animals. Results in Couette flow experiments are mean $\pm$ SE.

lower SR. As expected, values of each rheological parameter for the F98 suspension were higher when compared with other blood types, and decreased with increasing shear rates.

Quantitative comparisons of W and D were performed between blood types using Student–Newman–Keuls pairwise statistics of the mean ranks for each SR, with $p < 0.05$ considered to be significant. No differences were found at any SR between *control* and F68 groups or between *control*, F68 and PBS suspension at SR of 47 and 100 s^{-1}. Significant differences were found between normal aggregating erythrocytes (*control* and F68) and PBS suspended cells at SR of 1, 2, 5, 10 and 22 s^{-1} for W and at SR of 1, 2, 5 and 10 s^{-1} for D. Finally, W and D were significantly higher for the F98 group than for all other groups.

Based upon the results shown in Fig. 5, the bulk viscosity of each blood type may be predicted by parameters W and D since all three indices varied similarly as a function of SR. Linear stepwise backward regressions were used to determine these relations, with linear regression equations and correlation coefficients for viscosity versus W and D presented in Table 1. Based on the correlation coefficients, D is a somewhat better predictor of viscosity, relations between D and viscosity are shown in Fig. 6.

Table 1
Bulk viscosity as a function of ultrasound parameters D and W

Blood sample	Linear regression equation	Correlation coefficient r^2	p
PBS suspension	$\eta = 8.6$		
Control	$\eta = 9.12 + 4.24D$	0.98	<0.001
	$\eta = 12.60 + 1.85W$	0.93	<0.001
F68	$\eta = 8.41 + 5.38D$	0.98	<0.001
	$\eta = 12.35 + 2.67W$	0.95	<0.001
F98	$\eta = 8.72 + 0.71D$	0.97	NS (0.08)
	$\eta = 9.33 + 0.23W$	0.96	NS (0.10)

Notes: η is the bulk viscosity (mPa s) measured in Couette flow with a low-shear blood viscometer; D is the steady state acoustically determined ensemble averaged isotropic aggregate diameter, expressed in number of erythrocytes; W is the steady state acoustically determined ensemble averaged packing factor (no unit); NS – non-significant.

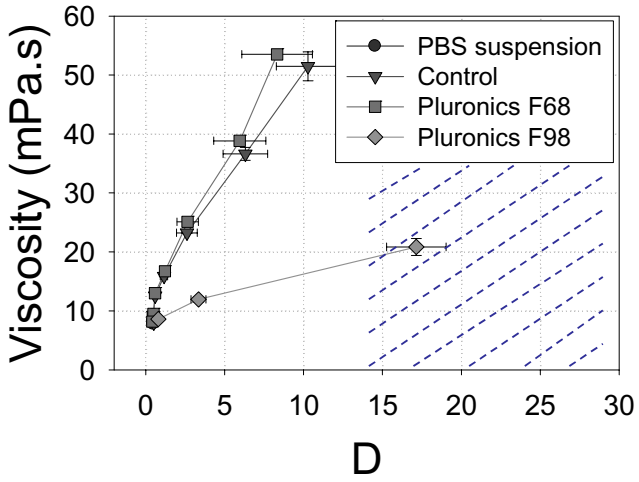

Fig. 6. Bulk viscosity as a function of the SFSE parameter D for the 4 blood types (PBS suspension, *control* blood, F68 and F98 coated erythrocytes) collected from 4 animals. Results in Couette flow experiments are mean ± SE. The dashed section marks the limits of applicability of the SFSE model.

The linear regression for F98 did not reach significance ($p = 0.08$) even when a third point at $D \approx 17$, which is outside the limits of applicability of the SFSE model, was utilized.

3.2. Ultrasound measures in tube flow

3.2.1. Erythrocyte aggregation and impact on velocity and shear rate profiles

Typical velocity profiles estimated by the speckle tracking algorithm are presented in Fig. 7 for flow rates of 1, 2, 5 and 10 ml/min, also shown as upward facing lines or curves are shear rate profiles calculated using Eq. (4). For the PBS suspension (a), velocity profiles were nearly parabolic ($n \approx 2$) for all shear rates. For *control* (b) and F68 (c) bloods, decreasing the flow rate provoked more blunting of velocity profiles, as reflected by monotonic increases of n. However, for F98 coated erythrocytes (d), decreasing the flow rate had the opposite effect, i.e. n decreased from 5.0 to 3.7 or 4.0 and hence less blunting occurred. As a further validation of the approach, volume integrations of velocity profiles were

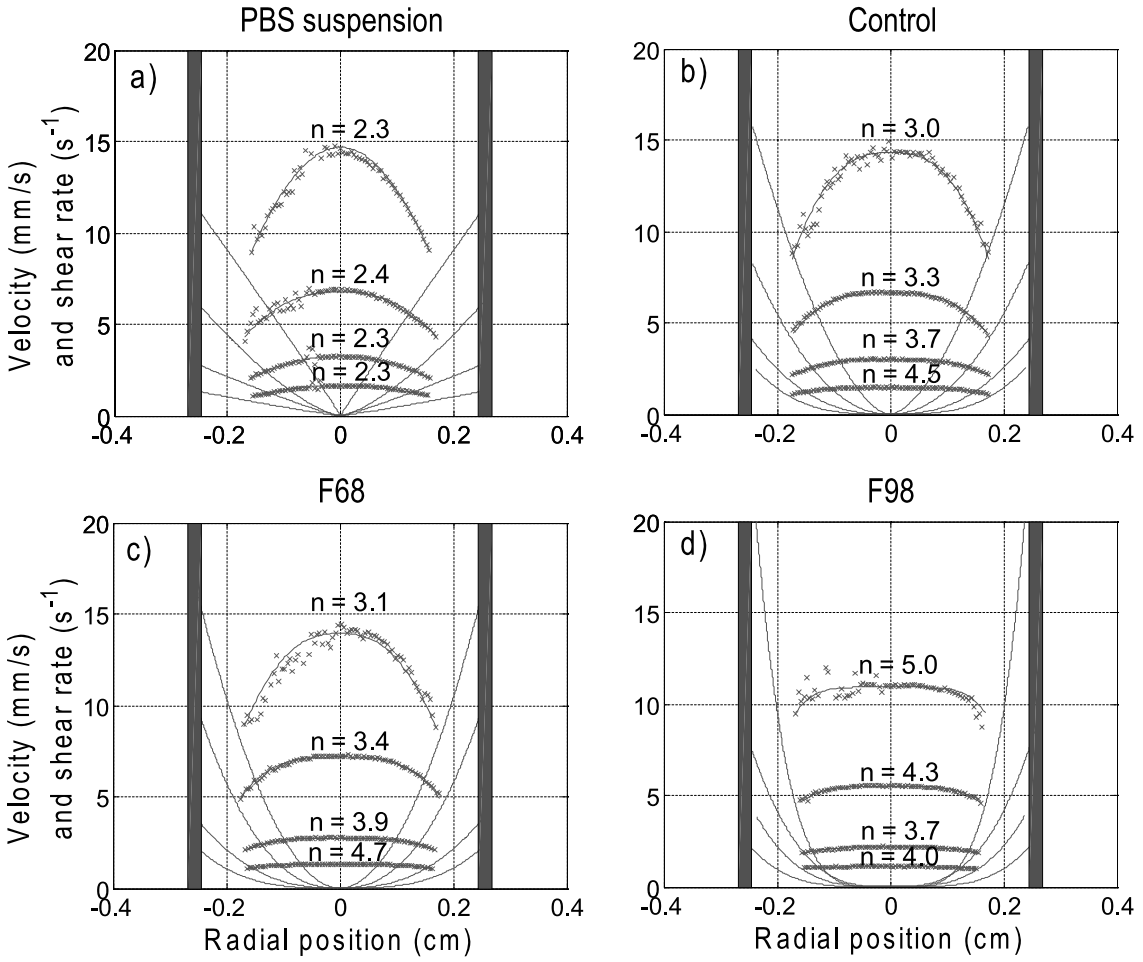

Fig. 7. Typical speckle tracking velocity results in tube flow for flow rates of 1, 2, 5 and 10 ml/min for the 4 blood types (PBS suspension, *control* blood, F68 and F98 coated erythrocytes). The shear rate profiles shown as upward facing lines or curves were deduced from Eq. (4). n is the viscosity power law exponent in Eqs (3) and (4).

compared with known flow rates of the pump in Fig. 8. The estimated flow rates were in excellent agreement for the non-aggregating PBS samples but were slightly underestimated for aggregating erythrocytes with the difference up to 10% for F98 samples.

3.2.2. W and D shear rate dependencies in tube flow

The SFSE model was applied to determine parameters W and D as in Couette flow experiments. Figure 9 presents results for *control* blood and F98 coated erythrocytes of the SR dependency of D for flow rates of 1, 2, 5 and 10 ml/min. F68 results were very similar to *control* data, whereas for the PBS suspension D was SR and flow rate independent ($D = 0.42 \pm 0.02$), the SR dependency of W was similar to that for D. Note that D decreased with increasing SR and flow rates for *control* blood, whereas for F98 coated erythrocytes, the opposite was observed: D increases with increasing SR and flow rates with a similar finding for W (not shown).

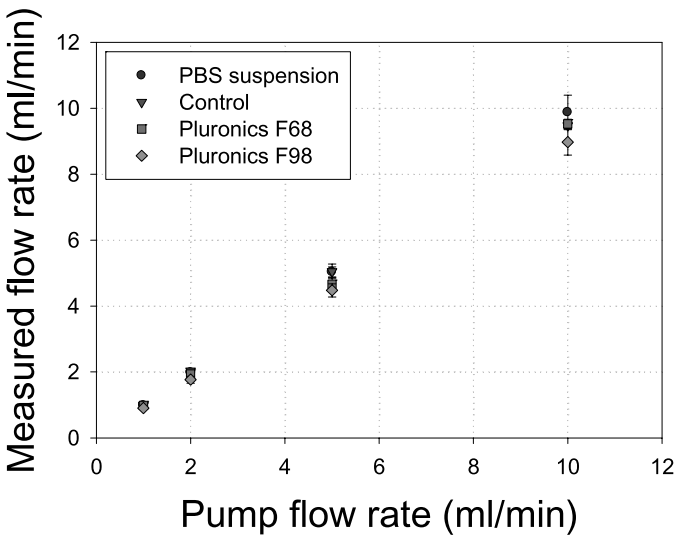

Fig. 8. Flow rate calculated from the volume integration of velocity profiles determined by speckle tracking as a function of the pump flow rate for the 4 blood types (PBS suspension, *control* blood, F68 and F98 coated erythrocytes) collected from 4 animals. Results in tube flow experiments are mean ± SE.

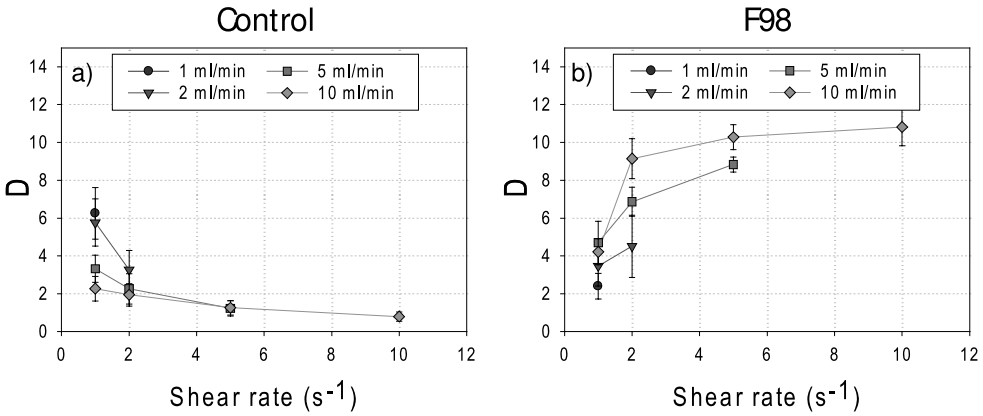

Fig. 9. Shear rate dependencies of D for (a) *control* blood and (b) F98 coated erythrocytes collected from 4 animals in tube flow rates of 1, 2, 5 and 10 ml/min. Results are mean ± SE. Tube shear rates were calculated from speckle tracking measurements.

3.3. Couette and tube flow comparisons

SR dependencies of W and D in both geometries are summarized in Fig. 10. For clarity, only the tube flow rate providing the highest values of W and D at a given SR are shown (see Fig. 9). Note that the SR was varied from 1 to 100 s^{-1} in Couette flow, whereas they ranged from 1 to 10 s^{-1} in tube flow. With the PBS suspension, W and D were slightly lower in tube flow and were SR independent for both geometries. For *control* and F68, lower values of W and D were also noted for tube flow, but for both geometries they decreased with increasing SR as expected. Note, however, that analysis of variance (ANOVA) tests revealed no statistical difference ($p > 0.05$) between both geometries at all SR for PBS,

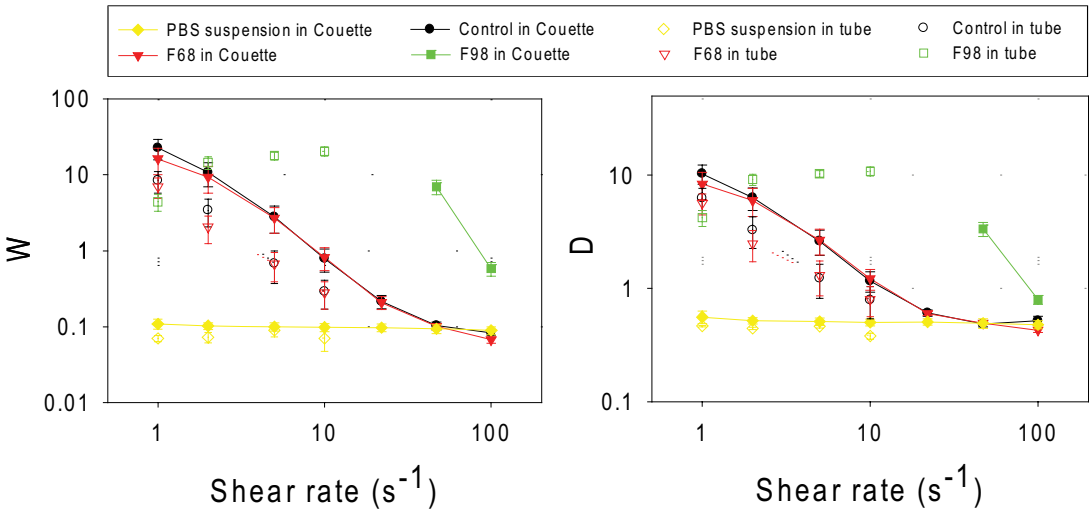

Fig. 10. Shear rate dependencies of (a) W and (b) D for the 4 blood types (PBS suspension, *control* blood, F68 and F98 coated erythrocytes) collected from 4 animals and circulated in Couette and tube flows.

control and F68 bloods. For F98, changes of W and D with SR were quite different (i.e., a decrease with SR in Couette flow and an increase in tube flow) but a clear comparison between both geometries was not possible because the range of SR did not overlap (Fig. 10).

3.4. Parametrical images of W and D in tube flow and viscosity predictions

Typical velocity vectors determined by speckle tracking (left column), parametric images of W, D and predicted viscosity maps are presented for *control* (Fig. 11) and F98 (Fig. 12) bloods. In these figures, the parametric images are superimposed on a conventional B-mode frame. F68 images were very similar to *control*; PBS suspension images were spatially homogenous. The "black hole" (BH) phenomenon can be clearly seen for the *control* blood (Fig. 11) as a hypoechoic zone in the tube center of B-mode and parametric images of W and D (see below for a discussion on the BH). Large BH with less contrast than *control* blood were noted at the highest flow rates for F98 samples. For *control* blood (Fig. 11), the larger clusters of erythrocytes were concentrated in a ring located midway between the center stream and the tube wall, and corresponded to increased viscosity layers. The F98 coating also affected the radial distribution of aggregates, as illustrated in Fig. 12: at low flow rates, the effect of the F98 coating on aggregation was not very pronounced but at higher flow rates large clusters formed close to the tube walls. Interestingly, and unexpectedly, the viscosity for F98 was not markedly increased in this region (see below).

4. Discussion

Erythrocyte aggregation (EA) can be characterized by its effect on $BSC(f)$ using descriptive acoustical parameters such as the 'integrated backscatter' (i.e., mean of the BSC intensity within the transducer frequency bandwidth) or the 'spectral slope' (i.e., linear regression of $BSC(f)$ on a log–log scale) [14,35,

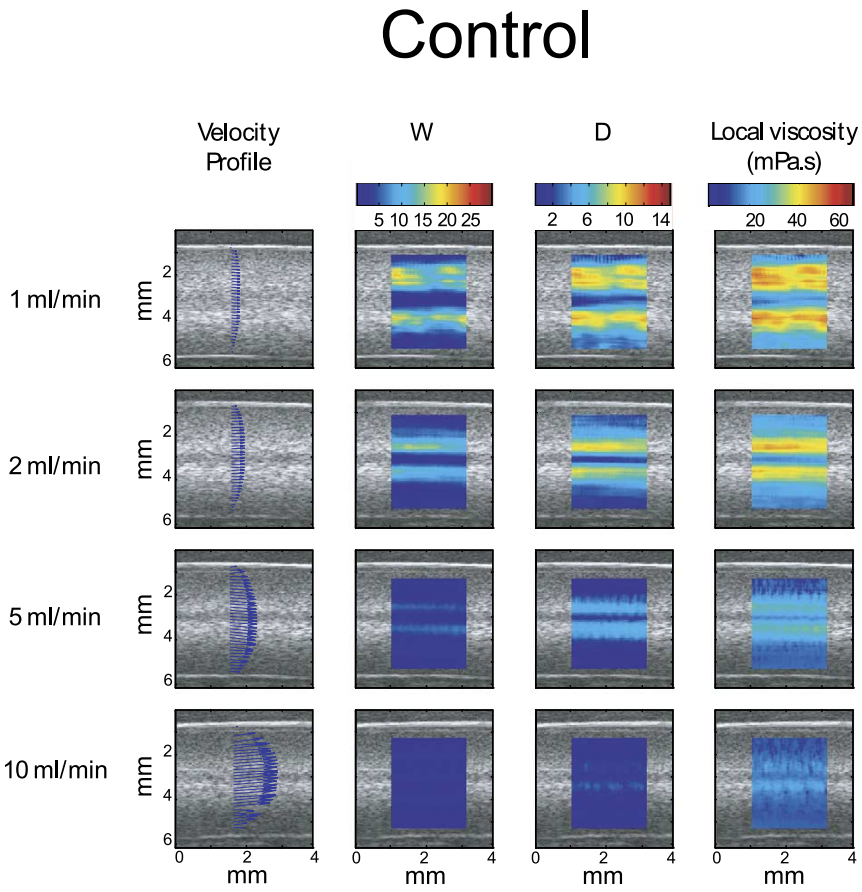

Fig. 11. Typical speckle tracking velocity vectors, parametric images of W and D, and local viscosity predictions for *control* blood in the tube flow geometry. For velocity scales, please refer to Fig. 7b where the magnitude of the velocity vectors and fitted power law profiles are represented. The "black hole" phenomenon surrounded by a bright ring can be seen in the center stream of B-mode, parametric-mode (W and D) and viscosity images at the smallest flow rates.

58]. Indeed, the use of BSC spectral information is commonly used because such parameters are more robust than fixed frequency US intensity measurements [59]. These parameters convey information on the erythrocyte spatial organization but are inherently dependent on the frequency and transducer bandwidth, which makes comparisons between studies an arduous task. Efforts to relate acoustical parameters to blood microstructure (e.g., with the structure factor) should prove to be more robust, informative and satisfying for quantitative assessment of tissue properties.

For blood, previous attempts to relate aggregate microstructures to scattering properties have generally failed when non-Rayleigh scattering and packing effects on $BSC(f)$ were considered. For example, the kinetics of EA after flow stoppage were quantified in a mock flow loop by concomitant increases in "effective" scatterer size and acoustic concentration (i.e., the product of scatterer concentration and squared acoustic impedance) [29] based on changes in $BSC(f)$. If an increase in scatterer size is coherent with aggregating erythrocytes, an increase in acoustic concentration is not as easily interpretable. Indeed, aggregation would rather decrease the number of "effective" scatterers, whereas the acoustic

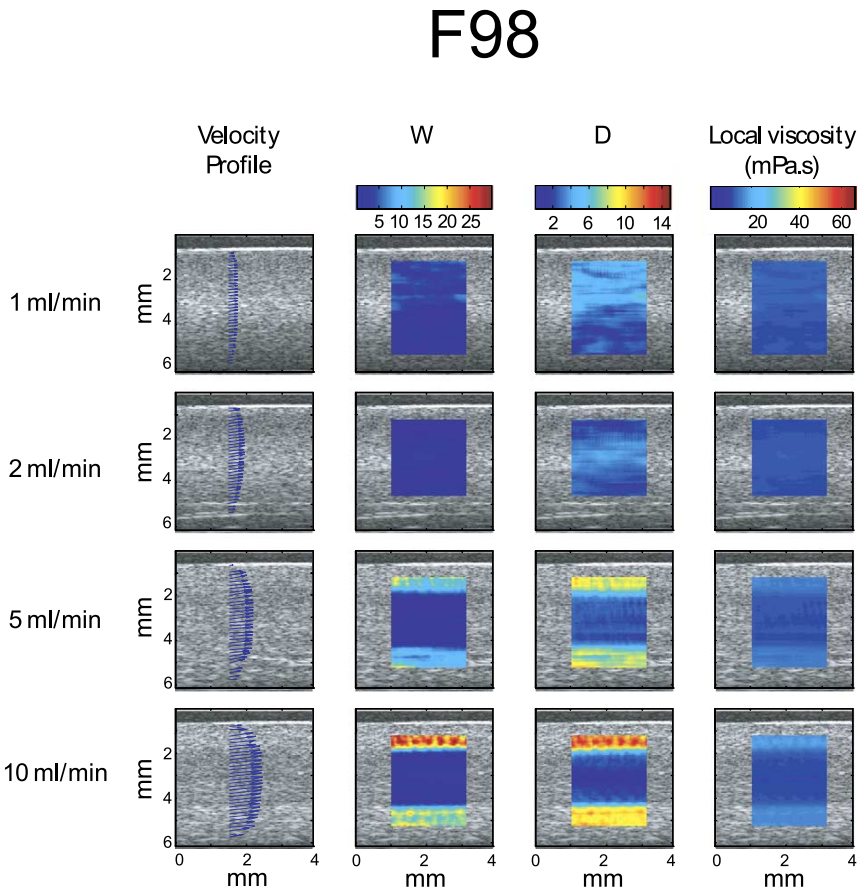

Fig. 12. Typical speckle tracking velocity vectors, parametric images of W and D, and local viscosity predictions for a hyper-aggregating F98 blood sample in the tube flow geometry. For velocity scales, please refer to Fig. 7d where the magnitude of the velocity vectors and fitted power law profiles are represented. Compared with Fig. 11, a larger "black hole" can be seen in the center stream at the highest flow rates. The bright ring is now located near the wall.

impedance would remain unchanged. The hypothesis that erythrocytes independently scatter US waves at a physiological hematocrit (e.g., 5 million erythrocytes/mm^3) can be questioned for this particular model. Another model, based on the Rayleigh scattering theory, established that W was related with the local erythrocyte concentration variance [37]. Interestingly, W increased with EA but the model was limited to small aggregates with a maximum size of 4 erythrocytes [31]. With an empirical approach, also based on Rayleigh scattering, BSC dependence on hematocrit was related to the aggregate size determined by considering cell packing within aggregates and of aggregates in the suspension [6,25], but surprisingly, predicted sizes clearly exceeding Rayleigh scattering limits with aggregate sizes of up to 240 erythrocytes per aggregate.

4.1. Advantages of the SFSE model

The structure factor formalism was introduced by our group to describe the effects of EA on $BSC(f)$ in non-Rayleigh conditions for densely packed scatterers [21,22,46]. It considers that variations of $BSC(f)$

with EA are strictly related to changes in the spatial organization of erythrocytes, considered individually as weak Rayleigh scatterers much smaller than the acoustic wavelength. The SFSE is a non-Rayleigh second-order approximation in f of the structure factor formalism that has several advantages. First, parameters W and D have a physical interpretability. W is related to the isothermal compressibility ξ_T of the tissue by $W = mKT\xi_T$, where m is the number density of scatterers, K the Boltzmann constant and T the absolute temperature. W is known to increase with the stickiness parameter of the analytical adhesive sphere model in a wide range of volume fractions [44]. This is also our observation with ultrasound, as W increased with aggregation, similarly to [31]. W also corresponds to the analytical formulation of the packing factor in the long wavelength limit [57], when there is no aggregation, which provides a lower boundary for this parameter. This lower boundary is well understood and varies with the hematocrit. At 40% hematocrit, Perkus–Yevick approximation predicts values of $W = 0.04$ for spheres and $W = 0.15$ for cylinders [50]. In our experiments, we obtained $W \approx 0.1$ for non-aggregated saline suspensions and, at high shear conditions, for aggregating erythrocytes (i.e., *control* and F68).

On the other hand, the parameter D of the SFSE model is an acoustically estimated diameter that is potentially of higher interest in hemorheology because its interpretation is easier than W. Nevertheless, its validation is difficult because, to the authors' knowledge, there is no means to experimentally assess aggregate sizes at 40% hematocrit. D is a non-dimensional number, defined as the ratio of the diameter of a fractal aggregate to the diameter of one erythrocyte, that is expected to be smaller than 1 for disaggregated erythrocytes. The apparent underestimation of the size estimate D for aggregated erythrocytes at 40% hematocrit has been previously discussed [62]. Nevertheless, in that prior publication it was shown that D was statistically correlated with the mean number of erythrocytes per aggregate, as assessed visually by microscopy at 6% hematocrit and measured acoustically at this same hematocrit.

Another advantage of the SFSE model is that W and D are parameters related to the tissue itself and should then, in theory, be independent of the frequency. In practice, because the SFSE is a second order model in kDa (see Eq. (2)), the use of a higher frequency or increased EA degrades the performance of the model. Increasing the order of the polynomial approximation of *BSC*(f) could theoretically extend the kDa range of applicability, but unfortunately it introduces instability in the minimization fitting algorithm. Hence the following frequency tradeoff had to be considered: (1) a larger bandwidth results in better W and D estimates, evidenced by a smaller variance, because more data are used for the polynomial fitting; (2) however, when W and D increase with aggregation, the kDa product also increases and the second order model reaches its limits of applicability, resulting in r^2 dropping for the curve fitting of *BSC*(f) and introducing important underestimation biases of W and D. This limit occurred for $D > 14$ for the frequency range considered in this study (9–28 MHz). By decreasing the upper frequency limit from 28 to 15 MHz for large aggregates in the F98 samples corrected this issue (data not shown) but introduced more variance in estimating smaller aggregates. Therefore, the frequency bandwidth to use must be appropriate for the levels of aggregation that are being characterized, this frequency range can be tested using r^2 (see Fig. 3). Note that for clarity, in this report the bandwidth was kept constant for all results thus limiting the applicability of the SFSE to $D < 14$.

4.2. Steady state Couette flow relationships between D and measured viscosities

Multiple linear regressions showed that W and D were collinear and that D was linearly related with the bulk viscosity. Regressions in Table 1 suggested that the shear rate dependent viscosity was explained by the high shear viscosity and a multiple or fraction of D. The Flory–Fox theory [20] predicts viscosity proportional to the volume of spherical particles in suspension. The finding that the viscosity

was proportional to a multiple or fraction of D is surprising and not fully understood. It is not clear to what extent the Flory–Fox theory for colloidal suspensions can be directly applied to dense fluid deformable corpuscles, such as erythrocytes. It seems reasonable to believe that erythrocyte deformation, interacting fractal clusters and their orientation should modify the Flory–Fox relation.

Another surprising result is that the multiplicative coefficient of D for F98 samples was almost six times smaller than for the other samples (see Fig. 6). Although the linear regression did not reach statistical significance ($p = 0.08$, see Table 1), the tendency of the slope for the F98 sample was nevertheless clearly smaller. Since higher shear rates were required to obtain similar D values with the F98 sample, it can be speculated that the aggregate morphology was extended, thus provoking a lower viscosity versus size relation; validation of this hypothesis requires future studies.

4.3. Parametrical images in tube flow

The objectives of the tube experiments were to illustrate the performance of the SFSE in a non-homogenous shear field. The presence of the BH in tube flow images illustrates the unique imaging potential of US to become a rheological tool with spatial resolution and sensitivity to EA. The BH was studied by different teams [38,41,48,64] and it is now generally accepted that it is the result of a transient state of aggregation in the center stream that is dependent on the tube entry length. Indeed, the blood flowing in the center, in the low shear region, travels in the tube more quickly and has less time to form aggregates than blood on a peripheral layer. This phenomenon is also amplified by the presence of a non-zero shear on peripheral layers that promotes aggregate formation by increasing the collision frequency between erythrocytes [16]. This aggregation kinetics related effect was still present after 3 minutes of shearing in a Couette flow for zero shear conditions, as reported previously (see Figs 2 and 3 in [62]). When clustering erythrocytes are insonified by the US probe, aggregates in the center may not have sufficient time to reach an equilibrium size as predicted by the local SR, velocity and probe position along the vessel.

The non-linear hematocrit dependence of the BSC was also suggested to explain the BH phenomenon. A decrease in H in the center axis was proposed by Yuan and Shung [64] based on the "tubular pinch" or "Segré–Silberberg" effect [7]. This behavior for fluid-like deformable corpuscles seems improbable based on earlier reports [55]: erythrocytes are rather concentrated near the center axis in that particular report. On the other hand, a local increase in hematocrit in the center axis due to erythrocyte migration towards the vessel center could provoke a decrease in BSC that may not necessarily correlate with a decrease in aggregate size. Using magnetic resonance imaging, shear rate variations in the gap of a large core Couette instrument were shown to induce migration of erythrocytes away from the walls [15], but the hematocrit variations in the center of the gap remained marginal (a few percent hematocrit). Note that a small core Couette device was used here, which should result in even smaller hematocrit variations in our data. In another magnetic resonance study, hematocrit spatial variations were shown to be non significant in tube flow [38]. Nevertheless, in a separate experiment, a 50% hematocrit hyperaggregating blood sample was prepared and sheared at 2 s^{-1} in our Couette apparatus to provide additional evidence that hematocrit changes could not explain our results. Expected high values of $W = 15$ and $D = 9$ were found. This illustrates that the SFSE could detect aggregation at an increased hematocrit. Also, if parameter H, an input in our model, is locally higher as it may be the case in the center stream, the SFSE would tend to overestimate W and D (data not shown). Moreover, an increase in H or EA in the center stream would cause a decrease in the spectral slope [35] and thus an increase in D that was not observed in our data. These results suggest that if hematocrit variations are present in the tube, such effects cannot

fully explain the BH. Spectral analysis of our data thus support a dominant low EA hypothesis due to very low shears and time-dependent transient effects, as clearly shown in Fig. 9a: at a given shear rate, the smallest flow rates promoted the largest aggregates. This also explains why W and D in tube flow were lower than the steady state Couette flow results in Fig. 10.

Another interesting but at a first glance unexpected observation was the increase in W and D with increasing SR for the F98 tube flow experiments (Figs 9b and 10), since for these suspensions, a SR increase promoted aggregate formation. Note that this effect was observed in another study [1] when horse blood, which is also characterized by very intense aggregation tendencies, was circulated in a tube flow setup. The mechanism explaining this phenomenon may be that more SR-induced collisions between erythrocytes are necessary to promote aggregation of cells with a high tendency to aggregate. However, as with other types of erythrocyte suspensions, disaggregation occurred with further increased the SR beyond the value inducing the maximum aggregation (see Fig. 10, Couette and tube flow data).

The low aggregation and progressive increase in W and D as the flow rate (shear rate) was increased can be visualized in Fig. 12 for F98 samples. This figure also shows that the maximum selected flow rate of 10 ml/min was not sufficient to induce erythrocyte disaggregation close to the tube wall, where the shear rate was maximum. Disaggregation was nonetheless noted close to the wall for *control* samples as the flow rate was increased (see Fig. 11). Interestingly, and of potential rheological and pathophysiological impact, is the observation of a ring with large aggregates close to the wall at the highest flow rates of 5 and 10 ml/min for F98 samples (Fig. 12), and a depleted ring with few or no aggregates close to the wall for *control* samples regardless of the flow rate (Fig. 11). For hyperaggregating erythrocytes such as F98 samples, the presence of high EA close to the wall could influence blood/vessel wall interactions.

As discussed earlier when interpreting results of Figs 5 and 6, the viscosity maps of Fig. 12 for F98 samples did not reflect the increased EA close to the wall as the flow rate was increased. The lower slope of the viscosity versus D and W relations for the Couette experiments of Fig. 6 can explain this observation. Likely, as mentioned before, the lower SR in tube flow ($SR < 22\ s^{-1}$ at all flow rates, see Fig. 7d) compared with Couette flow, where SR were varied from 47 to 100 s^{-1}, may have biased (i.e., underestimated) the prediction. The steady state Couette flow relation between viscosity and D that we used in our predictions of Fig. 12 and also Fig. 11 were based on the hypothesis that the increase in bulk viscosity was directly caused by an increase in aggregate size. Any consideration affecting the viscosity versus particle size relation, such as deformability, erythrocyte cluster orientation or elongation with increased flow, could not be accounted for in this simplistic approach.

4.4. Towards an in vivo assessment of the pathological impact of erythrocyte hyperaggregation

If the hematocrit is known, we have shown that precise and reproducible ultrasonic structure parameters, W and D, can be obtained with the SFSE model when an adequate US frequency bandwidth is available. *In vivo*, the attenuation of the pressure wave by intervening tissues such as skin, fat and vessel wall is a major difficulty that must be overcome. It is notable that the SFSE framework was used in a minimization routine called the Structure Factor Size and Attenuation Estimator (SFSAE) and allowed the simultaneous estimation of the attenuation of different phantom layers positioned between the US probe to study erythrocyte aggregates [23]. This approach could therefore potentially be used to characterize blood microstructure through the skin *in vivo*, although further validation is still needed.

The pathophysiological impact of erythrocyte hyperaggregation has been studied by transfusion of Pluronics coated erythrocytes by members of our group [5,60]. In the current study, it was shown that F98 coated pig erythrocytes exhibited increased clustering up to shear rates as high as 100 s^{-1}. The

presence of aggregation near the tube walls was quantified with US parametrical imaging *in situ*. The natural next step would be to locally measure EA *in vivo* using ultrasound and quantify the physiological effect of increasing the aggregability using Pluronics coatings.

5. Conclusions

It was demonstrated in this study that the SFSE, an US non-Rayleigh scattering model, could adequately characterize EA for non-aggregating, aggregating and Pluronics coated erythrocytes. Two parameters, the packing factor (W) and ensemble averaged aggregate isotropic diameter (D), were compared in Couette and tube flows and predictably quantified EA with respect to SR and to blood type for $D < 14$. In Couette flow, empirical blood type dependent relationships between D and viscosity were established. These relationships were then used to extrapolate local viscosity maps in tube flow. In tube flow, a "black hole" (BH) appeared for aggregating bloods under some flow conditions. Analysis of the backscattered spectral information with the SFSE model supported the hypothesis that the BH originates from a time related lower aggregation in the center stream. Increasing the aggregation tendency of erythrocytes (F98 blood) resulted in the presence of bigger aggregates near the walls at the highest flow rates (aggregates were present at shear rates up to 100 s^{-1} in Couette flow). Preliminary results also suggested that in near stasis conditions, a higher shear rate was necessary to promote aggregate formation with the F98 samples, resulting in larger BH. The *in vivo* significance of the BH remains to be established. Parametrical images, superimposed on B-mode displays, clearly illustrated the unique capacity of ultrasound to reveal spatially non-homogenous EA states. Ultrasound opens new perspectives for *in vivo* macrocirculatory studies on the impact of hemodynamic perturbations and complications caused by EA using high frequency US, which can be locally monitored and characterized non invasively thought the skin *in vivo* and *in situ*.

Acknowledgements

Supported by grants from the Canadian Institutes of Health Research (#MOP-84358 and #CMI-72323), Heart and Stroke Foundation of Canada (#PG-05-0313), National Institutes of Health of USA (#R01HL078655) and Natural Sciences and Engineering Research Council of Canada Ph.D. scholarship program (#ES D3-317051-2005).

References

[1] L. Allard and G. Cloutier, Power Doppler ultrasound scan imaging of the level of red blood cell aggregation: An *in vitro* study, *J. Vasc. Surg.* **30** (1999), 157–168.
[2] J.K. Armstrong, H.J. Meiselman, R.B. Wenby and T.C. Fisher, Modulation of red blood cell aggregation and blood viscosity by the covalent attachment of Pluronic copolymers, *Biorheology* **38** (2001), 239–247.
[3] J.K. Armstrong, R.B. Wenby, H.J. Meiselman and T.C. Fisher, The hydrodynamic radii of macromolecules and their effect on red blood cell aggregation, *Biophys. J.* **87** (2004), 4259–4270.
[4] P. Bagchi, P.C. Johnson and A.S. Popel, Computational fluid dynamic simulation of aggregation of deformable cells in a shear flow, *J. Biomech. Eng.* **127** (2005), 1070–1080.
[5] O.K. Baskurt, O. Yalcin, S. Ozdem, J.K. Armstrong and H.J. Meiselman, Modulation of endothelial nitric oxide synthase expression by red blood cell aggregation, *Am. J. Physiol. Heart Circ. Physiol.* **286** (2004), H222–H229.
[6] M. Boynard and J.C. Lelièvre, Size determination of red blood cell aggregates induced by dextran using ultrasound backscattering phenomenon, *Biorheology* **27** (1990), 39–46.

[7] C.G. Caro, T.J. Pedley, R.C. Schroter and W.A. Seed, *The Mechanics of the Circulation*, 1st edn, Oxford University Press, Toronto, 1978, pp. 1–514.
[8] S. Chien, Blood viscosity: Influence of erythrocyte aggregation, *Science* **157** (1967), 829–831.
[9] S. Chien, Biophysical behavior of red cells in suspensions, in: *The Red Blood Cell*, D.M. Surgenor, ed., Academic Press, New York, 1975, pp. 1031–1133.
[10] S.C. Christiansen, S.C. Cannegieter, T. Koster, J.P. Vandenbroucke and F.R. Rosendaal, Thrombophilia, clinical factors, and recurrent venous thrombotic events, *JAMA* **293** (2005), 2352–2361.
[11] G. Cloutier, M. Daronat, D. Savéry, D. Garcia et al., Non-Gaussian statistics and temporal variations of the ultrasound signal backscattered by blood at frequencies between 10 and 58 MHz, *J. Acoust. Soc. Am.* **116** (2004), 566–577.
[12] G. Cloutier and Z. Qin, Ultrasound backscattering from non-aggregating and aggregating erythrocytes – A review, *Biorheology* **34** (1997), 443–470.
[13] G. Cloutier and Z. Qin, Shear rate dependence of ultrasound backscattering from blood samples characterized by different levels of erythrocyte aggregation, *Ann. Biomed. Eng.* **28** (2000), 399–407.
[14] G. Cloutier, A. Zimmer, F.T. Yu and J.L. Chiasson, Increased shear rate resistance and fastest kinetics of erythrocyte aggregation in diabetes measured with ultrasound, *Diabet. Care* **31** (2008), 1400–1402.
[15] G.R. Cokelet, J.R. Brown, S.L. Codd and J.D. Seymour, Magnetic resonance microscopy determined velocity and hematocrit distributions in a Couette viscometer, *Biorheology* **42** (2005), 385–399.
[16] A.L. Copley, R.G. King and C.R. Huang, Erythrocyte sedimentation of human blood at varying shear rates, in: *Microcirculation*, J. Grayson and W. Zingg, eds, Plenum Press, New York, 1976, pp. 133–134.
[17] M.G.M. de Kroon, C.J. Slager, W.J. Gussenhoven, P.W. Serruys et al., Cyclic changes of blood echogenicity in high-frequency ultrasound, *Ultrasound Med. Biol.* **17** (1991), 723–728.
[18] J. Fang and R.G. Owens, Numerical simulations of pulsatile blood flow using a new constitutive model, *Biorheology* **43** (2006), 637–660.
[19] E.J. Feleppa, C.R. Porter, J. Ketterling, P. Lee et al., Recent developments in tissue-type imaging (TTI) for planning and monitoring treatment of prostate cancer, *Ultrason. Imaging* **26** (2004), 163–172.
[20] P.J. Flory and T.G.J. Fox, Treatment of intrinsic viscosity, *J. Am. Chem. Soc.* **73** (1951), 1904–1906.
[21] I. Fontaine, M. Bertrand and G. Cloutier, A system-based approach to modeling the ultrasound signal backscattered by red blood cells, *Biophys. J.* **77** (1999), 2387–2399.
[22] I. Fontaine, D. Savéry and G. Cloutier, Simulation of ultrasound backscattering by red cell aggregates: Effect of shear rate and anisotropy, *Biophys. J.* **82** (2002), 1696–1710.
[23] E. Franceschini, F.T.H. Yu and G. Cloutier, Simultaneous estimation of attenuation and structure parameters of aggregated red blood cells from backscatter measurements, *J. Acoust. Soc. Am.* **123** (2008), EL85–EL91.
[24] J. Fromageau, J.L. Gennisson, C. Schmitt, R.L. Maurice et al., Estimation of polyvinyl alcohol cryogel mechanical properties with 4 ultrasound elastography methods and comparison with gold standard testings, *IEEE Trans. Ultrason. Ferroelectr. Freq. Control* **54** (2007), 498–509.
[25] M. Hanss and M. Boynard, Ultrasound backscattering from blood: Hematocrit and erythrocyte aggregation dependence, in: *Ultrasonic Tissue Characterization II*, M. Linzer, ed., National Bureau of Standards, Gaithersburg, MD, 1979, pp. 165–169.
[26] B.M. Johnston, P.R. Johnston, S. Corney and D. Kilpatrick, Non-Newtonian blood flow in human right coronary arteries: transient simulations, *J. Biomech.* **39** (2006), 1116–1128.
[27] T. Khodabandehlou and C. Le Devehat, Hemorheological disturbances as a marker of diabetic foot syndrome deterioration, *Clin. Hemorheol. Microcirc.* **30** (2004), 219–223.
[28] H. Kitamura and S. Kawasaki, Detection and clinical significance of red cell aggregation in the human subcutaneous vein using a high-frequency transducer (10 MHz): A preliminary report, *Ultrasound Med. Biol.* **23** (1997), 933–938.
[29] H. Kitamura, B. Sigel, J. Machi, E.J. Feleppa et al., Roles of hematocrit and fibrinogen in red cell aggregation determined by ultrasonic scattering properties, *Ultrasound Med. Biol.* **21** (1995), 827–832.
[30] E. Krieger, B. van Der, Loo, B.R. Amann-Vesti, V. Rousson and R. Koppensteiner, C-reactive protein and red cell aggregation correlate with late venous function after acute deep venous thrombosis, *J. Vasc. Surg.* **40** (2004), 644–649.
[31] B. Lim and R.S. Cobbold, On the relation between aggregation, packing and the backscattered ultrasound signal for whole blood, *Ultrasound Med. Biol.* **25** (1999), 1395–1405.
[32] G.D.O. Lowe, A.J. Lee, A. Rumley, J.F. Price et al., Blood viscosity and risk of cardiovascular events: the Edinburgh artery study, *Br. J. Haematol.* **96** (1997), 168–173.
[33] S.M. MacRury, S.E. Lennie, P. McColl, R. Balendra et al., Increased red cell aggregation in diabetes mellitus: Association with cardiovascular risk factors, *Diabet. Med.* **10** (1993), 21–26.
[34] E.L. Madsen, M.F. Insana and J.A. Zagzebski, Method of data reduction for accurate determination of acoustic backscatter coefficients, *J. Acoust. Soc. Am.* **76** (1984), 913–923.
[35] S. Maruvada, K.K. Shung and S. Wang, High-frequency backscatterer and attenuation measurements of porcine erythrocyte suspensions between 30–90 MHz, *Ultrasound Med. Biol.* **28** (2002), 1081–1088.

[36] W.R. Milnor, *Hemodynamics*, 2nd edn, Williams & Wilkins, Baltimore, MD, 1989, pp. 1–387.
[37] L.Y.L. Mo and R.S.C. Cobbold, Theoretical models of ultrasonic scattering in blood, in: *Ultrasonic Scattering in Biological Tissues*, K.K. Shung and G.A. Thieme, eds, CRC Press, Boca Raton, FL, 1993, pp. 125–170.
[38] L.Y.L. Mo, G. Yip, R.S.C. Cobbold, C. Gutt et al., Non-Newtonian behavior of whole blood in a large diameter tube, *Biorheology* **28** (1991), 421–427.
[39] L.C. Nguyen, F.T. Yu and G. Cloutier, Cyclic changes in blood echogenicity under pulsatile flow are frequency dependent, *Ultrasound Med. Biol.* **34** (2008), 664–673.
[40] M.L. Oelze, W.D. O'Brien Jr., J.P. Blue and J.F. Zachary, Differentiation and characterization of rat mammary fibroadenomas and 4T1 mouse carcinomas using quantitative ultrasound imaging, *IEEE Trans. Med. Imaging* **23** (2004), 764–771.
[41] Z. Qin, L.G. Durand and G. Cloutier, Kinetics of the "black hole" phenomenon in ultrasound backscattering measurements with red blood cell aggregation, *Ultrasound Med. Biol.* **24** (1998), 245–256.
[42] D. Quemada, Towards a unified model of elasto-thixotropy of biofluids, *Biorheology* **21** (1984), 423–436.
[43] M.W. Rampling, H.J. Meiselman, B. Neu and O.K. Baskurt, Influence of cell-specific factors on red blood cell aggregation, *Biorheology* **41** (2004), 91–112.
[44] C. Regnaut and J.C. Ravey, Application of the adhesive sphere model to the structure of colloidal suspensions, *J. Chem. Phys.* **91** (1989), 1211–1221.
[45] P. Riha, M. Donner and J.F. Stoltz, Time-dependent formation of red blood cell aggregates and its influence on blood rheological behaviour, *J. Biol. Phys.* **19** (1993), 65–70.
[46] D. Savéry and G. Cloutier, A point process approach to assess the frequency dependence of ultrasound backscattering by aggregating red blood cells, *J. Acoust. Soc. Am.* **110** (2001), 3252–3262.
[47] D. Savéry and G. Cloutier, High-frequency ultrasound backscattering by blood: analytical and semianalytical models of the erythrocyte cross section, *J. Acoust. Soc. Am.* **121** (2007), 3963–3971.
[48] R.E.N. Shehada, R.S.C. Cobbold and L.Y.L. Mo, Aggregation effects in whole blood: Influence of time and shear rate measured using ultrasound, *Biorheology* **31** (1994), 115–135.
[49] M.D. Sherar, M.B. Noss and F.S. Foster, Ultrasound backscatter microscopy images the internal structure of living tumour spheroids, *Nature* **330** (1987), 493–495.
[50] K.K. Shung, On the ultrasound scattering from blood as a function of hematocrit, *IEEE Trans. Sonics Ultrasonics* **29** (1982), 327–331.
[51] K.K. Shung, R.A. Sigelmann and J.M. Reid, Scattering of ultrasound by blood, *IEEE Trans. Biomed. Eng.* **23** (1976), 460–467.
[52] B. Sigel, J. Machi, J.C. Beitler, J.R. Justin and J.C.U. Coelho, Variable ultrasound echogenicity in flowing blood, *Science* **218** (1982), 1321–1323.
[53] R.A. Sigelmann and J.M. Reid, Analysis and measurement of ultrasound backscattering from an ensemble of scatterers excited by sine-wave bursts, *J. Acoust. Soc. Am.* **53** (1973), 1351–1355.
[54] J.F. Stoltz and M. Donner, Red blood cell aggregation: Measurements and clinical applications, *Tr. J. Med. Sci.* **15** (1991), 26–39.
[55] S. Swarnamani and M. Singh, Analysis of erythrocyte aggregation mechanism in presence of dextran and magnetic field by ultrasound scattering in blood, *Biorheology* **26** (1989), 847–862.
[56] G.E. Trahey, J.W. Allison and O.T. von Ramm, Angle independent ultrasonic detection of blood flow, *IEEE Trans. Biomed. Eng*. **34** (1987), 965–967.
[57] V. Twersky, Low-frequency scattering by correlated distributions of randomly oriented particles, *J. Acoust. Soc. Am.* **81** (1987), 1609–1618.
[58] S.H. Wang and K.K. Shung, An approach for measuring ultrasonic backscattering from biological tissues with focused transducers, *IEEE Trans. Biomed. Eng*. **44** (1997), 549–554.
[59] K.A. Wear, T.A. Stiles, G.R. Frank, E.L. Madsen et al., Interlaboratory comparison of ultrasonic backscatter coefficient measurements from 2 to 9 MHz, *J. Ultrasound Med.* **24** (2005), 1235–1250.
[60] O. Yalcin, F. Aydin, P. Ulker, M. Uyuklu et al., Effects of red blood cell aggregation on myocardial hematocrit gradient using two approaches to increase aggregation, *Am. J. Physiol. Heart Circ. Physiol*. **290** (2006), H765–H771.
[61] J.W. Yarnell, I.A. Baker, P.M. Sweetnam, D. Bainton et al., Fibrinogen, viscosity, and white blood cell count are major risk factors for ischemic heart disease. The Caerphilly and Speedwell collaborative heart disease studies, *Circulation* **83** (1991), 836–844.
[62] F.T.H. Yu and G. Cloutier, Experimental ultrasound characterization of red blood cell aggregation using the structure factor size estimator, *J. Acoust. Soc. Am.* **122** (2007), 645–656.
[63] Y.W. Yuan and K.K. Shung, Ultrasonic backscatter from flowing whole blood. II: Dependence on frequency and fibrinogen concentration, *J. Acoust. Soc. Am.* **84** (1988), 1195–1200.
[64] Y.W. Yuan and K.K. Shung, Echoicity of whole blood, *J. Ultrasound Med.* **8** (1989), 425–434.
[65] J. Zhang, P.C. Johnson and A.S. Popel, Red blood cell aggregation and dissociation in shear flows simulated by lattice Boltzmann method, *J. Biomech.* **41** (2008), 47–55.

Assessment of accuracy of the structure-factor-size-estimator method in determining red blood cell aggregate size from ultrasound spectral backscatter coefficient

Ratan K. Saha[a)]
Laboratory of Biorheology and Medical Ultrasonics, University of Montreal Hospital Research Center (CRCHUM), 2099 Alexandre de Sève (Room Y-1619), Montréal, Québec H2L 2W5, Canada

Emilie Franceschini
Laboratoire de Mécanique et d'Acoustique LMA – CNRS UPR 7051, 31 Chemin Joseph Aiguier, 13402 Marseille, Cedex 20, France

Guy Cloutier[b,c)]
Laboratory of Biorheology and Medical Ultrasonics, University of Montreal Hospital Research Center (CRCHUM), 2099 Alexandre de Sève (Room Y-1619), Montréal, Québec H2L 2W5, Canada

(Received 28 October 2010; revised 11 February 2011; accepted 11 February 2011)

A computer simulation study to produce ultrasonic backscatter coefficients (BSCs) from red blood cell (RBC) clusters is discussed. The simulation algorithm is suitable for generating non-overlapping, isotropic, and fairly identical RBC clusters. RBCs were stacked following the hexagonal close packing (HCP) structure to form a compact spherical aggregate. Such an aggregate was repeated and placed randomly under non-overlapping condition in the three-dimensional space to mimic an aggregated blood sample. BSCs were computed between 750 KHz and 200 MHz for samples of various cluster sizes at different hematocrits. Magnitudes of BSCs increased with mean aggregate sizes at low frequencies (<20 MHz). The accuracy of the structure-factor-size-estimator (SFSE) method in determining mean aggregate size and packing factor was also examined. A good correlation ($R^2 \geq 0.94$) between the mean size of aggregates predicted by the SFSE and true size was found for each hematocrit. This study shows that for spherical aggregates there exists a region for each hematocrit where SFSE works most accurately. Typically, error of SFSE in estimating mean cluster size was <20% for dimensions between 14 and 17 μm at 40% hematocrit. This study suggests that the theoretical framework of SFSE is valid under the assumption of isotropic aggregates.
 [DOI: 10.1121/1.3561653]

PACS number(s): 43.80.Cs, 43.80.Qf, 43.20.Fn, 43.30.Ft [CCC] Pages: 2269–2277

I. INTRODUCTION

Some ultrasonic tissue characterization techniques generally consider frequency dependent information of backscatter echoes to quantify tissue structural properties, such as the size, acoustic impedance, number density of scattering particles, etc. This approach has been successfully used for the characterization of the eye,[1,2] liver,[3] kidney,[4] prostate,[5] breast tissues[6] and also to monitor cell apoptosis in order to evaluate the efficacy of cancer therapies.[7] Blood has also been characterized by employing this technique.[8] The main purpose of ultrasonic characterization of blood is to assess the level of red blood cell (RBC) aggregation, which is a surrogate marker of inflammation.[9] Readers may refer to Fig. 5 of Ref. 10 and Fig. 1 of Ref. 11 to see microscopic images of RBC aggregation and to illustrate how non-aggregated RBCs form clusters with time under different pro-aggregating conditions. An enhanced level of RBC aggregation is a pathological state and is associated with many circulatory diseases such as deep venous thrombosis, atherosclerosis, and diabetes mellitus. The ultrasonic backscatter technique has the potential to provide a method for non-invasive determination of RBC cluster size, consequently allowing one to address the role of RBC aggregation in the processes of such diseases.

Yu and Cloutier[10] recently proposed a parametric form of backscatter coefficient (BSC). They arrived at that mathematical form by using a second order Taylor series expansion of the structure factor and thus obtained two physically relevant parameters of aggregation: The mean diameter of aggregates D and the packing factor W. The packing factor is related to the volume ratio of RBCs known as the hematocrit (H), and is sensitive to the spatial arrangement of scatterers.[12,13] The parameter D estimates how many cells are attached as an aggregate. They used the parametric form of the BSC to analyze experimental data *in vitro* and obtained sound rheological results.[11] The method is referred as the structure-factor-size-estimator (SFSE). Franceschini *et al.*[14] further developed this model to incorporate attenuation effects of intervening tissues between the probe and the blood flow with the objective of providing a method applicable to *in vivo* situations. It was shown in that work that simultaneous evaluation of D, W,

[a)]Current address: Department of Physics, Ryerson University, 350 Victoria Street, Toronto, Ontario M5B 2K3, Canada.
[b)]Also at: Department of Radiology, Radio-Oncology and Nuclear Medicine, University of Montreal, Montréal, Québec H3T 1J4, Canada.
[c)]Author to whom correspondence should be addressed. Electronic mail: guy.cloutier@umontreal.ca

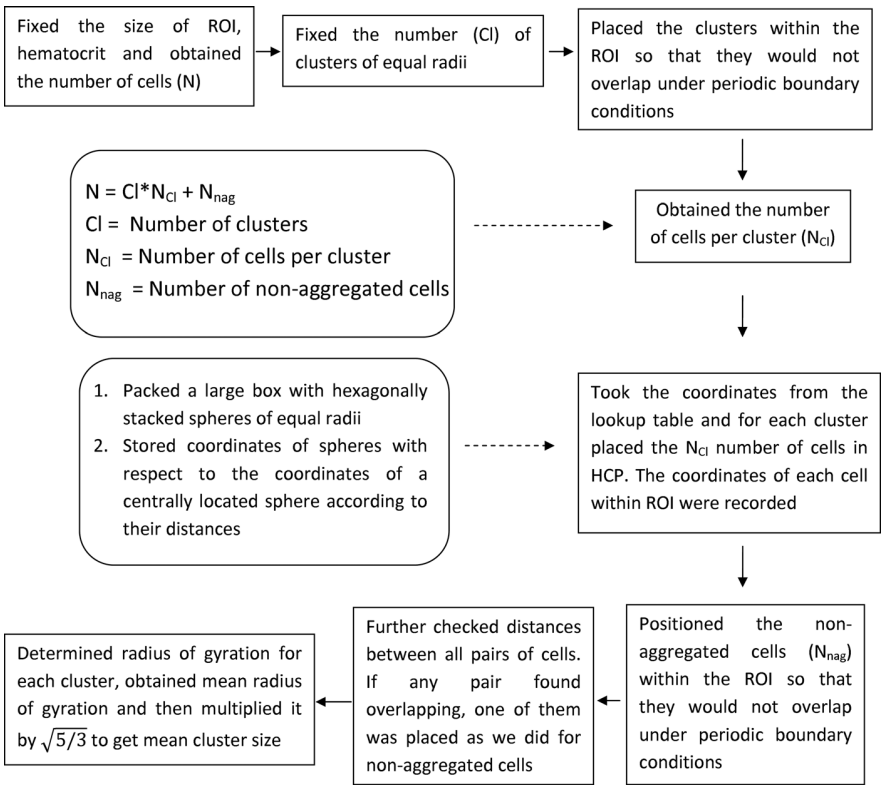

FIG. 1. Flow chart illustrating simulation steps to generate spherical clusters with HCP of red blood cells.

and of the attenuation coefficient of the intervening tissue layers could be obtained but the validation of the SFSE has been so far conducted only experimentally. However, the experimental assessment of accuracy of SFSE in determining the mean size of aggregates by optical means was possible only at a low hematocrit (6%), since RBCs are not visible with a microscope at a normal physiological hematocrit of typically 35%–55%.[10]

The aim of the work presented here is to describe a simple and rapid method to simulate randomly distributed compact RBC clusters in order to evaluate the accuracy of the SFSE method. The cells were assumed to be arranged in a spherical cluster in such a way so that a hexagonal close packing (HCP) structure was obtained. Note that this scheme provides the highest packing density [i.e., fractional volume occupied by spheres and also referred as the hematocrit (H)] that is about 0.74 for spheres.[15] Such an aggregate was repeated and placed randomly under non-overlapping condition in the three-dimensional (3D) space to mimic aggregated blood samples. The ensemble average of the BSC was determined by simulation from the samples comprising non-overlapping, isotropic, and fairly identical spherical RBC aggregates. Consequently, cluster size dependent ultrasound backscatter properties were studied. The accuracy of the SFSE method in estimating the mean cluster size was accomplished by comparing estimated results (using SFSE) and actual cluster sizes (determined by using the coordinates of cells attached to the clusters, known from the simulations) at hematocrits from 0.20 to 0.40, which is not possible experimentally by optical means. A low hematocrit of 0.20 is a condition that can be encountered in severe anemia. As far as the authors are aware, the approach described here has never been employed to generate RBC aggregates as well as to study ultrasound backscatter from a collection of such aggregates.

The paper is organized in the following way. In Sec. II we discuss the theoretical models describing ultrasonic backscatter by a collection of erythrocytes. Section III illustrates the simulation method. Results are presented in Sec. IV. Quality of our results in the light of experimental observations is discussed in Sec. V followed by a summary in Sec. VI.

II. THEORETICAL MODEL

The backscattering cross-section per unit volume or the BSC for the scattering of an incident plane wave with wave vector $\vec{k}$ by an ensemble of particles of uniform size can be cast in terms of the Percus–Yevick packing factor (W_{PY}), as described in Chapter 5 of Ref. 8,

$$\chi_b(-2\vec{k}) = mW_{PY}\sigma_b(-2\vec{k}), \tag{1}$$

where m is the number density of particles and it is related to the hematocrit (H) as $m = H/V_s$. Here, V_s denotes the volume of an equivalent sphere of a RBC, which is a good model of the backscattering cross-section $\sigma_b(-2\vec{k})$ (less than 5% error) below 18 MHz.[16] The subscript b here indicates backscattering. The Percus–Yevick packing factor (W_{PY}) for spatially random distribution of hard spherical particles with equal radii can be expressed as[8]

$$W_{PY} = \frac{(1-H)^4}{(1+2H)^2}. \tag{2}$$

The analytical expression of the backscattering cross-section for the scattering of an incident plane wave by a weak spherical scatterer of radius a can be derived by using the Born approximation and it is given by[17]

$$\sigma_b(-2\vec{k}) = \frac{1}{16\pi^2} V_s^2 k^4 \left(\frac{\kappa_e - \kappa}{\kappa} - \frac{\rho_e - \rho}{\rho_e}\right)^2 \times \left(3\frac{\sin 2ka - 2ka\cos 2ka}{(2ka)^3}\right)^2. \quad (3)$$

Here, κ and ρ indicate the adiabatic compressibility and density of the surrounding medium (blood plasma), respectively. The same quantities for the RBC scatterer are given by κ_e and ρ_e. Equation (1) is valid in the low frequency range and was observed to provide a good fit to experimental data for the backscattering of non-aggregated RBCs when probed at 7.5 MHz.[18]

On the other hand, the resultant backscatter signal from a collection of identical particles can be obtained by using the linear superposition principle for signals backscattered by individual particles. The corresponding BSC for a collection of particles can be written as[19,20]

$$\chi_b(-2\vec{k}) = m\left\langle \frac{1}{N}\left|\sum_{n=1}^{N}\exp(i2\vec{k}\bullet\vec{r}_n)\right|^2\right\rangle \sigma_b(-2\vec{k}) = mS(-2\vec{k})\sigma_b(-2\vec{k}), \quad (4)$$

where $S(-2\vec{k})$ is the structure factor of the medium and dictates how backscatter would vary with the spatial organization of particles. The symbol $\langle\rangle$ represents the ensemble average. The position vector $\vec{r}_n$ defines the center of the nth spherical scatterer in space and N is the total number of scatterers within the scattering volume (mentioned as the region of interest later in this article). In general, the structure factor of a medium containing particles distributed in the 3D space can be determined from the 3D Fourier transform of the spatial distribution of particles (see the Appendix of Refs. 13 and 21). However, if the direction of the interrogating wave coincides with an axis of the coordinate system of the region of interest (ROI), then Eq. (4) reduces to one dimensional form and therefore computation of structure factor becomes trivial. In this work, Eq. (4) was computed for samples composed of randomly distributed 3D RBC clusters which were isotropic and fairly similar in size. Accordingly, cluster size dependent backscatter was examined.

Recently, Yu and Cloutier[10] used a second order Taylor series expansion of the structure factor to obtain two physically relevant parameters, namely W and D. The parameter D was computed from the mean radius of gyration (R_g) of the aggregates. With this expansion Eq. (4) reduces to,

$$\chi_b(-2\vec{k}) = m(W - 4k^2R_g^2)\sigma_b(-2\vec{k}). \quad (5)$$

The radius (R_{sp}) of a homogeneous spherical object is related to its radius of gyration as $R_{sp} = \sqrt{5/3}R_g$ and thus the mean size of aggregates in terms of number of RBCs could be presented as, $D = R_{sp}/a$. Yu and Cloutier used Eq. (5) to fit measured backscatter data corresponding to different RBC aggregation levels and the technique was referred to the SFSE method. In the present study, we also employed Eq. (5) to fit simulated frequency dependent BSC curves obtained by computing Eq. (4) for different samples with various clustering conditions. This enabled us to examine cluster size dependent ultrasound backscatter by RBCs as well as to assess the SFSE method by comparing the mean cluster size from simulated aggregates to that predicted by the said method from simulated BSC.

III. SIMULATION METHOD

A. Simulation of spatial distributions of aggregated RBCs

Different approaches to simulate compact RBC aggregates have been explored. For example, RBC clusters could be generated by allowing particles to interact via a Morse type potential and then by evolving the system through random positioning of cells.[19] However, this technique is computationally intensive and can only produce random lose packing (RLP) configurations of particles with packing fractions of 0.60 ± 0.02 in three dimensions.[22] Moreover, previously only 5.5 dB enhancement of BSC was found at 7.5 MHz at the highest aggregating condition at $H = 0.40$ using this technique[19] and that is on the lower side compared to experimentally measured values. Alternatively, one can rely on algorithms to construct random close packing (RCP) configurations[23,24] that are expected to increase BSC. Jodrey and Tory[24] developed this algorithm to generate RCP of equal spheres from a random distribution of points. In that study, each point is the center of an inner and an outer sphere. RCP configuration was achieved by slowly shrinking the outer diameter and by eliminating overlapping of outer spheres. The procedure was terminated when two diameters became on the same order. The implementation of such RCP algorithms is not straightforward, they are computationally intensive and also the attainable packing fraction (0.64 ± 0.02) of particles is still limited.

On the other hand, a highest packing density (0.74) can be obtained by using regular packing schemes such as HCP or cubic close packing (CCP).[15] As mentioned earlier, it is expected that significant enhancement of BSC would be possible by using HCP of cells. In the current study, we followed this scheme to form an aggregate. The generation of such structure is simple and fast because cells have to be placed only at some defined locations. Such an aggregate prototype could be repeated and placed randomly in the 3D space to generate a tissue realization consisting of non-overlapping, isotropic, and fairly identical RBC clusters.

Initially, spatial locations of centers of the clusters of identical size were chosen randomly within the ROI under the condition that they would not overlap. The term "region of interest" is used to refer to the scattering volume. The periodic boundary conditions were imposed during this process. That means the clusters at the boundaries of the ROI would not overlap with the others at the opposite boundaries and thus removed the edge effect. The total number (fixed by the size of the ROI and the hematocrit) of cells was equally

divided (truncated to the nearest lower integer value) into these clusters and the cells were stacked by following a HCP structure for each cluster.

To accomplish this (see Fig. 1), at the beginning (in order to pack cells in HCP structure) a large number of spheres (arbitrarily chosen) representing RBCs were packed within a box. They were stacked in such a way that they formed a HCP structure.[15] After that, the coordinates of the centers of spheres with respect to the center of a sphere located at the central region of the box were recorded according to their distances and stored in a lookup table. The next step was to take the coordinates of the required number of RBC mimicking spheres from the lookup table. Accordingly, spheres were stacked with respect to the center of a cluster and thus the HCP structure was obtained for each cluster. Note that the lookup table provided the coordinates of the spheres with respect to the center of the cluster. However, to compute Eq. (4) one needed to know the position coordinates of the centers of those spheres with respect to the origin of the ROI. This could be easily obtained by summing the coordinates of the centers of those spheres and that of the cluster center. Similarly, spheres were stacked with respect to other cluster centers and also their coordinates with respect to the origin of the ROI were determined. The remaining spheres (those did not belonging to any cluster and behaving as disaggregated RBCs) were placed spatially at random in the ROI maintaining non-overlapping condition under periodic boundary conditions with the existing spheres. Further, an additional step was conducted to find overlapping pairs of cells. If they were found, then a new coordinate under non-overlapping condition was assigned for one of them. In this case too periodic boundary conditions were imposed while checking the non-overlapping condition of that cell with the others. In this way, spatial organization of spheres (most of them were included within clusters and others were randomly distributed spatially in the ROI) mimicking a tissue sample was obtained.

Figure 2(a) presents an arrangement of 51 spheres or RBCs in HCP forming a spherical 3D cluster. A realization of an aggregated blood tissue is shown in Fig. 2(b). As an example and for clarity of the figure, a smaller ROI ($200 \times 20 \times 20$ μm^3) occupied by the RBCs at 14% hematocrit is displayed. Note that the BSC curves shown in the later sections were computed for a ROI of $1000 \times 125 \times 125$ μm^3. Figure 2(b) contains four non-overlapping, identical, and randomly placed RBC clusters and each cluster is composed of 51 RBCs. These clusters maintained periodic boundary conditions. That means if a portion of a cluster crossed a boundary wall, then that portion appeared at the opposite side. The effects of periodic boundary conditions can be observed at least for two (1st and 3rd) clusters, as shown in Fig. 2(b), and thus some portions of those clusters appeared at the opposite sides.

The radius of gyration (R_g) of a cluster of that tissue sample was computed by using the distances of the constituent spheres with respect to the center of the cluster as,

$$R_g = \sqrt{\frac{3}{5}a^2 + \frac{1}{n_c}\sum_{j=1}^{n_c} r_j^2}, \tag{6}$$

where n_c is the total number of spheres forming a cluster and r_j is the distance of the center of the jth sphere from the cluster center. This was done for each cluster associated with a tissue realization and accordingly the mean radius of gyration ($\langle R_g \rangle$) of clusters was obtained. The mean size (R_{sim}) of clusters was then determined by multiplying the average radius of gyration with a factor $\sqrt{5/3}$ (i.e., $R_{\text{sim}} = \sqrt{5/3}\langle R_g \rangle$). Note that the non-aggregated RBCs were not taken into account during this estimation. Figure 1 summarizes this procedure through a flow chart diagram. The computed numerical value of R_{sim} acted as a gold standard and further used to assess accuracy of the SFSE.

B. Computation of a simulated BSC curve

As mentioned earlier, the size of the ROI was fixed to $1000 \times 125 \times 125$ μm^3. The simulated backscatter measurements were carried out for the scattering of incident plane waves propagating along the longest dimension of the ROI and that was considered as the x axis in this case. The length of the ROI along the x axis was sufficiently large and therefore provided good resolution in the frequency domain. However, much smaller dimensions were used along the two other lateral directions. This was done to restrict the volume of the ROI, the number of RBCs, and the computational time. The number of particles for this size of ROI was 35 919, 53 879, and 71 839 at 20%, 30%, and 40% hematocrits, respectively. Further, collections of particles were distributed randomly within the ROI, and the Fourier transformation of the spatial organization of particles was computed for those particles to

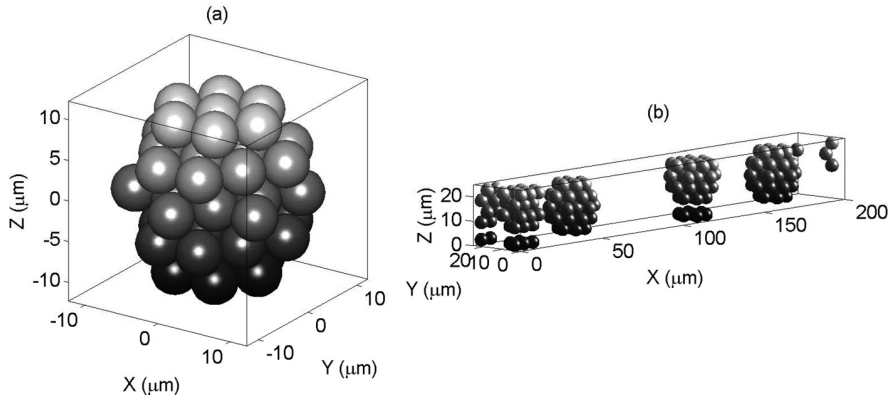

FIG. 2. (a) An arrangement of 51 spheres (representing RBCs) in HCP configuration forming a RBC cluster. (b) It shows a simulated aggregated blood tissue sample containing four clusters where each cluster is composed of 51 spheres. The non-overlapping clusters are randomly placed in the ROI under periodic boundary conditions. For clarity, a smaller ROI at a lower hematocrit ($H \approx 14\%$) is shown.

generate a BSC curve for the propagation of waves along the x axis only. Therefore, spectral characteristics were dependent upon the spatial organization of cells within the ROI along the direction of propagation of waves and were not affected by the periodic boundary conditions (which were used to generate spatial arrangements of cells). The spectral characteristics would be affected only if multiple ROIs attached together along that direction would have been considered.

The radius of the equivalent sphere of a RBC was fixed to 2.75 μm, corresponding to a typical RBC volume of 87 μm^3. The numerical values of density and compressibility of a RBC were assigned as $\rho_e = 1.092$ g/cm^3 and $\kappa_e = 34.1 \times 10^{-12}$ cm^2/dyne, respectively.[18] The same quantities for the ambient medium (plasma) were chosen as $\rho = 1.005$ g/cm^3 and $\kappa = 44.3 \times 10^{-12}$ cm^2/dyne, respectively.[18] For each sample, the cluster size frequency dependent BSC was obtained by evaluating Eq. (4) and a mean curve was determined from 250 different tissue realizations.

C. Fitting of a simulated mean BSC curve with the SFSE

The final step was to fit the simulated mean BSC curve with the SFSE between 5 MHz and the frequency corresponding to the first minimum of that curve on a log–log scale. The mean BSC curve generally exhibited minima at multiple frequencies depending upon the mean cluster size associated with that sample. The parameters W and R_{sp} were obtained by optimizing Eq. (5) and the simulated BSC curve. The optimization was carried out by using the "fminsearch" function of MATLAB 7.8.0.347 (R2009a). The estimated mean size (R_{sp}) of aggregates was then compared to the actual mean size (R_{sim}) obtained from the simulation to examine the accuracy of the SFSE method. This procedure was carried out at three hematocrit levels for different cluster sizes.

IV. RESULTS

Figures 3(a)–3(c) demonstrate variations of the BSC at some clustering conditions for three hematocrits over a large

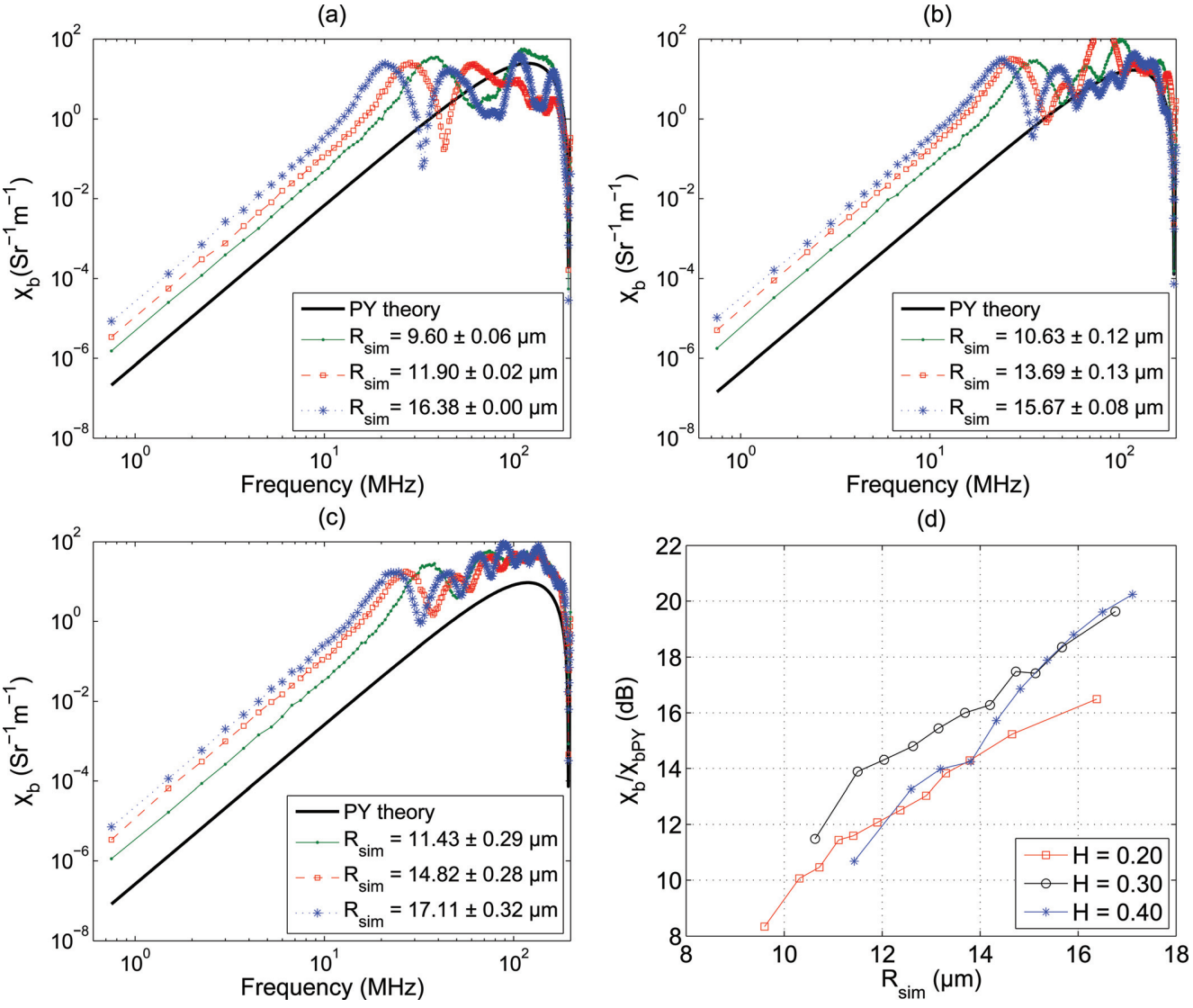

FIG. 3. (Color online) (a) Variations of the BSC with interrogating frequency at different simulated mean cluster sizes for $H = 0.20$. The black line corresponds to BSC predicted by the Percus–Yevick packing theory. (b) Same as (a) but for $H = 0.30$. (c) Same as (a) but for $H = 0.40$. (d) Increase of BSC with respect to that of the Percus–Yevick packing theory in decibel with cluster size at 7.5 MHz. Variations at three hematocrits are shown.

frequency range [750 KHz–200 MHz, computed using Eq. (4)]. The simulated clusters were tightly packed by the cells leaving small numbers of cells as non-aggregated cells. For example, for a sample simulated realization at 0.20 hematocrit [$R_{sim} = 9.60 \pm 0.06$ μm in Fig. 3(a)], 98.37% RBCs of the total number of cells formed aggregates and remaining 1.63% cells were distributed randomly in space. In another case at 0.40 hematocrit [$R_{sim} = 17.11 \pm 0.32$ μm, Fig. 3(c)] these numbers were 92.28% and 7.72%, respectively. The mean radius of simulated 3D isotropic clusters is presented in the legend denoting the corresponding aggregation level for each sample. BSC predicted by the Percus–Yevick (PY) packing theory is also shown for comparison. The PY theory describes backscatter properties of non-aggregated RBCs in the low frequency regime (1–30 MHz typically), where $ka < \pi/10$.[8] It was expected that PY results would not match with the simulated BSC curves because aggregated RBCs cannot be considered as spatially random distribution of spheres with equal radii and therefore the PY model is not valid for aggregated samples. It may also be noticed from Fig. 3 that BSC between 750 KHz and the frequency corresponding to the first maximum, increased as the cluster size increased for all samples. Moreover, the first minimum (or the first maximum) appeared at a lower frequency for a sample containing aggregates than that of the non-aggregated blood. For example, the first minimum in Fig. 3(a) occurred at about 195 MHz for the Percus–Yevick curve but it appeared at nearly 60 MHz for the first sample with simulated mean aggregate size of $R_{sim} = 9.60 \pm 0.06$ μm. Note that the position of the first minimum is a signature of the size of the scattering objects (either individual cells or clumps composed of collection of cells).[25] For any hematocrits, the first minimum appeared at lower frequencies as bigger aggregates were simulated.

Figure 3(d) illustrates how the BSC measured at 7.5 MHz (normalized by that of the PY theory and expressed in decibel) varies with the cluster size. It is evident from the figure that BSC increased as the mean size of clusters increased[26] and it is true for all hematocrits. Further, the relative increase of BSC with respect to that of the Percus–Yevick packing theory for a particular cluster size is always higher at $H = 0.30$ than that of $H = 0.20$. For instance, at $R_{sim} \approx 12.0$ μm the relative increase of BSC is about 12 dB for $H = 0.20$ but it is nearly 14 dB at $H = 0.30$. However, for $H = 0.40$, the relative increase is comparable to that of $H = 0.20$ up to $R_{sim} \approx 14.0$ μm and is similar to that of $H = 0.30$ beyond $R_{sim} \approx 15.0$ μm. Additionally, although we did not present it graphically, we observed that spectral slopes on a log–log scale between 1 and 10 MHz remained around 4 (Rayleigh scattering regime) for all samples at all three hematocrits.

Figure 4(a) displays simulated frequency dependent BSC curves fitted with the SFSE method for the same clustering conditions described in Fig. 3(a). The estimated values of R_{sp} and W are presented in the legend. It is clear from the figure that the second order expansion of the structure factor is insufficient to model the complex behavior of BSC. Indeed, some disagreements between the simulated and fitted SFSE curves are present, especially in the low frequency

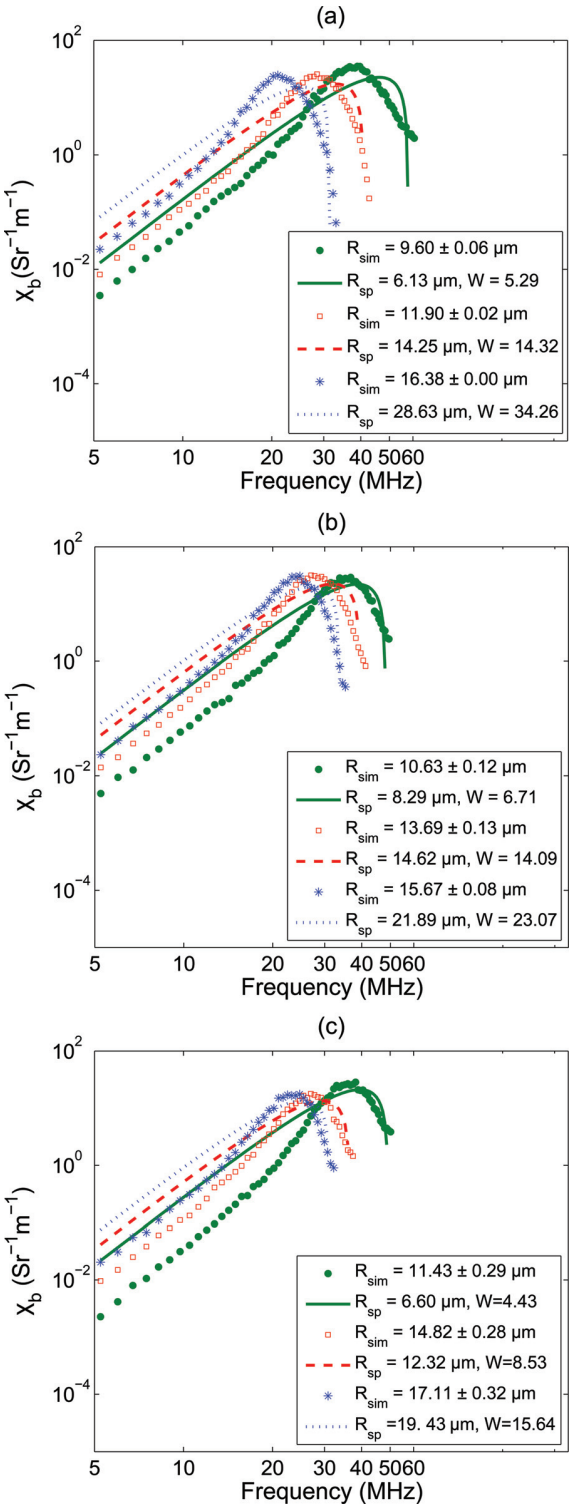

FIG. 4. (Color online) (a) BSC curves fitted with the SFSE model at different clustering conditions at $H = 0.20$. Both R_{sp} and W estimated by the SFSE method are given in the legend. (b) Same as (a) but for $H = 0.30$. (c) Same as (a) but for $H = 0.40$.

range, where each fitted curve over-estimates the BSC. Figures 4(b) and 4(c) demonstrate fittings of the BSC curves with SFSE, for $H = 0.30$ and 0.40, respectively. Fitting characteristics are similar to that of Fig. 4(a).

To assess the accuracy of the SFSE method, we have plotted [see Fig. 5(a)] the estimated values of R_{sp} as a

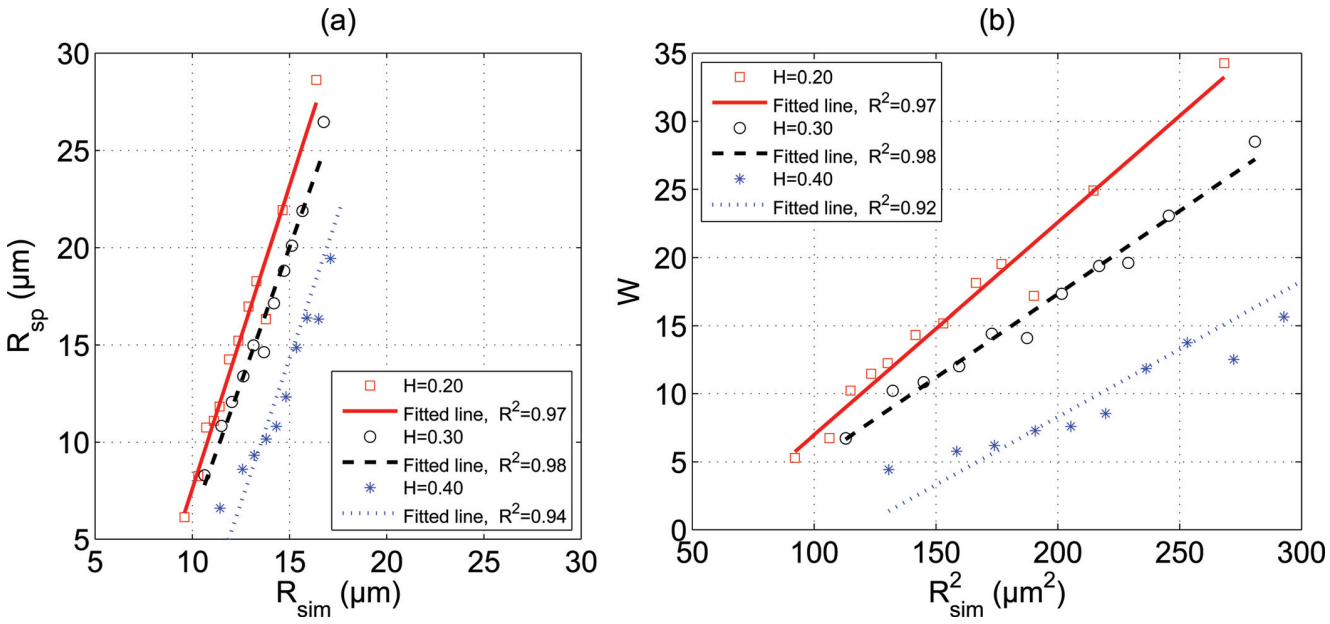

FIG. 5. (Color online) (a) Comparison of estimated aggregate size with actual aggregate size at three hematocrits ($H = 0.20$, 0.30, and 0.40). (b) Plot of W as a function of square of the actual aggregate size at different hematocrits.

function of R_{sim} for all three hematocrits. The linear regression lines are also shown in the figure. Although the SFSE model did not provide good fittings of the simulated BSCs, still excellent correlations ($R^2 \geq 0.94$) were found between estimated and true cluster sizes for each hematocrit. Furthermore, it can be seen that for each hematocrit there is a region where the SFSE method works at its best. For example, error associated with the prediction of the SFSE method is less than 20% when the mean size of aggregates varies between 14 and 17 μm at 40% hematocrit. However, below this range SFSE underestimates the aggregate size but above this range it overestimates the size, especially at the lower hematocrits. The variation of W with square of R_{sim} is shown in Fig. 5(b) for all hematocrits. It is evident that W and R_{sim} follow a quadratic relationship. Straight line fits were also obtained by using the least square fitting technique and good correlations ($R^2 \geq 0.92$) were found between W and R^2_{sim} for each hematocrit.

V. DISCUSSIONS

The scheme discussed in this paper is based on a phenomenological approach to simulate RBC clusters. It did not consider realistic interactions between the cells. It is a simple method because cells within a cluster were stacked in a particular way to form the HCP structure and provided tightly packed aggregates. This is also a fast method to generate tissue realizations mimicking aggregated erythrocyte samples because RBCs can be located at only defined positions. For example, at 40% hematocrit it took about 42 s in a remote computer cluster to generate a tissue configuration consisting of aggregates with a mean radius of 17.11 ± 0.32 μm. Similarly, for another sample (with a mean aggregate radius of 12.59 ± 0.29 μm) at that hematocrit, approximately 72 s was required to generate each configuration with the same computing platform. In this case the number of clusters was higher because it contained smaller aggregates than the previous one. Thus, the execution time was slightly more since it was needed to assign coordinates for more number of cluster centers at non-overlapping condition.

In this study, we found that BSC increased as the cluster size increased. For instance, nearly 17 dB enhancement of BSC at $H = 0.40$ was measured at 7.5 MHz frequency for the biggest cluster size (with mean radius of 17.11 ± 0.32 μm) with respect to that of non-aggregating blood [see Fig. 3(d)]. This observation is in accordance with previous experimental works. For example, Yuan and Shung[27] estimated approximately 15 dB increase of BSC at 7.5 MHz for porcine whole blood when the shear rate was decreased from 22 to 2 s^{-1}. Note that a reduction in shear rate promoted aggregation and consequently cluster size increased. The numerical values associated with the enhancement of BSC presented in this study confirmed the fact that the simulated

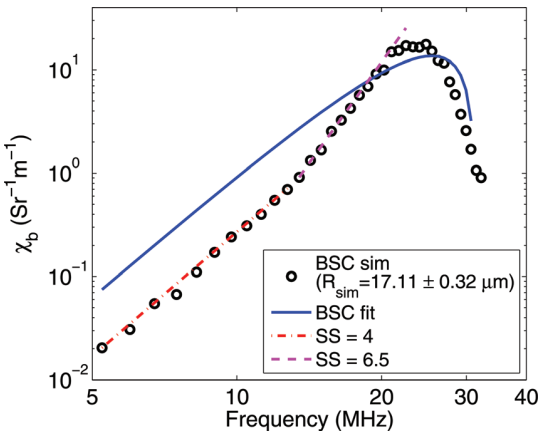

FIG. 6. (Color online) Illustration of changes in spectral slope for a simulated BSC curve.

aggregate sizes were in the same range to that of experiments. Also, the numerical values of the spectral slope that we computed remained around 4 within the 1–10 MHz frequency band, where the BSC curves exhibited linear variations with frequency on a log–log scale for all samples.

In addition to that, this was the first attempt to examine the accuracy of SFSE by using simulated backscatter signals from samples containing non-overlapping, isotropic, and fairly identical 3D clusters mimicking RBC aggregates (normally compact aggregates instead of rouleaux are formed *in vivo* under pathological conditions). This study provided us a way to compare predicted cluster sizes with that of simulations. We observed excellent correlations ($R^2 \geq 0.94$) between estimated and true cluster sizes for all hematocrits and also that the packing factor W maintained a quadratic relationship with the mean radius of aggregates (see Fig. 5). These findings are consistent with experimental results reported in Ref. 10. In that work, the mean sizes of RBC aggregates were determined from direct optical microscopy measurements for blood samples with 6% hematocrit at different time points of aggregation. In case of the ultrasonic method, the mean sizes were estimated with the SFSE from estimated backscattered spectra at 6% hematocrit. A good correlation ($R^2 \geq 0.76$) was found between optical and ultrasonic methods. As introduced earlier, this comparison was not carried out at typical human hematocrits (20%–55%) because it is almost impossible to get non-overlapping clusters for image processing.

The SFSE model quite satisfactorily fit to experimental BSC curves in Ref. 10, but in the present work we did not observe much agreement between fitted curves and simulated BSC data points (see Fig. 4). As an example, we are highlighting this behavior in Fig. 6. In this figure, a simulated BSC curve (corresponding to $R_{\text{sim}} = 17.11 \pm 0.32$ μm and $H = 0.40$) and the fitted SFSE curve are shown. Note that the spectral slope for the simulated curve is around 4 in the frequency band of 5–13 MHz but it is about 6.5 between 13 and 25 MHz. This is suggesting that the SFSE method cannot consider changes in spectral slope in the frequency bandwidth, where spectral slope remains positive. It may be noted that spectral slopes superior to 4 at low frequencies could also be observed in the experiments performed by Yu and Cloutier (see Fig. 4 in Ref. 10). Also, as discussed in Chapter 4 of Ref. 8 on the basis of a Gaussian correlation model and experimental evidences, spectral slopes greater than 4 might appear for dense media in the low frequency range. With simulations, we may have emphasized spectral slopes above 4 because we did not consider attenuation of waves, which is more important at higher frequencies. In addition to that, spectral slopes above 4 could be observed maybe because we did not consider poly-disperse clusters. In general, for poly-disperse clusters, the maxima and minima locations of BSC are different for different clusters and thus a relatively smoother BSC curve can be obtained.[28]

Although we did not observe good fits of the simulated BSC curves with the SFSE, the estimations of SFSE were in good agreement with some cluster size ranges. The results suggest that there lies a region where the SFSE method works at its best for each hematocrit. At 40% hematocrit, error associated with the prediction of SFSE in determining the cluster size was within 20% when mean aggregate sizes remained within 14–17 μm. Franceschini *et al.*[14] also mentioned in their paper that SFSE worked well for blood samples when mean radii of clusters were $\leq$13.90 μm for a Couette flow experiment and $\leq$10.02 μm for a tube flow experiment. They reached this conclusion by inspecting behaviors of correlation coefficients (BSC versus frequency of SFSE fittings). The upper limit of validity of the SFSE, as found from the current study, was also in the same range but we did not observe good performance of the SFSE for clusters with mean radii $<$14 μm. One possible reason for this discrepancy is that in simulations we dealt with tightly packed clusters but in reality clusters would not be that tight because of the presence of electrostatic repulsive potential. This potential would not allow cells to come very close to each other and thus would encourage forming loosely packed clusters, unless inflammatory related diseases are present to promote the formation of compact clusters. In other words, SFSE may work more accurately over a larger range for loosely packed clusters than tightly packed clusters.

As described earlier, the SFSE model has been derived by using a Taylor series expansion and retaining terms up to the second order. Therefore, contributions from the higher order terms have been neglected and that might explain the suboptimum fittings of BSC curves for some RBC clustering examples. Also, in this study, we modeled individual biconcave RBCs as spheres and studied BSC between 750 KHz and 200 MHz. The impact of modeling a RBC by a sphere on the frequency dependence of the backscatter cross-section has been studied and errors are introduced at frequencies above 18 MHz, typically.[16] The impact of this simplification on BSC and SFSE determinations of W and R_{sp} in the case of aggregating cells is unknown and still needs to be explored.

VI. CONCLUSIONS

A simulation algorithm suitable for generating non-overlapping, isotropic, and fairly identical RBC aggregates was presented. The RBCs considered as homogeneous spheres were assumed to follow a HCP structure to form compact spherical aggregates. Note that a very high packing density $\approx$0.74 for spheres can be achieved for this packing scheme. Such an aggregate prototype was repeated and placed randomly under non-overlapping condition in the 3D space to mimic aggregated blood samples. The method is simple, fast, and easy to implement. The frequency dependent BSCs were computed for samples with varying mean cluster sizes at different hematocrits. Consequently, cluster size dependent backscatter and efficacy of the SFSE method in determining the mean aggregate size were examined.

It was found that the BSC increased as the mean aggregate size increased and this was true for all hematocrits. For example, at $H = 0.40$, BSC increased from approximately 10 to 20 dB compared to that of non-aggregated blood sample at 7.5 MHz when the mean cluster size varied from 11.5 to 17 μm. Overall, 8 dB enhancements of BSC were observed for the other two hematocrits ($H = 0.20$ and 0.30) from lowest to highest cluster sizes considered in this study [see

Fig. 3(d)], at the same interrogating frequency. Although the SFSE did not provide good fits to the simulated BSC curves, still excellent correlations ($R^2 \geq 0.94$) between predicted (using the SFSE method) and true (known from simulations) mean size of aggregates were found for each hematocrit. The second estimated parameter W exhibited a quadratic relationship with mean size (R_{sim}) of RBC aggregates for each hematocrit and in this case good correlation coefficients ($R^2 \geq 0.92$) were also computed. In future, it would be interesting to incorporate real interactions between cells to form both isotropic (strong adhesive energy simulating pathological inflammatory conditions) and anisotropic (normal condition) clusters. Another interesting study might be to evaluate the performance of the Gaussian form factor model[4] to extract size information from backscatter spectra and compare that with SFSE prediction.

ACKNOWLEDGMENT

This work was supported by the Canadian Institutes of Health Research (Grant Nos., MOP-84358 and CMI-72323), the Heart and Stroke Foundation of Canada (Grant No., PG-05-0313), and the National Institutes of Health of USA (Grant No., RO1HL078655). The authors would like to acknowledge the "Réseau Québécois de Calcul de Haute Performance" (RQCHP), where simulations were carried out.

[1]F. L. Lizzi, M. Greenbaum, E. J. Feleppa, M. Elbaum, and D. J. Coleman, "Theoretical framework for spectrum analysis in ultrasonic tissue characterization," J. Acoust. Soc. Am. **73**(4), 1366–1373 (1983).
[2]E. J. Feleppa, F. L. Lizzi, D. J. Coleman, and M. M. Yaremko, "Diagnostic spectrum analysis in ophthalmology: A physical perspective," Ultrasound Med. Biol. **12**(8), 623–631 (1986).
[3]F. L. Lizzi, M. Ostromogilsky, E. J. Feleppa, M. C. Rorke, and M. M. Yaremko, "Relationship of ultrasonic spectral parameters to features of tissue microstructure," IEEE Trans. Ultrason. Ferroelectr. Freq. Control **34**(3), 319–329 (1987).
[4]M. F. Insana, R. F. Wagner, D. G. Brown, and T. J. Hall, "Describing small-scale structure in random media using pulse-echo ultrasound," J. Acoust. Soc. Am. **87**(1), 179–192 (1990).
[5]E. J. Feleppa, T. Liu, A. Kalisz, M. C. Shao, N. Fleshner, V. Reuter, and W. R. Fair, "Ultrasonic spectral-parameter imaging of the prostate," Int. J. Imaging Syst. Technol. **8**(1), 11–25 (1997).
[6]M. L. Oelze, W. D. O'Brien, Jr., J. P. Blue, and J. F. Zachary, "Differentiation and characterization of rat mammary fibroadenomas and 4T1 mouse carcinomas using quantitative ultrasound imaging," IEEE Trans. Med. Imaging **23**(6), 764–771 (2004).
[7]R. M. Vlad, N. M. Alajez, A. Giles, M. C. Kolios, and G. J. Czarnota, "Quantitative ultrasound characterization of cancer radiotherapy effects in vitro," Int. J. Radiat. Oncol. Biol. Phys. **72**(4), 1236–1243 (2008).
[8]K. K. Shung and G. A. Thieme, *Ultrasound Scattering in Biological Tissues* (CRC Press, Boca Raton, FL, 1993), Chap. 3, pp. 53–74.
[9]R. B. Ami, G. Barshtein, D. Zeltser, Y. Goldberg, I. Shapira, A. Roth, G. Keren, H. Miller, V. Prochorov, A. Eldor, S. Berliner, and S. Yedgar, "Parameters of red blood cell aggregation as correlates of the inflammatory state," Am. J. Physiol. Heart Circ. Physiol. **280**(5), H1982–H1988 (2001).
[10]F. T. H. Yu and G. Cloutier, "Experimental ultrasound characterization of red blood cell aggregation using the structure factor size estimator," J. Acoust. Soc. Am. **122**(1), 645–656 (2007).
[11]F. T. H. Yu, E. Franceschini, B. Chayer, J. K. Armstrong, H. J. Meiselman, and G. Cloutier, "Ultrasonic parametric imaging of erythrocyte aggregation using the structure factor size estimator," Biorheology **46**(4), 343–363 (2009).
[12]V. Twersky, "Low-frequency scattering by correlated distributions of randomly oriented particles," J. Acoust. Soc. Am. **81**(5), 1609–1618 (1987).
[13]I. Fontaine, M. Bertrand, and G. Cloutier, "A system-based approach to modeling the ultrasound signal backscattered by red blood cells," Biophys. J. **77**, 2387–2399 (1999).
[14]E. Franceschini, F. T. H. Yu, F. Destrempes, and G. Cloutier, "Ultrasound characterization of red blood cell aggregation with intervening attenuating tissue-mimicking phantoms," J. Acoust. Soc. Am. **127**(2), 1104–1115 (2010).
[15]C. Kittel, *Introduction to Solid State Physics* (John Wiley and Sons, Inc., New York, 1996) Chap. 1, pp. 1–26.
[16]D. Savéry and G. Cloutier, "High-frequency ultrasound backscattering by blood: Analytical and semi-analytical models of the erythrocyte cross-section," J. Acoust. Soc. Am. **121**(6), 3963–3971 (2007).
[17]P. M. Morse and K. U. Ingard, "*Theoretical Acoustics* (Princeton University Press, Princeton, NJ, 1968), Chap. 8, pp. 400–466.
[18]K. K. Shung, Y. W. Yuan, D. Y. Fei, and J. M. Tarbell, "Effect of flow disturbance on ultrasonic backscatter from blood," J. Acoust. Soc. Am. **75**(4), 1265–1272 (1984).
[19]R. K. Saha and G. Cloutier, "Monte Carlo study on ultrasound backscattering by three-dimensional distributions of red blood cells," Phys. Rev. E **78**, 061919 (2008).
[20]D. Savéry and G. Cloutier, "Effect of red cell clustering and anisotropy on ultrasound blood backscatter: A Monte Carlo study," IEEE Trans. Ultrason. Ferroelectr. Freq. Control **52**(1), 94–103 (2005).
[21]I. Fontaine, D. Savéry, and G. Cloutier, "Simulation of ultrasound backscattering by red cell aggregates: Effect of shear rate and anisotropy," Biophys. J. **82**, 1696–1710 (2002).
[22]E. L. Hinrichsen, J. Feder, and T. Jøssang, "Random packing of disks in two dimensions," Phys. Rev. A **41**(8), 4199–4209 (1990).
[23]J. G. Berryman, "Random close packing of hard spheres and disks," Phys. Rev. A **27**(2), 1053–1061 (1983).
[24]W. S. Jodrey and E. M. Tory, "Computer simulation of close random packing of equal spheres," Phys. Rev. A **32**(4), 2347–2351 (1985).
[25]R. K. Saha, S. K. Sharma, and M. C. Kolios, "Single cell size estimation from backscattered spectrum by using some weak scattering approximations," Can. Acoust. **38**(2), 31–34 (2010).
[26]B. G. Teh and G. Cloutier, "Modeling and analysis of ultrasound backscattering by spherical aggregates and rouleaux of red blood cells," IEEE Trans. Ultrason. Ferroelectr. Freq. Control **47**(4), 1025–1035 (2000).
[27]Y. W. Yuan and K. K. Shung, "Ultrasonic backscatter from flowing whole blood. II: Dependence on frequency and fibrinogen concentration," J. Acoust. Soc. Am. **84**(4), 1195–1200 (1988).
[28]R. M. Vlad, R. K. Saha, N. M. Alajez, S. Ranieri, G. J. Czarnota, and M. C. Kolios, "An increase in cellular size variance contributes to the increase in the ultrasound backscatter during cell death," Ultrasound Med. Biol. **36**(9), 1546–1558 (2010).

Forward Problem Study of an Effective Medium Model for Ultrasound Blood Characterization

Emilie Franceschini, *Member, IEEE*, Bloen Metzger, and Guy Cloutier, *Senior Member, IEEE*

***Abstract*—The structure factor model (SFM) is a scattering model developed to simulate the backscattering coefficient (BSC) of aggregated red blood cells (RBCs). However, the SFM can hardly be implemented to estimate the structural aggregate parameters in the framework of an inverse problem formulation. A scattering model called the effective medium theory combined with the SFM (EMTSFM) is thus proposed to approximate the SFM. The EMTSFM assumes that aggregates of RBCs can be treated as individual homogeneous scatterers, which have effective properties determined by the acoustical characteristics and concentration of RBCs within aggregates. The EMTSFM parameterizes the BSC by three indices: the aggregate radius, the concentration of RBCs within aggregates (the aggregate compactness), and the systemic hematocrit. The goodness of fit of the EMTSFM approximation in comparison with the SFM was then examined. Based on a 2-D study, the EMTSFM was found to approximate the SFM with relative errors less than 30% for a product of the wavenumber times the mean aggregate radius $kr_{ag} \leq 1.32$. The main contribution of this work is the parameterization of the BSC with the RBC aggregate compactness, which is of relevance in clinical hemorheology because it reflects the binding energy between RBCs.**

I. Introduction

Ultrasonic tissue characterization techniques using the RF backscattered signals have received broad interest for the past 25 years. One approach is to use the magnitude and frequency dependence of backscatter echoes to quantify the tissue structures such as the size, acoustic impedance, and concentration of the scatterers. This approach has been successfully used for the characterization of the eye [1], the prostate [2], apoptotic cells [3], and the breast [4]. Blood has also been studied by employing this technique [5], [6]. In the field of ultrasonic blood characterization, the objective is to assess the level of red blood cell (RBC) aggregation, which is a surrogate marker of inflammation [7]. It is well known that when RBCs are under low shear rates (<10 s^{-1}), they interact strongly with each other and form complex rouleaux, or 3-D structures. When the shear rate increases, these rouleaux or structures disaggregate. The aggregation phenomenon in human blood is normal, however hyperaggregation, an abnormal increase of RBC aggregation, is a pathological state associated with several circulatory diseases such as deep venous thrombosis, atherosclerosis, and diabetes mellitus. Ultrasonic blood characterization using the ultrasound backscatter technique has the potential to provide a method for the noninvasive estimation of the RBC aggregate size. This quantification would help to elucidate the role of RBC aggregation in the etiology of such diseases.

Ultrasound backscattering by blood is mainly due to RBCs that constitute the vast majority (97%) of the blood cellular content. Blood can thus be described as a biphasic fluid composed of RBCs immersed in plasma. Because RBCs are acoustically considered to be weak scatterers (impedance contrast between RBCs and plasma being around 13%), multiple scattering can be neglected. However, for such tissue, it is not straightforward to develop a theoretical scattering model because of the high density of RBCs (their volume fraction or hematocrit varies between 30 and 50%) and their ability to form aggregates. Theoretical efforts have been made to take into account the high density of RBCs [5], [8]–[10]. In the Rayleigh scattering regime (i.e., for a product of the wavenumber times the scatterer radius $ka \ll 1$), Twersky [9] proposed an expression of the backscattered intensity in terms of the single-particle backscattering cross section, number density of particles and packing factor. The packing factor is dependent on the hematocrit but independent of the frequency. This model succeeded in explaining the nonlinear relationship between the backscatter amplitude and hematocrit for non-aggregating RBCs [11] but failed to predict the magnitude and frequency dependence of backscatter echoes observed in *in vitro* experiments when considering aggregating RBCs. That is why Savery and Cloutier [12] proposed generalization of the packing factor theory for aggregating RBCs at a low hematocrit by introducing the frequency-dependent structure factor, named the structure factor model (SFM). This model was later generalized to a normal hematocrit of 40% [13]. The SFM sums the contributions from individual RBCs and models the RBC interaction by a statistical mechanics structure

Manuscript received August 17, 2011; accepted September 19, 2011. This work was supported by the Fonds Incitatifs Recherche 2010 of the Université de Provence and by a grant from the Canadian Institutes of Health Research (#MOP-84358).

E. Franceschini is with the Laboratoire de Mécanique et d'Acoustique (LMA), Centre National de la Recherche Scientifique (CNRS) UPR 7051, Marseille, France (e-mail: franceschini@lma.cnrs-mrs.fr).

B. Metzger is with the Institut Universitaire des Systèmes Thermiques Industriels (IUSTI), Centre National de la Recherche Scientifique (CNRS), Marseille, France.

G. Cloutier is with the Laboratory of Biorheology and Medical Ultrasonics, University of Montreal Hospital Research Centre (CRCHUM), Montreal, Quebec, Canada, and with the Department of Radiology, Radio-Oncology, and Nuclear Medicine, and the Institute of Biomedical Engineering, University of Montreal, Montreal, Quebec, Canada.

Digital Object Identifier 10.1109/TUFFC.2011.2129

TABLE I. ACOUSTICAL PROPERTIES OF BLOOD FOUND IN [11] AND [21].

	Density ρ (kg·m^{-3})	Compressibility κ (Pa^{-1})	Impedance Z (MRayl)
RBC*	1092	3.41×10^{-10}	1.766
Plasma	1021	4.09×10^{-10}	1.580

*RBC = red blood cells.

factor, which is, by definition, the Fourier transform of the spatial distribution of RBCs [12]–[14]. Note that the low-frequency limit of the structure factor is, by definition, the packing factor used under Rayleigh conditions, and that the structure factor cannot analytically be calculated contrary to the packing factor [9]. The SFM was largely used to perform simulation studies on RBC aggregation [12], [13], [15]–[17]. Simulations enabled prediction of the frequency dependence of the backscattering coefficient (BSC) from various RBC spatial distributions and thus helped the interpretation of experimental observations. However, the SFM cannot directly be used to estimate the RBC aggregate size in the framework of an inverse problem approach because of the intensive computational time required to assess the structure factor by realizing distributions of aggregating RBCs with simulations. Note that the SFM should not be confused with the structure factor size estimator (SFSE) recently proposed by Yu *et al.* [18], [19]. The SFSE approximates the SFM for practical assessments of RBC structural features (i.e., in an inverse problem formulation).

Yu *et al.* [18], [19] developed the SFSE scattering theory that approximates the SFM by using a second-order Taylor expansion of the structure factor. The SFSE is thus not as accurate as the SFM. The SFSE parameterizes the BSC by two structure indices: the packing factor and the mean aggregate diameter, assumed to be isotropic. However, experiments with pig blood in controlled flow devices [18], [19] and 3-D numerical simulations of isotropic aggregates [16] showed that the two indices are correlated and follow a quadratic relationship under the assumption of isotropic monodisperse aggregates, thus reducing the BSC parameterization to one structural index. Moreover, the SFSE model did not produce good fits to the simulated BSCs computed with the SFM [16, Fig. 4]. Thus, the SFSE model is not sufficient to approximate the SFM accurately; even if the relation between the simulated aggregate sizes and its SFSE parameterization followed a proportional relationship [16]. The goal of this paper is to propose a new scattering model that better approximates the SFM for structural RBC aggregate characterization.

The scattering theory we propose is based on an effective medium theory (EMT) combined with the SFM, labeled EMTSFM. The EMT was initially developed by Kuster and Toksoz [20] in the field of geophysics. Here, the EMT assumes that aggregates of RBCs can be treated as individual homogeneous scatterers, which have effective properties determined by the concentration of RBCs within aggregates and acoustical properties of blood constituents. The approximation of RBC aggregates as homogeneous effective particles is combined with the SFM to consider the concentrated blood medium. The effective particle interactions were thus modeled by a structure factor, as in [12] and [13]. The EMTSFM parameterizes the BSC by three indices: the aggregate radius, the internal hematocrit (i.e., the concentration of RBCs within aggregates, also called the aggregate compactness) and the systemic hematocrit. Note that the new EMTSFM model would allow characterizing, for the first time in the quantitative ultrasound field, the compactness of RBC aggregates (or of any other cellular structures). In the field of clinical hemorheology, assessing the compactness of RBC aggregates is of high clinical importance because it is related to the binding energy between cells. Normal RBC aggregates form rouleaux-type structures, whereas pathologies associated with stronger binding energies result in clumps of RBCs (close to a spherical isotropic packing).

The purpose of this study was to compare the EMTSFM and SFM in the framework of a forward problem study, i.e., determining the BSC from known distributions of RBCs with known acoustical parameters using both EMTSFM and SFM. The goodness of fit of the EMTSFM approximation in comparison with the SFM was examined as a function of the frequency and of the structural aggregate parameters (i.e., the aggregate size and the internal hematocrit). Because of the computational load required to generate 3-D RBC distributions with various internal hematocrits with the SFM, 2-D models were used for the BSC computation. Although limiting, this choice allowed us to simulate randomly various internal hematocrits for a given range of systemic hematocrits, and to isolate the effects of aggregate size and internal hematocrit on the BSC.

II. ULTRASOUND BACKSCATTERING THEORY

In the following, it is assumed that the incident wavelength λ is large compared with the RBC size. Consequently, the RBC shape could be approximated by a simple geometry having an equivalent volume of an RBC in 3-D or having an equivalent surface in 2-D [21]. In the present 2-D study, RBCs were modeled as parallel infinite cylinders of radius a, that have small contrast in acoustical properties relative to the plasma (see Table I). Two scattering models of RBC aggregation are presented in this section: the SFM and the new EMTSFM.

A. The Structure Factor Model (SFM)

The SFM of ultrasound backscattering by blood consists of summing contributions from individual RBCs and

modeling the RBC interaction by a statistical mechanics structure factor [12], [13], [15]. By considering a collection of N identical and weakly scattering RBCs, the BSC expression can be written as

$$\mathrm{BSC}_{\mathrm{SFM}}(-2\mathbf{k}) = m\sigma_b(-2\mathbf{k})S(-2\mathbf{k}), \tag{1}$$

where $\mathbf{k}$ is the incident wave vector and m is the number density of RBCs that is related to the systemic hematocrit ϕ as $m = \phi/A_p$ (where A_p is the RBC area). The backscattering cross section σ_b of a single weak RBC can be written as the product of the backscattering cross section of a single RBC in the Rayleigh limit [9, Eq. (16)] and the backscatter form factor F as

$$\sigma_b(-2\mathbf{k}) = \frac{k^3 A_p^2 \gamma_z^2}{2\pi} F(-2k, a) = \frac{k^3 A_p^2 \gamma_z^2}{2\pi}\left(\frac{J_1(2ka)}{ka}\right)^2, \tag{2}$$

where J_1 is the first-order Bessel function of the first kind and $\gamma_z = (Z_{\mathrm{RBC}} - Z_{\mathrm{plasma}})/Z_{\mathrm{plasma}}$ is the fractional variation of impedance between the RBC and its suspending medium (i.e., the plasma). The form factor F serves as a useful descriptor of a scatterer with a simple shape [21], [22] and characterizes here the cylindrical shape and size of the 2-D RBC scatterer. The demonstration of the cylindrical form factor expression in 2-D is given in the Appendix. The function S in (1) is the structure factor representing the spatial positioning of RBCs; it is defined by

$$S(-2\mathbf{k}) = E\left[\frac{1}{N}\left|\sum_{i=1}^{N} e^{-i2\mathbf{k}\mathbf{r}_i}\right|^2\right], \tag{3}$$

where E is the expected value of a random variable and $\mathbf{r}_i$ is the position vector defining the center of the ith RBC in space. Note that the aggregation phenomenon only affects the structure factor because RBC properties (i.e., σ_b) and the systemic hematocrit are expected to remain constant in the modeled region of interest.

In the case of disaggregated RBCs, the low-frequency limit of the structure factor is a constant with this model $[S(k) \to S(0) = W]$, which is the packing factor. The BSC expression can thus be simplified as

$$\mathrm{BSC}_{\mathrm{LF}}(-2\mathbf{k}) = mW\sigma_b(-2\mathbf{k}). \tag{4}$$

The most often used packing factor expression is based on the Percus-Yevick pair-correlation function for identical, hard, and radially symmetrical particles. The Percus-Yevick packing factor W_{PY} was first applied to blood by Shung *et al.*, and it is related to the systemic hematocrit in the 2-D space as [11]

$$W_{\mathrm{PY}} = \frac{(1-\phi)^3}{1+\phi}. \tag{5}$$

The packing factor reflects the positional correlation among particles: $W = 1$ for completely random distributions and W tends toward zero as the particle number and the spatial correlation between particles increase.

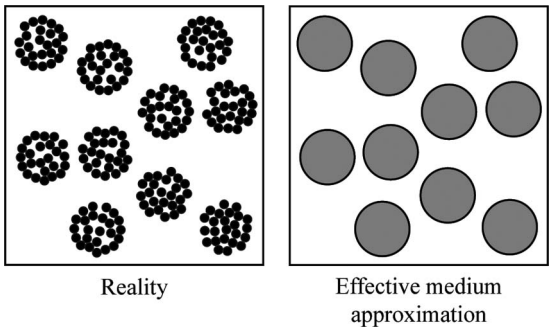

Fig. 1. Schematic representation of aggregates treated as individual scatterers. The aggregates of red blood cells in blood (left side) are assumed to be homogeneous particles (right side) with effective properties that depend on the internal hematocrit and on the density and compressibility of the red blood cells within them.

B. The Proposed Model: An Effective Medium Theory Combined With the SFM (EMTSFM)

As a first approximation, we assume that all the RBCs are aggregated in blood, that the aggregates are identical and isotropic and that the RBCs within the aggregates are evenly distributed. The EMTSFM assumes that aggregates of RBCs can be treated as individual homogeneous scatterers as shown in Fig. 1. Each aggregate is thus approximated by an effective single particle (i.e., in this 2-D study, an effective single cylinder) having a radius r_{ag}. The density ρ_{ag} and compressibility κ_{ag} of the new effective particle are determined by considering the EMT [20]. This means that ρ_{ag} and κ_{ag} are derived from the acoustical properties of the two fluids that constitute the aggregates (i.e., ρ_1, ρ_2, κ_1, and κ_2, where 1 indicates properties of RBCs and 2 those of plasma) and from the internal concentration of RBCs within the aggregates, defined as the internal hematocrit ϕ_i, as follows:

$$\begin{aligned} \rho_{\mathrm{ag}} &= \phi_i\rho_1 + (1-\phi_i)\rho_2 \\ \frac{1}{\kappa_{\mathrm{ag}}} &= \frac{\phi_i}{\kappa_1} + \frac{1-\phi_i}{\kappa_2}. \end{aligned} \tag{6}$$

The acoustic interaction of RBCs within aggregates is therefore taken into account with the EMT, similarly to the SFM, where it is considered by the structure factor that models the individual position of RBCs and their acoustical interaction, whether they are within an aggregate or not. The main advantage of the EMTSFM is the consideration of the compactness of aggregates with the parameter ϕ_i.

The BSC from blood is then obtained by summing contributions from individual effective particles of radius r_{ag} and modeling the effective particle interaction by a statistical mechanics structure factor, S_{ag}. The equivalent BSC expression is thus

$$\mathrm{BSC}_{\mathrm{eq}}(-2\mathbf{k}) = m_{\mathrm{ag}}\sigma_{\mathrm{ag}}(-2\mathbf{k})S_{\mathrm{ag}}(-2\mathbf{k}), \tag{7}$$

where m_{ag} is the number density of aggregates, which is related to the effective area fraction of aggregates, ϕ_{ag}. The effective area fraction of aggregates is equal to the area fraction of RBCs in blood, ϕ, divided by the internal hematocrit ϕ_i: $\phi_{\mathrm{ag}} = \phi/\phi_i$. The backscattering cross section, σ_{ag}, of an effective single cylinder was calculated using the fluid-filled cylinder model developed by Doolittle and Uberall [23]. That model provides an exact solution for the backscattering of sound by a single fluid cylinder, not necessarily small compared with the wavelength, in a surrounding fluid medium (i.e., the plasma). In the proposed forward problem study, the radius r_{ag}, density ρ_{ag}, and compressibility κ_{ag} of the aggregates, and the density, ρ_2, and compressibility, κ_2, of the plasma are known *a priori* (see Table I) such that the backscattered pressure of the effective fluid cylinder could be computed as a function of frequency. The structure factor S_{ag} was calculated for a collection of N_{ag} identical and disaggregated particles (mimicking RBC aggregates) of radius r_{ag}, randomly distributed as follows:

$$S_{\mathrm{ag}}(-2\mathbf{k}) = E\left[\frac{1}{N_{\mathrm{ag}}}\left|\sum_{i=1}^{N_{\mathrm{ag}}} e^{-i2\mathbf{k}\mathbf{r}_i'}\right|^2\right], \tag{8}$$

where $\mathbf{r}_i'$ are the position vectors defining the center of the ith effective particle (or aggregate) in space. Note that in the research field of optics [24], the applicability of the modeling approach based on the structure factor (called the interference approximation) is limited to a product $kR \leq 3.5$ (or $kR \leq 1.5$, respectively) for a relative refractive index of the particles equal to 1.19 (or 1.8), where R is the radius of isotropic identical particles. Because the relative acoustic impedance of RBCs, z_1/z_2, is around 1.12 (see Table I), we are thus expecting the same limitation for the EMTSFM (i.e., a validity of this modeling approach restricted to $kr_{\mathrm{ag}} \leq 3.5$).

In the low-frequency limit, for aggregate sizes which are small compared with the wavelength, the structure factor S_{ag} can be well approximated by the Percus-Yevick packing factor of (5) for effective particles. The equivalent BSC expression is thus simplified as

$$\mathrm{BSC}_{\mathrm{eq_{LF}}}(-2\mathbf{k}) = m_{\mathrm{ag}}\frac{(1-\phi_{\mathrm{ag}})^3}{1+\phi_{\mathrm{ag}}}\sigma_{\mathrm{ag}}(-2\mathbf{k}), \tag{9}$$

where σ_{ag} is calculated using the exact model of fluid-filled cylinders [23], such that, in comparison with (7), the only approximation is the structure factor S_{ag}.

III. Simulation Methods

The computation of the $\mathrm{BSC_{SFM}}$ and $\mathrm{BSC_{eq}}$ requires the knowledge of the structure factors S and S_{ag}, as described in (1) and (7). Because the structure factor S (or equivalently S_{ag}) is, by definition, a statistical quantity, an average of all structure factors obtained from several particle distributions can give an estimated value of S (or equivalently S_{a}). Note that 2-D models were used because of the computational time required to generate 3-D RBC distributions with the SFM. Although limiting, this choice allowed us to simulate randomly varied internal hematocrits for a given range of systemic hematocrits.

A. Computation of Particle Distributions

1) Distribution of RBCs for the Computation of S With the SFM: We describe here how random distributions for non-aggregating and aggregating RBCs were computed within the simulated surface area L^2 of 600^2 $\mu\mathrm{m}^2$. The RBC particle radius a was set to 2.75 μm for all simulations. In the case of disaggregated RBCs, particles were randomly distributed (using a random number generator) with non-overlapping positions to give the desired area fraction of RBCs in blood (i.e., the systemic hematocrit ϕ). In the case of aggregated RBCs, we first specified the aggregate radius and then aggregates were randomly distributed with non-overlapping positions to give the desired area fraction of aggregates ϕ_{ag}. RBC distributions within aggregates were then generated by considering the number of RBCs within aggregates n_i and the area fraction of RBCs within aggregates ϕ_i. It is important to emphasize that random particle distributions could be easily generated using a random number generator up to an area fraction of approximately 0.5. In our study, the area fraction of RBCs within aggregates ϕ_i could be enlarged, up to a maximum value $\phi_{i_{\max}}$ fixed at 0.6. The procedure we chose to reach such a high number of RBCs within aggregates is described in the following.

We first randomly distributed n_i RBCs in a total area that was larger than the aggregate area, such that the initial area fraction of RBCs within aggregates was lower than 0.5. Then, to increase this area fraction, the RBCs were submitted to an external force oriented toward the center of mass of the RBC spatial distribution. RBCs moved toward each other while a repulsive force prevented them from overlapping. These forces were maintained until the area fraction of RBCs inside the considered aggregate reached the desired area fraction ϕ_i. This distribution procedure was repeated for each aggregate, such that the distribution of RBCs within each aggregate was different. Note that this procedure is not time consuming if a small number of RBCs is used: herein the maximum number of RBCs within aggregates was 38 for the maximum aggregate radius of $7.95a = 21.86$ μm. The maximum value of aggregate area fraction $\phi_{\mathrm{ag}_{\max}}$ was thus fixed to 0.5 and as a consequence, the maximum value of the systemic hematocrit $\phi_{\max}$ was limited to: $\phi_{\max} = \phi_{\mathrm{ag}_{\max}}\,\phi_{i_{\max}} = 0.3$.

Fig. 2 illustrates spatial arrangements of RBCs for three internal hematocrits of 40%, 50%, and 60%. In these simulations, the aggregate radius had a constant value of $r_{\mathrm{ag}}/a = 6.32$ (i.e., $r_{\mathrm{ag}} = 17.39$ μm) and a constant systemic hematocrit of 20%.

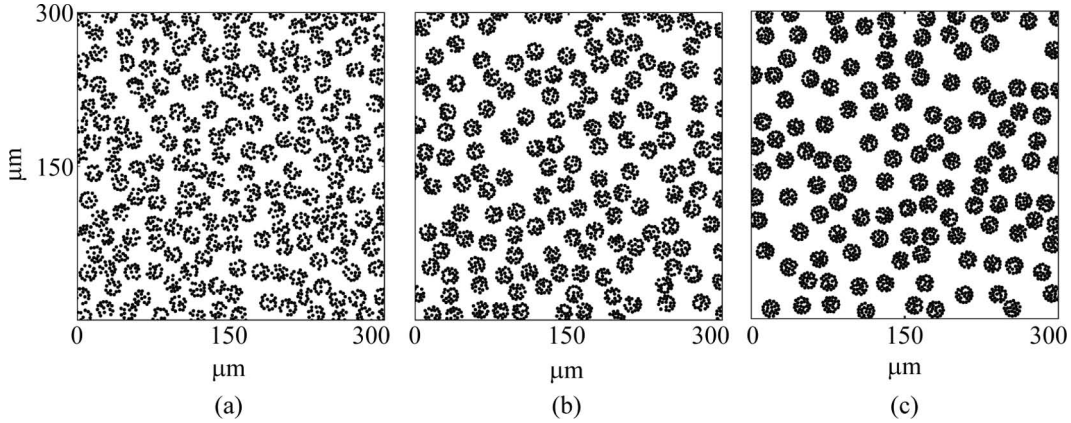

Fig. 2. Distributions of aggregated red blood cells for a constant aggregated radius $r_{ag} = 6.32a = 17.32$ μm and a constant systemic hematocrit $\phi = 20\%$ at three internal hematocrits: (a) $\phi_i = 40\%$, (b) $\phi_i = 50\%$, and (c) $\phi_i = 60\%$. The displayed areas are 300 × 300 μm to enhance the red blood cell visualization.

2) Distribution of Effective Particles for the Computation of S_{ag} With the EMTSFM: Once the effective particle radius was specified, particles were randomly distributed using a random number generator with non-overlapping positions to give the desired area fraction ϕ_{ag}. Several distributions were performed with different effective particle radii varying from $3.16a$ (= 8.69 μm) to $7.95a$ (= 21.86 μm) corresponding to different studied aggregate sizes.

B. BSC Computation

For each distribution of RBCs (or effective particles, respectively), density matrices D (or D_{ag}) were computed by dividing the square simulation plane L^2 in N_p^2 pixels (here, $N_p = 512$) and by counting the number of RBCs (or the number of effective particles) falling into each pixel. These matrices represented samplings of microscopic density functions defined by $D(r)$ for the BSC computation with the SFM or by $D_{ag}(r')$ for the BSC_{eq} computation with the proposed EMTSFM:

$$D(\mathbf{r}) = \sum_{i=1}^{N} \delta(\mathbf{r} - \mathbf{r}_i),$$
$$D_{ag}(\mathbf{r}') = \sum_{i=1}^{N_{ag}} \delta(\mathbf{r}' - \mathbf{r}_i'), \tag{10}$$

where N is the number of RBCs in blood, N_{ag} is the number of aggregates, and δ is the Dirac distribution. According to (3) and (8), and as explicitly described in [14, Appendix], the structure factors can thus be described by

$$S(-2\mathbf{k}) = E\left[\frac{1}{N}\left|\int D(\mathbf{r}) e^{-i2\mathbf{kr}} \mathrm{d}\mathbf{r}\right|^2\right] \text{ and}$$
$$S_{ag}(-2\mathbf{k}) = E\left[\frac{1}{N_{ag}}\left|\int D_{ag}(\mathbf{r}') e^{-i2\mathbf{kr}'} \mathrm{d}\mathbf{r}'\right|^2\right]. \tag{11}$$

Each structure factor was thus computed by averaging 2-D fast Fourier transforms (2-D FFT) of 400 density matrices for averaging purposes. The FFTs gave the structure factor values $S(-2\mathbf{k})$ and $S_{ag}(-2\mathbf{k})$ on a centered grid of wavevectors between $\pm\pi N_p/2L$ with a step of $\Delta k = \pi/L$. For the SFM, the BSC_{SFM} was thus obtained using (1). For the EMTSFM, the BSC_{eq} was computed using (7).

IV. Results

In the following, the relative errors for BSC_{eq} computed with the new EMTSFM were evaluated as $(BSC_{eq} - BSC_{SFM})/BSC_{eq}$, where the BSC_{SFM} of the SFM is assumed to be the exact solution.

A. Influence of the Internal Hematocrit

A key feature of the new simulation method was the possibility to simulate randomly various internal hematocrits corresponding to different degrees of compactness of aggregates. Frequency-dependent backscattering coefficients with different internal hematocrits from 30% to 60% are given in Figs. 3(a) and 3(b) at systemic hematocrits of 10% and 20% over a large frequency range (4 to 100 MHz). Corresponding relative errors for the BSC_{eq} are given in Figs. 3(c) and 3(d). It was assumed that the aggregates had a constant radius of $r_{ag}/a = 6.32$ (i.e., $r_{ag} = 17.39$ μm). Note that for the 20% systemic hematocrit, internal hematocrits smaller than 40% could not be computed because the corresponding area fractions of aggregates were too high: $\phi_{ag} > 0.5$. As seen in Figs. 3(a) and 3(b), as the internal hematocrit ϕ_i increases, the BSC_{SFM} amplitude increases at low frequencies (<23 MHz) and decreases at high frequencies (>28 MHz). The first peaks of the BSC_{SFM} are between 18.0 and 20.6 MHz for all simulated conditions. The relative error for BSC_{eq} was less than 30% for frequencies below 18 MHz [see Figs. 3(c) and 3(d)]. This 18 MHz frequency corresponds to a product $kr_{ag} = 1.27$. More generally, at frequencies less than 23 MHz, backscattering coefficients obtained with the SFM and the EMTSFM have the same behaviors: the first peaks of BSC_{SFM} and BSC_{eq} occur at the same frequencies

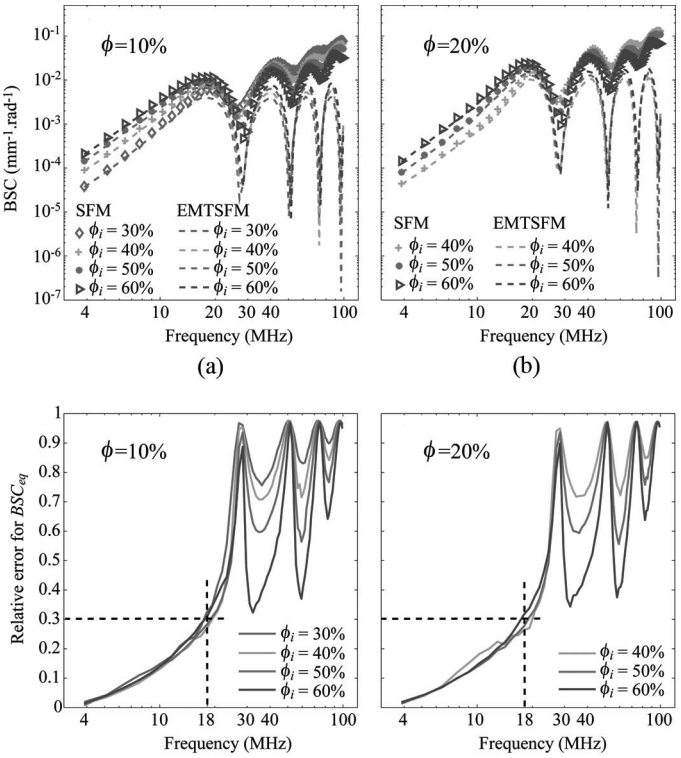

Fig. 3. (a) and (b) Dependence of the backscattering coefficients (BSCs) on the internal hematocrit: (a) $r_{ag}/a = 6.32$ and $\phi = 10\%$, and (b) $r_{ag}/a = 6.32$ and $\phi = 20\%$. The symbols are the BSC_{SFM} computed with the structure factor model (SFM) and the dashed lines are the BSC_{eq} computed with the effective medium theory combined with the SFM (EMTSFM). (c) and (d) Corresponding relative errors for the BSC_{eq} versus frequency.

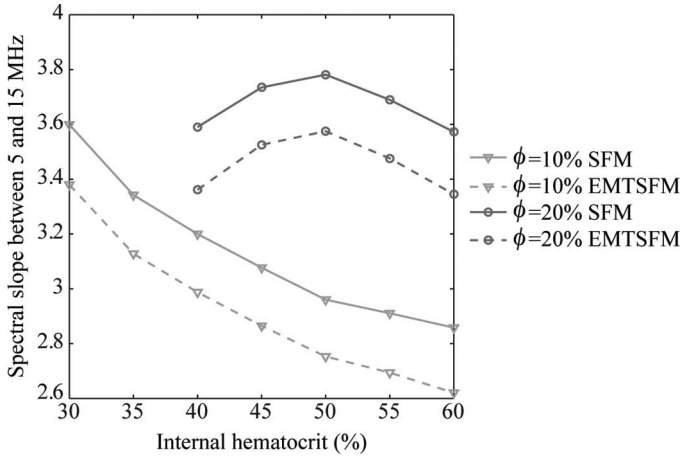

Fig. 4. Spectral slope in the frequency bandwidth 5 to 15 MHz as a function of the internal hematocrit at different systemic hematocrits, the aggregate size being fixed ($r_{ag}/a = 6.32$). The solid lines are the spectral slopes (SSs) for the BSC_{SFM} computed with the structure factor model (SFM) and the dashed lines are the SSs for the BSC_{eq} computed with the effective medium theory combined with the SFM (EMTSFM).

and the magnitude of both BSC_{SFM} and BSC_{eq} increase as the internal hematocrit increases.

A quantitative ultrasonic parameter that has often been used for tissue characterization is the spectral slope (SS). The SS is the linear slope of the BSC as a function of frequency on a log-log scale. The variation of SS with the internal hematocrit is given in Fig. 4 for systemic hematocrits of 10% and 20%. The solid lines represent the SSs for the BSC_{SFM} computed with the SFM and the dashed lines represent the SSs for the BSC_{eq} computed with the EMTSFM. For both SFM and EMTSFM, the SS behavior versus the internal hematocrit is the same: the SS decreases with increasing internal hematocrit, except for the configuration $\phi = 20\%$, $\phi_i = 40\%$. Note also that the SS of the EMTSFM slightly underestimated the SS of the SFM with a maximum difference of 0.23.

B. Influence of the Aggregate Size

Fig. 5 shows backscattering coefficients as a function of frequency for different aggregate sizes and for systemic hematocrits of 10%, 20%, and 30%. In these simulations, the internal hematocrit was the highest: $\phi_i = 60\%$. The symbols represent the BSC_{SFM} computation for the disaggregated case ($r_{ag}/a = 1$) and for aggregated cases with radii of $r_{ag}/a = 3.16$, 5.0, and 7.07. The corresponding BSC_{eq} computed with the EMTSFM [see (7)] are given in dashed lines. For frequencies less than 20 MHz, the amplitudes of both BSC_{SFM} and BSC_{eq} increase with the size of aggregates. Moreover, the peaks of both BSC_{SFM} and BSC_{eq} occur at lower frequencies as the aggregate radius increases.

The low-frequency approximation of the EMTSFM (i.e., using the Percus-Yevick packing factor) was also studied for the same configurations. The BSC_{eq} values computed by (9) are given in Fig. 6, along with plots of the BSC_{SFM} computed with the SFM. As expected, the error for $BSC_{eq_{LF}}$ is larger than the error for BSC_{eq} at high frequencies. The error between $BSC_{eq_{LF}}$ and BSC_{SFM} increases as the systemic hematocrit ϕ increases. Nevertheless, it is interesting to observe that at low frequencies less than 5 MHz, the amplitude of the $BSC_{eq_{LF}}$ matches the exact BSC_{SFM} very well, as expected.

For systemic hematocrits of 10%, 20%, and 30%, the relative errors for BSC_{eq} and $BSC_{eq_{LF}}$ were studied for a constant value of the internal hematocrit $\phi_i = 60\%$ and for eleven sizes of r_{ag}/a varying from 3.16 to 7.95 with a step of around 0.5. For each case, the frequency limit f_l and the corresponding product $k_l r_{ag}$ for which the relative error was less than 30% were determined. Results are summarized in Fig. 7. The solid lines are for the EMTSFM and the dashed lines for the low-frequency approximation of the EMTSFM using the Percus-Yevick packing factor. Fig. 7 reveals that the EMTSFM gives accurate estimates of BSC_{SFM} until $kr_{ag} \leq 1.32$ on average (i.e., for all the tested values of r_{ag}/a), whereas the EMTSFM at low frequency is only accurate until approximately $kr_{ag} \leq 0.73$.

Fig. 8 shows the influence of the aggregate size on the SS for different systemic hematocrits. The solid lines represent the SSs for the BSC_{SFM} computed with the SFM and the dashed lines represent the SSs for the BSC_{eq} computed with the EMTSFM. The results of SS presented in

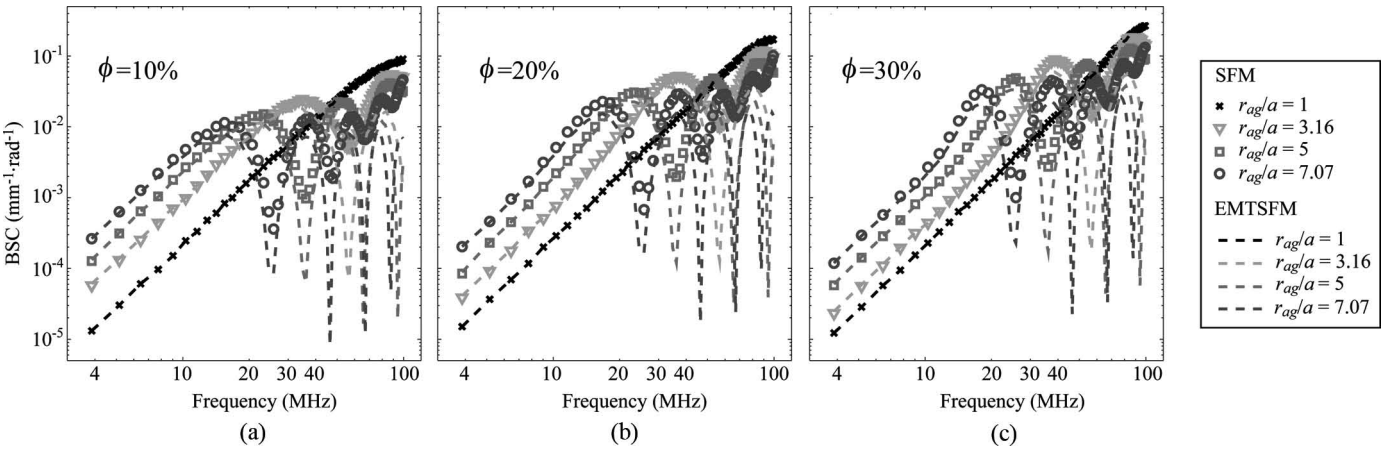

Fig. 5. Dependence of the backscattering coefficients (BSCs) for different aggregate sizes and a constant internal hematocrit $\phi_i = 60\%$ at systemic hematocrits of 10%, 20%, and 30%. The symbols are the $\mathrm{BSC_{SFM}}$ computed with the structure factor model (SFM) and the dashed lines are the $\mathrm{BSC_{eq}}$ computed with the effective medium theory combined with the SFM (EMTSFM).

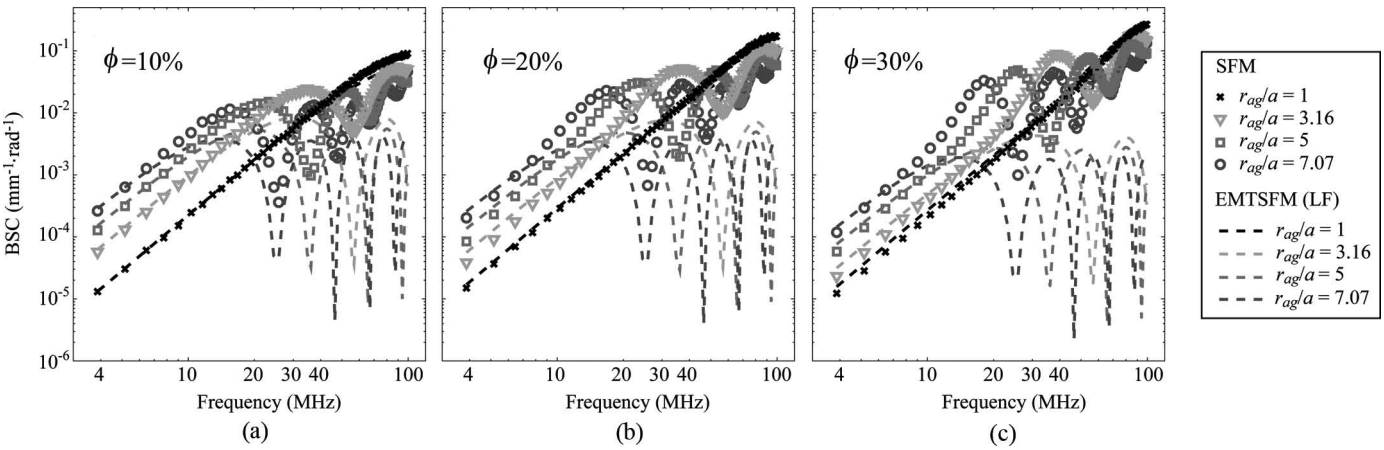

Fig. 6. Dependence of the backscattering coefficients (BSCs) for different aggregate sizes and a constant internal hematocrit $\phi_i = 60\%$ at systemic hematocrits of 10%, 20%, and 30%. The symbols are the $\mathrm{BSC_{SFM}}$ computed with the structure factor model (SFM) and the dashed lines are the $\mathrm{BSC_{eq_{LF}}}$ computed with the effective medium theory combined with the SFM (EMTSFM) using the Percus-Yevick approximation.

Fig. 8 showed that the backscattered power by disaggregated RBCs ($r_{\mathrm{ag}}/a = 1$) increased with the third power of wave frequency (SS = 3), as was expected using the Rayleigh theory in 2-D. The SS behavior with the aggregate size is the same for both SFM and EMTSFM: as the aggregate size increases, the SS decreases at $\phi = 10\%$, whereas the SS increases at $\phi = 20\%$ and 30%. The maximum difference between slopes of the EMTSFM and slopes of the SFM is around 0.35 for all studied hematocrits (i.e., relative error for the SS of $\mathrm{BSC_{eq}}$ around 9%) and it corresponds to the largest aggregate size.

V. Discussion

A. Limitation of the EMTSFM With Respect to kr_{ag}

Based on the new EMTSFM theory, the BSC from aggregated RBCs was parameterized by three indices: the aggregate size, internal hematocrit, and systemic hematocrit. The aim of our study was to estimate the goodness of fit of the EMTSFM approximation in comparison with the SFM. We found that the EMTSFM had a relative error of less than 30% for a mean product $kr_{\mathrm{ag}} \leq 1.32$ at all internal hematocrits and systemic hematocrits studied. Although the EMTSFM gave estimates with large errors for $kr_{\mathrm{ag}} > 1.32$, the EMTSFM fitted very well the $\mathrm{BSC_{SFM}}$ curve computed with the SFM for all tested factors (i.e., r_{ag}, ϕ_i, and ϕ) in the frequency bandwidth between 4 MHz and the frequency position of the first peak. This result is qualitatively consistent with works in optics [24], in which the limits of applicability of the interference approximation based on the structure factor were found for a volume fraction of particles smaller than 10% and for a product $kR \leq 3.5$ (or $kR \leq 1.5$, respectively) when the relative refractive index of the particles is 1.19 (or 1.8). These limits were determined by comparing theoretical predictions of the interference approximation with theoretical predictions of a much more exact quasi-crystalline approximation and with experimental data of a polystyrene latex suspension in water. In comparison with our results in acoustics in which the relative acoustic impedance of

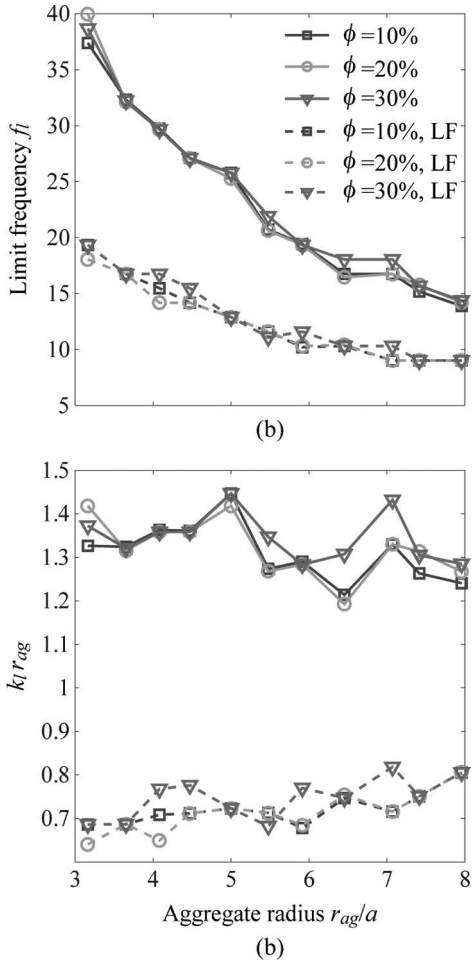

Fig. 7. (a) Frequency limit f_l for which the relative error of BSC_{eq} was less than 30% as a function of the aggregate size studied. The solid lines are the effective medium theory combined with the structure factor model (EMTSFM) and the dashed lines are the low-frequency approximation of the EMTSFM. (b) Corresponding product $k_l r_{ag}$.

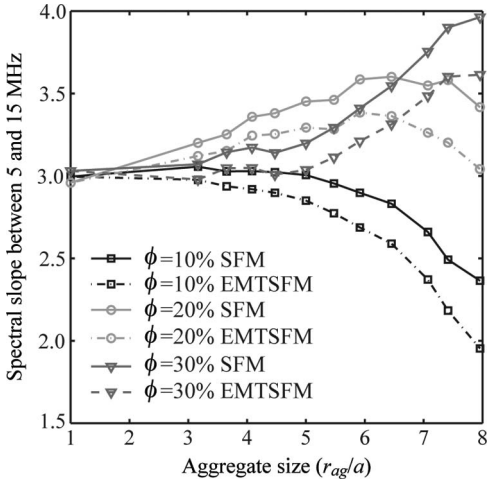

Fig. 8. Spectral slope in the frequency bandwidth 5 to 15 MHz as a function of the aggregate size at different systemic hematocrits, the internal hematocrit being fixed ($\phi_i = 60\%$ for aggregated red blood cells). The solid lines are the spectral slopes (SSs) for the BSC_{SFM} computed with the structure factor model (SFM) and the dashed lines are the SSs for the BSC_{eq} computed with the effective medium theory combined with the SFM (EMTSFM).

the RBCs is around 1.12, the limit of applicability of the proposed EMTSFM in terms of particle size is surprisingly close to the optic limit $kR \leq 1.5$, when one considers a large relative refractive index of 1.8. In terms of particle concentration, the EMTSFM showed no limitation with respect to the studied hematocrit (up to 30%), contrary to the interference approximation, valid up to a volume fraction of 10%.

B. Variation of the Spectral Slope With ϕ_i and With r_{ag}

On the goodness of the EMTSFM modeling the SS, notice that the variations of SS with ϕ_i and r_{ag} followed similar trends for both SFM and EMTSFM (Figs. 4 and 8). The SS of the EMTSFM slightly underestimated the SS of the SFM with a maximum relative error of 9%. As can be observed in Fig. 8, as the aggregate size increased, the difference between slopes of the EMTSFM and SFM increased. This is due to the constant frequency bandwidth chosen between 5 and 15 MHz for all studied aggregate sizes. Indeed, in the frequency bandwidth between 4 MHz and the frequency position of the first peak, the relative error for the BSC_{eq} increased with the frequency as was shown in Figs. 3(c) and 3(d). Because the relative error was less than 30% for a mean product $kr_{ag} \leq 1.32$, the mean relative error in the frequency bandwidth 5 to 15 MHz for the smallest aggregates was smaller than the relative error for the largest aggregates in the same frequency bandwidth.

Contrary to blood modeling, the ultrasound characterization of tissues such as the breast [4] or the liver [25] assumes scatterers to be randomly distributed at a low number density. Tissue models are generally based on 3-D spatial autocorrelation functions describing the shape and isotropic random distribution of scatterers in the medium, and modeling of the spatial autocorrelation function could be Gaussian, spherical, or exponential [22], [25]. Based on these models, the SS is an indicator of the scatterer size, and a decrease in slope usually corresponds to an increase in scatterer size [25]. That is why it is interesting to discuss the variation of the SS with the aggregate size in the framework of the SFM or EMTSFM which consider the structure factor (see Fig. 8). For the lowest systemic hematocrit of 10%, the SS decreased with the increase in aggregate size. Because the hematocrit is low, the known behavior of the SS was observed. However, the SS increased with the aggregate size for systemic hematocrits of 20 and 30%. The structure factor, which models the spectral behavior of the scatterer spatial distributions, caused this behavior of the SS. Indeed, according to (1) [or (7), respectively], the BSC_{SFM} frequency dependence (or the BSC_{eq} frequency dependence) is determined by the frequency dependences of σ_b and S (or σ_{ag} and S_{ag}). To illustrate this, the structure factors S and S_{ag} corresponding, respectively, to the SFM and the EMTSFM are displayed in Fig. 9 for a fixed systemic hematocrit $\phi = 30\%$, a fixed internal hematocrit $\phi_i = 60\%$, and three aggregate radii $r_{ag}/a = 3.16$, 5.0, and 7.07. The plot of S is represented in

a larger frequency bandwidth up to 320 MHz to show the high-frequency oscillations of the structure factor around 1. In the frequency bandwidth 5 to 15 MHz, the frequency dependence of the structure factors S and S_{ag} do not follow a simple power law, because the structure factors S and S_{ag} versus frequency on a log-log scale are non-linear curves. One could observe that, in the frequency bandwidth 5 to 15 MHz, both the structure factors S and S_{ag} increase with the frequency, and the larger the aggregate size is, the larger is the increase. That is why the SS for both BSC_{SFM} and BSC_{eq} increased above 3 with the aggregate size for this studied systemic hematocrit of 30%. The increase of SS with the aggregate size we observed in the current study is consistent with an earlier 2-D numerical simulation study performed by Fontaine and Cloutier [17]. In this 2-D study, the SS between 5 and 25 MHz could increase from 3.1 to 3.3 when the level of aggregation increased for a hematocrit of 40%. Moreover, *in vitro* Couette flow experiments performed in [18] showed the SS greater than 4 between 9 and 15 MHz for shear rates of 2 and 10 s^{-1} at a systemic hematocrit of 40% [18, Fig. 4(b)].

It is important to note that we found that the SS decreased as ϕ_i increased for all studied systemic hematocrits. On the other hand, the behavior of the SS as a function of the aggregate size depended on the systemic hematocrit. As a consequence, the parameter SS seems well adapted to observe a change in the internal hematocrit. However, in experimental conditions where effects of aggregate size and internal hematocrit are mixed, the SS cannot be a useful index for blood characterization.

C. Computation of RBC Distributions

The method we proposed here to obtain the RBC spatial distribution did not take into consideration realistic interactions between RBCs. It was a simple and fast method to generate samples containing non-overlapping, identical, and isotropic aggregates. The main advantage of this method was the possibility to have various internal hematocrits with the same size of aggregates. The simulation results showed that the frequency position of the BSC first peak was very little affected by changes in the internal hematocrit, whereas it was greatly affected by changes in the aggregate size. Indeed, the change in frequency position was only 1.5 MHz (and, respectively, 2.1 MHz) for the hematocrit of 10% (and 20%) when the internal hematocrit increased from 30 to 60%. Moreover, theoretical predictions of the BSC with the SFM showed that its amplitude increases as r_{ag} and ϕ_i increase (see Figs. 3 and 5). To our knowledge, the influence of the internal hematocrit on the BSC has not been studied previously, mainly because of the simulation methods used to realize distributions of aggregating RBCs. These methods were based on particle dynamics or statistical mechanics [12], [13], [15]–[17] and had the objective of mimicking the rheological behavior of blood. The RBC distributions obtained showed aggregates with anisotropic shape [12], [13], [15], [17], [26] and a polydispersity in terms of aggregate sizes, aggregate shapes, and internal hematocrits [12], [13], [15]–[17]. As mentioned previously, contrary to those earlier studies, the 2-D simulation method we proposed for distributing RBCs allowed isolation of the effects of the aggregate size and internal hematocrit to better understand the role of each parameter. In that sense, our study has provided some insights into the influence of the aggregate size and internal hematocrit on the BSC frequency dependency. The internal hematocrit and the aggregate size can greatly influence the BSC amplitude. The frequency position of the BSC first peak was found not to be significantly affected by changes in the internal hematocrit, whereas it was greatly affected by changes in the aggregate size.

D. On the Use of the EMTSFM In Vivo

Although the present work allowed a fundamental study on the influences of the internal hematocrit and aggregate

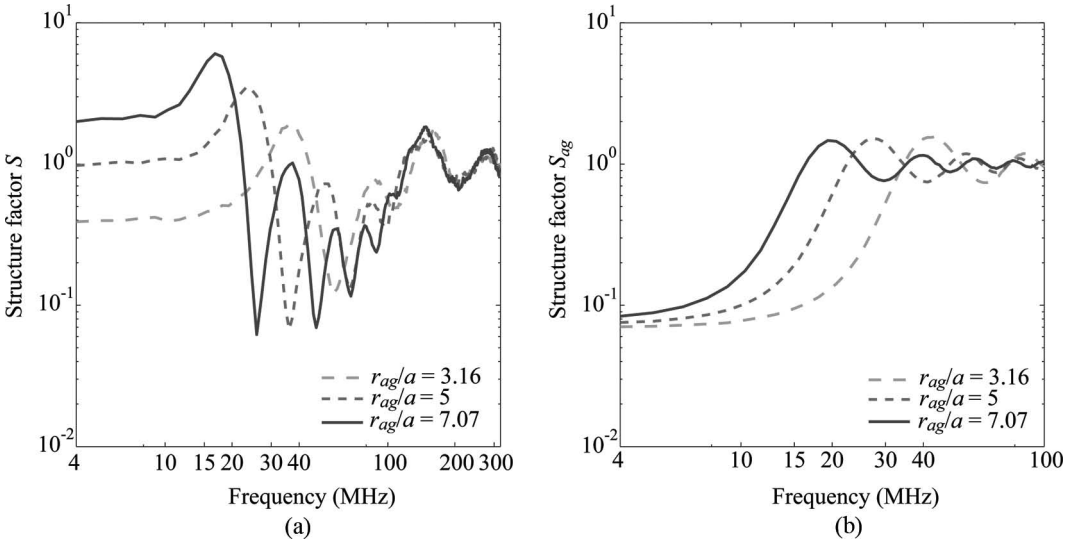

Fig. 9. (a) Structure factors S versus frequency used in the computation of the structure factor model (SFM) for a fixed systemic hematocrit $\phi = 30\%$, a fixed internal hematocrit $\phi_i = 60\%$, and three aggregate radii $r_{ag}/a = 3.16$, 5.0, and 7.07. (b) Structure factors S_{ag} versus frequency used in the computation of the effective medium theory combined with the SFM (EMTSFM) for the same aggregating conditions.

size on the BSC, the method we chose to distribute particles was limited to area fractions of aggregates $\phi_{ag} \leq 0.5$, area fraction of RBCs within aggregates $\phi_i \leq 0.6$, and systemic hematocrits $\phi \leq 0.3$. One might thus question the use of the EMTSFM for *in vivo* experiments with a physiological hematocrit ϕ typically varying between 0.3 and 0.5. It is important to recall that the only intensive computation with the proposed EMTSFM is the structure factor S_{ag}, which needs the computation of effective particle distributions. If one considers the application of the EMTSFM *in vivo*, 3-D effective particle distributions must be considered as well as the range of typical volume fractions. For example, the volume fraction of RBCs within aggregates ϕ_i may physiologically be larger than 60% because RBCs are deformable. By considering a systemic hematocrit of 40% (and 20%, respectively) and extrema values of ϕ_i between 60 and 90%, the volume fraction of aggregates ϕ_{ag} would then vary between 44 and 66% (between 22 and 33%). For future simulations, particle distributions in 3-D could be easily generated using a random number generator up to a volume fraction of approximatively 0.3, meaning that the method used to compute the BSC_{eq} in this paper may easily be applied in 3-D up to a volume fraction ϕ of 20%. For such low volume fractions of cells, one could envisage the use the EMTSFM for other biomedical applications such as cancer [4], [27], where the cells can be locally densely packed (see, for example, [4, Fig. 5]). In the case of blood applications, to deal with a physiological hematocrit of 40% and a maximum volume fraction of aggregates of 66%, one may envisage distributing particles in a random close packing configuration in which the attainable volume fraction could be up to 64% [28].

On the use of the EMTSFM *in vivo*, one can also question the practical value of that model assuming isotropic aggregates. In human blood, low shear rates can promote the formation of RBC aggregates having anisotropic (i.e., rouleaux) or isotropic (i.e., clump) structures. The rouleaux-like pattern is typically associated with normal blood. However, as the binding energy between RBCs increases with inflammation [29], aggregates form clump structures such as in diabetes mellitus [30], [31]. The assumption of isotropic aggregates in the EMTSFM is thus valid as far as we are concerned with the study of pathological states. In the case of normal human rouleaux of RBCs, if the EMTSFM is applied to estimate structural parameters such as the internal hematocrit and the aggregate size, this assumption would obviously create a bias against the parameter estimation.

Another important aspect to consider is the assumption of identical aggregates in the current EMTSFM implementation. Under *in vivo* conditions with ultrasound measurements on a blood vessel, the shear rate distribution varies with the radial position, and consequently, the aggregate size distribution does too. That is why the backscattered echoes from blood are generally analyzed over a rectangular or a Hamming window which is moved along the RF signal to examine the whole vessel at different depths [19], [32]. For example, at a central frequency of 25 MHz, the window length was typically around 400 μm [19], [32], [33]. RBC aggregates may thus be assumed to be locally identical. However, one may also expect that the aggregate size varies around a mean value for a given radial position within a blood vessel. An interesting simulation study was recently performed in 2-D by Vlad *et al.* [34]. According to this paper, the increase in particle size variance (or equivalently, in aggregate size variance) is expected to increase the BSC amplitude and not to significantly affect the frequency position of the BSC first peak [34, Fig. 2]. One could thus predict the bias against the parameter estimation with the EMTSFM if there is a variance in aggregate sizes. The discussion next considers small and large aggregates with respect to the observation of Vlad *et al.* [34].

In the case of small aggregates, the BSC first peak occurs at high frequencies and is thus generally not captured in the measured frequency bandwidth of the transducer (typically from 12 to 38 MHz for a 100% bandwidth at 25 MHz). Readers may refer to [18, Fig. 4(b)] and to [19, Fig. 3] to see measured BSCs from aggregating porcine RBCs in a controlled Couette flow. Because of the predicted increase in BSC amplitude with the increase in particle size variance [34], the assumption of identical aggregates in the current study may result in overestimations of the aggregate size and of the internal hematocrit. On the other hand, in the case of large aggregates, the BSC first peak occurs at low frequencies and would likely be within the measured frequency bandwidth of the transducer. In this case, the assumption of identical aggregates may not greatly affect the aggregate size estimation but may result in an overestimation of the internal hematocrit. The EMTSFM is thus expected to better estimate the size of large aggregates and the estimation of the internal hematocrit may be overestimated in the case of polydisperse aggregates, whatever their dimensions.

VI. Conclusion

The SFM is recognized to be a good model to simulate the BSC from aggregated RBCs. However, it cannot directly be applied to estimate the structural aggregate parameters in the framework of an inverse problem formulation. The EMTSFM was thus proposed to approximate the SFM and the goodness of fit of the EMTSFM in comparison with the SFM was examined. Contrary to the SFM, the EMTSFM can be implemented to estimate structural aggregate parameters.

The EMTSFM parameterizes the BSC by three indices: the aggregate size, the internal hematocrit (or aggregate compactness), and the systemic hematocrit. In comparison with the SFM, the EMTSFM provided accurate quantitative estimates of the BSC for $kr_{ag} \leq 1.32$ for the studied conditions. Moreover, even if $kr_{ag} > 1.32$, the EMTSFM provided a good approximation of the BSC: indeed, the BSC amplitude was well approximated in the frequency bandwidth between 4 MHz and the frequency position of the first peak, and the high-frequency positions of peaks were well identified.

Another important finding was the variation of the SS with ϕ_i and r_{ag}. The SSs for both $\mathrm{BSC}_{\mathrm{SFM}}$ and $\mathrm{BSC}_{\mathrm{eq}}$ computed with the SFM and EMTSFM followed the same trends of variations with ϕ_i and r_{ag}. We found that the SS decreased as the internal hematocrit increased for all studied systemic hematocrits. On the other hand, the behavior of the SS as a function of the aggregate size depended on the systemic hematocrit. For the largest hematocrits (20 and 30%), the SS increased as the aggregate size increased. Consequently, the SS cannot be a useful index for blood characterization of RBC aggregation.

To conclude, the EMTSFM approximates the SFM satisfactorily for a product $kr_{\mathrm{ag}} \leq 1.32$. This suggests that the EMTSFM is an adequate model for blood characterization. An important contribution of this new model is the parameterization of the BSC with the aggregate compactness, which is a structural parameter not available in any other modeling strategies proposed in quantitative ultrasound imaging. In the future, it would be interesting to study two other important factors: the polydispersity in terms of aggregate sizes and internal hematocrits, and the non-sphericity of the aggregates. Another important study would be the estimation of structural aggregate parameters with the EMTSFM that could be compared with existing methods such as the SFSE [16], [18], [19] and the traditional Gaussian model developed by Lizzi [6], [25].

Appendix

The form factor is generally given in 3-D [21], [22]. That is why the demonstration to obtain the 2-D form factor of a fluid infinite cylinder of radius a is given here. In the Born approximation (i.e., for weak scattering conditions), the form factor has a simple expression that is related to the spatial Fourier spectrum of the impedance contrast (see [21, Eq. (5)] for the form factor expression in 3-D):

$$F(-2k,a) = \frac{1}{A_p^2\gamma_z^2}\left|\int_{A_p}\gamma_z(\mathbf{r})e^{2i\mathbf{kr}}\mathrm{d}^2\mathbf{r}\right|^2. \tag{12}$$

We can introduce cylindrical coordinates to obtain

$$\begin{aligned} F(-2k,a) &= \frac{1}{A_p^2\gamma_z^2}\left|\int_0^a\int_{-\pi}^{\pi}\gamma_z e^{2ikr\cos(\theta)}r\mathrm{d}r\mathrm{d}\theta\right|^2 \\ &= \frac{1}{A_p^2}\left|\int_0^a 2\pi r J_0(2kr)\mathrm{d}r\right|^2 \\ &= \frac{(2\pi)^2}{(\pi a^2)^2}\left(\frac{2kaJ_1(2ka)}{(2k)^2}\right)^2 \\ &= \left(\frac{J_1(2ka)}{ka}\right)^2, \end{aligned} \tag{13}$$

where J_0 is the Bessel function of the first kind of order 0.

Acknowledgments

The authors thank Prof. R. E. Challis for his helpful discussion on the effective medium approach.

References

[1] E. J. Feleppa, F. L. Lizzi, D. J. Coleman, and M. M. Yaremko, "Diagnostic spectrum analysis in ophthalmology: A physical perspective," *Ultrasound Med. Biol.*, vol. 12, no. 8, pp. 623–631, 1986.

[2] E. J. Feleppa, T. Liu, A. Kalisz, M. C. Shao, N. Fleshner, and V. Reuter, "Ultrasonic spectral-parameter imaging of the prostate," *Int. J. Imaging Syst. Technol.*, vol. 8, no. 1, pp. 11–25, 1997.

[3] M. C. Kolios, G. J. Czarnota, M. Lee, J. W. Hunt, and M. D. Sherar, "Ultrasonic spectral parameter characterization of apoptosis," *Ultrasound Med. Biol.*, vol. 28, no. 5, pp. 589–597, 2002.

[4] M. L. Oelze and J. F. Zachary, "Examination of cancer in mouse models using high frequency quantitative ultrasound," *Ultrasound Med. Biol.*, vol. 32, no. 11, pp. 1639–1648, 2006.

[5] L. Y. L. Mo and R. S. C. Cobbold, "Theoretical models of ultrasonic scattering in blood," in *Ultrasonic Scattering in Biological Tissues*, K. K. Shung and G. A. Thieme, Eds., Boca Raton, FL: CRC, 1993, ch. 5, pp. 125–170.

[6] H. Kitamura, B. Sigel, J. Machi, E. J. Feleppa, J. Sokil-Melgar, and J. Justin, "Roles of hematocrit and fibrinogen in red cell aggregation determined by ultrasonic scattering properties," *Ultrasound Med. Biol.*, vol. 21, no. 6, pp. 827–832, 1995.

[7] R. B. Ami, G. Barshtein, D. Zeltser, Y. Goldberg, I. Shapira, A. Roth, G. Keren, H. Miller, V. Prochorov, A. Eldor, S. Berliner, and S. Yedgar, "Parameters of red blood cell aggregation as correlates of the inflammatory state," *Am. J. Physiol. Heart Circ. Physiol.*, vol. 280, no. 5, pp. H1982–H1988, 2001.

[8] L. Y. L. Mo and R. S. C. Cobbold, "A stochastic model of the backscattered Doppler ultrasound from blood," *IEEE Trans. Biomed. Eng.*, vol. 33, no. 1, pp. 20–27, 1986.

[9] V. Twersky, "Low-frequency scattering by correlated distributions of randomly oriented particles," *J. Acoust. Soc. Am.*, vol. 81, no. 5, pp. 1609–1618, 1987.

[10] L. Y. L. Mo and R. S. C. Cobbold, "A unified approach to modeling the backscattered Doppler ultrasound from blood," *IEEE Trans. Biomed. Eng.*, vol. 39, no. 5, pp. 450–461, 1992.

[11] K. K. Shung, "On the ultrasound scattering from blood as a function of hematocrit," *IEEE Trans. Sonics Ultrason.*, vol. SU-29, no. 6, pp. 327–331, 1982.

[12] D. Savéry and G. Cloutier, "A point process approach to assess the frequency dependence of ultrasound backscattering by aggregating red blood cells," *J. Acoust. Soc. Am.*, vol. 110, no. 6, pp. 3252–3262, 2001.

[13] I. Fontaine, D. Savery, and G. Cloutier, "Simulation of ultrasound backscattering by red blood cell aggregates: Effect of shear rate and anisotropy," *Biophys. J.*, vol. 82, no. 4, pp. 1696–1710, 2002.

[14] I. Fontaine, M. Bertrand, and G. Cloutier, "A system-based approach to modeling the ultrasound signal backscattered by red blood cells," *Biophys. J.*, vol. 77, no. 5, pp. 2387–2399, 1999.

[15] D. Savéry and G. Cloutier, "Effect of red cell clustering and anisotropy on ultrasound blood backscatter: A Monte Carlo study," *IEEE Trans. Ultrason. Ferroelectr. Freq. Control*, vol. 52, no. 1, pp. 94–103, 2005.

[16] R. K. Saha, E. Franceschini, and G. Cloutier, "Assessment of accuracy of the structure-factor-size-estimator method in determining red blood cell aggregate size from ultrasound spectrum backscattering coefficient," *J. Acoust. Soc. Am.*, vol. 129, no. 4, pp. 2269–2277, 2011.

[17] I. Fontaine and G. Cloutier, "Modeling the frequency dependence (5–120 MHz) of ultrasound backscattering by red cell aggregates in shear flow at a normal hematocrit," *J. Acoust. Soc. Am.*, vol. 113, no. 5, pp. 2893–2900, 2003.

[18] F. T. H. Yu and G. Cloutier, "Experimental ultrasound characterization of red blood cell aggregation using the structure factor size estimator," *J. Acoust. Soc. Am.*, vol. 122, no. 1, pp. 645–656, 2007.

[19] F. T. H. Yu, E. Franceschini, B. Chayer, J. K. Armstrong, H. J. Meiselman, and G. Cloutier, "Ultrasonic parametric imaging of erythrocyte aggregation using the structure factor size estimator," *Biorheology*, vol. 46, no. 4, pp. 343–363, 2009.

[20] G. T. Kuster and M. N. Toksoz, "Velocity and attenuation of seismic waves in two-phase media: Part I. Theoretical formulations," *Geophysics*, vol. 39, no. 5, pp. 587–606, 1974.

[21] D. Savery and G. Cloutier, "High-frequency ultrasound backscattering by blood: Analytical and semi-analytical models of the erythrocyte cross section," *J. Acoust. Soc. Am.*, vol. 23, no. 4, pp. 3963–3971, 2007.

[22] M. F. Insana and D. G. Brown, "Acoustic scattering theory applied to soft biological tissues," in *Ultrasonic Scattering in Biological Tissues*, K. K. Shung and G. A. Thieme, Eds., Boca Raton, FL: CRC, 1993, ch. 4, pp. 76–124.
[23] R. D. Doolittle and H. Uberall, "Sound scattering by elastic cylindrical shells," *J. Acoust. Soc. Am.*, vol. 39, no. 2, pp. 272–275, 1965.
[24] V. P. Dick and A. P. Ivanov, "Extinction of light in dispersive media with high particle concentrations: Applicability limits of the interference approximation," *J. Opt. Soc. Am.*, vol. 16, no. 5, pp. 1034–1039, 1999.
[25] F. L. Lizzi, M. Ostromogilsky, E. J. Feleppa, M. C. Rorke, and M. M. Yaremko, "Relationship of ultrasonic spectral parameters to features of tissue microstructure," *IEEE Trans. Ultrason. Ferroelectr. Freq. Control*, vol. 34, no. 3, pp. 319–329, 1987.
[26] B. Lim and R. S. C. Cobbold, "On the relation between aggregation, packing and the backscattered ultrasound signal for whole blood," *Ultrasound Med. Biol.*, vol. 25, no. 9, pp. 1395–1405, 1999.
[27] T. E. Doyle, A. T. Tew, K. H. Warnick, and B. L. Carruth, "Simulation of elastic wave scattering in cells and tissues at the microscopic level," *J. Acoust. Soc. Am.*, vol. 125, no. 3, pp. 1751–1767, 2009.
[28] W. S. Jodrey and E. M. Tory, "Computer simulation of close random packing of equal spheres," *Phys. Rev. A*, vol. 32, no. 4, pp. 2347–2351, 1985.
[29] X. Weng, G. Cloutier, R. Beaulieu, and G. O. Roederer, "Influence of acute-phase proteins on erythrocyte aggregation," *Am. J. Physiol.*, vol. 271, no. 6, pp. H2346–H2352, 1996.
[30] H. Schmid-Schönbein, H. Malotta, and F. Striesow, "Erythrocyte aggregation: Causes, consequences and methods of assessment," *Ned. Tijdschr. Klin. Chem.*, vol. 15, pp. 88–97, 1990.
[31] H. Schmid-Schönbein, G. Gallasch, J. V. Gosen, E. Volger, and H. J. Klose, "Red cell aggregation in blood flow. I. New methods of quantification," *Klin. Wochenschr.*, vol. 54, no. 4, pp. 149–157, 1976.
[32] F. T. H. Yu, J. K. Armstrong, J. Tripette, H. J. Meiselman, and G. Cloutier, "A local increase in red blood cell aggregation can trigger deep vein thrombosis: Evidence based on quantitative cellular ultrasound imaging," *J. Thromb. Haemost.*, vol. 9, no. 3, pp. 481–488, 2011.
[33] E. Franceschini, F. T. H. Yu, F. Destrempes, and G. Cloutier, "Ultrasound characterization of red blood cell aggregation with intervening attenuating tissue-mimicking phantoms using the structure factor size and attenuation estimator," *J. Acoust. Soc. Am.*, vol. 127, pp. 1104–1115, 2010.
[34] R. M. Vlad, R. K. Saha, N. M. Alajez, S. Ranieari, G. J. Czarnota, and M. C. Kolios, "An increase in cellular size variance contributes to the increase in ultrasound backscatter during cell death," *Ultrasound Med. Biol.*, vol. 36, no. 9, pp. 1546–1558, 2010.

Emilie Franceschini received her M.S. degree in mechanical engineering from the Ecole Supérieure d'Ingénieurs de Marseille in 2003, and her Ph.D. degree in acoustics from the University of Provence, Marseille, 2006. In 2007, she was a Postdoctoral Fellow at the Laboratory of Biorheology and Medical Ultrasonics, Research Center of the University of Montreal Hospital, Montreal, QC. Since October 2008, she has been a Researcher at the French National Centre for Scientific Research (CNRS) in the Laboratory of Mechanics and Acoustics CNRS–UPR 7051, Marseille. Her current research interests include ultrasound imaging for biomedical applications, inverse problems, and ultrasound characterization of biological tissues at the microscopic level. She is a member of the French Acoustical Society (SFA) and IEEE.

Bloen Metzger received his M. S. degree from the Ecole Normale Supérieure de Lyon in 2003, and his Ph.D. degree in physics from the University of Provence, Marseille in 2006. In 2007, he was a Postdoctoral Fellow at the Benjamin Levich Institute, New York, NY. Since October 2007, he has been a Researcher at the French National Centre for Scientific Research (CNRS) in the laboratory IUSTI CNRS–UMR 6595, Marseille. His current research interests include microhydrodynamics, suspension flows at low Reynolds numbers, hydrodynamic diffusion, and heat and mass transfers in sheared suspensions.

Guy Cloutier (S'89–M'90–SM'07) obtained his B.Eng. degree in electrical engineering in 1984, and his M.Sc. and Ph.D. degrees in biomedical engineering in 1986 and 1990, respectively. Between 1990 and 1992, he was a post-doctoral fellow at The Pennsylvania State University with Prof. K. Kirk Shung. Prof. Cloutier is Director of the Laboratory of Biorheology and Medical Ultrasonics at the University of Montreal Hospital Research Center (http://www.lbum-crchum.com), and Professor of Radiology and Biomedical Engineering at the University of Montreal. His research interests are in quantitative ultrasound imaging of red blood cell aggregation; quasi-static and dynamic ultrasound elastography of atherosclerotic plaques, vascular aneurysms, deep vein thrombi, and breast cancers; 3-D morphologic and hemodynamic assessment of lower limb arterial stenoses; and mathematical and biomechanical modeling. He has published more than 120 peer-reviewed articles in these fields, holds 8 patents, and was recipient of the National Scientist award of the Fonds de Recherche en Santé du Québec (2004–2009).

Comparison of Three Scattering Models for Ultrasound Blood Characterization

Emilie Franceschini, *Member, IEEE*, Ratan K. Saha, and Guy Cloutier, *Senior Member, IEEE*

***Abstract*—Ultrasonic backscattered signals from blood contain frequency-dependent information that can be used to obtain quantitative parameters reflecting the aggregation level of red blood cells (RBCs). The approach is based on estimating structural aggregate parameters by fitting the spectrum of the backscattered radio-frequency echoes from blood to an estimated spectrum considering a theoretical scattering model. In this study, three scattering models were examined: a new implementation of the Gaussian model (GM), the structure factor size estimator (SFSE), and the new effective medium theory combined with the structure factor model (EMTSFM). The accuracy of the three scattering models in determining mean aggregate size and compactness was compared by 2-D and 3-D computer simulations in which RBC structural parameters were controlled. Two clustering conditions were studied: 1) the aggregate size varied and the aggregate compactness was fixed in both 2-D and 3-D cases, and 2) the aggregate size was fixed and the aggregate compactness varied in the 2-D case. For both clustering conditions, the EMTSFM was found to be more suitable than GM and SFSE for characterizing RBC aggregation.**

I. Introduction

Quantitative ultrasound (US) techniques are mainly based on the frequency analysis of backscattered signals by biological tissues to determine physical properties of the average tissue microstructure. These techniques rely on theoretical scattering models to fit the spectrum of backscattered echoes to an estimated spectrum using an appropriate model. The theoretical scattering model most frequently used for this purpose is the Gaussian model (GM) [1], [2], which yields two tissue properties: the average scatterer size and the acoustic concentration (i.e., the product of the scatterer number density by the square of the relative impedance difference between scatterers and the surrounding medium). This approach has been used to characterize dilute scattering media such as the eye [3], prostate [4], and breast [5]. Blood has also been studied with this technique [6], although estimations could be biased.

Manuscript received May 22, 2013; accepted August 7, 2013. This work was supported by the Fonds Incitatifs Recherche of the Université de Provence and by an operating grant from the Canadian Institutes of Health Research (grant number MOP-84358).

E. Franceschini is with the Laboratoire de Mécanique et d'Acoustique (LMA), CNRS UPR 7051, Aix-Marseille University, Marseille, France (e-mail: franceschini@lma.cnrs-mrs.fr).

R. K. Saha is with the Saha Institute of Nuclear Physics, Applied Material Science Division, Bidhannagar, Kolkata, India.

G. Cloutier is with the Laboratory of Biorheology and Medical Ultrasonics, University of Montreal Hospital Research Centre (CRCHUM), Montreal, QC, Canada, and with the Department of Radiology, Radio-Oncology and Nuclear Medicine, and Institute of Biomedical Engineering, University of Montreal, Montreal, QC, Canada (e-mail: guy.cloutier@umontreal.ca).

DOI http://dx.doi.org/10.1109/TUFFC.2013.2829

An important contribution of ultrasonic blood characterization is to assess the level of red blood cell (RBC) aggregation, which is a surrogate marker of inflammation [7]. It is well known that when RBCs are under low shear rates ($<10\ s^{-1}$), they interact strongly with each other and form complex rouleaux or 3-D structures. When the shear rate increases, these rouleaux or compact structures disaggregate. This aggregation phenomenon is normal in human blood, however hyperaggregation is a pathological state associated with several circulatory diseases, such as deep venous thrombosis, atherosclerosis, and diabetes mellitus. Blood characterization using US backscatter techniques provides a unique opportunity to monitor RBC aggregation noninvasively and *in vivo* within blood vessels. This quantification may help to elucidate the role of RBC aggregation in the etiology of such diseases.

US backscatter by blood is mainly due to RBCs that constitute the vast majority (97%) of the blood cellular content. Blood can thus be described as a biphasic fluid composed of RBCs immersed in plasma. Because RBCs are acoustically considered as weak scatterers (impedance contrast between RBCs and plasma being around 13%), multiple scattering can be neglected. However, for such tissue, it is not straightforward to develop a theoretical scattering model because of the high density of RBCs (their volume fraction or hematocrit varies between 30% and 50%) and their ability to form aggregates. The structure factor model (SFM) [8], [9] is a US scattering model proposed to simulate the backscatter coefficient (BSC) of aggregated RBCs. The SFM sums the acoustic contributions from individual RBCs and models their interaction by a statistical mechanics structure factor, which is by definition the Fourier transform of the spatial distribution of RBCs [8], [9]. However, the SFM can hardly be implemented to estimate the structural aggregate parameters in the framework of an inverse problem formulation because of the intensive computational time required to assess the structure factor with distributions of aggregating RBCs. That is why Yu and Cloutier [10] developed the structure factor size estimator (SFSE) scattering theory, which approximates the SFM by using a second-order Taylor expansion of the structure factor. The SFSE is thus not as accurate as the SFM. The SFSE estimates two physical parameters describing the microstructure of RBC aggregates: the packing factor, which increases with erythrocyte clustering, and the average aggregate isotropic radius. However, experiments with pig blood in controlled flow devices [10] and 3-D numerical simulations of isotropic monodisperse aggregates [11] recently showed that the two indices are correlated and follow a quadratic

relationship, thus reducing the BSC parameterization to one structural index.

A scattering model called the effective medium theory combined with the SFM (EMTSFM) was recently proposed to better approximate the SFM [12]. It assumes that aggregates of RBCs can be treated as individual homogeneous scatterers which have effective properties determined by the acoustical characteristics and concentration of RBCs within aggregates. The EMTSFM allows characterization of the radius, and for the first time in the quantitative US field, the compactness of RBC aggregates [12]. In the field of clinical hemorheology [13], assessing the compactness of RBC aggregates is of high clinical importance because it is related to the binding energy between cells. Normal RBC aggregates form rouleaux-type structures, whereas pathologies associated with stronger binding energies result in clumps of RBCs (close to a spherical isotropic packing) [14], [15].

In our previous study [12], the EMTSFM and the SFM were compared in the framework of a forward-problem study to determine the BSC from a known distribution of RBCs with known acoustical parameters. The goodness of the approximation of the EMTSFM in comparison with the SFM was examined as a function of frequency and structural aggregate parameters (aggregate size and compactness). Based on a 2-D simulation study, the EMTSFM was found to approximate the SFM with relative errors less than 30% for a product of the wavenumber times the mean aggregate radius $kr_{\mathrm{ag}} \leq 1.32$ [12]. The goals of the present paper are:

- to evaluate the EMTSFM in an inverse-problem framework, i.e., to determine RBC structural features from the measured BSC, and
- to compare the EMTSFM with two other scattering models: the SFSE and a new implementation of the GM slightly modified to treat aggregating scatterers.

To our knowledge, there is no means to experimentally assess aggregate sizes at a normal physiological hematocrit of 40% because RBCs at that hematocrit are opaque to light. It would thus not be feasible to quantitatively evaluate the performance of the different models with real experimental data. In the field of blood imaging and characterization, the assessment of accuracy of a scattering model was only performed at a low hematocrit of 6% by comparing optical and acoustic measurements of RBC aggregate sizes [10]. In the current paper, we thus aim to determine the performance of three theoretical scattering models (the new implementation of the GM, the SFSE, and the EMTSFM) to extract the aggregation parameters from computer simulations where RBC structural parameters (such as the hematocrit, the aggregate size, and compactness) are known.

The important contribution of the EMTSFM is the parameterization of the BSC with the aggregate compactness [12], which is a structural parameter not available in any other modeling strategies proposed in quantitative US. The potential of the EMTSFM and of the two other scattering models in estimating the aggregate compactness was examined by 2-D computer simulations based on the SFM in controlled clustering configurations (when the aggregate compactness varies and the aggregate radius is fixed). This clustering condition was only conducted in 2-D because of the computational load required to generate 3-D RBC distributions with various aggregate compactnesses with the SFM [12]. Some 3-D computer simulations were also used in the same controlled clustering configurations as those used in 2-D (when the aggregate size varies and the aggregate compactness is fixed) to compare the BSC behavior between 2-D and 3-D simulations, and estimated structural aggregate parameters with the three scattering models.

II. Computer Simulations Based on the Structure Factor Model (SFM)

This section presents computer simulations performed to predict the frequency dependence of the BSC from aggregated RBCs based on the SFM. In the following, it is assumed that the incident wavelength λ is large compared with the RBC size. Consequently, the RBC shape could be approximated by a simple geometry having an equivalent surface in 2-D or having an equivalent volume of a RBC in 3-D [16]. RBCs were modeled as parallel infinite cylinders in the 2-D case and as spheres in the 3-D case of radius a, that have small contrast in acoustical properties relatively to the plasma (see Table I). This RBC shape approximation has some limitations for larger frequencies (>20 MHz) and will be discussed later in Section V-C.

The SFM describing US backscatter by biological tissues consists of summing contributions from cells and modeling the cellular interaction by a statistical mechanics structure factor [8], [9]. By considering a collection of N identical and weak scattering RBCs, the BSC expression can be written as

$$\mathrm{BSC}_{\mathrm{SFM}}(-2k) = m\sigma_{\mathrm{b}}(-2k)S(-2k), \tag{1}$$

where k is the wavenumber and m is the number density of RBCs, which is related to the systemic hematocrit ϕ as $m = \phi/A_{\mathrm{p}}$ (where A_{p} is the RBC area) for 2-D modeling, or as $m = \phi/V_{\mathrm{p}}$ (where V_{p} is the RBC volume) for 3-D modeling. The backscattering cross section σ_{b} of a single weak RBC was calculated using the fluid infinite cylinder expression in the 2-D case [12] or using the fluid-filled sphere expression in the 3-D case [17], [18], given by

TABLE I. Acoustical Properties of Blood Found in [16] and [21].

	Density ρ (kg·m^{-3})	Compressibility κ (Pa^{-1})	Impedance Z (MRayl)
RBC	1092	3.41×10^{-10}	1.766
Plasma	1021	4.09×10^{-10}	1.580

$$\sigma_{\mathrm{b}}(-2k) = \frac{k^3 A_{\mathrm{p}}^2 \gamma_z^2}{2\pi}\left(\frac{J_1(2ka)}{ka}\right)^2 \text{ in the 2-D case}$$
$$= \frac{k^4 V_{\mathrm{p}}^2 \gamma_z^2}{4\pi^2} \times \left(3\frac{\sin(2ka) - 2ka\cos(2ka)}{(2ka)^3}\right)^2 \text{ in the 3-D case,} \quad (2)$$

where J_1 is the first-order Bessel function of the first kind and γ_z is the relative impedance difference between the RBC and its suspending medium (i.e., the plasma). The function S is the structure factor representing the spatial positioning of RBCs, and is defined by

$$S(-2k) = E\left[\frac{1}{N}\left|\sum_{i=1}^{N} e^{-i2\boldsymbol{k}\boldsymbol{r}_i}\right|^2\right], \quad (3)$$

where E represents the expected value of a random variable and $\boldsymbol{r}_i$ is the position vector defining the center of the ith RBC in space. In general, the structure factor of a medium containing RBCs distributed in a 2-D space (or in the 3-D space) can be determined from the 2-D Fourier transform (or 3-D Fourier transform) of the spatial distribution of particles (see [19, Appendix]).

The computation of the $\mathrm{BSC_{SFM}}$ using the SFM requires an intensive computation because of the calculation of the structure factor S as described in (1). Because the structure factor is by definition a statistical quantity, an average of structure factors from several RBC spatial distributions can give an estimated value of S. Because of the computational load to generate aggregating RBC distributions, a simple and fast method was used to randomly generate non-overlapping RBC aggregates which were isotropic and similar in size. For the 2-D and 3-D computer simulations, the simulated $\mathrm{BSC_{SFM}}$ were obtained from the method described in [12, Section III] and [11, Section III], respectively. Note that 2-D simulations are computationally less intensive but significant insights can be gained by studying 2-D systems. On the other hand, 3-D simulations are intuitively appealing because they better mimic experimental situations, but are computationally important. These methods are briefly summarized in the following.

Random distributions for aggregating RBCs were computed within the simulated surface area of 600×600 $\mu\mathrm{m}^2$ in the 2-D case and within the simulated volume of $1000 \times 125 \times 125$ $\mu\mathrm{m}^3$ in the 3-D case. The RBC radius a was set to 2.75 μm for all simulations. We first specified the systemic hematocrit ϕ, the aggregate radius r_{ag}, and the aggregate compactness ϕ_i (i.e., the RBC concentration within aggregates). Aggregates of identical radii r_{ag} and of identical compactness ϕ_i were then randomly distributed with non-overlapping positions to give the desired concentration of aggregates $\phi_{\mathrm{ag}} = \phi/\phi_i$. Note that in the case of the 3-D study, a small number of non-aggregated RBCs was added to reach the desired systemic hematocrit. This means that all RBCs were aggregated in blood in the 2-D case, whereas in the 3-D case, a fraction of RBCs were aggregated and the rest remained disaggregated. Finally, RBC distributions within aggregates were generated as follows:

- in the 2-D case, the locations of the RBCs were generated using external and repulsive forces to obtain random RBC positions inside each aggregate, such that the distribution of RBCs within each aggregate was different [12]. This technique allowed several aggregation configurations to be studied: 1) the aggregate size varied and the aggregate compactness was fixed to 0.6, and 2) the aggregate compactness varied from 0.3 to 0.6 and the aggregate size was fixed.
- in the 3-D case, the RBCs were stacked by following a hexagonal close packing (HCP) structure for each aggregate, such that the distribution of RBCs within each aggregate was identical. This HCP structure provides the highest compactness, at about 0.74 for spheres [11]. Therefore, this technique allowed several aggregation configurations to be studied in which the aggregate size varied and the aggregate compactness was fixed at 0.74.

For each distribution of RBCs, the 2-D or 3-D Fourier transformation of the spatial organization of RBCs was then computed to obtain the corresponding structure factor. A mean structure factor was determined from 400 different tissue realizations in the 2-D case (see [12, Section III-B]) and from 250 different tissue realizations in the 3-D case (see [11, Section III-B]).

III. Ultrasound Backscattering Modeling for the Estimation of Structural Aggregate Parameters

As seen in Section II, the SFM allows simulation of the BSC from RBCs whatever the RBC spatial distribution (i.e., disaggregated or aggregated RBCs and/or with various aggregate sizes and compactnesses). However, the SFM can hardly be implemented to estimate structural parameters in the framework of an inverse problem formulation because of the intensive computational time to assess the structure factor by realizing distributions of RBCs with simulations. That is why two scattering theories, named the SFSE and the EMTSFM, have recently been developed to approximate the SFM for practical assessments of RBC structural features (i.e., in an inverse problem formulation). This section presents these two scattering theories (the SFSE and the EMTSFM) as well as the GM also used for tissue characterization. In this work, we present a new implementation of the GM model inspired by our development on EMTSFM. All three theories fit a curve to the simulated $\mathrm{BSC_{SFM}}$ from blood to estimate aggregation parameters using the minimization routine fminsearch in Matlab (The MathWorks Inc., Natick, MA); i.e., a Nelder–Mead simplex method. Note that this fit was realized in

$$\sigma_{\mathrm{ag}}(-2k) = \frac{k^3\pi r_{\mathrm{ag}}^4\gamma_{z_{\mathrm{ag}}}^2}{2}\left(\frac{J_1(2kr_{\mathrm{ag}})}{kr_{\mathrm{ag}}}\right)^2 \text{ in the 2-D case}$$
$$= \frac{4k^4 r_{\mathrm{ag}}^6\gamma_{z_{\mathrm{ag}}}^2}{9}\left(3\frac{\sin(2kr_{\mathrm{ag}}) - 2kr_{\mathrm{ag}}\cos(2kr_{\mathrm{ag}})}{(2kr_{\mathrm{ag}})^3}\right)^2 \text{ in the 3-D case} \quad (8)$$

the frequency bandwidth from 4 MHz to the frequency corresponding to the first minimum of the $\mathrm{BSC_{SFM}}$ (i.e., after the frequency-dependent increase in BSC followed by a peak and a reduction to its first minimum).

A. The Structure Factor Size Estimator (SFSE)

The SFSE developed by Yu and Cloutier [10] approximates the SFM with a second-order Taylor expansion of the structure factor in k as follows:

$$S(-2k) \approx W - 4(kR_{\mathrm{g}}a)^2 \text{ in the 2-D case}$$
$$\approx W - 4(kR_{\mathrm{g}}a)^2 \approx W - \frac{12}{5}(kR_{\mathrm{sp}}a)^2 \text{ in the 3-D case,} \quad (4)$$

where W is the low-frequency limit of the structure factor ($S(k)|_{k\to 0}$), called the packing factor [20], [21], and R_{g} is the radius of gyration of RBC aggregates, assumed to be isotropic and expressed in number of RBCs [10]. Note that in the 3-D case, R_{g} is related to the isotropic radius R_{sp} of an aggregate (expressed in number of RBCs) by $R_{\mathrm{g}} = \sqrt{3/5}R_{\mathrm{sp}}$ [11], [22]. By assuming identical RBCs, and recombining (1) and (4), the SFSE model approximates the BSC as

$$\mathrm{BSC_{SFSE}}(-2k) = \frac{1}{2\pi}mk^3A_{\mathrm{p}}^2\gamma_z^2\left(\frac{J_1(2ka)}{ka}\right)^2$$
$$\times\left(W - 4(kR_{\mathrm{g}}a)^2\right) \text{ in the 2-D case}$$
$$= \frac{1}{4\pi^2}mk^4V_{\mathrm{p}}^2\gamma_z^2\left(3\frac{\sin(2ka) - 2ka\cos(2ka)}{(2ka)^3}\right)^2$$
$$\times\left(W - \frac{12}{5}(kR_{\mathrm{sp}}a)^2\right) \text{ in the 3-D case.} \quad (5)$$

The SFSE assumes that the hematocrit ϕ, the RBC radius a, and the acoustical properties of plasma and RBCs are known *a priori*. Therefore, (5) presents only two unknowns that characterize the aggregate structure: W and R_{g} (or equivalently, W and R_{sp} in the 3-D case). Estimated values of W^* and R_{g}^* (or equivalently, W^* and R_{sp}^* in the 3-D case) were determined by fitting the simulated $\mathrm{BSC_{SFM}}$ given by (1) with $\mathrm{BSC_{SFSE}}$ given by (5).

B. The Effective Medium Theory Combined With the Structure Factor Model (EMTSFM)

The EMTSFM assumes that all the scatterers are aggregated, that the aggregates are identical and isotropic, and that the scatterers within aggregates are evenly distributed [12]. In the case of blood backscatter, the model consists of treating the RBC aggregates as individual homogeneous particles of radius r_{ag}. These homogeneous particles are characterized by a density ρ_{ag} and a compressibility κ_{ag} derived from the acoustical properties of the two fluids constituting them (i.e., ρ_1, ρ_2, κ_1, and κ_2, where 1 indicates properties of RBCs and 2 indicates those of plasma), and from the internal concentration of RBCs within the aggregates, defined as the aggregate compactness ϕ_i, as follows:

$$\rho_{\mathrm{ag}} = \phi_i\rho_1 + (1-\phi_i)\rho_2$$
$$\frac{1}{\kappa_{\mathrm{ag}}} = \frac{\phi_i}{\kappa_1} + \frac{1-\phi_i}{\kappa_2}. \quad (6)$$

The BSC from blood is then obtained by summing contributions from individual effective particles of radius r_{ag} and modeling the effective particle interaction by a statistical mechanics structure factor S_{ag}. The equivalent BSC expression is thus given by [12]

$$\mathrm{BSC_{EMTSFM}}(-2k) = m_{\mathrm{ag}}\sigma_{\mathrm{ag}}(-2k)S_{\mathrm{ag}}(-2k), \quad (7)$$

where S_{ag} is the structure factor of a collection of N_{ag} randomly distributed identical particles of radius r_{ag} and m_{ag} is the number density of aggregates, which is related to the effective aggregate concentration ϕ_{ag}. The effective aggregate concentration is equal to the RBC concentration in blood ϕ divided by the aggregate compactness ϕ_i: $\phi_{\mathrm{ag}} = \phi/\phi_i$. The backscatter cross section of an effective single-particle σ_{ag} was calculated using the fluid infinite cylinder expression in the 2-D case [12] or using the fluid-filled sphere expression in the 3-D case [17], [18] given by (8), see above, where z_{ag} is the impedance of the equivalent particle and $\gamma_{z_{\mathrm{ag}}}$ is the relative impedance difference between the equivalent particle and the plasma ($\gamma_{z_{\mathrm{ag}}} = (z_{\mathrm{ag}} - z_2)/z_2$). For a random distribution of hard cylinders in 2-D, the structure factor was numerically computed as described in Appendix A. For a random distribution of hard spheres in 3-D, the structure factor can be analytically calculated as established by Wertheim [23]. The analytical expression for the structure factor in the 3-D case is described in Appendix B.

By assuming that the hematocrit ϕ, the RBC radius a, and the acoustical properties of plasma and RBCs are known *a priori*, the unknown parameters are the radius of aggregates r_{ag} and their compactness ϕ_i. The unknown

parameters were estimated by matching the simulated $\mathrm{BSC_{SFM}}$ given by (1) with the theoretical $\mathrm{BSC_{EMTSFM}}$ given by (7).

C. The Gaussian Model (GM)

Using the GM, the BSC is modeled with a spatial autocorrelation function describing the shape and distribution of scatterers in the medium. The scattering sites are assumed to be randomly distributed and of simple geometric shapes, represented as Gaussian scatterers mimicking continuous changes in impedance. In this framework, the BSC can be written as the product of the theoretical BSC under Rayleigh scattering and the backscatter form factor (see [18, Eqs. (74)–(76)] for the GM formulation in 3-D). The form factor describes the frequency dependence of BSC attributed to the size and shape of the prototype scatterer. The Gaussian form factor has been used for many applications [3]–[6]. It represents tissue structures as continuously varying distributions of acoustic impedance fluctuations about the mean value, and the effective radius is related to the impedance distribution of the scatterers.

The BSC for the GM formulation is written as the product of the BSC in the Rayleigh limit and the backscatter form factor as [18]

$$\begin{aligned}\mathrm{BSC_{GM}}(-2k) &= \frac{k^3 S_s^2 n_z}{2\pi} e^{-2k^2d^2} \\ &= \frac{\pi k^3 a_{\mathrm{eff}}^4 n_z}{2} e^{-k^2 a_{\mathrm{eff}}^2} \text{ in the 2-D case} \\ &= \frac{k^4 V_s^2 n_z}{4\pi^2} e^{-2k^2d^2} \\ &= \frac{4k^4 a_{\mathrm{eff}}^6 n_z}{9} e^{-0.827k^2 a_{\mathrm{eff}}^2} \text{ in the 3-D case,}\end{aligned} \tag{9}$$

where n_z is the acoustic concentration (i.e., the product of the number density of scatterers times the square of the relative impedance difference γ_z between scatterers and the surrounding tissue). In the 2-D case (or respectively in the 3-D case), the characteristic dimension d is related to the area of the effective scatterer S_s by $S_s = 2\pi d^2$ [or related to the volume of the effective scatterer V_s by $V_s = (2\pi d^2)^{3/2}$]. Continuous isotropic media can be characterized by the correlation distance d, in the same way that discrete isotropic media are characterized by a scatterer radius [18]. The effective radius of the scatterer a_{eff} is related to the correlation distance d by setting values of S_s (or V_s, respectively) for a continuum model equal to the area of an effective cylinder (or equal to the volume of an effective scatterer) of radius a_{eff}: $S_s = 2\pi d^2 = \pi a_{\mathrm{eff}}^2$ or $V_s = (2\pi d^2)^{3/2} = (4/3)\pi a_{\mathrm{eff}}^3$.

Estimates of the effective radius a_{eff}^* and acoustic concentration n_z^* were determined by fitting the simulated $\mathrm{BSC_{SFM}}$ given by (1) with the $\mathrm{BSC_{GM}}$ given by (9). Effective radii a_{eff} estimated with the GM have been hypothesized to be related to the aggregate radii, and the acoustic concentration n_z is postulated to be the product of the number density of aggregates times the square of the relative impedance difference between aggregates and the plasma as follows:

$$\begin{aligned}n_z &= \gamma_{z_{\mathrm{ag}}}^2 \frac{\phi_{\mathrm{ag}}}{\pi a_{\mathrm{eff}}^2} = \left(\frac{z_{\mathrm{ag}} - z_2}{z_2}\right)^2 \frac{\phi}{\phi_i \pi a_{\mathrm{eff}}^2}, \text{ in the 2-D case} \\ &= \gamma_{z_{\mathrm{ag}}}^2 \frac{3\phi_{\mathrm{ag}}}{4\pi a_{\mathrm{eff}}^3} = \left(\frac{z_{\mathrm{ag}} - z_2}{z_2}\right)^2 \frac{3\phi}{4\phi_i \pi a_{\mathrm{eff}}^3}, \text{ in the 3-D case,}\end{aligned} \tag{10}$$

where z_{ag} is the effective impedance of the aggregates approximated by the mixing law: $z_{\mathrm{ag}} = \phi_i z_1 + (1 + \phi_i) z_2$. Because the hematocrit ϕ and the acoustical properties of plasma and RBCs are assumed to be known *a priori*, the aggregate compactness can be deduced from the estimated parameters a_{eff}^* and n_z^* by using (10) as follows:

$$\begin{aligned}\phi_i^* &= \frac{\pi {a_{\mathrm{eff}}^*}^2 n_z^* z_2^2}{\phi(z_2 - z_1)^2} \text{ in the 2-D case} \\ &= \frac{4\pi {a_{\mathrm{eff}}^*}^3 n_z^* z_2^2}{3\phi(z_2 - z_1)^2} \text{ in the 3-D case.}\end{aligned} \tag{11}$$

This means that the new proposition of the GM was employed in our study as an effective medium model, but unlike the EMTSFM, the GM is not combined with the SFM (such that the GM is assumed to be accurate only at low systemic hematocrits). In the following, we thus give the estimated parameters a_{eff}^* and ϕ_i^* with the GM, instead of the classical estimated parameters a_{eff}^* and n_z^*.

IV. Results

This section gives the results of the inverse problem obtained for 2-D and 3-D computer simulations with the three aforementioned backscattering models: SFSE, EMTSFM, and GM.

A. Results Obtained From the 2-D Computer Simulations

For the 2-D computer simulations, we first studied clustering configurations in which the aggregate compactness was fixed to $\phi_i = 60\%$ and the aggregate radius r_{ag}/a varied, and then clustering configurations in which the aggregate radius was fixed to $r_{\mathrm{ag}}/a = 6.32$ and the aggregate compactness ϕ_i varied.

1) Results for the SFSE: The SFSE was first examined for systemic hematocrits of 10%, 20%, and 30% when the aggregate size varied and the aggregate compactness was fixed to a high value: $\phi_i = 60\%$. Fig. 1 shows $\mathrm{BSC_{SFM}}$ as a function of frequency for different aggregate sizes and systemic hematocrits. The symbols represent the $\mathrm{BSC_{SFM}}$ computation for the disaggregated case ($r_{\mathrm{ag}}/a = 1$) and for aggregation with radii $r_{\mathrm{ag}}/a = 3.16$, 5.0 and 7.07. Also represented by dashed lines in Fig. 1 are the corresponding $\mathrm{BSC_{SFSE}}$ fitted curves. The first peaks of the simulated

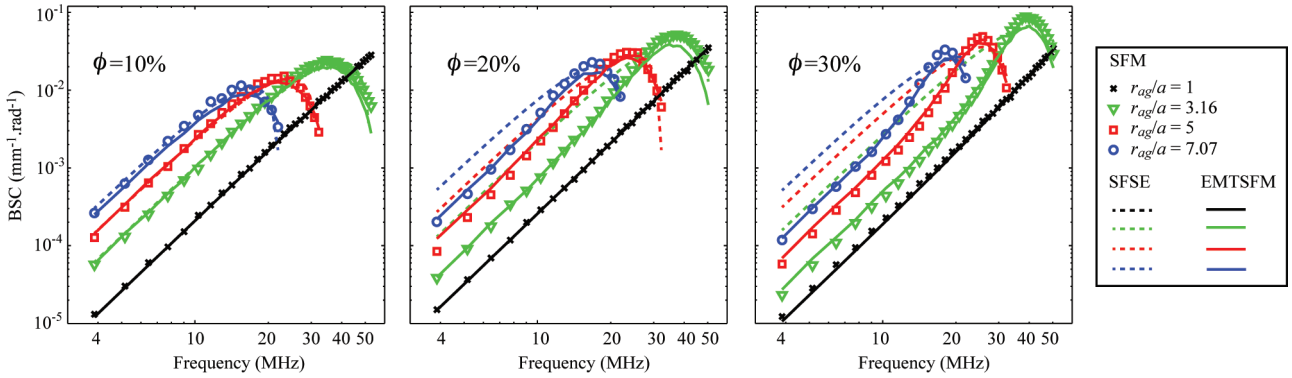

Fig. 1. Frequency-dependent backscatter coefficients (BSCs) for different aggregate sizes and a constant aggregate compactness $\phi_i = 60\%$ at systemic hematocrits of 10%, 20%, and 30%. The symbols represent the BSC_{SFM} computation. The dashed lines represents the corresponding fitting with the SFSE, whereas the solid lines expresses the fitting with the EMTSFM.

BSC_{SFM} occur at lower frequencies as the aggregate radius increases. Because the fitting curves with the SFSE were realized in the frequency bandwidth from 4 MHz to the frequency corresponding to the first minimum of the BSC_{SFM} (except for the disaggregated case, for which the frequency bandwidth is from 4 to 50 MHz), the bandwidth used for the fitting becomes smaller as the aggregate radius increases. It is clear from the figure that the SFSE provided better fits for the lower hematocrit of 10%. As the hematocrit increases, the SFSE model is insufficient to predict the behavior of BSC_{SFM}, especially in the low-frequency range. The estimated values of W^* and R_g^* are given in Table II for systemic hematocrits of 10%, 20%, and 30%. In this table, the relative error for parameter R_g^* corresponds to: $\varepsilon_{R_g^*} = (R_g^* - (r_{ag}/a))/(r_{ag}/a)$. Fig. 2(a) shows the estimated values of R_g^* as a function of the actual aggregate radii r_{ag}/a for all hematocrits. Also represented are the corresponding linear regression lines showing good correlation $r^2 \geq 0.95$ at all hematocrits. For radii r_{ag}/a between 4.47 and 7.95, relative errors $\varepsilon_{R_g^*}$ were less than 30% for hematocrits of 10% and 20%. It is interesting to notice that estimated parameters W^* and R_g^* follow a linear relation for all hematocrits [see Fig. 2(b)].

The SFSE was also evaluated at systemic hematocrits of 10% and 20% when the aggregate size r_{ag}/a was fixed at 6.32 and the aggregate compactness ϕ_i varied from 30% to 60%. It is important to emphasize that 2-D random particle distributions could be easily generated using a random number generator up to an area fraction of approximately 0.5. For the 20% systemic hematocrit, aggregate compactnesses smaller than 40% could not be computed because the corresponding area fractions of aggregates were too high: $\phi_{ag} > 0.5$. Similarly, the variation of the aggregate compactness could not be performed at a systemic hematocrit of 30% because the area fractions of aggregates are already equal to 0.5 for an aggregate compactness $\phi_i = 60\%$. Fig. 3 displays BSC_{SFSE} in dashed lines for the following clustering conditions: $r_{ag}/a = 6.32$ and ϕ_i varying from 30% to 60%. One can observe large differences between simulated and fitted SFSE curves, especially at low frequencies where the fitted curves overestimate the BSC_{SFM} amplitude. These differences are larger at $\phi = 20\%$. The estimated values of R_g^* for different aggregate compactnesses are plotted in Fig. 4(a). Although the true radius is fixed, estimated R_g^* increases with the aggregate compactness at both hematocrits. We found no correlation between the actual fixed radius and the estimated radii ($r^2 < 0.06$). Notice the linear relation between W^* and R_g^* when the aggregate compactness varies [see Fig. 4(b)], as observed previously in Fig. 2(b) when the aggregate radius r_{ag}/a was changed.

2) Results for the EMTSFM: The BSC curves fitted with the EMTSFM are shown in solid lines in Fig. 1 for the case of varying values of r_{ag}/a, and in Fig. 3 for varying ϕ_i. In both cases, the EMTSFM provided good fittings to the simulated BSC_{SFM} curves for all systemic hemato-

TABLE II. VALUES OF THE AGGREGATE RADIUS AND COMPACTNESS USED FOR COMPUTATION OF THE SIMULATED BSC_{SFM}, AND VALUES OF PARAMETERS FOUND WITH THE SFSE.

SFM		$\phi = 10\%$			$\phi = 20\%$			$\phi = 30\%$		
r_{ag}/a	ϕ_i (%)	W^*	R_g^*	$\varepsilon_{R_g^*}$ (%)	W^*	R_g^*	$\varepsilon_{R_g^*}$ (%)	W^*	R_g^*	$\varepsilon_{R_g^*}$ (%)
1	100	0.61	0.39	−61.00	0.37	0.39	−61.00	0.17	0.38	−62.00
3.16	60	3.12	1.50	−52.53	3.29	1.56	−50.63	2.67	1.32	−58.23
5	60	7.41	3.81	−23.80	6.95	3.64	−27.20	5.31	3.04	−39.20
7.07	60	15.82	7.99	13.01	13.57	7.18	1.56	8.58	5.33	−24.61

Aggregating conditions: r_{ag}/a varies, ϕ varies, $\phi_i = 60\%$ (except in the case of diaggregated RBCs where $\phi_i = 100\%$). The parameter ε indicates the relative error.

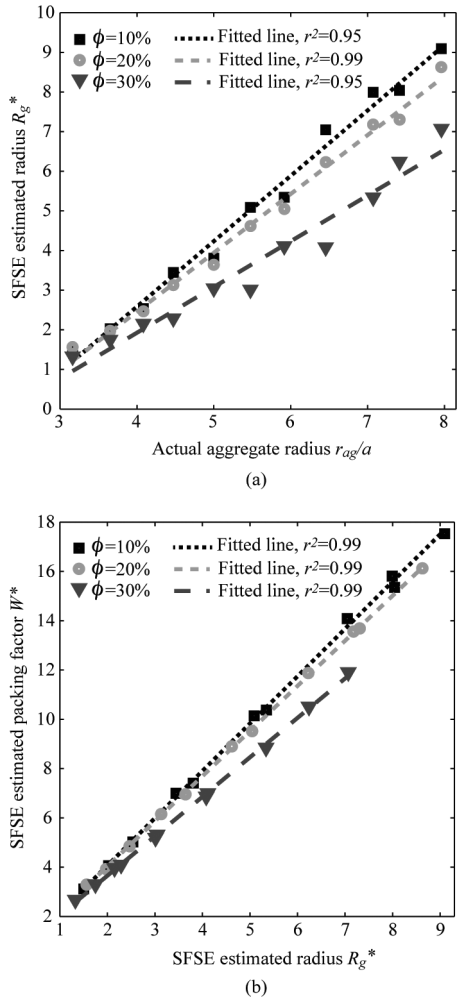

Fig. 2. (a) Comparison of R_g^* estimated with SFSE and the actual aggregate size r_{ag}/a for the three systemic hematocrits 10%, 20%, and 30%. (b) Linear relationships between W^* and R_g^*. Results presented here correspond to the configuration where r_{ag}/a varies and ϕ_i is fixed.

crits. For the clustering conditions in which the aggregate radius varied and the aggregate compactness was constant, the estimated values r_{ag}^*/a and ϕ_i^* and the corresponding relative errors are given in Fig. 5 for systemic hematocrits of 10%, 20%, and 30%. For the clustering conditions in which the aggregate compactness varied and the aggregate radius was constant, the results are shown in Fig. 6 for systemic hematocrits of 10% and 20%. For the EMTSFM, the relative errors for each parameter correspond to

$$\varepsilon_{r_{ag}^*} = \frac{(r_{ag}^*/a) - (r_{ag}/a)}{(r_{ag}/a)} \quad \text{and} \quad \varepsilon_{\phi_i^*} = \frac{\phi_i^* - \phi_i}{\phi_i}. \quad (12)$$

In both sub-studies in which the aggregate radius and compactness varied, a very good correspondence can be observed between true and estimated aggregate sizes and compactnesses. The relative errors for the estimated aggregate radii and compactnesses were less than 13% and 14%, respectively, for all hematocrits and for all studied aggregating configurations.

3) Results for the GM: Fig. 7 presents the $\mathrm{BSC_{SFM}}$ curves fitted with the GM for several aggregate sizes at the same clustering conditions as in Fig. 1. The GM provided overestimations in the low-frequency range for all

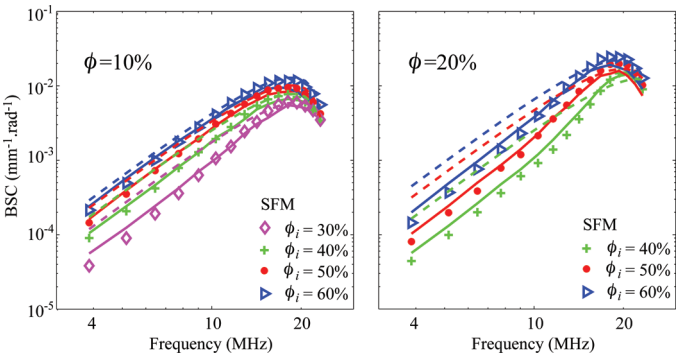

Fig. 3. Frequency-dependent backscatter coefficients (BSCs) computed with the SFM for different aggregate compactnesses and a constant aggregate size $r_{ag}/a = 6.32$ at systemic hematocrits of 10% and 20%, and corresponding fitting with the SFSE (in dashed lines) and with the EMTSFM (in solid lines).

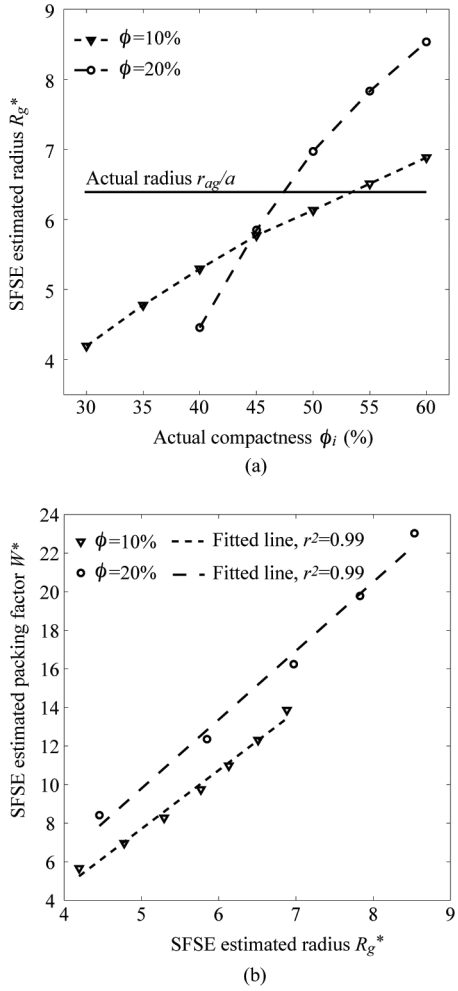

Fig. 4. (a) Aggregate size R_g^* estimated with the SFSE as a function of different aggregate compactnesses for systemic hematocrits of 10% and 20%. The solid line represents the actual aggregate size $r_{ag}/a = 6.32$. (b) Linear relationships between W^* and R_g^*. Results presented here correspond to the configuration where ϕ_i varies and r_{ag}/a is fixed.

systemic hematocrits. Excellent correlations ($r^2 \geq 0.92$) were found between the estimated and true aggregate radii for all hematocrits (data not shown). The estimated values a^*_{eff}/a and ϕ_i^* from the GM and the corresponding relative errors are given in Fig. 8. For systemic hematocrits of 10% and 20%, the estimated radii and compactnesses are quantitatively satisfactory with relative errors less than 15%. However, for $\phi = 30\%$, the relative errors increase to 40%.

For the clustering conditions in which the aggregate compactness varied and the aggregate radius was constant, the results are shown in Fig. 9 for systemic hematocrits of 10% and 20%. As previously observed with the SFSE, the estimated effective radius increases as the aggregate compactness increases. The estimated radii and compactnesses matched the true parameters at $\phi = 10\%$ with relative errors less than 17%. However, for $\phi = 20\%$, large relative errors (up to 74%) were obtained.

4) Comparison of the Errors Between the Simulated BSC and the Fitted Curves With the Three Scattering Models: The errors (i.e., differences) between the simulated BSC and the fitted curves with the three scattering models (SFSE, EMTSFM, and GM) are presented in Fig. 10. The logarithm of the error is shown to enhance readability.

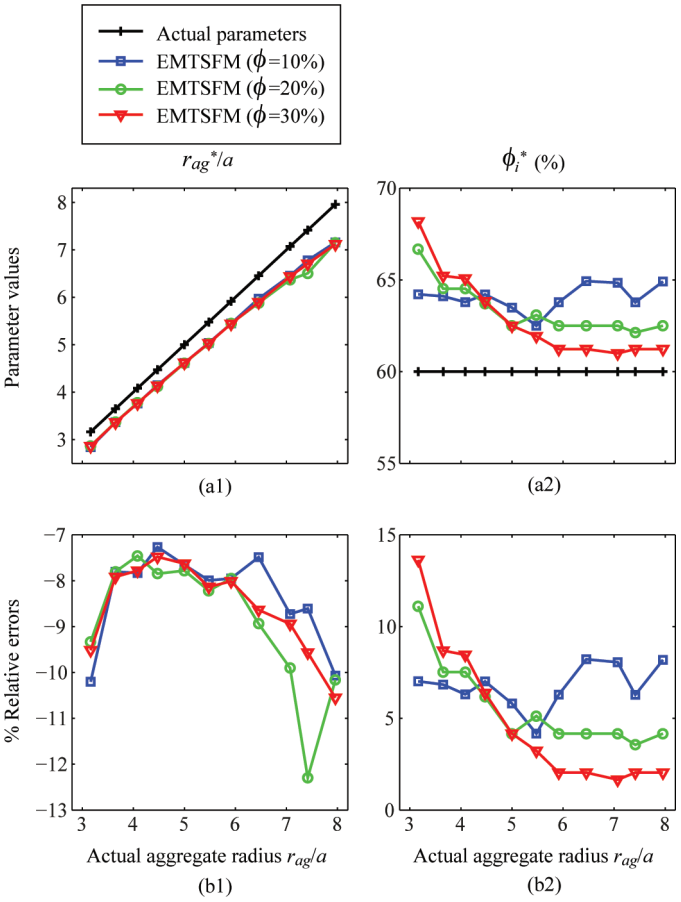

Fig. 5. (a) Values of r^*_{ag}/a and ϕ_i^* estimated by the EMTSFM as a function of the actual aggregate radius for the three systemic hematocrits of 10%, 20%, and 30%. Also represented are actual values of r_{ag}/a and ϕ_i. (b) Corresponding relative errors of r^*_{ag}/a and ϕ_i^*.

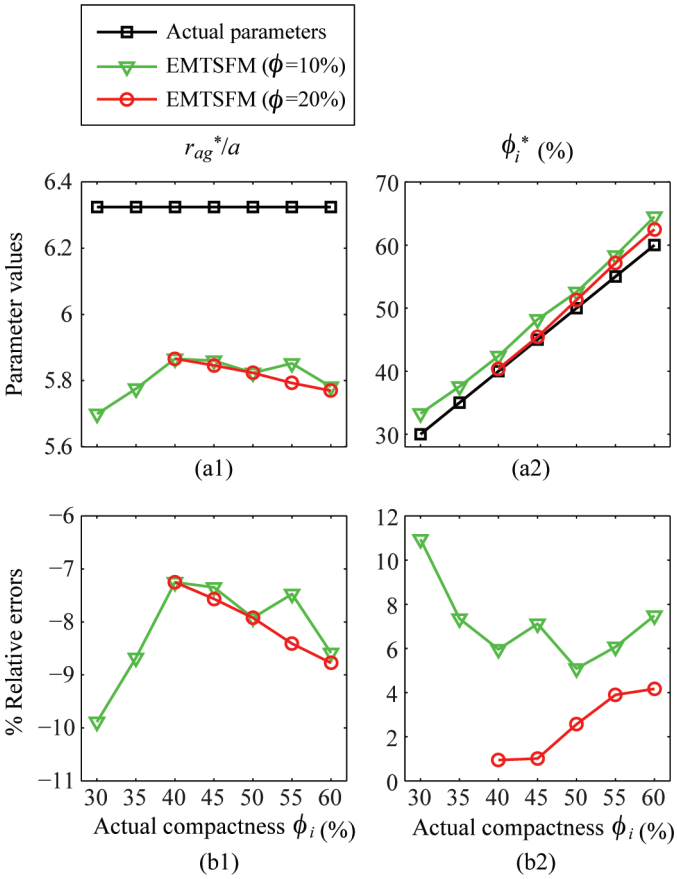

Fig. 6. (a) Values of r^*_{ag}/a and ϕ_i^* estimated by the EMTSFM as a function of the actual aggregate compactness for the systemic hematocrits of 10% and 20%. Also represented are actual values of r_{ag}/a and ϕ_i. (b) Corresponding relative errors of r^*_{ag}/a and ϕ_i^*.

The error reveals how the models fit the data. It is clear from the figure that errors were smaller with the EMTSFM and larger with the GM for each hematocrit. For the aggregating conditions in which the aggregate radius varied, the error decreases as the radius increases. When the aggregate radius increases, the frequency bandwidth used for the fit becomes smaller, and therefore the number of frequencies used for the error computation decreases.

B. Results Obtained From the 3-D Computer Simulations

For the 3-D computer simulations, the GM, SFSE, and EMTSFM were examined when the aggregate size varied and the aggregate compactness was fixed to a high value: $\phi_i = 74\%$.

It is important to note that the 3-D simulated aggregates were highly packed, leaving small numbers of particles as non-aggregated RBCs. For each tissue realization, the actual mean aggregate radius r_{ag} was computed using [11, Eq. (6)], and then the concentration of aggregated RBCs ϕ' was computed as

$$\phi' = \frac{\phi_i N_{\text{ag}} (4/3)\pi r_{\text{ag}}^3}{1000 \times 125 \times 125 \times (10^{-6})^3}. \tag{13}$$

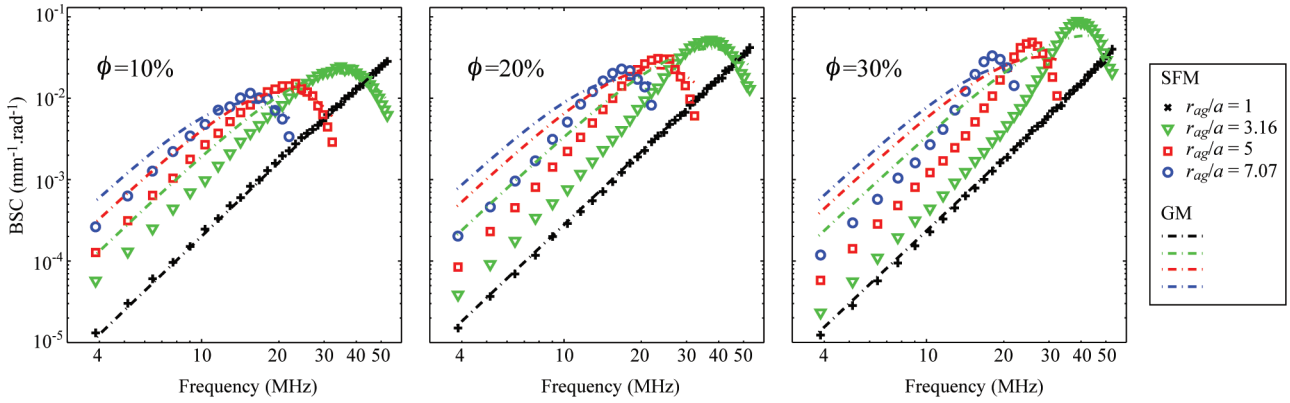

Fig. 7. Frequency-dependent backscatter coefficients (BSCs) computed with the SFM for different aggregate sizes and a constant aggregate compactness $\phi_i = 60\%$ at systemic hematocrits of 10%, 20%, and 30%, and corresponding fitting with the GM.

Fig. 11(a) shows the values of ϕ' as a function of the mean aggregate radius r_{ag}/a for the three systemic hematocrits of 20%, 30%, and 40%. The percentage of disaggregated RBCs was between 20% and 30% for the systemic hematocrit of 20% and between 27% and 37% for the systemic hematocrit of 40%. Note that the three models presented in Section III assumed that all RBCs were aggregated in blood and that aggregates had identical shape and size. Consequently, during the inversion procedure of the 3-D BSC data, we neglected the contribution of the disaggregated RBCs on the simulated $\mathrm{BSC_{SFM}}$ and we replaced the hematocrit ϕ by the value of the concentration of aggregated RBCs ϕ'.

Figs. 11(b) and 11(c) show $\mathrm{BSC_{SFM}}$ as a function of frequency for several aggregate sizes and systemic hematocrits of 30% and 40%. Also represented in Figs. 11(b) and 11(c) are corresponding fitted curves obtained with the SFSE, EMTSFM, and GM. The fitted GM and SFSE

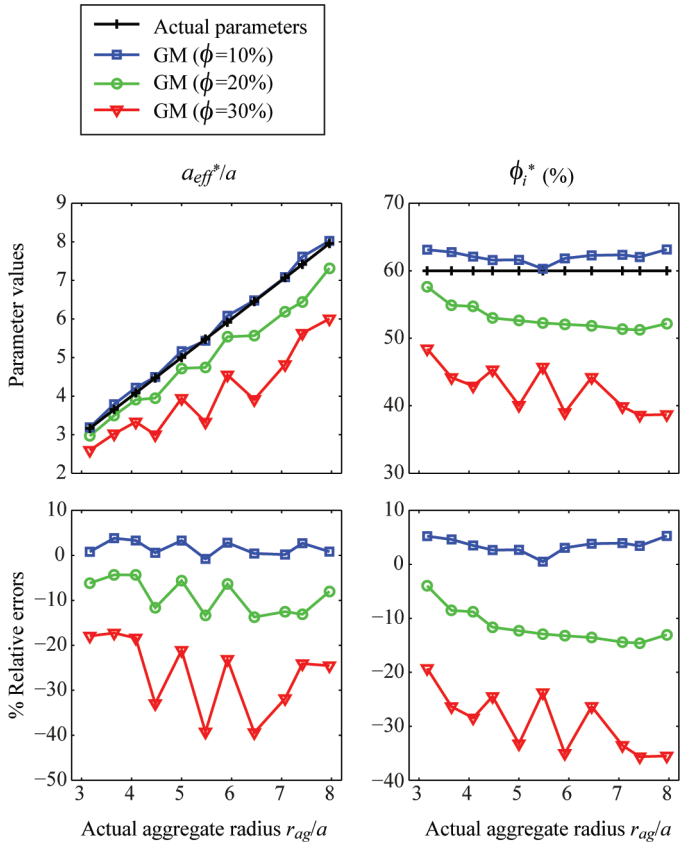

Fig. 8. (Top) Values of a_{eff}^*/a and ϕ_i^* estimated by the GM as a function of the actual aggregate radius for the three systemic hematocrits of 10%, 20%, and 30%. Also represented are actual values of r_{ag}/a and ϕ_i. (Bottom) Corresponding relative errors of a_{eff}^*/a and ϕ_i^*.

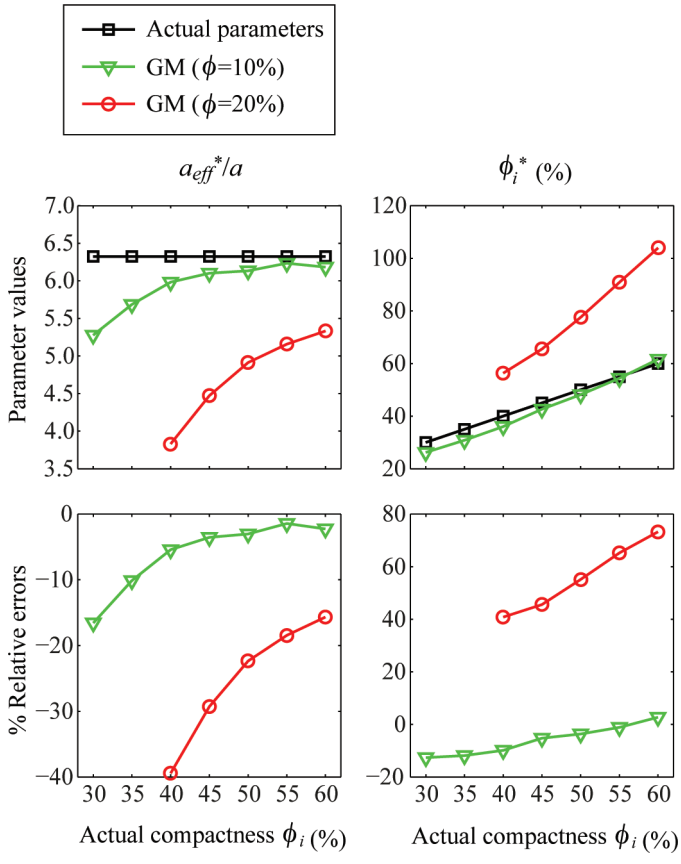

Fig. 9. (Top) Values of a_{eff}^*/a and ϕ_i^* estimated by the GM as a function of the actual aggregate compactness for the systemic hematocrits of 10% and 20%. Also represented are actual values of r_{ag}/a and ϕ_i. (Bottom) Corresponding relative errors of a_{eff}^*/a and ϕ_i^*.

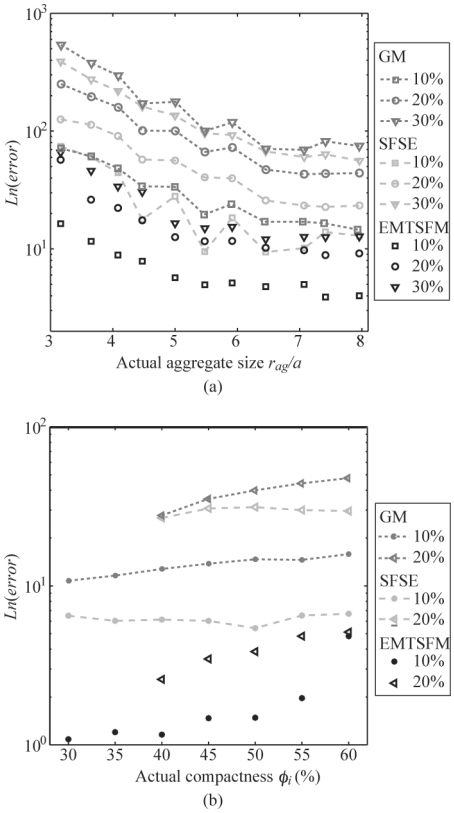

Fig. 10. Logarithm of the error between the simulated BSC_{SFM} and the fitted curves with the three scattering models GM, SFSE, and EMTSFM. (a) As a function of the actual aggregate size for the clustering configuration where r_{ag}/a varies and ϕ_i is fixed. (b) As a function of the actual aggregate compactness for the clustering configuration where ϕ_i varies and r_{ag}/a is fixed.

curves did not produce good fits to the 3-D data and overestimated the BSC_{SFM} amplitude (especially in the low frequency range), as observed in the 2-D case (see Figs. 1 and 7). On the contrary, the EMTSFM provided good fittings to the simulated BSC_{SFM} curves.

The results obtained with the SFSE were already presented in a previous article [11]. Excellent correlations ($r^2 \geq 0.94$) were found between the estimated and true aggregate radii for all hematocrits (see [11, Fig. 5(a)]). It can also be seen in [11, Fig. 5(a)] that for each hematocrit there is an aggregate size range for which the SFSE method works at its best. For example, relative errors for estimated radii were less than 20% for true radius values between 14 and 17 μm at the hematocrit of 40%. The parameters W^* and R^*_{sp} followed a quadratic relationship (as in [11, Fig. 5(b)]).

Fig. 12 gives the values of r^*_{ag} and ϕ^*_i estimated with the EMTSFM and corresponding relative errors that were less than 15% and 23%, respectively, for all hematocrits. Fig. 13 gives the values of a^*_{eff} and ϕ^*_i estimated with the GM and corresponding relative errors. The estimated radii with the new formulation of the GM are quantitatively satisfactory, with relative errors less than 9% for all hematocrits. The relative errors for the estimated compactnesses with the GM are larger with relative errors up to 32% for the hematocrits of 20% and 30%, and up to 76% for the hematocrit of 40%.

V. Discussion and Conclusions

Three scattering models for the characterization of RBC aggregation were examined. From these models, the gold-standard simulated BSC_{SFM} was fitted and aggregation parameters were extracted. The SFSE has been developed for blood characterization and the GM is a model that has been used in various tissue studies. Herein, the radius estimates R_g from the SFSE and a_{eff} from the GM were hypothesized to represent the aggregate size.

A. Clustering Conditions in Which the Aggregate Radius Varied and the Aggregate Compactness Was Constant (2-D and 3-D Computer Simulations)

The 2-D and 3-D computer simulations were performed on the same clustering configuration in which the aggre-

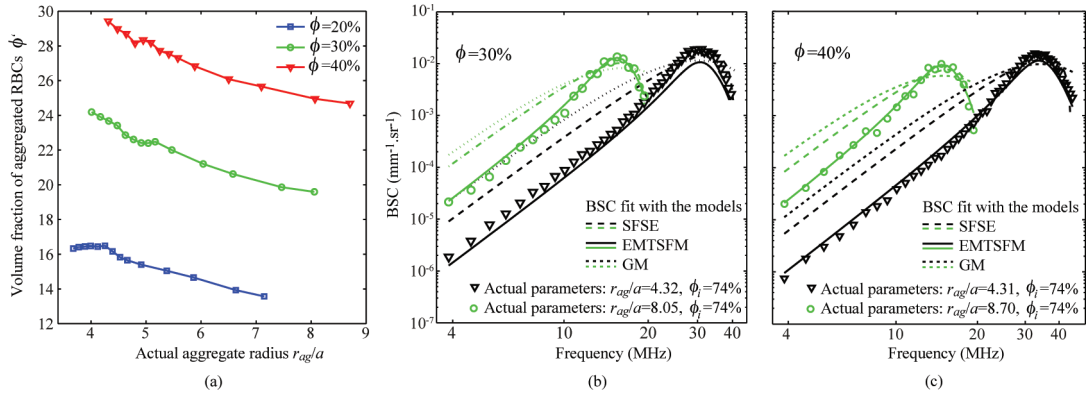

Fig. 11. (a) Concentration of aggregated red blood cells (RBCs) ϕ' as a function of the mean aggregate radius r_{ag}/a for the three systemic hematocrits of 20%, 30%, and 40%. (b) and (c) Frequency-dependent backscatter coefficients (BSCs) computed with the SFM in the 3-D case for different aggregate sizes and a constant aggregate compactness $\phi_i = 74\%$ at systemic hematocrits of 30% and 40%, and corresponding fitting with the SFSE model, the EMTSFM, and the GM.

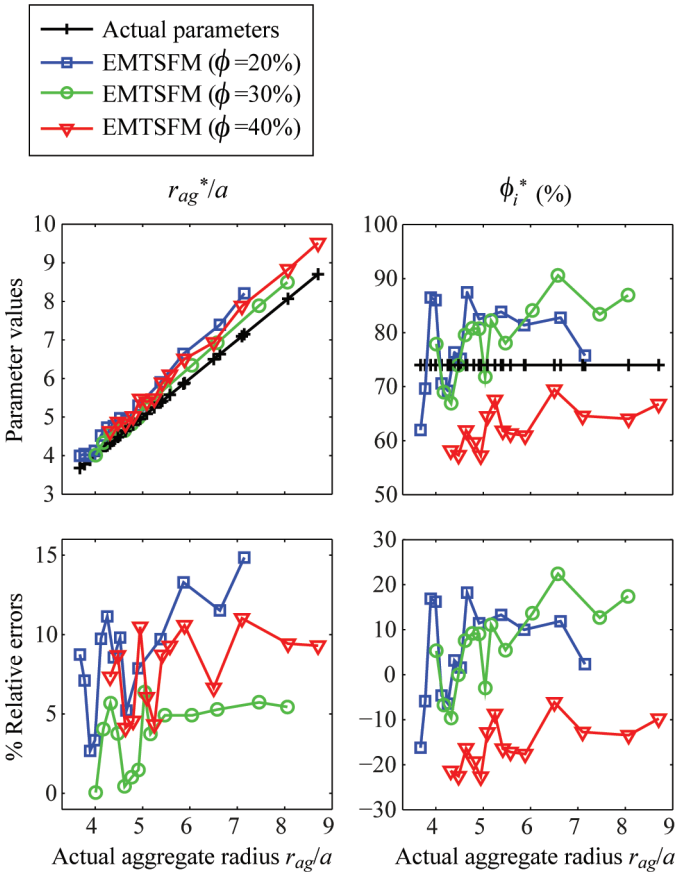

Fig. 12. (Top) Values of r_{ag}^*/a and ϕ_i^* estimated by the EMTSFM as a function of the actual aggregate radius for the three systemic hematocrits of 20%, 30%, and 40%. Also represented are actual values of r_{ag}/a and ϕ_i. (Bottom) Corresponding relative errors of r_{ag}^*/a and ϕ_i^*.

gate radius varied and the aggregate compactness was constant. It is interesting to observe the same BSC_{SFM} behavior for both 2-D and 3-D studies. Indeed, the simulated BSC_{SFM} amplitude increases with the size of aggregates and the BSC_{SFM} first peaks occur at lower frequencies as the aggregate radius increases (see Fig. 1 in the 2-D case, and Figs. 11(b) and 11(c) and [11, Fig. 4] in the 3-D case). Moreover, as can be observed in Figs. 1 and 7 in the 2-D case and in Fig. 11 in the 3-D case, the data fitting qualities obtained with the three models were quite similar. In both 2-D and 3-D cases, it is clear that the GM and the SFSE are insufficient to model the complex behavior of BSC and that the EMTSFM was the model that better fitted the BSC data for all studied hematocrits.

Although the SFSE model did not produce good spectral fits to the BSC data for 2-D and 3-D computer simulations, significant correlations were found between the estimated and true radii with r^2 superior to 0.95 at all hematocrits (see Fig. 2(a) and [11, Fig. 5(a)]). However, the estimated aggregation parameters W^* and R_g^* followed a linear relationship in our 2-D simulation study. This relation was also found to be quadratic in 3-D numerical simulations [11] and under experimental conditions [10]. It means that the BSC parameterization can be reduced to one parameter and that no new information can be obtained with the parameter W^*.

The EMTSFM and the GM used as effective medium models gave quantitatively satisfactory radius estimates with relative errors less than 15% for the 10% and 20% hematocrits in the 2-D case, and for all hematocrits in the 3-D case. For the highest systemic hematocrit, the aggregate compactnesses were better estimated with the EMTSFM, with relative errors less than 14% in the 2-D case (and less than 23% in the 3-D case), whereas the relative errors were between 19% and 36% in the 2-D case (and between 59% and 76% in the 3-D case) for the GM. These results with the EMTSFM and the GM were somewhat anticipated because the assumption of a random distribution of scatterers used by the GM fails because of the spatial correlation between scatterers in a dense medium [24]. To conclude, the EMTSFM was more suitable than the GM and SFSE for characterizing the aggregate microstructure in both 2-D and 3-D studies.

B. Clustering Conditions in Which the Aggregate Compactness Varied and the Aggregate Radius Was Constant (2-D Computer Simulations)

For the highest simulated hematocrit of 20%, the aggregate radii normalized by the RBC radius were estimated between 4.34 and 8.55 using the SFSE model and between 3.83 and 5.33 using the GM (see Figs. 4(a) and 9), whereas the actual aggregate radius was $r_{ag}/a = 6.32$. Therefore, we found no correlation between the actual fixed aggregate radius and the estimated radii. The GM and SFSE cannot take into account a variation in the aggregate compactness at a large hematocrit, because it is interpreted as a change in the aggregate size.

In the case of the SFSE, one could have expected a fixed value of the estimated radius R_g^* and a variation of the estimated packing factor W^*, when the aggregate radius was fixed and the aggregate compactness varied. However, both R_g^* and W^* increased as the true aggregate compactness was raised. The estimated parameters R_g^* and W^* followed linear relations for all hematocrits [see Fig. 4(b)], as observed previously in Fig. 2(b) when the aggregate radius r_{ag}/a was changed. It means that W^* and R_g^* carry the same information and that the BSC parameterization is reduced to one parameter.

The estimated parameters using the EMTSFM presented in Fig. 6 show that the model gave quantitatively satisfactory estimates for all aggregate compactnesses and for all studied hematocrits. Contrary to the GM and SFSE, the EMTSFM provided a quasi-constant aggregate radii between 5.7 and 5.9 for both studied hematocrits. Moreover, the aggregate compactnesses were estimated with relative errors less than 12% at both studied hematocrits for that model. The errors between simulated BSC_{SFM} and the fitted curves were also smaller with the EMTSFM, as can be observed in Fig. 10(b). To conclude, the EMTS-

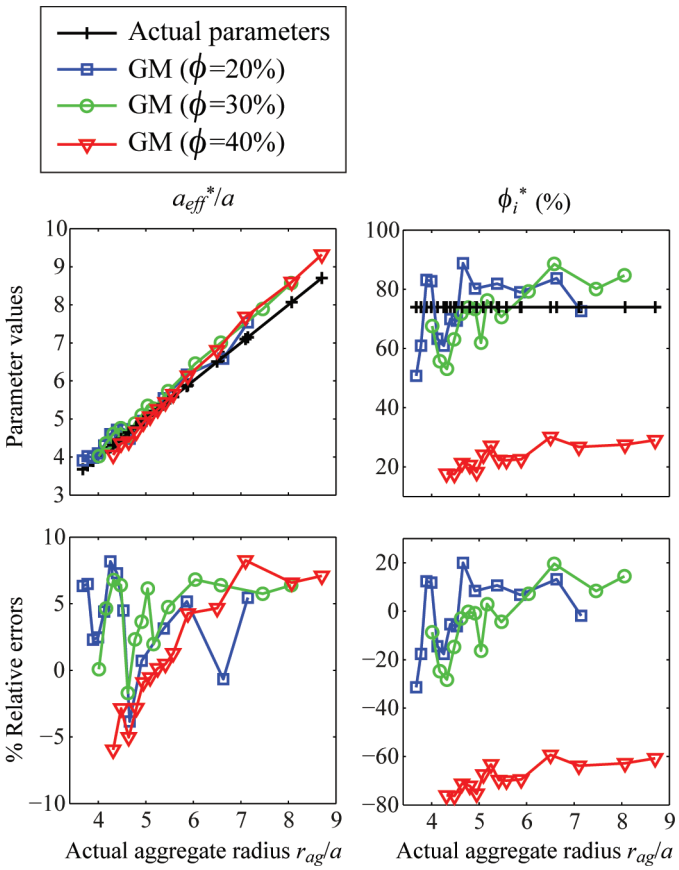

Fig. 13. (Top) Values of a_{eff}^*/a and ϕ_i^* estimated by the GM as a function of the actual aggregate radius for the three systemic hematocrits of 20%, 30%, and 40%. Also represented are actual values of r_{ag}/a and ϕ_i. (Bottom) Corresponding relative errors of a_{eff}^*/a and ϕ_i^*.

FM was the model that better explained the simulated BSC_{SFM}.

C. Computation of RBC Distributions and of BSC_{SFM}

The two methods we used here to obtain the RBC spatial distributions did not take into consideration realistic interactions between RBCs. These methods were already presented in [12] and [11] for the 2-D and 3-D computer simulations, respectively. They were simple and fast methods to generate samples containing non-overlapping, identical and isotropic aggregates. The 3-D computer simulations allowed better mimicking of real data but they are time consuming (see [11, Sections III-A and V] to obtain a quick review of different approaches for simulating compact RBC aggregates). To simulate the BSC data with the SFM reference model, the method we chose to distribute RBCs in the 3-D case allowed 1) studying of various aggregate sizes with the same aggregate compactness and 2) reaching the physiological hematocrit of 40% by mixing identical RBC aggregates and disaggregated RBCs. Because studied scattering models assumed that all RBCs were aggregated in blood and because the average percentage of disaggregated RBCs was small (around 25%), the influence of the disaggregated RBCs on the simulated BSC_{SFM} was neglected during the inversion procedure of the 3-D BSC data. Contrary to the 3-D modeling, the method we chose to distribute RBCs in the 2-D case allowed 1) studying of the clustering condition in which the aggregate compactness varies and the aggregate size is fixed and 2) having only aggregated RBCs in blood. However, the 2-D computer simulations were limited to a maximum hematocrit of 30% because of the difficulty to simulate with the SFM values greater than 30%. To clarify, the main difficulty in the 2-D case was to distribute compact aggregates and to have only aggregated RBCs in blood. The maximum value of the aggregate area fraction $\phi_{\text{ag}_{\max}}$ was fixed to 0.5, corresponding to the maximum particle area fraction that can be easily generated using a random number generator. The procedure we chose to distribute the RBCs within aggregates allows reaching a maximum value of aggregate compactness $\phi_{i_{\max}}$ equal to 0.6 (see [12, Section III-B]). As a consequence, the maximum value of the systemic hematocrit was limited to $\phi_{\max} = \phi_{\text{ag}_{\max}}\phi_{i_{\max}} = 0.3$.

We also modeled individual biconcave RBCs as spheres of equivalent volume in the 3-D study and studied BSC between 4 and 45 MHz. The impact of modeling a RBC by a sphere on the frequency dependence of the backscatter cross section has been studied and errors are introduced above 20 MHz [16], [25]. The impact of this simplification on the simulated BSC_{SFM} and structural aggregate estimates with the three models (SFSE, GM, and EMTSFM) is unknown and still needs to be explored.

D. On the Use of the EMTSFM In Vivo

The EMTSFM assumes that all RBCs are aggregated in blood and that aggregates are identical and isotropic. Therefore, the BSC behavior obtained in our simulations has pronounced frequency peaks. In experimental conditions [10], the BSC behavior was smoother and the peaks were less pronounced. The reason behind this might be that real blood contains several sizes of aggregates and, because the location of BSC peaks are different for different aggregate populations, a relatively smoother BSC curve can be obtained. Another important aspect to consider is the assumption of isotropic aggregates. In human blood, low shear rates can promote the formation of RBC aggregates having anisotropic (i.e., rouleaux) or isotropic (i.e., clump) structures. The rouleaux-like pattern is typically associated with normal blood. However, as the binding energy between RBCs increases with inflammation [26], aggregates form clump structures, as in diabetes mellitus [14], [15]. The assumption of isotropic aggregates in the EMTSFM is thus valid as far as we are concerned with the study of pathological states. In the case of normal human rouleaux of RBCs, if the EMTSFM is applied to estimate structural parameters such as the aggregate size and compactness, this assumption would obviously create a bias against the parameter estimation. Therefore, future improvements should consider incorporating

the aggregate anisotropy and the polydispersity in terms of aggregate size and compactness to provide an optimal model for the inversion of experimental data. Future validations may also evaluate the EMTSFM in a controlled Couette flow experiment with ghost RBCs (i.e., optically visible RBCs with no hemoglobin and viable membrane properties) coated with dextran polymers to change attractive energies between erythrocytes and thus modulate the aggregate compactness and size.

Another difficulty in applying the EMTSFM *in vivo* is that the spectral content of backscattered echoes is also affected by attenuation caused by intervening tissue layers (such as the skin) between the probe and the blood flow. To correctly evaluate microstructural parameters, it is thus of major interest to take into account tissue attenuation effects. Note that the SFSE was slightly modified to introduce the attenuation term in the BSC expression and was named the structure factor size and attenuation estimator (SFSAE) [27]. The SFSAE allows to determine simultaneously blood structural parameters (i.e., W^* and R_{g}^*) and the total attenuation [28], [29]. Future improvements of the EMTSFM should incorporate the tissue attenuation as for the SFSAE. This means that the EMTSFM should be slightly modified by introducing the attenuation term to simultaneously estimate the RBC aggregate size, compactness, and the total attenuation.

Appendix A
Numerical Computation of the Structure Factor S_{AG} for Hard Cylinders in 2-D

Because there is no analytical expression of the structure factor S_{ag} for hard cylinders in 2-D [30], [31], S_{ag} was numerically computed for several values of ϕ_{ag} varying from 0.01 to 0.5 with a step of 0.01. This means that, in the 2-D case, the cylinder concentration ϕ_{ag} was rounded to the second decimal for the computation of S_{ag} in (7). Note that the computation of S_{ag} depends not only on the area fraction ϕ_{ag} but also on the effective particle radius r_{ag}. That is why S_{ag} that depends on r_{ag} was computed in a dimensionless way as described next.

For each specified value of ϕ_{ag}, aggregates of an arbitrarily normalized (dimensionless) radius of 1/60 were randomly distributed within a dimensionless surface area $L'^2 = 1 \times 1$ with non-overlapping positions using a random number generator. The corresponding density matrix D' was computed by dividing the square simulation plane L'^2 into N_{p}^2 pixels (herein, $N_{\mathrm{p}} = 512$) and by counting the number of particles falling into each pixel. The Fourier transformation of the density matrix D' was then computed to generate a structure factor S_{ag}. A mean S_{ag} was determined by repeating this procedure 400 times. When the value of the effective particle radius r_{ag} was specified, the centered grid of wavevectors for the structure factor S_{ag} was computed between $\pm(\pi N_p)/(2 \times 60 r_{\mathrm{ag}})$ with a step of $\Delta k = \pi/60 r_{\mathrm{ag}}$ (i.e., by putting the simulated surface length $L' = 60 r_{\mathrm{ag}}$).

Appendix B
Analytical Expression of the Structure Factor S_{AG} For Hard Spheres in 3-D

The structure factor S for hard spheres is given by [23], [32]

$$S(k) = \frac{1}{1 - 4\pi m d^3 \int_0^1 z^2 \frac{\sin(2kz)}{2kz} c(z) \mathrm{d}z}, \tag{14}$$

where m is the number density of hard spheres, d is the hard sphere diameter, and $c(z)$ is the direct correlation function given by [23], [32]

$$-c(z) = \begin{cases} c_0 + c_1 \dfrac{z}{d} + c_3 \left(\dfrac{z}{d}\right)^3 & \text{for } z \le d \\ 0 & \text{for } z > d. \end{cases} \tag{15}$$

The coefficients c_0, c_1, and c_3 are given by [23], [32]

$$\begin{aligned} c_0 &= \frac{(1+2\phi)^2}{(1-\phi)^4} \\ c_1 &= -\frac{6\phi(1+\phi/2)^2}{(1-\phi)^4} \\ c_2 &= \frac{\phi}{2} c_0 = \frac{\phi(1+2\phi)^2}{2(1-\phi)^4}. \end{aligned} \tag{16}$$

References

[1] F. L. Lizzi, M. Ostromogilsky, E. J. Feleppa, M. C. Rorke, and M. M. Yaremko, "Relationship of ultrasonic spectral parameters to features of tissue microstructure," *IEEE Trans. Ultrason. Ferroelectr. Freq. Control*, vol. 34, no. 3, pp. 319–329, 1987.

[2] M. F. Insana, R. F. Wagner, D. G. Brown, and T. J. Hall, "Describing small-scale structure in random media using pulse-echo ultrasound," *J. Acoust. Soc. Am.*, vol. 87, no. 1, pp. 179–192, 1990.

[3] E. J. Feleppa, F. L. Lizzi, D. J. Coleman, and M. M. Yaremko, "Diagnostic spectrum analysis in ophthalmology: A physical perspective," *Ultrasound Med. Biol.*, vol. 12, no. 8, pp. 623–631, 1986.

[4] E. J. Feleppa, T. Liu, A. Kalisz, M. C. Shao, N. Fleshner, and V. Reuter, "Ultrasonic spectral-parameter imaging of the prostate," *Int. J. Imaging Syst. Technol.*, vol. 8, no. 1, pp. 11–25, 1997.

[5] M. L. Oelze, W. D. O'Brien, J. P. Blue, and J. F. Zachary, "Differentiation and characterization of rat mammary fibroadenomas and 4T1 mouse carcinomas using quantitative ultrasound imaging," *IEEE Trans. Med. Imaging*, vol. 23, no. 6, pp. 764–771, 2004.

[6] H. Kitamura, B. Sigel, J. Machi, E. J. Feleppa, J. Sokil-Melgar, and J. Justin, "Roles of hematocrit and fibrinogen in red cell aggregation determined by ultrasonic scattering properties," *Ultrasound Med. Biol.*, vol. 21, no. 6, pp. 827–832, 1995.

[7] R. B. Ami, G. Barshtein, D. Zeltser, Y. Goldberg, I. Shapira, A. Roth, G. Keren, H. Miller, V. Prochorov, A. Eldor, S. Berliner, and S. Yedgar, "Parameters of red blood cell aggregation as correlates of the inflammatory state," *Am. J. Physiol. Heart Circ. Physiol.*, vol. 280, no. 5, pp. H1982–H1988, 2001.

[8] D. Savery and G. Cloutier, "A point process approach to assess the frequency dependence of ultrasound backscattering by aggregating red blood cells," *J. Acoust. Soc. Am.*, vol. 110, no. 6, pp. 3252–3262, 2001.

[9] I. Fontaine, D. Savery, and G. Cloutier, "Simulation of ultrasound backscattering by red blood cell aggregates: Effect of shear rate and anisotropy," *Biophys. J.*, vol. 82, no. 4, pp. 1696–1710, 2002.

[10] F. T. H. Yu and G. Cloutier, "Experimental ultrasound characterization of red blood cell aggregation using the structure factor size estimator," *J. Acoust. Soc. Am.*, vol. 122, no. 1, pp. 645–656, 2007.
[11] R. K. Saha, E. Franceschini, and G. Cloutier, "Assessment of accuracy of the structure-factor-size-estimator method in determining red blood cell aggregate size from ultrasound spectrum backscattering coefficient," *J. Acoust. Soc. Am.*, vol. 129, no. 4, pp. 2269–2277, 2011.
[12] E. Franceschini, B. Metzger, and G. Cloutier, "Forward problem study of an effective medium model for ultrasound blood characterization," *IEEE Trans. Ultrason. Ferroelectr. Freq. Control*, vol. 58, no. 12, pp. 2668–2679, 2011.
[13] O. K. Baskurt, M. R. Hardeman, M. W. Rampling and H. J. Meiselman, Eds., *Handbook of Hemorheology and Hemodynamics*, Washington, DC: IOS Press, 2007.
[14] H. Schmid-Schonbein, H. Malotta, and F. Striesow, "Erythrocyte aggregation: Causes, consequences, and methods of assessment," *Tijdschr NVKS*, vol. 15, pp. 88–97, 1990.
[15] H. Schmid-Schonbein, G. Gallasch, J. V. Gosen, E. Volger, and H. J. Klose, "Red cell aggregation in blood flow. I. New methods of quantification," *Klin. Wochenschr.*, vol. 54, no. 4, pp. 149–157, 1976.
[16] D. Savery and G. Cloutier, "High-frequency ultrasound backscattering by blood: Analytical and semi-analytical models of the erythrocyte cross section," *J. Acoust. Soc. Am.*, vol. 23, no. 4, pp. 3963–3971, 2007.
[17] P. M. Morse and K. U. Ingard, *Theoretical Acoustics*. Princeton, NJ: Princeton University Press, 1968, ch. 8, pp. 400–466.
[18] M. F. Insana and D. G. Brown, "Acoustic scattering theory applied to soft biological tissues," in *Ultrasonic Scattering in Biological Tissues*, K. K. Shung and G. A. Thieme, Eds., Boca Raton, FL: CRC Press, 1993, ch. 4, pp. 76–124.
[19] I. Fontaine, M. Bertrand, and G. Cloutier, "A system-based approach to modeling the ultrasound signal backscattered by red blood cells," *Biophys. J.*, vol. 77, no. 5, pp. 2387–2399, 1999.
[20] V. Twersky, "Low-frequency scattering by correlated distributions of randomly oriented particles," *J. Acoust. Soc. Am.*, vol. 81, no. 5, pp. 1609–1618, 1987.
[21] K. K. Shung, "On the ultrasound scattering from blood as a function of hematocrit," *IEEE Trans. Sonics Ultrason.*, vol. SU-29, no. 6, pp. 327–331, 1982.
[22] A. Guinier and J. Fournet, *Small Angle Scattering of X-Rays*. New York, NY: Wiley Interscience, 1955, ch. 14, pp. 637–669.
[23] M. S. Wertheim, "Exact solution of the Percus–Yevick integral equation for hard spheres," *Phys. Rev. Lett.*, vol. 10, no. 8, pp. 321–323, 1963.
[24] E. Franceschini and R. Guillermin, "Experimental assessment of four ultrasound scattering models for characterizing concentrated tissue-mimicking phantoms," *J. Acoust. Soc. Am.*, vol. 132, no. 6, pp. 3735–3747, 2012.
[25] C. C. Coussios, "The significance of shape and orientation in single-particle weak-scatterer models," *J. Acoust. Soc. Am.*, vol. 112, no. 3, pt. 1, pp. 906–915, 2002.
[26] X. Weng, G. Cloutier, R. Beaulieu, and G. O. Roederer, "Influence of acute-phase proteins on erythrocyte aggregation," *Am. J. Physiol.*, vol. 271, no. 6, pt. 2, pp. H2346–H2352, 1996.
[27] E. Franceschini, F. T. H. Yu, F. Destrempes, and G. Cloutier, "Ultrasound characterization of red blood cell aggregation with intervening attenuating tissue-mimicking phantoms," *J. Acoust. Soc. Am.*, vol. 127, no. 2, pp. 1104–1115, 2010.
[28] F. T. H. Yu, J. K. Armstrong, J. Tripette, H. J. Meiselman, and G. Cloutier, "A local increase in red blood cell aggregation can trigger deep vein thrombosis: Evidence based on quantitative cellular ultrasound imaging," *J. Thromb. Haemost.*, vol. 9, no. 3, pp. 481–488, 2011.
[29] J. Tripette, A. Y. Denault, L. Allard, B. Chayer, L. P. Perrault, and G. Cloutier, "Ultrasound monitoring of RBC aggregation as a real-time marker of the inflammatory response in a cardiopulmonary bypass swine model," *Crit. Care Med.*, vol. 41, no. 8, pp. e171–e178, 2013.
[30] C. F. Tejero and J. A. Cuesta, "Hard-sphere and hard-disk freezing from the differential formulation of the generalized effective liquid approximation," *Phys. Rev. E*, vol. 47, no. 1, pp. 490–495, 1993.
[31] X. Guo and U. Riebel, "Theoretical direct correlation function for two-dimensional fluids of monodisperse hard spheres," *J. Chem. Phys.*, vol. 125, no. 14, art. no. 144504, 2006.
[32] N. W. Ashcroft, "Structure and resistivity of liquid metals," *Phys. Rev.*, vol. 145, no. 1, pp. 83–90, 1966.

Emilie Franceschini received her M.S. degree in mechanical engineering from the Ecole Supérieure d'Ingénieurs de Marseille in 2003, and the Ph.D. degree in acoustics from the University of Provence, Marseille, in 2006. In 2007, she was a Postdoctoral Fellow at the Laboratory of Biorheology and Medical Ultrasonics, Research Center of the University of Montreal Hospital, Montreal, QC. Since October 2008, she has been a Researcher at the French National Centre for Scientific Research (CNRS) in the Laboratory of Mechanics and Acoustics CNRS UPR 7051, Marseille. Her current research interests include ultrasound imaging for biomedical applications, inverse problems, and ultrasound characterization of biological tissues at the microscopic level. She is a member of the French Acoustical Society (SFA) and IEEE.

Ratan K. Saha obtained his B.Sc. degree in physics (studied at A.B.N. Seal College, Coochbehar, India) from the University of North Bengal, Siliguri, India, in 1996 and received his M.Sc. degree in physics from Jadavpur University, Kolkata, India, in 1999. He carried out his Ph.D. work at the Saha Institute of Nuclear Physics, Kolkata from 2000 to 2006. He then joined the Laboratory of Biorheology and Medical Ultrasonics, Research Center of the University of Montreal Hospital, Montreal, Canada, as a postdoctoral fellow from 2007 to 2008. He also worked as a postdoctoral fellow at Ryerson University, Toronto, Canada, from 2009 to 2011. Since October 2011, he has been a postdoctoral fellow at the Saha Institute of Nuclear Physics and his current research interests include ultrasonic and photoacoustic characterizations of soft tissues.

Guy Cloutier (S'89–M'90–SM'07) obtained his B.Eng. degree in electrical engineering in 1984, and his M.Sc. and Ph.D. degrees in biomedical engineering in 1986 and 1990, respectively. Between 1990 and 1992, he was a postdoctoral fellow at The Pennsylvania State University with Prof. K. Kirk Shung. Prof. Cloutier is Director of the Laboratory of Biorheology and Medical Ultrasonics at the University of Montreal Hospital Research Center (www.lbum-crchum.com), and Professor of Radiology and Biomedical Engineering at the University of Montreal. His research interests are in quantitative ultrasound imaging of red blood cell aggregation, quasi-static and dynamic ultrasound elastography of atherosclerotic plaques, vascular aneurysms, deep vein thrombi and breast cancers, 3-D morphologic and hemodynamic assessment of lower limb arterial stenoses, and mathematical and biomechanical modeling. He has published more than 140 peer-reviewed articles in these fields, holds 11 patents, and was recipient of the National Scientist award of the Fonds de Recherche en Santé du Québec (2004 to 2009).

Ultrasound characterization of red blood cell aggregation with intervening attenuating tissue-mimicking phantoms

Emilie Franceschini,[a] François T. H. Yu, and François Destrempes
Laboratory of Biorheology and Medical Ultrasonics, University of Montreal Hospital Research Center (CRCHUM), Pavillon J. A. de Sève (Room Y-1619), 2099 Alexandre de Sève, Montréal, Québec H2L 2W5, Canada

Guy Cloutier
Laboratory of Biorheology and Medical Ultrasonics, University of Montreal Hospital Research Center (CRCHUM), Pavillon J. A. de Sève (Room Y-1619), 2099 Alexandre de Sève, Montréal, Québec, H2L 2W5, Canada and Department of Radiology, Radio-Oncology and Nuclear Medicine and Institute of Biomedical Engineering, University of Montreal, Montreal, Québec, H3T IJ4, Canada

(Received 10 June 2009; revised 22 November 2009; accepted 27 November 2009)

The analysis of the ultrasonic frequency-dependent backscatter coefficient of aggregating red blood cells reveals information about blood structural properties. The difficulty in applying this technique *in vivo* is due to the frequency-dependent attenuation caused by intervening tissue layers that distorts the spectral content of signals backscattered by blood. An optimization method is proposed to simultaneously estimate tissue attenuation and blood structure properties, and was termed the structure factor size and attenuation estimator (SFSAE). An ultrasound scanner equipped with a wide-band 25 MHz probe was used to insonify porcine blood sheared in both Couette and tubular flow devices. Since skin is one of the most attenuating tissue layers during *in vivo* scanning, four skin-mimicking phantoms with different attenuation coefficients were introduced between the transducer and the blood flow. The SFSAE gave estimates with relative errors below 25% for attenuations between 0.115 and 0.411 dB/MHz and $kR < 2.08$ (k being the wave number and R the aggregate radius). The SFSAE can be useful to examine *in vivo* and *in situ* abnormal blood conditions suspected to promote pathophysiological cardiovascular consequences.
 [DOI: 10.1121/1.3277200]

PACS number(s): 43.80.Cs, 43.35.Bf, 43.35.Yb, 43.80.Ev [FD] Pages: 1104–1115

I. INTRODUCTION

Ultrasonic tissue characterization techniques using the radio frequency (rf) backscattered signals have received broad interest for the past 25 years. One approach is to use the magnitude and frequency dependence of the rf backscatter spectrum in order to quantify the tissue structures such as the size, acoustic impedance, and concentration of the scatterers. Many *in vitro* and *in vivo* experiments have been performed to demonstrate the utility of this approach for characterizing the eye,[1,2] liver,[3] kidney,[4] prostate,[5] and breast.[6] Recently, the frequency dependence of the ultrasound (US) backscatter coefficient was studied to assess the level of red blood cell (RBC) aggregation.[7]

It is well known that when RBCs are under low shear rates ($< 10\ s^{-1}$), they interact strongly with each other and form complex three-dimensional (3D) rouleaux structures. When the shear rate increases, rouleaux structures disaggregate. This phenomenon is normal and occurs in the circulation of many mammalian species. However, RBC hyperaggregation, an abnormal increase in RBC aggregation, is a pathological state associated with several circulatory diseases such as deep venous thrombosis, atherosclerosis, and diabetes mellitus. These pathologies inflict particular sites (inferior members for thrombosis, arterial bifurcations for atherosclerosis, and the foot and eye for diabetes). It would thus be of great interest to elucidate the role of flow-dependent rheological parameters, such as RBC aggregation, in the etiology of these pathologies *in vivo* and *in situ* with US techniques. To achieve this goal, the backscattering coefficient from blood was parametrized: two indices describing RBC aggregation, the packing factor and mean aggregate diameter, were extracted from the structure factor size estimator (SFSE).[7] The SFSE is a second-order data reduction model based on the structure factor and adapted to a dense medium such as blood. This approach is based on the analysis of the backscattered power spectrum that contains information about the size, spatial organization, concentration, and mechanical properties of scatterers (i.e., RBCs). The difficulty in using the SFSE *in vivo* is that the spectral content of backscattered echoes is also affected by attenuation caused by intervening tissue layers between the probe and the blood flow. More generally, US scatterer size estimation techniques for tissue characterization are facing similar challenges and several approaches to this problem have been developed.[8–23]

In vitro attenuation measurement methods are difficult to transfer *in vivo* since most of the clinical studies can be performed only in a single-transducer backscatter configuration. Indeed, *in vitro* backscatter coefficient measurements are generally compensated with an estimation of the attenuation using transmission mode[8,9] or reflection mode with a reflector on the opposite side of the examined tissue,[10,11] which is

[a]Present address: Laboratoire de Mécanique et d'Acoustique LMA, CNRS UPR 7051, 31 chemin Joseph Aiguier, 13402 Marseille Cedex 20, France.

difficult to implement in clinical practice. Many researchers have then attempted to improve the *in vivo* backscatter power spectrum estimates by assuming *a priori* attenuation values for the different intervening tissue layers.[12–14] Thicknesses of the intervening tissues are evaluated from the backscattered signals and typical attenuation values are assigned to each tissue, based on the results found in the relevant literature. Unfortunately, the tissue attenuation coefficients vary among patients (see, for example, the detailed review of the literature on tissue attenuation by Goss *et al.*[15]) and must be determined on a patient-specific basis. Several research groups have thus developed *in vivo* measurement techniques to evaluate the frequency-dependent attenuation for the compensation of the backscatter power spectrum.[16–19] Recently, Bigelow and co-workers[20–22] introduced a new algorithm that has the advantage to estimate simultaneously the effective radius of the tissue microstructure and the total attenuation. These two parameters were determined by using a single minimization method that fits the spectrum of the backscattered rf echoes from the region of interest (ROI) to an estimated spectrum by an appropriate model. In our previous work, this last strategy has been adapted for estimation of RBC scatterer sizes.[23] Blood structural parameters and total attenuation were determined simultaneously by using an optimization method, termed the structure factor size and attenuation estimator (SFSAE).

The goal of this paper was to further develop the SFSAE and assess its ability to evaluate three parameters (the packing factor, mean aggregate diameter, and total attenuation) with *in vitro* experiments mimicking *in vivo* conditions. To ensure that the global minimum of the optimization strategy is found, the algorithm was modified by employing an exhaustive search on the attenuation, combined with an analytical solution for the two blood structure parameters given for a fixed value of the attenuation, rather than a trust-region technique[24] used in our previous paper.[23] Porcine RBCs were first sheared in a Couette flow system, and ultrasonic rf echoes were obtained using a 25 MHz center-frequency transducer. Four skin-mimicking phantoms with different attenuation coefficients were introduced between the transducer and the blood flow. Other experiments were conducted in a tubular flow allowing to be closer to the *in vivo* situation.

The theoretical framework describing the SFSAE development is given in Sec. II. Section III explains the two experimental setups. Section IV presents results and compares the new SFSAE with the SFSE with compensation for attenuation. The validation of the method is finally discussed in Sec. V.

II. STRUCTURE FACTOR SIZE AND ATTENUATION ESTIMATOR (SFSAE)

Ultrasonic scattering from blood is mainly caused by the RBCs. Indeed, blood can be mechanically described as a colloidal suspension of RBCs in plasma. RBCs constitute the vast majority (97%) of the cellular content of blood and occupy a large volume fraction (hematocrit) of 35%–45% under normal conditions. These RBCs cannot be treated as independent scatterers since particle interactions (collision, attraction, deformation, and flow dependent motions) are strong. The theoretical model of US backscattering by blood that we developped[7] is based on the particle approach,[25,26] which consists of summing contributions from individual RBCs and modeling the RBC interaction by a particle pair-correlation function. Assuming that all the RBCs in the insonified blood are identical and using the Born approximation (weak scattering), the model predicts that the theoretical backscatter coefficient of blood is given by[23]

$$BSC_{theor}(k) = m\sigma_b(k)S(k)A(k), \tag{1}$$

where k is the wavenumber, m is the number density of RBCs in blood, σ_b is the backscattering cross section of a single RBC, S is the structure factor describing the spatial organization of RBCs, and A is the frequency-dependent attenuation function. The number density of RBCs m can be estimated by measuring the hematocrit H by microcentrifugation; m is then given by $m=H/V_s$, where V_s is the volume of a RBC (typically 87 μm^3). The backscattering cross-section σ_b of a weak scatterer small compared to the wavelength (Rayleigh scatterer) can be determined analytically as follows:

$$\sigma_b(k) = \frac{1}{4\pi^2}k^4V_s^2\gamma_z^2, \tag{2}$$

where $\gamma_z=(Z_{\mathrm{RBC}}-Z_{\mathrm{plasma}})/Z_{\mathrm{plasma}}$ is the fractional variation of impedance between the RBC and its suspending medium (i.e., the plasma). The structure factor S is by definition the Fourier transform of the pair-correlation function[26] g and can be approximated by its second-order Taylor expansion[7] in k as

$$S(k) = 1 + m\int (g(r)-1)e^{-2jkr}dr \approx W - \frac{12}{5}(kR)^2. \tag{3}$$

In this expression, $g(r)$ represents the probability of finding two particles separated by a distance r. W is the low-frequency limit of the structure factor $[\,S(k)|_{k\to 0}]$ called the packing factor.[26,27] R is the radius of 3D RBC aggregates assumed to be isotropic. We introduce $D=R/a$ as the isotropic diameter of an aggregate (expressed in number of RBCs) with a the radius of one RBC sphere-shaped model of volume V_s. The attenuation function A is given by

$$A(k) = e^{-4\alpha_0 k/8.68(c/2\pi)} = e^{-4\alpha_0 f/8.68}, \tag{4}$$

where c is the mean speed of sound in the intervening tissue layers, f is the frequency in MHz, and α_0 is the attenuation coefficient (in dB/MHz) defined by $\alpha_0=\Sigma_i\alpha_i e_i$, where α_i and e_i are, respectively, the intervening tissue layer attenuations (in dB/cm MHz) and thicknesses. One can note in Eq. (4) the coefficient 8.68 that expresses unit conversion from decibels to neper: $\alpha_0[\mathrm{Np/MHz}]=\alpha_0[\mathrm{dB/MHz}]/8.68$. According to the above equation, we thus assume, as a first approximation, that the attenuation increases linearly with the frequency: $\alpha(f)=\alpha_0 f/8.68$. Altogether, we obtain the following expression for the theoretical backscatter coefficient from blood:

$$BSC_{theor}(k) = \frac{1}{4\pi^2} mk^4 V_s^2 \gamma_z^2 \left(W - \frac{12}{5}(ka)^2 D^2 \right) e^{-4\alpha_0 k/8.68(c/2\pi)}. \quad (5)$$

In particular, for a given value of the wavenumber k (equivalently, a given value of the frequency f) and a given value of the attenuation coefficient α_0, $BSC_{theor}(k)$ is a linear function of the variables W and D^2.

The measured backscatter coefficient reported in this study was computed as

$$BSC_{meas}(k) = BSC_{ref}(k) \frac{\overline{P_{\text{meas}}(k)}}{\overline{P_{\text{ref}}(k)}}. \quad (6)$$

In Eq. (6), the mean backscattered power spectrum $\overline{P_{\text{meas}}}$ was obtained by averaging the power spectra of 20 backscattered echoes from blood. The mean power spectrum $\overline{P_{\text{ref}}}$ was obtained from a reference sample of non-aggregated RBCs at a low hematocrit of 6% (i.e., Rayleigh scatterers).[28] In this case, 20 echoes were also averaged. The backscatter coefficient of this reference sample BSC_{ref} was estimated by using the expression of the Perkus–Yevick packing factor for spheres W_{PYs} (that is a function of the hematocrit H) as follows:[26,27]

$$BSC_{ref}(k) = m\sigma_b(k) W_{\text{PYs}} = m\sigma_b(k) \frac{(1-H)^4}{(1+2H)^2}. \quad (7)$$

This reference sample was used to compensate the backscattered power spectrum $\overline{P_{\text{meas}}}$ for the electromechanical system response, and the depth-dependent diffraction and focusing effects caused by the US beam.

The packing factor W, aggregate diameter D, and total attenuation along the propagation path α_0 were determined by matching the measured BSC_{meas} given by Eq. (6) with the theoretical BSC_{theor} given by Eq. (5). For this purpose, we searched values of $(W, D^2, \alpha_0) \in (0,\infty)\times(0,\infty)\times[0,1]$, W and D being variables without dimension and α_0 expressed in dB/MHz, minimizing the cost function which synthesizes all of the wavenumbers k_i $(i=1\cdots N)$ within the −20 dB bandwidth of $\overline{P_{\text{meas}}}$:

$$\begin{aligned} F(W, D^2, \alpha_0) &= \sum_i \| BSC_{meas}(k_i) - BSC_{theor}(k_i) \|^2, \\ &= \sum_i \left\| BSC_{meas}(k_i) - \frac{1}{4\pi^2} mk_i^4 V_s^2 \right. \\ &\quad \left. \times \gamma_z^2 \left(W - \frac{12}{5}(k_i a)^2 D^2 \right) e^{-4\alpha_0 k/8.68(c/2\pi)} \right\|^2. \end{aligned} \quad (8)$$

The cost function had in the majority of cases reported in this study one minimum, as was observed by plotting the cost function surface $F(W, D^2, \alpha_0)$ with varying values of α_0. An example is given in Fig. 1. That is why a simple minimization routine *lsqnonlin* in MATLAB (The MathWorks, Inc., Natick, MA), i.e., a trust-region method based on the interior-reflective Newton method,[24] was first employed in our previous paper.[23] Nevertheless, on a possibility of the appearance of several minima, an exhaustive search on the value of α_0 was employed in this paper in order to ensure

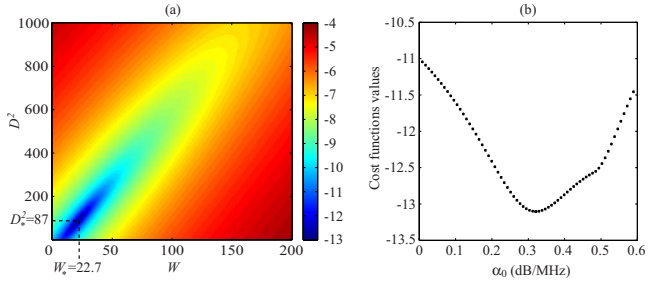

FIG. 1. (Color online) (a) Typical aspect of the logarithm of the cost function $F(W, D^2, \alpha_0)$ for a fixed value of α_0. The logarithm is shown here in order to enhance the visual contrast. This cost function has one minimum denoted (W_*, D^2_*) that depends on α_0. (b) Typical aspect of the function $\log(F(W_*, D^2_*, \alpha_0))$ for varying values of α_0 (W_* and D^2_* being calculated for each α_0). This cost function has a single minimum.

that the global minimum is found. If the value of α_0 is fixed, a quadratic function of the two variables W and D^2 is obtained, as can be seen from Eq. (8), and by calculating its critical points, a system of two linear equations of two unknowns can be easily solved. One can show using the Cauchy–Schwartz' inequality that the determinant of this system never vanishes (unless all frequencies are equal) and thus that the solution is unique. If the unique solution of this system denoted $(W_*(\alpha_0), D^2_*(\alpha_0))$ is such that $W_*(\alpha_0) \leq 0$ or $D^2_*(\alpha_0) \leq 0$, then the cost function $F(W, D^2, \alpha_0)$ has no global minimum on $(0,\infty)\times(0,\infty)$ (with the value of α_0 fixed). Also, this case means that the value of α_0 has to be rejected, since it is meaningless. Otherwise, the global minimum of $F(W, D^2, \alpha_0)$ on $(0,\infty)\times(0,\infty)$ occurs at $(W_*(\alpha_0), D^2_*(\alpha_0))$. In practice, there is a maximal value α_* of α_0 between 0 and 1 dB/MHz, for which $W_*(\alpha_0) \geq 0$ and $D^2_*(\alpha_0) \geq 0$. Thus, the global minimum of $F(W, D^2, \alpha_0)$ on the domain $(0,\infty)\times(0,\infty)\times[0,\alpha_*]$ is the global minimum of the function $F(W_*(\alpha_0), D^2_*(\alpha_0), \alpha_0)$ on the interval $[0,\alpha_*]$. The optimal value of α_0 can thus be obtained upon sweeping the interval $[0,\alpha_*]$. In our tests, we started the exhaustive search with a step of 10^{-5} dB/MHz. Then, the step was iteratively decreased by a factor of 10^{-1} dB/MHz, while the search is performed on the interval of length twice the preceeding step around the best value obtained so far. The iterative (multiresolution) exhaustive search was stopped after a step of 10^{-20} dB/MHz. At the end of the SFSAE algorithm, a simple test allowed to verify the validity of the solution. If the solution (W, D^2, α_0) of the optimization problem was such that W or D^2 was on the inferior boundary of the domain (i.e., W or D^2 are equal to zero), the solution was rejected since such values of W or D^2 are unrealistic. This last point will be discussed later in Sec. V D.

III. METHODS

A. Blood sample preparation

Blood from two different pigs were used for the two experiments in a Couette device and in a tube. This fresh porcine whole blood was obtained from a local slaughter house and anticoagulated with 3 g/l of ethylene diamine tetra acetic acid (EDTA). Then the whole blood was centri-

fuged and the plasma and buffy coat were removed. Two blood samples were then prepared for each experiment: (i) a H6 reference sample, which was a 6% hematocrit non-aggregating RBCs resuspended in physiological saline solution, and (ii) a 40% hematocrit T40 test sample, which consisted of RBCs resuspended in plasma to promote aggregation.

B. *In vitro* experiments

1. In vitro experiments in a Couette flow system (Couette device)

US measurements were first performed in a Couette device to produce a linear blood velocity gradient at a given shear rate (see Fig. 1 in Ref. 29). The system consists of a rotating inner cylinder with a diameter of 160 mm surrounded by a fixed concentric cylinder of diameter 164 mm. A 60 ml blood sample was sheared in the 2 mm annular space between both coaxial cylinders. An US scanner (Vevo 660, Visualsonics, Toronto, Canada) equipped with the RMV 710 probe was used in B-mode. The oscillating single-element focused circular transducer had a center frequency of 25 MHz, a diameter of 7.1 mm, and a focal depth of 15 mm. We acquired RF data from this scanner at a sampling frequency of 250 MHz with 8 bit resolution (Gagescope, model 8500CS, Montreal, Canada). The probe was mounted in the side wall of the fixed outer cylinder and was positioned to have its focal zone at the center of the gap between both cylinders. To ensure ultrasonic coupling, the hole within the outer stationary cylinder (containing the probe) was filled with a liquid agar gel based mixture. When solidified, this gel was cut to match the curvature of the cylinder to avoid any flow disturbance. The gel was a mixture of distilled water, 3% (w/w) agar powder (A9799, Sigma Chemical, Saint-Louis, MO), 10% (w/w) glycerol, and a specific concentration of 50 μm cellulose scattering particles (S5504 Sigmacell, Sigma Chemical, Saint-Louis, MO) that determined the attenuation coefficient. Five experiments were performed with five mixtures having SigmaCell (SC) concentrations varying from 0% to 1% (w/w). The 0% concentration constituted the non-attenuating gel and the four other mixtures mimicked skin attenuations.

All US measurements were made at room temperature. Prior to each measurement, the T40 blood was sheared at 200 s^{-1} during 30 s to disrupt RBC aggregates. The shear rate was then reduced to residual values of 5, 10, 20, 30, and 50 s^{-1} for 90 s until an equilibrium in the state of aggregation was reached. For each shear rate, 20 B-mode images were constructed from acquired rf echoes each 4 s for a total period of analysis of 80 s. Each image contained 384 vertical lines. For 180 vertical lines at the center of the B-mode images, echoes were selected with a rectangular window of axial length 0.4 mm at 20 depths every 0.031 mm (i.e., with 92% overlap between windows). For each depth, the power spectra of the backscattered rf echoes were averaged over 20 acquisitions (corresponding to the 20 acquired B-mode images) to provide $\overline{P_{\text{meas}}}$. This protocol was repeated five times with the same blood and with each of the five agar-based phantoms.

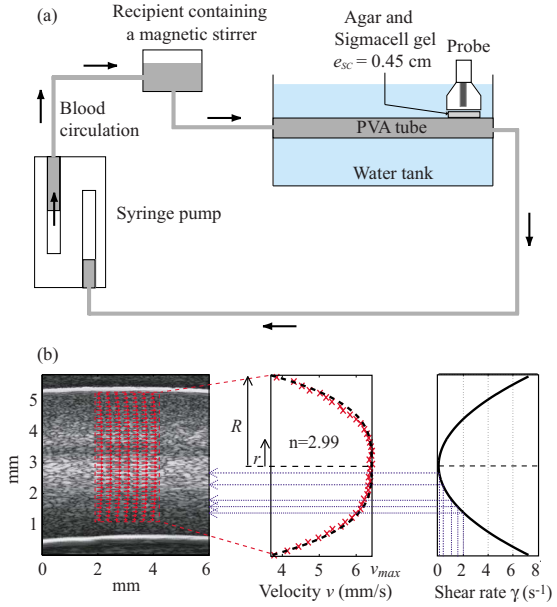

FIG. 2. (Color online) (a) Diagram of the experimental apparatus used in the tubular flow experiments. (b) Echographic image of the T40 blood in the tube (obtained with the US scanner Visualsonics) and estimates of particle displacement fields by B-mode speckle tracking and corresponding mean velocity and shear rate as a function of depths in the tube.

Then, the T40 blood was removed and the H6 sample was introduced in the Couette device. The H6 sample was sheared at 50 s^{-1} and coupled with the 0% SC concentration agar gel. Echoes were windowed as for the H40 sample at the same depths and their power spectra were averaged over 20 acquisitions to obtain $\overline{P_{\text{ref}}}$. This reference power spectrum allowed to normalize the average power spectrum $\overline{P_{\text{meas}}}$ [as described in Eq. (6), Sec. II].

2. In vitro experiments in a tube

In order to be closer to *in vivo* conditions, US measurements were also performed in a tubular flow device. The experimental test section was an horizontal tube made of polyvinyl alcohol (PVA) cryogel. This tube had an internal diameter of 4.9 mm and a length of 10 cm, and was immersed in a tank filled with degassed water at room temperature. The US measurements were made at a position 7 cm from the tube entrance with the Vevo 660 US scanner. The transducer focal point at 15 mm was positioned at the middle of the tube, imaged in the longitudinal plane. The T40 blood sample was circulated in the PVA tube using a double syringe pump (Harvard PHD 2000) at a constant flow rate from the outflow syringe, to the tube and the second inflow syringe. In order to ensure that the RBCs are disaggregated at the tube entrance, the T40 sample blood passed through a small recipient containing a magnetic stirrer just before entering the PVA tube, as indicated in Fig. 2(a). Similarly to the Couette experiments (Sec. III B 1), a layer of gel was placed between the probe and the tubular flow. Five experiments were successively performed on the same blood with five mixtures having SC concentrations: 0%, 1%, 1.5%, 2%, and 2.5% (w/w).

The flow rate was chosen equal to 5 ml/min to promote

TABLE I. Values of the average attenuations $\overline{\alpha_{SC}}$ of skin-mimicking phantoms expressed in dB/cm MHz and corresponding attenuation coefficients $\overline{\alpha_{SC}}e_{SC}$ expressed in dB/MHz for the Couette and tube experiments.

Sigmacell (SC) concentration (%)	Attenuation $\overline{\alpha_{SC}}$ (dB/cm/MHz)	Attenuation coefficient for the Couette flow device $\overline{\alpha_{SC}}e_{SC}$ (e_{SC}=1.3 cm) (dB/MHz)	Attenuation coefficient for the tube flow device $\overline{\alpha_{SC}}e_{SC}$ (e_{SC}=0.45 cm) (dB/MHz)
0	0.0054 ± 0.0015	0.0070 ± 0.0019	0.0024 ± 0.0006
0.25	0.088 ± 0.018	0.115 ± 0.024	⋯
0.5	0.168 ± 0.023	0.219 ± 0.030	⋯
0.75	0.246 ± 0.027	0.320 ± 0.035	⋯
1	0.316 ± 0.031	0.411 ± 0.040	0.142 ± 0.014
1.5	0.475 ± 0.053	⋯	0.214 ± 0.024
2	0.633 ± 0.051	⋯	0.285 ± 0.023
2.5	0.768 ± 0.060	⋯	0.346 ± 0.027

RBC aggregation and when 30 ml of blood had circulated in the tube, 20 B-mode images were constructed for 80 s. The data were processed as described for the *in vitro* experiment in the Couette device, except that echoes were selected with a rectangular window of length 0.4 mm at 65 depths every 0.031 mm (again with 92% overlaps). A reference measurement was done by using the H6 sample circulating in the tube at a flow rate of 5 ml/min. Echoes were windowed as for the H40 sample at the same 65 depths and their power spectra were averaged over 20 acquisitions to obtain $\overline{P_{ref}}$. One can note here that $\overline{P_{ref}}$ allow to compensate $\overline{P_{meas}}$ not only for the electromechanical system response, and the depth-dependent diffraction and focusing effects caused by the US beam, but also for the US response of the PVA cryogel tube.

3. Attenuation measurements for comparison with the SFSAE attenuation estimates

The attenuation coefficients of the reference (0% SC) and of the skin-mimicking phantoms were determined by using a standard substitution method. The Vevo 660 US scanner equipped with the same RMV 710 25 MHz transducer was used in M-mode and in transmission/reception with a reflector on the opposite side of the phantom for reflection measurements. Reflected signals were recorded both with and without the agar gel sample in the acoustic path. The attenuation coefficient was then estimated using a log spectral difference technique.[30] For a given concentration of SC, measurements were obtained from two different sample thicknesses, and for each, six regions were scanned for averaging purpose. In our experimental devices, thicknesses of skin-mimicking phantoms e_{SC} were fixed to 1.3 cm in the case of the Couette device and 0.45 cm for the tubular flow experiments. Values of the average attenuations $\overline{\alpha_{SC}}$ expressed in dB/cm MHz and of the attenuation coefficients $\overline{\alpha_{SC}}e_{SC}$ expressed in dB/MHz for the Couette and tube experiments are reported in Table I. As it can be observed in this table, attenuation coefficients of skin-mimicking phantoms were in the same range as the human dermis (which is 0.21 dB/MHz at 14–50 MHz considering a 1 mm dermis thickness[31]).

For the Couette device configuration, blood attenuation was also measured at different shear rates in the reflection mode. The gel had a 0% SC concentration, the probe was used in M-mode and the rotating inner cylinder was used as the reflector. For each shear rate, acquisitions of 20 rf lines were performed both with blood and with water in the Couette device. The water acquisition was used for normalization. For each acquisition, blood attenuation was estimated using the log spectral difference technique. These values were then averaged to provide $\overline{\alpha_{blood}}$. Values obtained were 0.053 ± 0.011, 0.036 ± 0.008, 0.024 ± 0.005, 0.016 ± 0.003, and 0.015 ± 0.003 dB/mm MHz for shear rates of 5, 10, 20, 30, and 50 s^{-1}, respectively.

4. Reference measurements for blood structural parameters with the 0% SC concentration phantom for in vitro experiments

For both *in vitro* devices, experiments with the 0% SC phantom were realized in order to have reference results on packing factors W_{ref} and aggregate diameters D_{ref}. For these reference measurements, the measured backscatter coefficient was compensated for predetermined values of blood and 0% SC phantom attenuations and thus computed as follows:

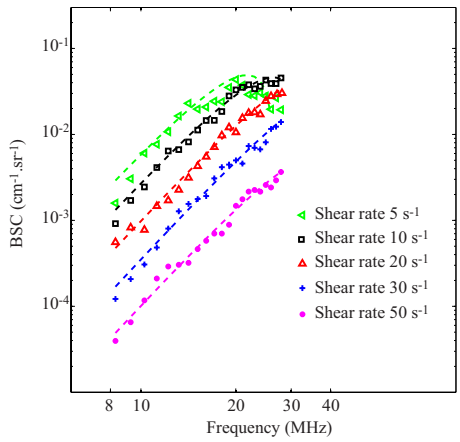

FIG. 3. (Color online) Backscatter coefficients for blood sheared at different residual shear rates and measured with the 0% SC concentration phantom, and corresponding fitting with the classical SFSE with compensation for blood attenuation (in dashed lines).

TABLE II. Reference values of the packing factor $\overline{W_{\text{ref}}}$ and diameter $\overline{D_{\text{ref}}}$ obtained with the SFSE at different residual shear rates. The parameter r^2 represents the correlation coefficient of the fitted SFSE model on experimental data BSC_{meas}.

Shear rate (s^{-1})	$\overline{W_{\text{ref}}}$	$\overline{D_{\text{ref}}}$	r^2
5	24.56 ± 2.82	10.11 ± 0.72	0.67 ± 0.02
10	9.14 ± 1.89	4.59 ± 0.78	0.95 ± 0.02
20	3.90 ± 0.79	2.68 ± 0.54	0.93 ± 0.03
30	1.39 ± 0.34	1.35 ± 0.38	0.95 ± 0.02
50	0.44 ± 0.040	0.82 ± 0.23	0.95 ± 0.03

$$BSC_{meas}(k) = BSC_{ref}(k)\frac{\overline{P_{\text{meas}}(k)}}{\overline{P_{\text{ref}}(k)}} \times e^{-4/8.68(\alpha_{\text{blood}}e_{\text{blood}}+\alpha_{\text{SC}}e_{\text{SC}})k(c/2\pi)}, \quad (9)$$

and the parameters W_{ref} and D_{ref} were deduced by fitting the measured backscatter coefficient to the theoretical backscatter coefficient using the classical SFSE:[7]

$$BSC_{theor}(k) = \frac{1}{4\pi^2}mk^4V_s^2\gamma_z^2\left(W_{\text{ref}} - \frac{12}{5}(ka)^2D_{\text{ref}}^2\right). \quad (10)$$

The parameters W_{ref} and D_{ref} were assumed to be true values of packing factors and aggregate diameters at all shear rates, and will be compared in Sec. IV with packing factors and diameters estimated by the SFSAE when skin-mimicking phantoms were used.

IV. RESULTS

A. *In vitro* experiments in the Couette device

Figure 3 shows the typical BSC_{meas} as a function of frequency for different residual shear rates in the case of 0% SC (i.e., reference measurements). Also represented are corresponding fitted curves obtained with the SFSE after compensation for predetermined values of blood attenuation. The parameters W_{ref} and D_{ref} were estimated over 20 depths and 180 rf lines of the B-mode image (i.e., 3600 estimations) in a chosen ROI. Their mean values $\overline{W_{\text{ref}}}$, $\overline{D_{\text{ref}}}$ as well as their standard deviations $\sigma_{W_{\text{ref}}}$, $\sigma_{D_{\text{ref}}}$ are reported in Table II. It can be noticed that the BSC_{meas} amplitude as well as the estimation of the parameters $\overline{W_{\text{ref}}}$ and $\overline{D_{\text{ref}}}$ decrease when the shear rate increases (i.e. when the level of aggregation becomes smaller). Also given in Table II is the correlation coefficient r^2 in order to assess the goodness of fit between the model and the measured data. It reveals that the highest level of aggregation (at 5 s^{-1}) had the worst fit, i.e., $r^2=0.67$.

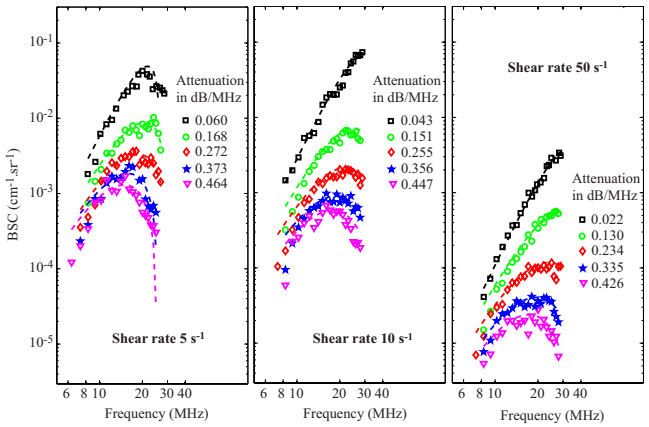

FIG. 4. (Color online) Measured backscatter coefficients for blood sheared at 5, 10, and 50 s^{-1} and with each of the five phantoms. The corresponding fitted models (in dashed lines) are the SFSE for the 0% SC phantom with compensation for blood attenuation (black squares) and the SFSAE for the four skin-mimicking phantoms (0.25%, 0.5%, 0.75%, and 1% SC).

Typical results of the SFSAE minimization procedure for the different agar phantoms at shear rates of 5, 10, and 50 s^{-1} are given in Fig. 4. The attenuations given in Fig. 4 correspond to the reference total attenuations $\overline{\alpha_{\text{ref}}}$ i.e., the sum of $\overline{\alpha_{\text{SC}}}$ and $\overline{\alpha_{\text{blood}}}$ estimated in the reflection mode as shown in Sec. III B 3. For all shear rates, an increase in the total attenuation has the effect of decreasing the amplitude of the BSC_{meas} at all frequencies and also has an effect of moving the peak of the BSC_{meas} at lower frequencies. It is very interesting to observe how attenuation influences the well-known quasi-Rayleigh backscattering behavior of disaggregated RBCs (i.e., at a shear rate of 50 s^{-1}). Indeed, for the 50 s^{-1} shear rate combined with the 0% SC concentration (reference measurement), the frequency dependence of the BSC_{meas} is close to f^4 and is thus quasi-linear on our log compressed scale, as expected. In the presence of attenuation, the frequency dependencies of the BSC_{meas} are drastically modified.

TABLE III. Reference values of the packing factor $\overline{W_{\text{ref}}}$ and diameter $\overline{D_{\text{ref}}}$ obtained with the SFSE (0% SC), and values of the packing factor $\bar{W}$, diameter $\bar{D}$, and attenuation $\overline{\alpha_0}$ obtained with the SFSAE (0.25%, 0.5%, 0.75%, and 1% SC) at the shear rate 5 s^{-1} in the Couette flow device. The parameter ϵ indicates the relative error and r^2 the correlation coefficient of the fitted SFSAE model on experimental data BSC_{meas}.

SC (%)	0	0.25	0.5	0.75	1
$\overline{W_{\text{ref}}}$	24.56 ± 2.82	⋯	⋯	⋯	⋯
$\bar{W}$	⋯	36.97 ± 12.40	23.33 ± 8.96	26.83 ± 8.65	23.01 ± 6.83
ϵ_W (%)	⋯	50.53	−0.65	9.24	−6.31
$\overline{D_{\text{ref}}}$	10.11 ± 0.72	⋯	⋯	⋯	⋯
$\bar{D}$	⋯	10.87 ± 1.74	9.05 ± 1.61	11.11 ± 1.68	11.08 ± 1.68
ϵ_D (%)	⋯	7.52	−10.48	9.89	9.59
$\overline{\alpha_{\text{ref}}}$ (dB/MHz)	0.060 ± 0.018	0.168 ± 0.035	0.272 ± 0.041	0.373 ± 0.046	0.464 ± 0.051
$\overline{\alpha_0}$ (dB/MHz)	⋯	0.246 ± 0.045	0.314 ± 0.046	0.409 ± 0.048	0.445 ± 0.051
ϵ_{α_0} (%)	⋯	46.43	15.44	9.65	−4.09
r^2	0.67 ± 0.02	0.81 ± 0.06	0.79 ± 0.05	0.79 ± 0.07	0.74 ± 0.05

TABLE IV. Reference values of the packing factor $\overline{W_{\text{ref}}}$ and diameter $\overline{D_{\text{ref}}}$ obtained with the SFSE (0% SC), and values of the packing factor $\bar{W}$, diameter $\bar{D}$, and attenuation $\overline{\alpha_0}$ obtained with the SFSAE (0.25%, 0.5%, 0.75%, and 1% SC) at the shear rate 10 s^{-1} in the Couette flow device. The parameter ϵ indicates the relative error and r^2 the correlation coefficient of the fitted SFSAE model on experimental data BSC_{meas}.

SC (%)	0	0.25	0.5	0.75	1
$\overline{W_{\text{ref}}}$	9.14 ± 1.89	⋯	⋯	⋯	⋯
$\bar{W}$	⋯	10.14 ± 3.03	9.35 ± 2.73	9.08 ± 1.93	10.86 ± 3.88
ϵ_W (%)	⋯	10.94	2.29	−0.65	18.81
$\overline{D_{\text{ref}}}$	4.59 ± 0.78	⋯	⋯	⋯	⋯
$\bar{D}$	⋯	5.25 ± 1.01	4.83 ± 0.81	4.84 ± 0.55	5.07 ± 1.26
ϵ_D (%)	⋯	14.38	5.23	5.45	10.45
$\overline{\alpha_{\text{ref}}}$ (dB/MHz)	0.043 ± 0.010	0.151 ± 0.032	0.255 ± 0.038	0.356 ± 0.043	0.447 ± 0.048
$\overline{\alpha_0}$ (dB/MHz)	⋯	0.172 ± 0.061	0.283 ± 0.053	0.367 ± 0.033	0.410 ± 0.057
ϵ_{α_0} (%)	⋯	13.91	10.98	3.09	−8.28
r^2	0.95 ± 0.02	0.86 ± 0.06	0.84 ± 0.08	0.86 ± 0.08	0.81 ± 0.06

The parameters W, D, and α_0 were estimated over 20 depths and 180 rf lines of the B-mode image in the same ROI used for the reference measurements. Their mean values $\bar{W}$, $\bar{D}$, $\overline{\alpha_0}$ and corresponding r^2 are reported in Tables III, IV and V for shear rates of 5, 10, and 50 s^{-1}, respectively. The values of $\bar{W}$ and $\bar{D}$ from the SFSAE are quite similar to the reference values of $\overline{W_{\text{ref}}}$ and $\overline{D_{\text{ref}}}$, as well as the total attenuation $\overline{\alpha_0}$ from the SFSAE are similar to the reference total attenuation $\overline{\alpha_{\text{ref}}}$, except for the shear rate of 5 s^{-1} and the 0.25% SC skin-mimicking phantom. In these tables, the relative errors for each parameter ϵ_W, ϵ_D, and ϵ_{α_0} correspond, respectively, to $(\bar{W}-\overline{W_{\text{ref}}})/\overline{W_{\text{ref}}}$, $(\bar{D}-\overline{D_{\text{ref}}})/\overline{D_{\text{ref}}}$, and $(\overline{\alpha_0}-\overline{\alpha_{\text{ref}}})/\overline{\alpha_{\text{ref}}}$.

Figure 5 shows quantitative images superimposed on the gray-scale B-mode images of the blood sheared at 10 s^{-1} in the Couette device. The color of each pixel was assigned based on the value of the parameters estimated by the SFSE with the 0% SC phantom and by the SFSAE with the four skin-mimicking phantoms. The color bars relate the pixels in the quantitative images to the estimated parameters (W, D, and α_0) in the chosen ROI. The black pixels in the ROI correspond to rejected solutions of the optimization method (when the estimated packing factor W or diameter D^2 was found equal to zero, which is unrealistic). A clear distinction between images of the estimated total attenuation with the four skin-mimicking phantoms is apparent, which was expected, whereas images of the estimated parameters W and D are quite similar, which was also wished.

For each residual shear rate, quantitative images for the three parameters W, D, and α_0 were constructed. The average estimates are summarized in Fig. 6. The lower and upper error bars for relative errors correspond to

$$\epsilon_{\text{lower}} = \frac{(\bar{X}-\sigma_X)-(\overline{X_{\text{ref}}}-\sigma_{X_{\text{ref}}})}{\overline{X_{\text{ref}}}-\sigma_{X_{\text{ref}}}},$$

$$\epsilon_{\text{upper}} = \frac{(\bar{X}+\sigma_X)-(\overline{X_{\text{ref}}}+\sigma_{X_{\text{ref}}})}{\bar{X}+\sigma_{X_{\text{ref}}}}, \tag{11}$$

where X represents one of the estimated parameters W, D, or α_0. For all shear rates and all skin-mimicking phantoms, the SFSAE gave quantitatively satisfactory estimates of $\bar{W}$ and $\bar{D}$ with relative absolute errors below 25%, except for the shear rate of 5 s^{-1} and the 0.25% SC skin-mimicking phantom.

The use of the SFSAE when there is little attenuation (i.e., the 0% SC phantom) was also investigated. Figure 7 presents the averaged parameters $\bar{W}$, $\bar{D}$, and $\overline{\alpha_0}$ obtained from the SFSAE with the 0% SC phantom. In this experiment, the total attenuation came mainly from the blood

TABLE V. Reference values of the packing factor $\overline{W_{\text{ref}}}$ and diameter $\overline{D_{\text{ref}}}$ obtained with the SFSE (0% SC), and values of the packing factor $\bar{W}$, diameter $\bar{D}$, and attenuation $\overline{\alpha_0}$ obtained with the SFSAE (0.25%, 0.5%, 0.75%, and 1% SC) at the shear rate 50 s^{-1} in the Couette flow device. The parameter ϵ indicates the relative error and r^2 the correlation coefficient of the fitted SFSAE model on experimental data BSC_{meas}.

SC (%)	0	0.25	0.5	0.75	1
$\overline{W_{\text{ref}}}$	0.44 ± 0.10	⋯	⋯	⋯	⋯
$\bar{W}$	⋯	0.46 ± 0.19	0.53 ± 0.21	0.38 ± 0.15	0.35 ± 0.11
ϵ_W (%)	⋯	4.54	20.45	−13.64	−20.45
$\overline{D_{\text{ref}}}$	0.82 ± 0.23	⋯	⋯	⋯	⋯
$\bar{D}$	⋯	0.89 ± 0.24	0.98 ± 0.28	0.90 ± 0.21	1.02 ± 0.19
ϵ_D (%)	⋯	8.54	19.51	9.76	24.39
$\overline{\alpha_{\text{ref}}}$ (dB/MHz)	0.022 ± 0.005	0.130 ± 0.027	0.234 ± 0.033	0.335 ± 0.038	0.426 ± 0.043
$\overline{\alpha_0}$ (dB/MHz)	⋯	0.148 ± 0.059	0.287 ± 0.060	0.370 ± 0.061	0.409 ± 0.063
ϵ_{α_0} (%)	⋯	13.85	22.65	10.45	−3.99
r^2	0.95 ± 0.03	0.91 ± 0.04	0.90 ± 0.06	0.86 ± 0.05	0.86 ± 0.06

$(0.015 \leq \alpha_{blood} \leq 0.053$ dB/MHz) and a little part from the SC phantom (0.007 dB/MHz). Also represented in Fig. 7 are the SFSAE results with the 0.25% SC phantom in order to compare the SFSAE performance in the presence of higher attenuation. When there is little attenuation, estimates of $\bar{W}$ were less accurate for shear rates of 5, 10, and 20 s^{-1} (in comparison with $\bar{W}$ obtained with the four other SC phantoms) with relative errors between 25% and 42%. Estimates of $\overline{\alpha_0}$ were between 0.041 and 0.133 dB/MHz, so the total attenuation were overestimated giving the largest relative errors between 124% and 211%.

Finally, to support the discussion reported later, the packing factor W_{comp} and the diameter of the aggregates D_{comp} were also evaluated by compensating the BSC_{meas} in the SFSE with the predetermined values measured in reflection mode (Sec. III B 3). Values of W_{comp} and D_{comp} were averaged over 20 depths and 180 lines of the B-mode image in the same ROI used for the reference measurements to provide $\overline{W_{comp}}$ and $\overline{D_{comp}}$. Results are presented in Fig. 8. The relative errors are below 25% for all shear rates and all skin-mimicking phantoms.

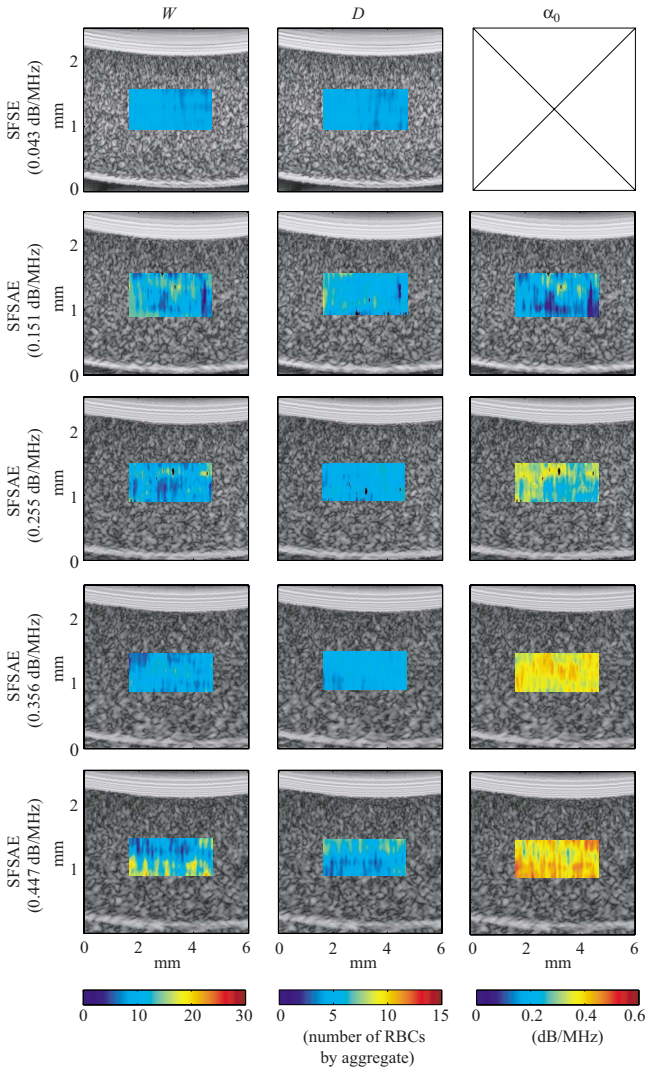

FIG. 5. (Color online) Quantitative images of blood sheared at 10 s^{-1} in the Couette device superimposed on the gray-scale B-mode images. Parameters were estimated by the classical SFSE with compensation for blood attenuation for the 0% SC concentration (top panel) and by the SFSAE for the four skin-mimicking phantoms.

B. *In vitro* experiments in the tubular flow device

Figure 9 shows quantitative images superimposed on the gray-scale B-mode images of tubular blood flow for each skin-mimicking phantom. As observed in the Couette experiment, a clear distinction between images of the estimated total attenuation is apparent, whereas images of the estimated parameters W and D are quite similar.

In order to know the shear rate profile in the tube, a speckle tracking method[32] was used to obtain the displacement fields of RBCs, as shown in Fig. 2(b). The displacement of the speckle pattern between each frame is then related to the velocity through the time elapsed between the images. The mean velocity profile across the tube was fitted to the following simple power-law model:

$$v(r) = v_{max}(1 - (r/R)^n), \tag{12}$$

where $v(r)$ is the mean velocity at radius r, R is the radius of the tube, v_{max} is the maximum velocity, and n is the power-law exponent ($n=2$ for parabolic flow). As expected, the velocity profile was slightly blunted due to RBC aggregation with $n=2.99$ [see Fig. 2(b)]. The shear rate profile, $\gamma(r)$, was deducted from this velocity profile by computing the derivative of $v(r)$:

$$\gamma(r) = -\frac{\partial v(r)}{\partial r} = n v_{max} \frac{r^{n-1}}{R^n}. \tag{13}$$

Five shear rates were selected on the shear rate profile (i.e., 0.1, 0.3, 1, 1.5, and 2 s^{-1}) corresponding to specific depths [see Fig. 2(b)] and thus corresponding to specific blood thicknesses (i.e., 2.7, 2.9, 3.4, 3.6, and 3.8 mm). For each

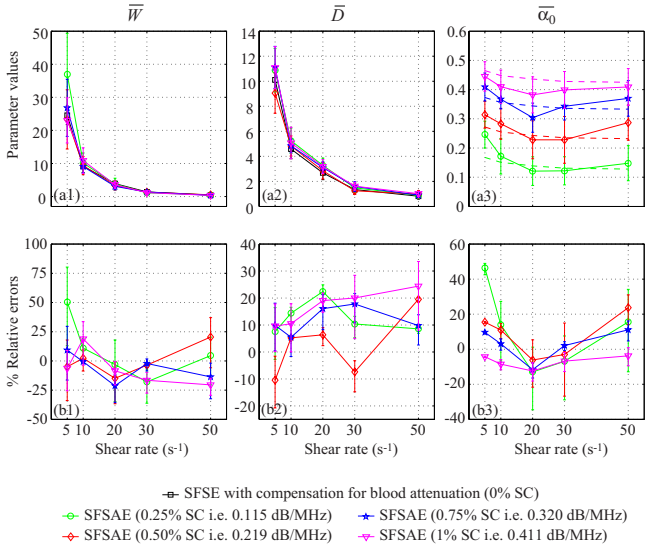

FIG. 6. (Color online) (a) Values of $\bar{W}$, $\bar{D}$, and $\overline{\alpha_0}$ (in dB/MHz) for different residual shear rates estimated by the SFSAE for the four skin-mimicking phantoms in the Couette experiments (mean ± standard deviation). Also represented are values of $\overline{W_{ref}}$ and $\overline{D_{ref}}$ estimated by the classical SFSE with compensation for blood attenuation for the 0% SC concentration and values of $\overline{\alpha_{ref}}$ in dashed lines. (b) Corresponding relative errors of $\bar{W}$, $\bar{D}$, and $\overline{\alpha_0}$.

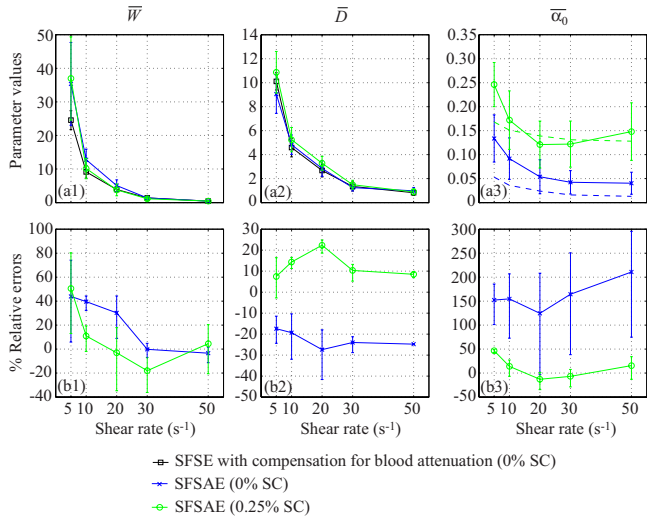

FIG. 7. (Color online) (a) Values of $\overline{W}$, $\overline{D}$, and $\overline{\alpha_0}$ (in dB/MHz) for different residual shear rates estimated by the SFSAE for the 0% and 0.25% SC concentrations. Also represented are values of $\overline{W_{\text{ref}}}$ and $\overline{D_{\text{ref}}}$ estimated by the classical SFSE with compensation for blood attenuation for the 0% SC concentration and values of $\overline{\alpha_{\text{ref}}}$ in dashed lines. (b) Corresponding relative errors of $\overline{W}$, $\overline{D}$, and $\overline{\alpha_0}$.

shear rate, values of W, D, and α_0 were simultaneously estimated by the SFSAE and averaged over three depths (one specific depth and their two adjacent depths, i.e., ± 0.031 mm) and 180 lines of the B-mode image. These average values of $\overline{W}$ and $\overline{D}$ obtained with the SFSAE were compared with average values of $\overline{W_{\text{ref}}}$ and $\overline{D_{\text{ref}}}$ evaluated by the SFSE with attenuation-compensation. The reference total attenuation $\overline{\alpha_{\text{ref}}}$ was the sum of $\overline{\alpha_{\text{SC}}} e_{\text{SC}}$ estimated in the reflection mode (see Sec. III B 3) and of $\overline{\alpha_{\text{blood}}} e_{\text{blood}}$, with e_{blood} varying for each shear rate. The blood attenuation $\overline{\alpha_{\text{blood}}}$ was

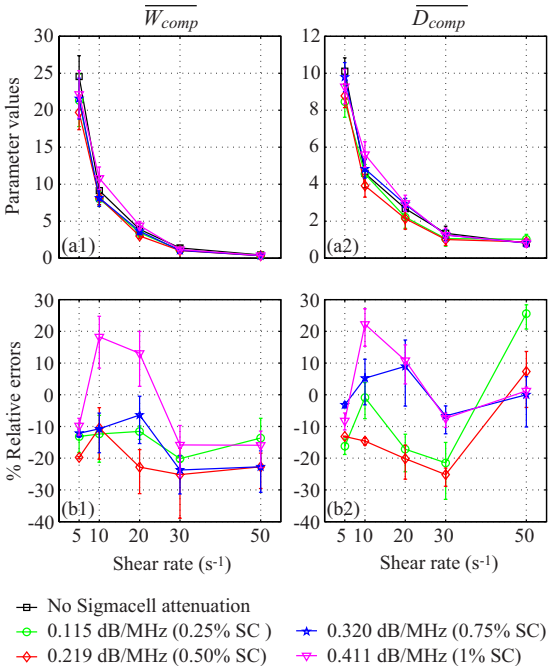

FIG. 8. (Color online) (a) Values of $\overline{W_{\text{comp}}}$ and $\overline{D_{\text{comp}}}$ for different residual shear rates estimated by the classical SFSE with compensation for attenuation by taking predetermined values measured in reflection mode for the four skin-mimicking phantoms (mean $\pm$ standard deviation). (b) Corresponding relative errors of $\overline{W_{\text{comp}}}$ and $\overline{D_{\text{comp}}}$.

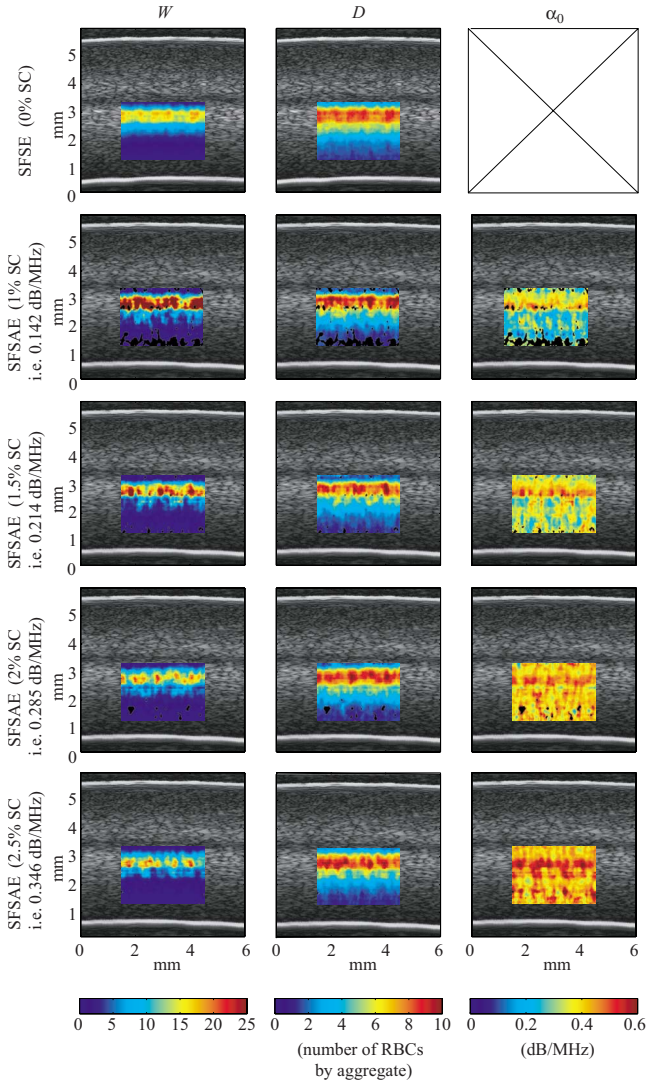

FIG. 9. (Color online) Quantitative images of blood sheared in a tube superimposed on the gray-scale B-mode images. Parameters were estimated by the classical SFSE with compensation for blood attenuation for the 0% SC concentration (top panel) and by the SFSAE for the four skin-mimicking phantoms.

arbitrarily chosen to be equal to 0.028 dB/mm MHz. This point will be discussed later in Sec. V A. Figure 10 summarizes these results. The SFSAE gave estimates of $\overline{W}$, $\overline{D}$, and $\overline{\alpha_0}$ with relative errors below 25% for all skin-mimicking phantoms at shear rates between 0.3 and 2 s^{-1}. Worse estimates were obtained for the smallest shear rate of 0.1 s^{-1}: for 1% and 1.5% SC concentrations, relative errors for $\overline{W}$ were 61% and 32%, respectively, those for $\overline{\alpha_0}$ were 56% and 47%, respectively, whereas those for $\overline{D}$ remained below 20%.

V. DISCUSSION

A. The difficulty to measure the blood attenuation in a tube flow device

The following discussion intends to explain why blood attenuation values in function of the shear rate cannot be obtained directly by measurements in a tube by a standard substitution method. The ideal protocol would be to realize blood attenuation measurements on a Couette apparatus (as

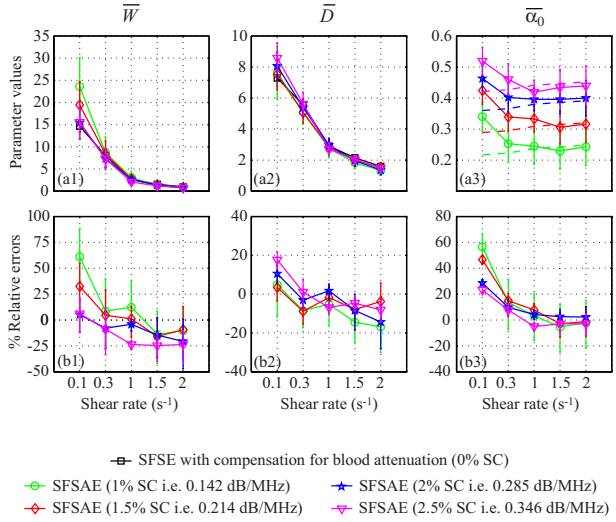

FIG. 10. (Color online) (a) Values of $\bar{W}$, $\bar{D}$, and $\bar{\alpha_0}$ (in dB/MHz) for different shear rates estimated by the SFSAE for the four skin-mimicking phantoms in the tube experiments (mean ± standard deviation). Also represented are values of $\overline{W_{\text{ref}}}$ and $\overline{D_{\text{ref}}}$ estimated by the classical SFSE with compensation for blood attenuation for the 0% SC concentration and values of $\overline{\alpha_{\text{ref}}}$ in dashed lines. (b) Corresponding relative errors of $\bar{W}$, $\bar{D}$ and $\bar{\alpha_0}$.

performed in Sec. III B 3) for the different shear rates present in the tube. In our experiments, the tube was not long enough (kinetic time) to obtain the same aggregate sizes as in the Couette device, that is why we chose a mean blood attenuation equal to 0.028 dB/mm MHz corresponding to the average of blood attenuations estimated with the Couette device for the different shear rates (see Sec. III B 3).

B. Limitations of the SFSAE with respect to *kR* and attenuation

For both Couette and tubular flow devices, the SFSAE gave good estimates of W, D, and α_0 with relative errors below 25% for all skin-mimicking phantoms and for all shear rates, except for the smallest shear rates and the smallest attenuations (0.115 dB/MHz for the Couette and 0.142 dB/MHz for the tube): relative errors for W were around 50% (Couette) and 61% (tube), for α_0 around 48% (Couette) and 56% (tube), for D below 25% as indicated in Figs. 6 and 10. In the tube experiment, one can also notice that relative errors for $\bar{\alpha_0}$ were always worse at the smallest shear rate (0.1 s^{-1}) for all skin-mimicking phantoms. For the peculiar case when there is little attenuation (i.e., ≤0.06 dB/MHz), the SFSAE did not give accurate results (absolute relative errors reaching 42% for W and 211% for α_0).

For the Couette device, the correlation coefficients given in Tables III–V reveal that the SFSAE produced quite good fits to data for all skin-mimicking phantoms and all shear rates, i.e., $0.74 \leq r^2 \leq 0.91$. Nevertheless, for both SFSE and SFSAE models, the smallest r^2 values occurred at the lowest shear rate of 5 s^{-1}. It is illustrated by fits of SFSE and SFSAE models in Fig. 4 that are worse at 5 s^{-1} (in comparison with fits at 10 and 50 s^{-1}), especially for the largest attenuation.

Considering the correlation coefficients and the accuracy of the estimates, both SFSE and SFSAE seem to reach their limit of applicability for large aggregate sizes: for the Couette experiments, typically $\overline{D_{\text{ref}}}$=10.11 in Table II (i.e., kR =2.88 with f=25 MHz) and for the tube experiments, typically $\overline{D_{\text{ref}}}$=7.29 in Fig. 10 (i.e., kR=2.08). To conclude, the SFSAE performed well for $kR<2.08$ and for total attenuations between 0.115 and 0.411 dB/MHz. In the following, these bounds will define the SFSAE validity domain, i.e., the domain where the SFSAE gives accurate estimates of W, D, and α_0.

It is interesting to note that the limitations of the SFSAE can be used to interpret the attenuation quantitative images obtained in the tubular flow device (Fig. 9). Indeed, these images are less homogeneous compared to those obtained in the Couette device since the standard deviations for attenuation were between 0.052 and 0.082 dB MHz for the tube and between 0.033 and 0.063 dB/MHz for the Couette. It is clearly linked with the presence of shear rates (<0.3 s^{-1}) in the tube experiments that result in large aggregate sizes outside the validity domain of the SFSAE.

C. Comparison of the SFSAE and SFSE with compensation for attenuation

For the Couette experiments, relative errors for $\bar{W}$ and $\bar{D}$ were generally below 25% (except for one value) with the SFSAE (Fig. 6) and with the SFSE with attenuation-compensation (Fig. 8). For W at 5 s^{-1} and a 0.25% SC, the SFSAE was not in its validity domain. In the SFSAE validity domain, the accuracy of the estimates obtained with the SFSAE was thus as satisfactory as those obtained with the SFSE with attenuation-compensation. The SFSAE has the major advantage to be easily applicable *in vivo* contrary to the SFSE attenuation-compensation method, needing the attenuation and thickness of the tissue intervening layers to be known.

D. Rejected solutions

In Figs. 5 and 9, one can notice the rejected solutions represented in black pixels. These solutions were rejected because their estimated diameters were equal to 0 (whereas the estimated packing factors never vanish). One might think that these rejected solutions come from cost functions having several local minima. Several cases of rejected solutions were studied and their corresponding cost functions had always a unique global minimum (data not shown).

To better understand what happened in these special cases, Fig. 11(a) represents two backscatter coefficients for blood sheared at 20 s^{-1} in the Couette flow device and measured with the 0.25% SC concentration phantom. Although both experimental backscatter coefficient were quite similar, the corresponding fitted models with the SFSAE gave two very different estimates of W, D, and α_0. One estimation corresponds to a kept solution and the other to a rejected solution with an estimate of D equal to 0. In Fig. 12 the mean values of $\bar{W}$, $\bar{D}$, and $\bar{\alpha_0}$ are summarized for the kept and rejected solutions estimated with the SFSAE for all shear rates and for the 0.25% SC concentration phantom. It can be observed, for the rejected solutions, that both $\bar{W}$ and $\bar{\alpha_0}$ were overestimated. This phenomenon can be explained by the

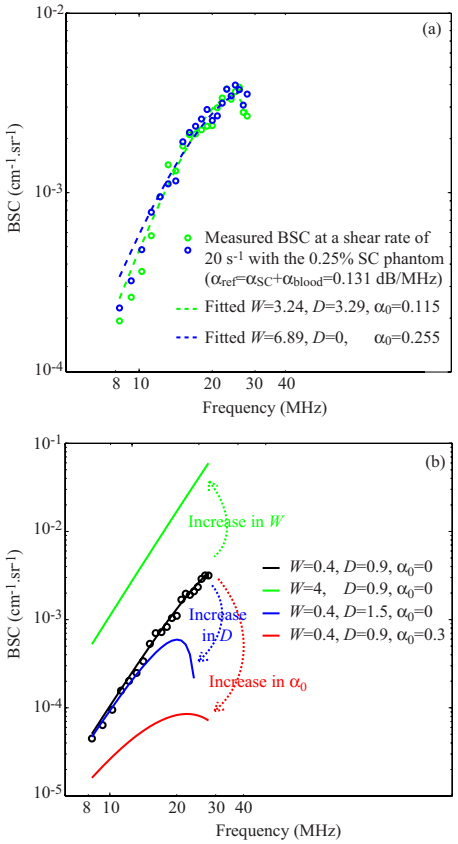

FIG. 11. (Color online) (a) Two backscatter coefficients for blood sheared at 20 s^{-1} in the Couette flow device and measured with the 0.25% SC phantom, and corresponding fitted models with the SFSAE. (b) Effect of increasing W, D, and α_0 on the backscattering coefficient on the SFSAE model.

difficulty to evaluate simultaneously three parameters that have the same effect on the backscatter coefficient as explained below. Figure 11(b) illustrates the respective effect of varying W, D, and α_0 on the backscatter coefficient. We arbitrarily selected a shear rate of 50 s^{-1} (i.e., a quasi-disaggregated case) and no SC attenuation. An increase in W has the effect of increasing the amplitude of the backscatter

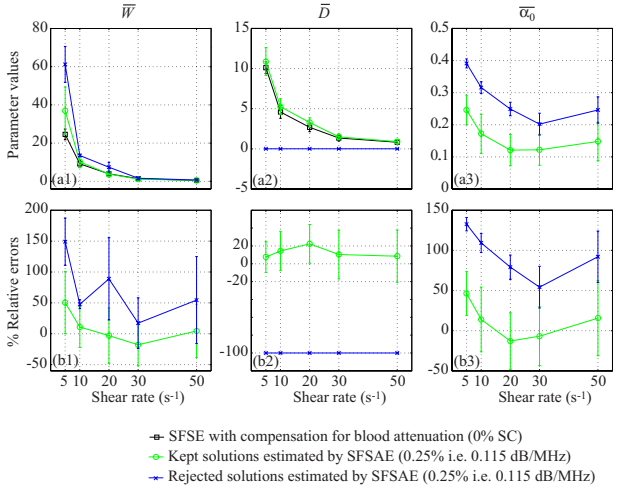

FIG. 12. (Color online) (a) Values of $\bar{W}$, $\bar{D}$, and $\overline{\alpha_0}$ (in dB/MHz) for the kept and rejected solutions of the SFSAE for different residual shear rates and for the 0.25% SC concentration phantom in the Couette experiment (mean ± standard deviation). (b) Corresponding relative errors of $\bar{W}$, $\bar{D}$, and $\overline{\alpha_0}$.

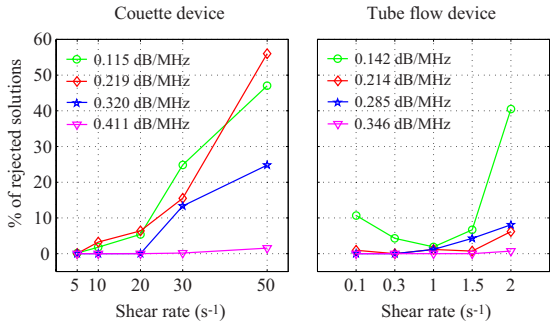

FIG. 13. (Color online) Percentage of rejected solutions in the ROIs: 20 depths and 180 RF lines for the Couette and 3 depths and 180 RF lines for the tube.

coefficient at all frequencies; whereas increasing D has an effect on the frequency dependence. But more interesting is to observe that an increase in α_0 has the effect of decreasing the amplitude and also of modifying the frequency dependence of the backscatter coefficient. It is thus difficult to estimate simultaneously these three parameters, because a modification in α_0 plays the same role (i.e., effects on the amplitude and the frequency dependence) that modifications in W (i.e., amplitude) and D (i.e., frequency dependence). The typical example given in Fig. 11(a) and parameter values presented in Fig. 12 can now be better understood. When the optimization method gives an unrealistic estimate of D equal to 0, the frequency dependence of the backscatter coefficient is only given by α_0, which is overestimated. But since increasing α_0 has also the effect of decreasing the amplitude of the backscatter coefficient, the overestimation of α_0 goes with the overestimation of W.

Figure 13 gives the percentage of rejected solutions in the ROIs (i.e., 20 depths and 180 rf lines for the Couette, as shown in Fig. 5, and three depths and 180 rf lines for the tube) at each shear rate for both Couette and tubular flow devices. For both devices, it can be clearly observed that percentages of rejected solutions are highest for experiments with the smallest attenuation (0.25% SC for the Couette and 1% SC for the tube) and with the highest shear rate, i.e., with quasi-disaggregated RBCs (50 s^{-1} for the Couette and 2 s^{-1} for the tube). The rejected solutions were thus more important when the frequency dependence was nearly Rayleigh. In our previous study,[23] we did not reject solution, that is why bad estimates were obtained for quasi-disaggregated RBCs. The rejection of some solutions was vital for having accurate results in the cases of quasi-disaggregated RBCs and of small total attenuation.

E. On the use of the SFSAE *in vivo*

The accuracy of the SFSAE was quantitatively demonstrated in a validity domain. One might question the use of this method *in vivo*. Although the SFSAE gave estimates with large errors for $kR > 2.08$ and $\alpha_0 \leq 0.06$ dB/MHz, the estimated parameters presented in Figs. 6 and 10 show that the SFSAE gave qualitatively satisfactory estimates for all SC phantoms at all shear rates, since the estimates of $\bar{W}$ and $\bar{D}$ versus shear rates had the same behaviors as $\overline{W_{\text{ref}}}$ and $\overline{D_{\text{ref}}}$. It means that the validity of estimates is possible for *in vivo*

experiments, since the SFSAE is able to predict the aggregation state and attenuation tendencies.

VI. CONCLUSION

Aggregating porcine RBCs were examined using US via *in vitro* experiments in Couette and tubular flow devices. Estimates of blood structural parameters and total attenuation were made from the frequency dependence of the US backscatter using the SFSAE model. This study revealed that the SFSAE provided accurate quantitative estimates of blood microstructure parameters W and D for $kR < 2.08$ and for total attenuations between 0.115 and 0.411 dB/MHz. In this validity domain, the results obtained with the SFSAE was quantitatively as satisfactory as those obtained with the SFSE with attenuation-compensation (i.e., when prior information on the attenuation is available). Outside this validity domain, the SFSAE was able to give the aggregation state tendency.

The SFSAE has been shown to be able of estimating blood backscattering properties in the presence of tissue intervening layers. This method is easily applicable *in vivo* because of the simultaneous estimation of the blood structural properties and total attenuation, contrary to the SFSE attenuation-compensation method, needing the attenuation and thickness of the tissue intervening layers to be known. Future works should focus on *in vivo* and *in situ* assessment of the pathophysiological impact of abnormal RBC aggregation on the cardiovascular system.

ACKNOWLEDGMENTS

This work was supported by the Canadian Institutes of Health Research (Grant Nos. MOP-84358 and CMI-72323), by the Heart and Stroke Foundation of Canada (Grant No. PG-05-0313), and by the National Institutes of Health of USA (Grant No. RO1HL078655).

[1]F. L. Lizzi, M. Greenebaum, E. J. Feleppa, and M. Elbaum, "Theoretical framework for spectrum analysis in ultrasonic tissue characterization," J. Acoust. Soc. Am. **73**, 1366–1373 (1983).
[2]E. J. Feleppa, F. L. Lizzi, D. J. Coleman, and M. M. Yaremko, "Diagnostic spectrum analysis in ophthalmology: A physical perspective," Ultrasound Med. Biol. **12**, 623–631 (1986).
[3]F. L. Lizzi, M. Ostromogilsky, E. J. Feleppa, M. C. Rorke, and M. M. Yaremko, "Relationship of ultrasonic spectral parameters to features of tissue microstructure," IEEE Trans. Ultrason. Ferroelectr. Freq. Control **33**, 319–329 (1986).
[4]M. F. Insana, J. G. Wood, and T. J. Hall, "Identifying acoustic scattering sources in normal renal parenchyma in vivo by varying arterial and ureteral pressures," Ultrasound Med. Biol. **18**, 587–599 (1992).
[5]E. J. Feleppa, T. Liu, A. Kalisz, M. C. Shao, N. Fleshner, and V. Reuter, "Ultrasonic spectral-parameter imaging of the prostate," Int. J. Imaging Syst. Technol. **8**, 11–25 (1997).
[6]M. L. Oelze, W. D. O'Brien, J. P. Blue, and J. F. Zachary, "Differentiation and characterization of rat mammary fibroadenomas and 4T1 mouse carcinomas using quantitative ultrasound imaging," IEEE Trans. Med. Imaging **23**, 764–771 (2004).
[7]F. T. H. Yu and G. Cloutier, "Experimental ultrasound characterization of red blood cell aggregation using the structure factor size estimator," J. Acoust. Soc. Am. **122**, 645–656 (2007).
[8]M. O'Donnell, J. W. Mimbs, and J. G. Miller, "Relationship between collagen and ultrasonic backscatter in myocardial tissue," J. Acoust. Soc. Am. **69**, 580–588 (1981).
[9]M. F. Insana, T. J. Hall, and J. L. Fishback, "Identifying acoustic scattering sources in normal renal parenchyma from the anisotropy in acoustic properties," Ultrasound Med. Biol. **17**, 613–626 (1991).
[10]K. A. Wear, M. R. Milunski, S. A. Wickline, J. E. Perez, B. E. Sobel, and J. G. Miller, "Differentiation between acutely ischemic myocardium and zones of completed infarction in dogs on the basis of frequency-dependent backscatter," J. Acoust. Soc. Am. **85**, 2634–2641 (1989).
[11]A. F. W. Van Der Steen, J. M. Thijssen, J. A. W. M. Van Der Laak, G. P. J. Ebben, and P. C. M. de Wilde, "Correlation of histology and acoustic parameters of liver tissue on a microscopic scale," Ultrasound Med. Biol. **20**, 177–186 (1994).
[12]K. A. Wear, B. S. Garra, and T. J. Hall, "Measurements of ultrasonic backscatter coefficients in human liver and kidney *in vivo*," J. Acoust. Soc. Am. **98**, 1852–1857 (1995).
[13]T. J. Hall, M. F. Insana, L. A. Harrison, and G. G. Cox, "Ultrasonic measurement of glomerular diameters in normal adult humans," Ultrasound Med. Biol. **22**, 987–997 (1996).
[14]Z. F. Lu, J. A. Zagzebski, and F. T. Lee, "Ultrasound backscatter and attenuation in human liver with diffuse disease," Ultrasound Med. Biol. **25**, 1047–1054 (1999).
[15]S. A. Goss, R. L. Johnston, and F. Dunn, "Comprehensive compilation of empirical ultrasonic properties of mammalian tissues," J. Acoust. Soc. Am. **64**, 423–457 (1978).
[16]P. He and J. F. Greenleaf, "Application of stochastic analysis to ultrasonic echoes—Estimation of attenuation and tissue heterogeneity from peaks of echo envelope," J. Acoust. Soc. Am. **79**, 526–534 (1986).
[17]L. X. Yao, J. A. Zagzebski, and E. L. Madsen, "Backscatter coefficient measurements using a reference phantom to extract depth-dependent instrumentation factors," Ultrason. Imaging **12**, 58–70 (1990).
[18]B. J. Oosterveld, J. M. Thijssen, P. C. Hartman, R. L. Romijn, and G. J. E. Rosenbusch, "Ultrasound attenuation and texture analysis of diffuse liver disease: Methods and preliminary results," Phys. Med. Biol. **36**, 1039–1064 (1991).
[19]V. Roberjot, S. L. Bridal, P. Laugier, and G. Berger, "Absolute backscatter coefficient over a wide range of frequencies in a tissue-mimicking phantom containing two populations of scatterers," IEEE Trans. Ultrason. Ferroelectr. Freq. Control **43**, 970–978 (1996).
[20]T. A. Bigelow, M. L. Oelze, and W. D. O'Brien, "Estimation of total attenuation and scatterer size from backscatter ultrasound waveforms," J. Acoust. Soc. Am. **117**, 1431–1439 (2005).
[21]T. A. Bigelow and W. D. O'Brien, "Signal processing strategies that improve performance and understanding of the quantitative ultrasound SPECTRAL FIT algorithm," J. Acoust. Soc. Am. **118**, 1808–1819 (2005).
[22]T. A. Bigelow and W. D. O'Brien, "Evaluation of the Spectral Fit algorithm as functions of frequency range and Δka_{eff}," IEEE Trans. Ultrason. Ferroelectr. Freq. Control **52**, 2003–2010 (2005).
[23]E. Franceschini, F. T. H. Yu, and G. Cloutier, "Simultaneous estimation of attenuation and structure parameters of aggregated red blood cells from backscatter measurements," J. Acoust. Soc. Am. **123**, EL85–EL91 (2008).
[24]T. F. Coleman and Y. Li, "A reective Newton method for minimizing a quadratic function subject to bounds on some of the variables," SIAM J. Optim. **6**, 10401058 (1996).
[25]L. Y. L. Mo and R. S. C. Cobbold, "Theoretical models of ultrasonic scattering in blood," in *Ultrasonic Scattering in Biological Tissues*, edited by K. K. Shung and G. A. Thieme (CRC, Boca Raton, FL, 1993), Chap. 5, pp. 125–170.
[26]V. Twersky, "Low-frequency scattering by correlated distributions of randomly oriented particles," J. Acoust. Soc. Am. **81**, 1609–1618 (1987).
[27]K. K. Shung, "On the ultrasound scattering from blood as a function of hematocrit," IEEE Trans. Ultrason. Ferroelectr. Freq. Control **SU-26**, 327–331 (1982).
[28]S. H. Wang and K. K. Shung, "An approach for measuring ultrasonic backscattering from biological tissues with focused transducers," IEEE Trans. Biomed. Eng. **44**, 549–554 (1997).
[29]L. C. Nguyen, F. T. H. Yu, and G. Cloutier, "Cyclic changes in blood echogenicity under pulsatile flow are frequency dependent," Ultrasound Med. Biol. **34**, 664–673 (2008).
[30]R. Kuc and M. Schwartz, "Estimating the acoustic attenuation coefficient slope for liver from reflected ultrasound signals," IEEE Trans. Sonics Ultrason. **SU-26**, 353–362 (1979).
[31]I. Raju and M. A. Srinivasan, "High-frequency ultrasonic attenuation and backscatter coefficients of *in vivo* normal human dermis and subcutaneous fat," Ultrasound Med. Biol. **27**, 1543–1556 (2001).
[32]R. E. N. Shehada and R. S. C. Cobbold, "Ultrasound methods for investigating the non-newtonian characteristics of whole blood," IEEE Trans. Ultrason. Ferroelectr. Freq. Control **41**, 96–104 (1994).

Simultaneous estimation of attenuation and structure parameters of aggregated red blood cells from backscatter measurements

Emilie Franceschini, François T. H. Yu, and Guy Cloutier
Laboratory of Biorheology and Medical Ultrasonics, University of Montreal Hospital Research Center, 2099 Alexandre de Sève (room Y-1619), Montréal, Québec, H2L 2W5, Canada
franceschiniemilie@yahoo.fr, francoisyu@videotron.ca, francoisyu@videotron.ca, guy.cloutier@umontreal.ca

Abstract: The analysis of the ultrasonic frequency-dependent backscatter coefficient of aggregating red blood cells reveals information about blood structural properties. The difficulty in applying this technique *in vivo* is due to the frequency-dependent attenuation caused by intervening tissue layers that distorts the spectral content of backscattering properties from blood microstructures. An optimization method is proposed to simultaneously estimate tissue attenuation and blood structure factor. With *in vitro* experiments, the method gave satisfactory estimates with relative errors below 22% for attenuations between 0.101 and 0.317 dB/cm/MHz, signal-to-noise ratios >28 dB and $kR<2.7$ (k being the wave number and R the aggregate radius).

PACS numbers: 43.80.Qf, 43.80.Cs, 43.35.Bf, 43.35.Yb [CC]
Date Received: October 5, 2007 **Date Accepted:** January 15, 2008

1. Introduction

Ultrasonic (US) backscattered echoes from blood contain frequency-dependent information that can be used to obtain quantitative parameters reflecting the aggregation state of red blood cells (RBCs). Recently, two parameters describing RBC aggregation, the packing factor and mean fractal aggregate diameter, were extracted from the structure factor size estimator (SFSE).[1] The SFSE is a second-order data reduction model based on the structure factor and adapted to a dense medium such as blood. This approach is based on the analysis of the backscattered power spectrum that contains information about the size, spatial organization, concentration and mechanical properties of scatterers (i.e., RBCs). The difficulty in applying the SFSE *in vivo* is that the spectral content of backscattered echoes is also affected by attenuation caused by intervening tissue layers between the probe and the blood flow. More generally, ultrasound scatterer size estimation techniques for tissue characterization (such as liver, kidney, prostate or breast) are facing similar challenges.[2,3] To correctly evaluate microstructural parameters, it is thus of major interest to take into account tissue attenuation effects. A few groups[2,4,5] developed measurement techniques to evaluate the frequency-dependent attenuation in order to compensate *a posteriori* the backscattered power spectrum. The goal of this letter is to further develop this strategy for *in vivo* measures of RBC scatterer sizes. We propose to simultaneously determine blood structural parameters and total attenuation by using an optimization method, termed the structure factor size and attenuation estimator (SFSAE).

This method consists in fitting the spectrum of the backscattered radio-frequency (rf) echoes from blood to an estimated spectrum by a modified SFSE model. This approach is similar to that presented by Bigelow *et al.*,[3] who estimated the effective radius of tissue microstructure and total attenuation from simulated backscattered signals. Herein, *in vitro* experimental evaluation of the SFSAE is performed. Porcine RBCs were sheared in a Couette flow system, and ultrasonic rf echoes were obtained using a 25 MHz center-frequency transducer. Since skin is one of the most attenuating tissue layers during *in vivo* scanning, three skin-mimicking phantoms with different attenuation coefficients were successively introduced between the

transducer and the blood flow. This study shows the SFSAE ability to evaluate three parameters (the packing factor, mean fractal aggregate diameter, and total attenuation).

2. Structure factor size and attenuation estimator

Blood can be seen as a very dense suspension of red cells. These RBCs cannot be treated as independent scatterers since particle interactions (collision, attraction, deformation, flow dependent motions) are strong. The theoretical model of ultrasound backscattering by blood that we developed[1] is based on the particle approach,[6,7] which consists of summing contributions from individual RBCs and modeling the RBC interaction by a particle pair-correlation function. Assuming that the Born approximation is valid (weak scattering), the model proposed in Ref. 1 can be modified to predict the theoretical backscatter coefficient from blood

$$BSC_{\text{theor}}(k) = m\sigma_b(k)S(k)A(k), \tag{1}$$

where k is the wave vector, m is the number density of RBCs in blood estimated by measuring the hematocrit H by microcentrifugation ($m=H/V_s$, where V_s is the volume of a RBC), σ_b is the backscattering cross section of a single RBC, S is the structure factor describing the spatial organization of RBCs, and A is the frequency-dependent attenuation function. The backscattering cross section σ_b of a weak scattering particle small compared to the wavelength (Rayleigh scatterer) can be determined analytically as follows: $\sigma_b(k)=1/(4\pi^2)k^4V_s^2\gamma_z^2$, where γ_z is the variation of impedance between the RBC and its suspending medium (i.e., the plasma). The structure factor S is by definition the Fourier transform of the pair-correlation function[7] g and can be approximated by its second-order Taylor expansion[1] in k as

$$S(k) = 1 + m\int (g(r)-1)e^{-2jkr}dr \approx W - \frac{12}{5}(kR)^2. \tag{2}$$

In this expression, $g(r)$ represents the probability of finding two particles separated by a distance r. W is the low-frequency limit of the structure factor ($S(k)|_{k\to 0}$) called the packing factor.[7,8] R is the radius of three-dimensional (3D) RBC aggregates assumed to be isotropic. We introduce $D=R/a$ as the isotropic diameter of an aggregate (expressed in number of RBCs) with a the radius of one RBC sphere-shaped model of volume V_s. The attenuation function A is given by: $A(k)=e^{-4\alpha_0 f}$, where f is the frequency and α_0 is the attenuation coefficient (in dB/MHz) defined by: $\alpha_0=\Sigma_i\alpha_i e_i$, where α_i and e_i are, respectively, the intervening tissue layer attenuations (in dB/cm/MHz) and thicknesses. According to the above equation, we thus assume, as a first approximation, that the attenuation linearly increases with the frequency: $\alpha(f)=\alpha_0 f$.

The measured backscatter coefficient reported in this study was computed as

$$BSC_{\text{meas}}(k) = BSC_{\text{ref}}(k)\frac{\overline{P_{\text{meas}}(k)}}{\overline{P_{\text{ref}}(k)}}. \tag{3}$$

In Eq. (3), the mean backscattered power spectrum $\overline{P_{\text{means}}}$ was obtained by averaging the power spectra of 400 backscattered echoes from blood. The mean power spectrum $\overline{P_{\text{ref}}}$ was obtained from a reference sample of non-aggregated RBCs at a low hematocrit of 6% (i.e., Rayleigh scatterers).[9] In this case, 400 echoes were also averaged. The backscatter coefficient of this reference sample BSC_{ref} was estimated using the "Rayleigh estimation" approach used by Yu and Cloutier,[1] which theoretical value is given by Eq. (13) in Ref. 8 (three-dimensional Perkus Yevick packing factor for cylinders). This reference sample was used to compensate the backscattered power spectrum $\overline{P_{\text{meas}}}$ for the electromechanical system response, and the depth-dependent diffraction and focusing effects caused by the US beam.

The packing factor W, aggregate diameter D and total attenuation along the propagation path α_0 were determined by matching the measured BSC_{meas} given by Eq. (3) with the theoretical BSC_{theor} given by Eq. (1). For this purpose, we searched values of W, D, and α_0

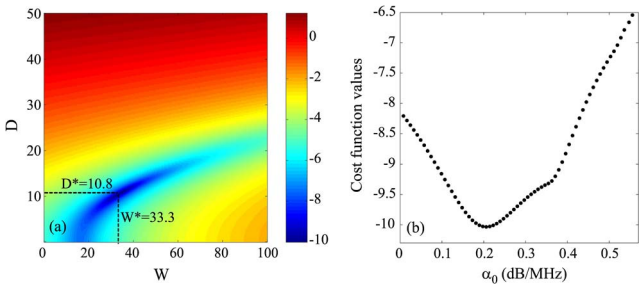

Fig. 1. (Color online) (a) Typical aspect of the logarithm of the cost function $F(W,D,\alpha_0)$ for a fixed value of α_0. The logarithm is shown here in order to enhance the visual contrast. This cost function has one minimum denoted $(W*,D*)$ that depends on α_0. (b) Typical aspect of the function $\log(F(W*,D*,\alpha_0))$ for varying values of α_0 ($W*$ and $D*$ being calculated for each α_0). This cost function has a single minimum.

minimizing the cost function $F(W,D,\alpha_0)=\|BSC_{\text{meas}}-BSC_{\text{theor}}\|^2$. In all studied cases, the cost function seemed to have a unique global minimum, as was observed by plotting the cost function surface $F(W,D)$ with varying values of α_0. An example is given in Fig. 1.

3. Methods

3.1 Experimental setup

US measurements were performed in a Couette flow system to produce a linear blood velocity gradient at a given shear rate (see Fig. 1 in Ref. 10). The system consisted of a rotating inner cylinder with a diameter of 160 mm surrounded by a fixed concentric cylinder of diameter 164 mm. A 60 ml blood sample was sheared in the 2 mm annular space between the two coaxial cylinders. The US scanner (Vevo 770, Visualsonics, Toronto, Canada) equipped with the RMV 710 probe was used in M mode for this study. The single-element focused circular transducer had a center frequency of 25 MHz, a diameter of 7.1 mm and a focal depth of 15 mm. We operated at a sampling frequency of 250 MHz with 8 bits resolution (Gagescope, model 8500CS, Montreal, Canada). The probe was mounted in the sidewall of the fixed outer cylinder and was positioned to have its focal zone at the center of both cylinders. To ensure ultrasonic coupling, the hole within the outer stationary cylinder (containing the probe) was filled with a liquid agar gel based mixture. When solidified, this gel was cut to match the curvature of the cylinder to avoid any flow disturbance. The gel was a mixture of distilled water, 3% (w/w) agar powder (A9799, Sigma Chemical, Saint Louis, MO), 8% (w/w) glycerol, and a specific concentration of 50 μm cellulose scattering particles (S5504 Sigmacell, Sigma Chemical, Saint Louis, MO) that determined the attenuation coefficient. Four experiments were performed with four mixtures having Sigmacell (SC) concentrations varying from 0% to 0.75% (w/w). The 0% concentration constituted the nonattenuating gel and the three other mixtures mimicked skin attenuations.

3.2 Attenuation measurements

The attenuation coefficients of the reference (0%) and three skin-mimicking phantoms α_p were determined by using a standard substitution method. Two transducers with center frequencies of 25 MHz (Vevo 770, Visualsonics, Toronto, Canada) and 20 MHz (V317-SM Panametrics, Waltham, MA) were coaxially aligned facing each other for transmission measurements. Transmitted signals were recorded both with and without the agar gel sample in the acoustic path. The attenuation coefficient was then estimated using a log spectral difference technique.[11] For a given concentration of SC, measurements were obtained from two different sample thicknesses, and for each, four regions were scanned for averaging purpose. Values obtained were 0.007 ± 0.002, 0.101 ± 0.028, 0.208 ± 0.029, and 0.317 ± 0.039 dB/cm/MHz for SC concentrations of 0, 0.25, 0.50, and 0.75%, respectively. The thickness of the skin-mimicking phantoms

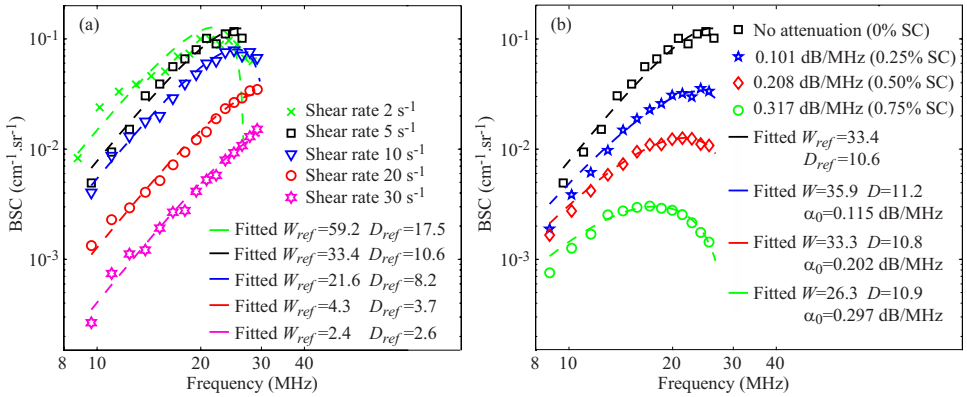

Fig. 2. (Color online) (a) Backscatter coefficients for blood sheared at different residual shear rates and measured with the 0% Sigmacell (SC) concentration phantom (no attenuation), and corresponding fitting with the classical SFSE with no compensation for attenuation. (b) Backscatter coefficients for blood sheared at 5 s^{-1} and measured with each of the four phantoms. The corresponding fitted models are the SFSE for the 0% SC phantom, and the SFSAE for the three other skin-mimicking phantoms (0.25, 0.5, and 0.75% SC).

e_p being fixed to 1 cm, their attenuation coefficients were thus in the same range as the human dermis (0.21 dB/MHz at 14–50 MHz considering a 1 mm dermis thickness[12]).

3.3 Blood preparation and measurement protocol

Fresh porcine whole blood was obtained from a local slaughterhouse, centrifuged and the plasma and buffy coat were removed. Two blood samples were then prepared: (i) a H6 reference sample, which was a 6% hematocrit non-aggregating RBCs resuspended in saline solution; and (ii) a 40% hematocrit T40 test sample, which consisted of RBCs resuspended in plasma to promote aggregation. The H6 sample was sheared at 50 s^{-1} and coupled with the 0% SC concentration agar gel. Echoes were selected with a rectangular window of length 0.8 mm at four depths every 0.2 mm (i.e., with 75% overlap between windows). For each depth, the power spectra of the backscattered echoes were averaged over 400 acquisitions to provide P_{ref}. Then, the H6 sample was removed and the T40 blood was introduced in the Couette device. In the first 30 s, a shear rate of 500 s^{-1} was applied to disrupt RBC aggregates. The shear rate was then reduced to residual values of 2, 5, 10, 20, and 30 s^{-1} for 90 s. After that, for each shear rate, acquisitions of 400 rf lines were performed for 80 s. Echoes were windowed as for the H6 sample at the same depths and their power spectra were averaged to obtain P_{meas}. This protocol was repeated four times with the four agar-based phantoms.

3.4 Reference measurements with the 0% SC concentration phantom

The experiment with the 0% SC phantom was realized in order to have reference results on packing factors W_{ref} and aggregate diameters D_{ref} obtained from the classical SFSE.[1] These parameters were assumed to be true values of packing factors and aggregate diameters for all shear rates, and will be compared in the next section with packing factors and diameters estimated by the SFSAE and by the SFSE when skin-mimicking phantoms are used.

It is important to emphasize the fact that the H6 reference sample was also measured with the 0% SC phantom. The phantom attenuation, although small with no SC, therefore affected equivalently both spectra P_{meas} and P_{ref} in Eq. (3). The resulting measured backscatter coefficient BSC_{ref} was thus not biased by attenuation. The terminology "no attenuation" was used for this experiment in the following.

4. Results and discussion

Figure 2(a) reports results on W_{ref} and D_{ref} for the SFSE in the case of no attenuation. Typical results of the SFSAE minimization procedure for the different agar phantoms at a shear rate of

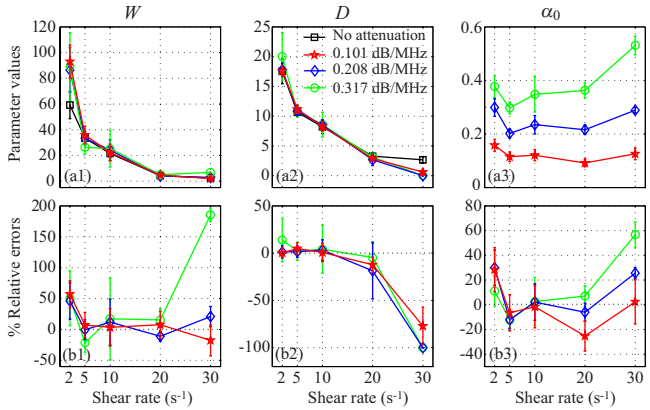

Fig. 3. (Color online) (a) Values of W, D, and α_0 (in dB/MHz) for different residual shear rates estimated by the classical SFSE for the 0% SC concentration and by the SFSAE for the three skin-mimicking phantoms. (b) Corresponding relative errors.

5 s^{-1} are given in Fig. 2(b). All results on W, D, and α_0 from the SFSAE are summarized in Fig. 3 for all residual shear rates. In this figure, the relative errors for each parameter correspond to: $(W-W_{\text{ref}})/W_{\text{ref}}$, $(D-D_{\text{ref}})/D_{\text{ref}}$, and $(\alpha_0-\alpha_{\text{ref}})/\alpha_{\text{ref}}$, with α_{ref} measured in transmissions. More specifically, α_{ref} corresponds to $\Sigma_i \alpha_i e_i = (\alpha_p e_p + \alpha_{\text{blood}} e_{\text{blood}})$, where $\alpha_p e_p$ is the skin-mimicking phantom attenuation estimated in transmission, and $\alpha_{\text{blood}} e_{\text{blood}}$ is the blood attenuation taken equal to 0.022 dB/MHz (Ref. 1) for all shear rates. To underline the necessity to take into account the attenuation, parameters W_{nocomp} and D_{nocomp} were evaluated with the SFSE without attenuation compensation when skin-mimicking phantoms were used. Because of the frequency-dependent distortion produced by the attenuating medium, large relative errors can be seen in Fig. 4(a) for both parameters. However, by compensating the backscatter coefficients

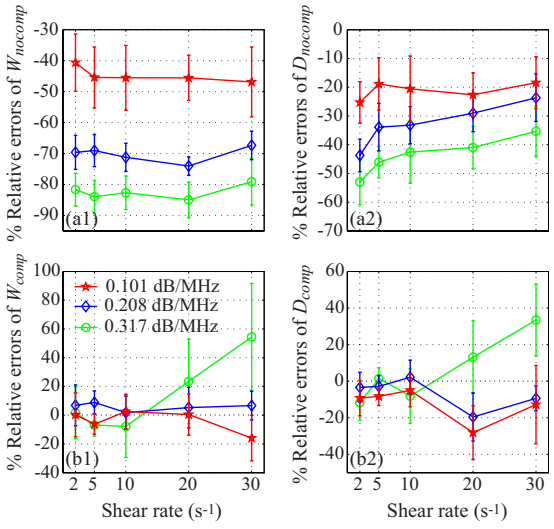

Fig. 4. (Color online) Relative errors of the packing factor and aggregate diameter for the three skin-mimicking phantoms obtained with the SFSE (a) with no compensation for attenuation (W_{nocomp} and D_{nocomp}), and (b) with attenuation compensation using the attenuation values estimated in transmission (W_{comp} and D_{comp}). Parameters W_{nocomp} and W_{comp} and similarly D_{nocomp} and D_{comp} are compared with W_{ref} and D_{ref}, respectively.

in the SFSE with the value measured in transmission (Sec. 3.2), relative errors in Fig. 4(b) are largely reduced to values comparable to those estimated with the SFSAE [see Fig. 3(b)].

The SFSAE (Fig. 3) gave quantitatively satisfactory estimates of W, D, and α_0 with relative errors below 22%, for shear rates between 5 and 20 s^{-1}. The SFSE with attenuation compensation [Fig. 4(b)] gave estimates of W_{comp} and D_{comp} with relative errors below 12% for shear rates between 2 and 10 s^{-1}, and below 28% for the shear rate of 20 s^{-1}. However, for the SFSAE, the average estimates for the shear rate of 2 s^{-1} were less accurate (relative errors below 57% for W and below 30% for α_0). The estimation of D was satisfactory at that shear rate (relative errors below 14%). The worse results of W, D, and α_0 were obtained at 30 s^{-1} for the highest attenuation.

The apparent limit of applicability of the SFSAE method for shear rates of 2 and 30 s^{-1} may be explained by considering the following. At 2 s^{-1}, for the frequency bandwidth considered (9–30 MHz), the SFSE and consequently the SFSAE seem to reach their limit of applicability for large aggregate sizes (typically $D_{ref}=17.5$ in Fig. 2(a), i.e., $kR=4.8$). This limit is illustrated by the bad fit of the SFSE model in Fig. 2(a) at 2 s^{-1}. The bad estimations of the SFSAE at 30 s^{-1} are explained by the fact that the aggregate diameters were estimated to zero and attenuations were overestimated. At this high shear rate, RBC aggregation is partially inhibited and the signal-to-noise ratio (SNR) of our measurements was reduced (≈ -4 dB between 20 and 30 s^{-1} for all phantoms). The accuracy of the estimates was thus degraded with increasing attenuations, as can be seen from the large relative errors at the highest attenuation with the SFSAE but also with the SFSE with attenuation compensation (W_{comp} and D_{comp}).

To conclude, the SFSAE performed well for $kR<2.7$ (i.e., $D=10$ at 5 s^{-1}) and under the condition that the SNR is sufficiently good (SNR$>$28 dB corresponding to the SNR at 30 s^{-1} for the 0.25% SC). Although the SFSAE gave less accurate estimates for 2 and 30 s^{-1}, the estimated parameter values presented in Fig. 3(a) show that the SFSAE gave qualitatively satisfactory estimates for the three SC skin-mimicking phantoms at all shear rates, since the estimates of W and D versus shear rates had the same behaviors as W_{ref} and D_{ref}.

5. Conclusions

The performance of the new SFSAE was assessed with experimental measurements on blood in a Couette flow device. The accuracy of the estimates obtained with the SFSAE was not as satisfactory as those obtained with the SFSE with attenuation compensation (i.e., when *a priori* are known about the attenuation). Nevertheless, the SFSAE has the major advantage to be easily applicable *in vivo* because of the simultaneous estimation of the blood structural properties and total attenuation (contrary to the SFSE attenuation-compensation method, needing the attenuation and thickness of the tissue intervening layers to be known). This work thus confirms the *in vivo* applicability of RBC aggregate size and structure estimations. Complementary studies are nevertheless required to determine the validity domain of the SFSAE according to kR and attenuation.

Acknowledgments

This work was supported by the Canadian Institutes of Health Research (Grant Nos. MOP-84358 and CMI-72323), by the Heart and Stroke Foundation of Canada (Grant No. PG-05-0313), and by the National Institutes of Health of USA (Grant No. RO1HL078655). Dr. Cloutier is recipient of a National Scientist award of the Fonds de la Recherche en Santé du Québec. The authors are also thankful to Dr. F. Destrempes for his helpful discussion on the optimization tool.

References

[1]F. T. H. Yu and G. Cloutier, "Experimental ultrasound characterization of red blood cell aggregation using the structure factor size estimator," J. Acoust. Soc. Am. **122**, 645–656 (2007).
[2]V. Roberjot, S. L. Bridal, P. Laugier, and G. Berger, "Absolute backscatter coefficient over a wide range of frequencies in a tissue-mimicking phantom containing two populations of scatterers," IEEE Trans. Ultrason. Ferroelectr. Freq. Control **43**, 970–978 (1996).
[3]T. A. Bigelow, M. L. Oelze, and W. D. O'Brien, "Estimation of total attenuation and scatterer size from

backscatter ultrasound waveforms," J. Acoust. Soc. Am. **117**, 1431–1439 (2005).
[4]P. He and J. F. Greenleaf, "Application of stochastic analysis to ultrasonic echoes—Estimation of attenuation and tissue heterogeneity from peaks of echo envelope," J. Acoust. Soc. Am. **79**, 526–534 (1986).
[5]B. J. Oosterveld, J. M. Thijssen, P. C. Hartman, R. L. Romijn, and G. J. E. Rosenbusch, "Ultrasound attenuation and texture analysis of diffuse liver disease: Methods and preliminary results," Phys. Med. Biol. **36**, 1039–1064 (1991).
[6]L. Y. L. Mo and R. S. C. Cobbold, "Theoretical models of ultrasonic scattering in blood," in *Ultrasonic Scattering in Biological Tissues*, edited by K. K. Shung and G. A. Thieme (CRC, Boca Raton, FL, 1993), Chap. 5, pp. 125–170.
[7]V. Twersky, "Low-frequency scattering by correlated distributions of randomly oriented particles," J. Acoust. Soc. Am. **81**, 1609–1618 (1987).
[8]K. K. Shung, "On the ultrasound scattering from blood as a function of hematocrit," IEEE Trans. Sonics Ultrason. **SU-29**, 327–331 (1982).
[9]S. H. Wang and K. K. Shung, "An approach for measuring ultrasonic backscattering from biological tissues with focused transducers," IEEE Trans. Biomed. Eng. **44**, 549–554 (1997).
[10]L.-C. Nguyen, F. Yu, and G. Cloutier, "*In vitro* study of frequency-dependent blood echogenicity under pulsatile flow," Proc.-IEEE Ultrason. Symp. 2007, 2507–2510.
[11]R. Kuc and M. Schwartz, "Estimating the acoustic attenuation coefficient slope for liver from reflected ultrasound signals," IEEE Trans. Sonics Ultrason. **SU-26**, 353–362 (1979).
[12]B. I. Raju and M. A. Srinivasan, "High-frequency ultrasonic attenuation and backscatter coefficients of *in vivo* normal human dermis and subcutaneous fat," Ultrasound Med. Biol. **27**, 1543–1556 (2001).

B.2 Compréhension de la diffusion ultrasonore par des fantômes de tumeurs denses

A5 FRANCESCHINI E. & GUILLERMIN R.
2012 Experimental assessment of four ultrasound scattering models for characterizing concentrated tissue-mimicking phantoms, **J. Acoust. Soc. Amer. 132**(6) 3735-3747.

A3 FRANCESCHINI E., GUILLERMIN R., TOURNIAIRE F., ROFFINO S., LAMY E.,& LANDRIER J.-F.
2014 Structure Factor Model for understanding the measured backscatter coefficients from concentrated cell pellet biophantoms, **J. Acoust. Soc. Amer. 135**(6) 3620-3631.

Experimental assessment of four ultrasound scattering models for characterizing concentrated tissue-mimicking phantoms

Emilie Franceschini[a] and Régine Guillermin
Laboratoire de Mécanique et d'Acoustique LMA–CNRS UPR 7051, Aix-Marseille Université, Centrale Marseille, 13402 Marseille Cedex 20, France

(Received 11 June 2012; revised 8 October 2012; accepted 15 October 2012)

Tissue-mimicking phantoms with high scatterer concentrations were examined using quantitative ultrasound techniques based on four scattering models: The Gaussian model (GM), the Faran model (FM), the structure factor model (SFM), and the particle model (PM). Experiments were conducted using 10- and 17.5-MHz focused transducers on tissue-mimicking phantoms with scatterer concentrations ranging from 1% to 25%. Theoretical backscatter coefficients (BSCs) were first compared with the experimentally measured BSCs in the forward problem framework. The measured BSC versus scatterer concentration relationship was predicted satisfactorily by the SFM and the PM. The FM and the PM overestimated the BSC magnitude at actual concentrations greater than 2.5% and 10%, respectively. The SFM was the model that better matched the BSC magnitude at all the scatterer concentrations tested. Second, the four scattering models were compared in the inverse problem framework to estimate the scatterer size and concentration from the experimentally measured BSCs. The FM did not predict the concentration accurately at actual concentrations greater than 12.5%. The SFM and PM need to be associated with another quantitative parameter to differentiate between low and high concentrations. In that case, the SFM predicted the concentration satisfactorily with relative errors below 38% at actual concentrations ranging from 10% to 25%.
 [http://dx.doi.org/10.1121/1.4765072]

PACS number(s): 43.35.Bf, 43.35.Yb, 43.80.Vj, 43.80.Cs [CCC] Pages: 3735–3747

I. INTRODUCTION

Quantitative ultrasound (QUS) techniques are based on the frequency-based analysis of the signals backscattered from biological tissues to determine the physical properties of the average tissue microstructures. These tissue characterization techniques aim to differentiate between diseased and healthy tissue and to detect cancer tumors. QUS techniques rely on theoretical scattering models to fit the spectrum of the echoes backscattered by biological tissues to an estimated spectrum using an appropriate model. The theoretical scattering model most frequently used for this purpose is the Gaussian model (GM) developed by Lizzi[1,2] that yields two tissue properties: The average scatterer size and the acoustic concentration (i.e., the product of the scatterer number density by the square of the relative impedance difference between the scatterers and the surrounding medium). This approach has been successfully used to characterize the eye,[3] prostate,[4] breast,[5–7] apoptotic cells,[8] and cancerous lymph nodes.[9] Other theoretical scattering models such as the fluid-filled sphere model (FFSM)[6,7] and the solid sphere model[10] [which we refer to here as the Faran model (FM)] have also been used to predict average scatterer sizes by modeling the medium by an ensemble of fluid or solid spheres. In the aforementioned models (GM, FFSM and FM), the scatterers were assumed to be randomly distributed (i.e., to have a low scatterer concentration), and multiple scattering was neglected (in line with the Born approximation). Under these hypotheses, the power of the backscattered signals increases linearly with the scatterer concentration and depends on the size and acoustic properties of the tissue scattering structures. This linear relationship has been used to monitor the scatterer size and concentration.

However, the assumption that the scatterers are randomly distributed may not hold in tumors with densely packed cells.[11] This means that a scattering theory involving a high cell concentration (i.e., accounting for a dense medium) should improve QUS techniques to determine the microstructural properties of tissues. Some theoretical efforts have been made in the field of ultrasonic blood characterization to take the high cell concentrations into account[12] because the concentration of red blood cells in blood (or hematocrit) ranges between 30% and 50%. In the Rayleigh scattering regime (i.e., where the product of the wavenumber by the scatterer radius is $ka \ll 1$), Twersky[13] developed a particle model (PM) giving an expression for the backscattered intensity in terms of the single-particle backscattering cross section, the particle number density, and the packing factor. The packing factor is a measure of orderliness in the spatial arrangement of particles. It depends on the cell concentration but not on the frequency. The PM succeeded in explaining the nonlinear relationship between the backscatter amplitude and the scatterer concentration in the case of non-aggregating red blood cells.[14] Again in the field of blood characterization, the PM was later generalized to include any cell spatial distributions (i.e., aggregating red blood cell distributions) by introducing the frequency dependent structure factor and called the structure factor model (SFM).[15,16] The SFM sums the contributions from individual cells and models the cellular interaction by a statistical mechanics structure factor, which is defined as

[a]Author to whom correspondence should be addressed. Electronic mail: franceschini@lma.cnrs-mrs.fr

the Fourier transform of the spatial distribution of the cells.[15,16] Note that the low frequency limit of the structure factor is by definition the packing factor used under Rayleigh conditions.[13] Until quite recently, the PM and SFM were only used for blood characterization purposes, but Vlad *et al.*[11] have performed two-dimensional computer simulations based on the SFM to explain the backscatter behavior as a function of the particle size variance in the case of centrifuged cells undergoing cell death processes. These centrifuged cells mimicked the spatial distribution and packing of tumor cells.[11]

The aim of this study was to compare the backscatter coefficient (BSC) predictions given by four theoretical scattering models, namely, the GM, FM, PM, and SFM, with the BSCs measured experimentally on tissue-mimicking phantoms. These phantoms consisted of polyamide microspheres (mean radius, 6 μm) suspended in water at various scatterer concentrations ranging from 1% to 25%. The high scatterer concentrations were used to mimic densely packed cells in tumors. Ultrasonic backscatter measurements were performed at frequencies ranging from 6 to 22 MHz. The theoretical BSCs based on different scattering models were first compared with the BSCs measured experimentally in the forward problem framework, i.e., the theoretical BSCs were determined from known structural and acoustical properties of the polyamide microspheres. Second, comparisons were made between the four theoretical scattering models in the inverse problem framework to estimate the scatterer size and concentration from the experimentally measured BSCs. To our knowledge, the scatterer concentration has never been previously determined using the PM and SFM. Last, the validity of the PM and the SFM as means of determining scatterer concentrations is discussed.

II. SCATTERING

Four scattering models, GM, FM, SFM, and PM, are presented in this section. For all four scattering models, the formulations were written for monodisperse spheres, and it was assumed that no multiple scattering occurred among the scatterers. When solving the inverse problem in the framework of each theory, the acoustical properties of spheres and the surrounding fluid were assumed to be known *a priori*, and a minimization procedure was used to fit a curve to the measured BSC to estimate the size a^* and concentration ϕ^* of the scatterers.

A. The GM

The BSC can be modeled using a spatial autocorrelation function describing the shape and distribution of the scatterers in the medium. The scattering sites are usually assumed to be randomly distributed and to have simple geometric shapes, which can be modeled in the form of Gaussian scatterers representing continuous functions of changing impedance. In this framework, the BSC can be expressed as the product of the BSC in the Rayleigh limit and the backscatter form factor.[17] The form factor describes the frequency dependence of the scattering based on the size and shape of the scatterers. The Gaussian form factor has been used for many applications.[3–9] It describes tissue structures as continuously varying distributions of acoustic impedance fluctuations about the mean value, and the effective radius is related to the impedance distribution of the scatterer.

The theoretical BSC used with the GM formulation is therefore written as follows:[5,17]

$$BSC_{GM}(k) = \frac{k^4 V_s^2 n_z}{4\pi^2} e^{-0.827k^2a^2}, \tag{1}$$

where k is the wave number, V_s the sphere volume, n_z the acoustic concentration, and a the mean effective radius of the scatterer.

The effective radius a^* and the acoustic concentration n_z^* were determined by comparing the logarithm of the experimental BSC values, denoted BSC_{exp}, with the logarithm of the theoretical BSC_{GM} given by Eq. (1) as previously done by Oelze *et al.*[6] Note that this fit was realized in the frequency bandwidth from 6 to 22 MHz.

B. The FM

The original theory developed by Faran[18] provides an exact solution for the scattering of sound by a solid sphere in a surrounding fluid medium and therefore includes shear waves in addition to compressional waves. The sphere is assumed to be insonified by a harmonic plane wave and to be located far from the point at which the scattered pressure field is observed. In the present study, the differential backscattering cross section at 180° for a single scatterer σ_b was computed for a sphere of radius a using Faran's theory[18] and then scaled by the number density to obtain the BSC from an ensemble of identical solid spheres as follows:

$$BSC_{FM}(k) = \frac{\phi}{V_s}\sigma_b(k), \tag{2}$$

where ϕ is the scatterer concentration. The ratio ϕ/V_s, denoted m, corresponds to the number density of spheres.

The values of the unknown parameters were estimated by matching the experimentally measured BSC_{exp} with the theoretical BSC_{FM} given by Eq. (2). For this purpose, we searched for values of $(a, \phi) \in [0, 50]\times[0.001, 0.74]$, where a was expressed in μm, minimizing the cost function:

$$F_{FM}(a,\phi) = \sum_i \|BSC_{FM}(k_i) - BSC_{\text{exp}}(k_i)\|^2. \tag{3}$$

Note that the maximum concentration was fixed to 0.74, which corresponds to the closely packed hexagonal arrangement. The cost function synthesizes all the wavenumbers k_i $(i = 1,\ldots, N)$ in the 6–22 MHz frequency bandwidth. Figures 1(a) and 1(b) give an example of a cost function surface $F_{\text{FM}}(a, \phi)$ obtained from the experiments performed with an actual microsphere radius of 6 μm and an actual concentration of 2.5% presented in the following text in Sec. III. It can be seen from this figure that at a given value of the radius, the cost functions have a single minimum. Figure 1(c) shows the gradient in the region of interest (ROI) around the values of the actual parameters.

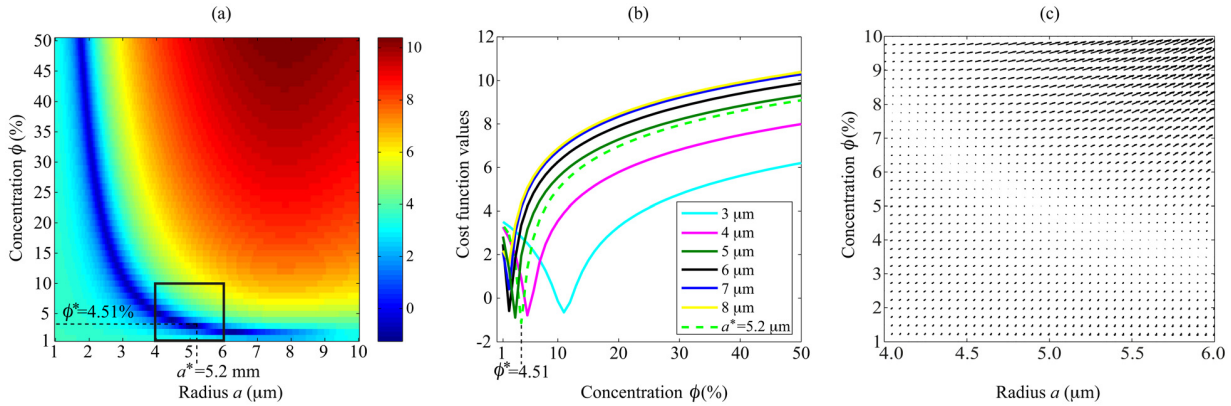

FIG. 1. (Color online) (a) Typical aspect of the logarithm of the cost function $F_{FM}(a, \phi)$ for the FM obtained from the experiments with actual microsphere radius of 6 μm and actual concentration of 2.5%. The logarithm is shown here to enhance the visual contrast. Black rectangle indicates the ROI used to compute the gradient in subplot (c). (b) Typical aspects of the function log $[F_{FM}(a, \phi)]$ obtained with several fixed values of a. These cost functions have a single minimum. (c) Direction and relative magnitude of the gradient in the ROI around the values of the actual parameters.

Because there exists no analytical expression for σ_b using Faran's theory,[18] an exhaustive search was conducted on the value of a to minimize the cost function F_{FM} given by Eq. (3). In these studies, we started the exhaustive search in the 1–50 μm range with a 5 μm step. The step was then decreased to 0.1 μm, while performing the search 10 μm around, the best value obtained so far. At each fixed value of the radius, the parameter ϕ was obtained using a trust-region-reflective algorithm with a minimization routine *lsqnonlin* in MATLAB (The MathWorks, Natick, MA).

C. The SFM and the PM

The SFM[15] is based on the assumption that at high scatterer concentrations, interference effects are mainly caused by correlations between the spatial positions of individual scatterers. The SFM has generally been applied to an ensemble of fluid spheres to model red blood cells in blood.[15,16,19] Herein, the SFM was slightly adapted to the case of an ensemble of solid spheres that are homogeneously distributed in space. In comparison with the Faran model described in Eq. (2), the SFM considers the interference effects relatively easily by replacing the single-particle backscattering contribution $\sigma_b(k)$ by the product $\sigma_b(k)S(k)$, where $S(k)$ is the structure factor depending on the scatterer concentration and the pattern of the spatial arrangement of the scatterers. By considering an ensemble of identical solid spheres of radius a, the theoretical BSC for the SFM formulation is given by

$$BSC_{SFM}(k) = \frac{\phi}{V_s}\sigma_b(k)S(k), \tag{4}$$

where the differential backscattering cross section σ_b was calculated using the Faran's theory. The structure factor S is related by definition to the three-dimensional (3D) Fourier transform of the total correlation function $[g(\mathbf{r}) - 1]$ as follows:

$$S(k) = 1 + m\int \Big(g(\mathbf{r}) - 1\Big)e^{-2j\mathbf{kr}}d\mathbf{r}. \tag{5}$$

where $g(\mathbf{r})$ is the pair-correlation function, which is the probability of finding two particles separated by the distance $\mathbf{r}$. In this case, the structure factor can be interpreted as being a line of the 3D Fourier transform of the total correlation function $[g(\mathbf{r}) - 1]$, the line being in the direction of the incident wave (see appendix of Ref. 20). The structure factor S therefore depends only on the modulus k of the wave vector $\mathbf{k}$. The structure factor cannot be calculated analytically for a complex spatial positioning of particles as occurs in the case of aggregates of particles. However, for an ensemble of identical hard spheres homogeneously distributed, an analytical expression for the structure factor can be obtained as established by Wertheim.[21] The modified version of the analytical expression for the structure factor used here is described in detail in the Appendix.

In the low frequency limit, the structure factor tends toward a constant value $S(k) \to S^0 = W$ called the packing factor.[13] The most commonly used expression for the packing factor is based on the Percus–Yevick pair-correlation function for identical, hard, and radially symmetric particles. The Percus–Yevick packing factor W_{PY} is related with the scatterer concentration ϕ as follows:[13]

$$W_{PY} = \frac{(1-\phi)^4}{(1+2\phi)^2}. \tag{6}$$

In comparison with the SFM described in Eq. (4), the theoretical BSC for the PM is thus obtained by replacing the structure factor S by the Percus–Yevick packing factor W_{PY} as follows:

$$BSC_{PM}(k) = \frac{\phi}{V_s}\frac{(1-\phi)^4}{(1+2\phi)^2}\sigma_b(k). \tag{7}$$

Estimated values of a^* and ϕ^* were determined by fitting the measured BSC_{exp} to the theoretical BSC_{SFM} given by Eq. (4) in the case of the SFM [or with the theoretical BSC_{PM} given by Eq. (7) in the case of the PM]. For this purpose, we searched for values of $(a, \phi) \in [0, 50] \times [0.001, 0.74]$, where a was expressed in μm, minimizing the cost function:

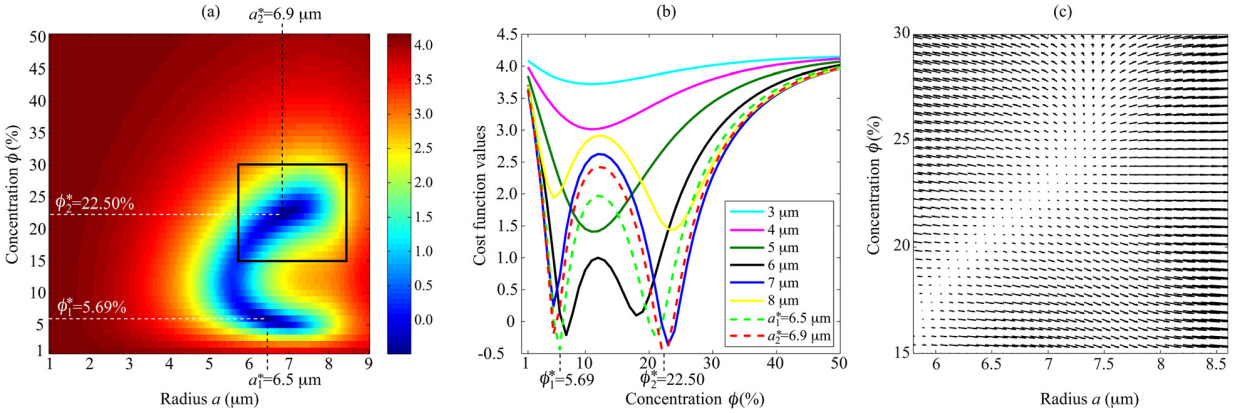

FIG. 2. (Color online) (a) Typical aspect of the logarithm of the cost function $F_{\mathrm{SFM}}(a, \phi)$ for the SFM obtained from the experiments with actual microsphere radius of 6 μm and actual concentration of 20%. The logarithm is shown here to enhance the visual contrast. This cost function has two possible solutions (a_1^*, ϕ_1^*) and (a_2^*, ϕ_2^*). Black rectangle indicates the ROI used to compute the gradient in subplot (c). (b) Typical aspects of the function log $[F_{\mathrm{SFM}}(a, \phi)]$ obtained with several fixed values of a. These cost functions can display either one or two minima. (c) Direction and relative magnitude of the gradient in the ROI around the values of the actual parameters.

$$F_{SFM}(a,\phi)=\sum_i \|BSC_{SFM}(k_i)-BSC_{\exp}(k_i)\|^2, \text{ for the SFM,}$$
$$F_{PM}(a,\phi)=\sum_i \|BSC_{PM}(k_i)-BSC_{\exp}(k_i)\|^2, \text{ for the PM.} \quad (8)$$

The cost function had several local minima as observed by plotting the cost function surfaces. Figures 2(a) and 2(b) give an example of a cost function surface $F_{\mathrm{SFM}}(a, \phi)$ for the SFM obtained from the experiments performed with an actual microsphere radius of 6 μm and an actual concentration of 20% described in the following text in Sec. III. Similar behavior was observed in the case of the PM. One can observe that at a given value of the radius, the cost functions show either one or two minima. In the case of two minima, one minimum corresponds to a low scatterer concentration estimate and the other one to a high concentration estimate. This point will be discussed in the following text in Sec. V C. Figure 2(c) shows the gradient in the ROI around the values of the actual parameters.

The same procedure was used to estimate a^* and ϕ^* with the SFM and the PM. Because no analytical expression for σ_b is available in the framework of Faran's theory,[18] as mentioned in the preceding text, an exhaustive search was conducted on the values of a in the 1–50 μm range to minimize the cost function F_{SFM} (or F_{PM}) given by Eq. (8). Because the cost functions can display two minima, we searched for two concentration estimates ϕ_1 and ϕ_2 at each given value of a, using a trust-region-reflective algorithm with the MATLAB nonlinear data-fitting *lsqnonlin* (The MathWorks, Natick, MA). The concentration value obtained ϕ_1 (or ϕ_2, respectively) corresponds to the minimum of the cost function obtained with an initial concentration of $\phi^{\mathrm{init}}=0.001$ (or $\phi^{\mathrm{init}}=0.74$) at the beginning of the minimization routine. By varying the value of a, two possible solutions (a_1^*, ϕ_1^*) and (a_2^*, ϕ_2^*) were obtained, corresponding to a low initial value and a high initial value of the concentration at the beginning of the minimization routine. The solution (a^*,ϕ^*) corresponds to the minimum value between $F_{\mathrm{SFM}}(a_1^*, \phi_1^*)$ and $F_{\mathrm{SFM}}(a_2^*, \phi_2^*)$ with the SFM [or equivalently $F_{\mathrm{PM}}(a_1^*, \phi_1^*)$ and $F_{PM}(a_2^*, \phi_2^*)$ with the PM]. Note that in some cases, the values of $F_{SFM}(a_1^*, \phi_1^*)$ and $F_{\mathrm{SFM}}(a_2^*, \phi_2^*)$ [or equivalently the values of $F_{\mathrm{PM}}(a_1^*, \phi_1^*)$ and $F_{\mathrm{PM}}(a_2^*, \phi_2^*)$ for the PM] are equal.

III. METHODS

A. Tissue-mimicking phantoms

The tissue-mimicking phantoms consisted of polyamide microspheres with a radius of 6 ± 2 μm (orgasol 2001 EXD NAT1, Arkema, France) gently stirred in water. The size distribution of the microspheres measured using optical microscopy is presented in Fig. 3. The tissue-mimicking phantoms usually consisted of microspheres in agar–agar phantom. In the present study, the microspheres were suspended in water because agar–agar phantoms consisting of polyamide microspheres are difficult to degas at high scatterer concentration (>15%). The phantoms had identical scatterer sizes but different scatterer concentrations ranging from 1% to 25%. The acoustic parameters (the sound speed c, density ρ, impedance z, and Poisson's ratio) of the polyamide microspheres are given in Table I. The tissue-mimicking phantoms were designed to mimic the structural and acoustical properties of

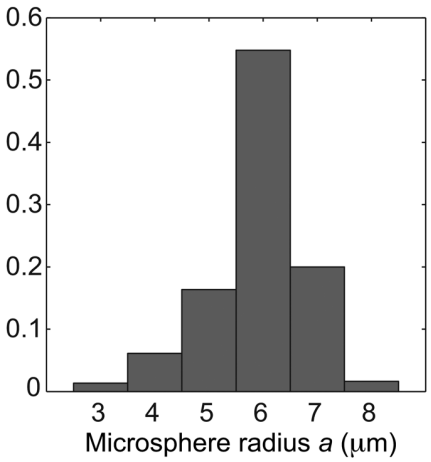

FIG. 3. Normalized histogram of the microsphere radii.

TABLE I. Summary of the parameters used to calculate the theoretical BSC response of the polyamide microsphere. Comparisons with parameters for human acute myeloid leukemia cell OCI-AML-5 used in Baddour and Kolios (Ref. 22).

	Polyamide microsphere	OCI-AML-5 nucleus	OCI-AML-5 cell
Radius a (μm)	6	4.55	5.75
Sound speed c (m/s)	2300	1503	1535
Density ρ (kg/m^3)	1030	1430	1240
Impedance z (Mrayl)	2.37	2.15	1.90
Poisson's ratio	0.42	0.42	0.487

densely packed cells in tumors. The properties of the cell components are not well known and vary widely in the literature. Table I gives an example of cell properties used by Baddour and Kolios[22] and Doyle *et al.*[23] Note that the impedance and Poisson's ratio of polyamide microspheres are similar to those of human acute myeloid leukemia cell nuclei.

B. Experimental setup

Two broadband focused transducers with center frequencies of 10 and 17.5 MHz (and focuses of 14.2 and 13.8 mm, respectively) were used in these experiments. The pulse-echo acquisition system was composed of an Olympus model 5072 PR pulser-receiver and a Gagescope model 8500CS acquisition board. The transducer was placed in an agar–agar gel, i.e., a solidified mixture of distilled water and 2% (w/w) agar powder (A9799, Sigma Aldrich, France) so that the distance between the transducer and the suspension was equal to 13.2 mm in the 10 MHz experiment (and 12.8 mm in the 17.5 MHz experiment). The transducer focus was therefore positioned below the agar–agar/suspension interface at a distance of 1 mm. The suspension was stirred in a beaker with a magnetic agitator to prevent sedimentation. Sixty RF lines were acquired and stored. Echoes were selected in the focal zone with a rectangular window $d = 0.13$ cm in length. The power spectra of the backscattered RF echoes were then averaged to provide $\overline{P_{\text{meas}}}$. This procedure was repeated twice with the two transducers at each scatterer concentration.

C. Attenuation measurements

The attenuation coefficients of the tissue-mimicking phantoms were determined using a standard substitution method. The 10 MHz transducer was used in the reflection mode with a reflector on the opposite side as shown in Fig. 4. At each phantom concentration, acquisitions of 100 RF lines were performed both with the suspension and with water. The water acquisition was used for normalization. At each acquisition, the phantom attenuation was calculated using log spectral difference technique.[24] These values were then averaged to obtain α_{ph} and are summarized in Fig. 5.

D. BSC estimation

The measured BSC values reported in this study were computed using the normalization technique for focused

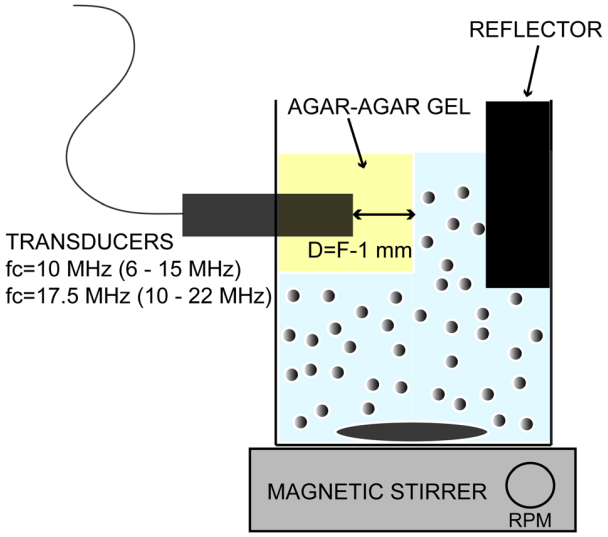

FIG. 4. (Color online) Diagram of the experimental setup used to perform the attenuation measurement.

transducers described by Wang and Shung.[25] This normalization technique consists of using a reference scattering medium instead of a perfect flat reflector on condition that the BSC of the reference scattering medium is known or can be determined.[25] The reference scattering medium allows to compensate the measured backscattered power spectrum $\overline{P_{\text{meas}}}$ for the electromechanical system response and the depth-dependent diffraction and focusing effects caused by the ultrasound beam. In the case of blood ultrasound characterization, the reference scattering medium is generally a low 6% hematocrit red blood cell suspension.[25,26] Because the radius of one red blood cell sphere-shaped model is around 2.75 μm, the corresponding theoretical BSC is given by the classical version of the PM written for an ensemble of identical Rayleigh scatterers [see Eq. (7) in Ref. 26]. In the present study, the reference scattering medium used was a suspension of polyamide

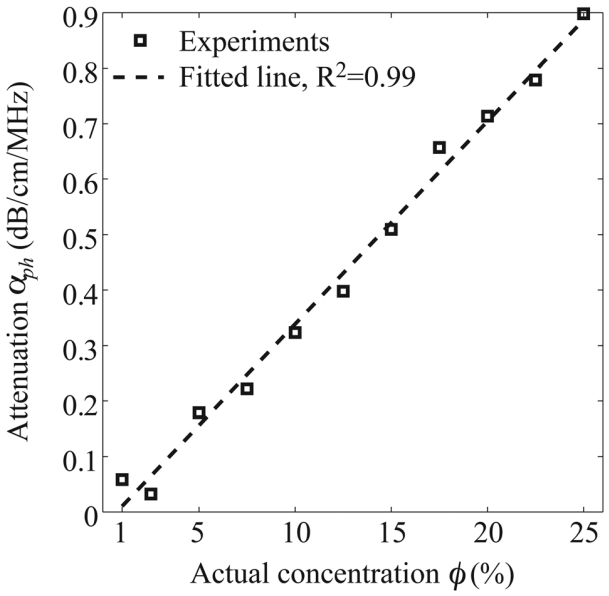

FIG. 5. Attenuation α_{ph} of the tissue-mimicking phantoms as a function of the actual concentration.

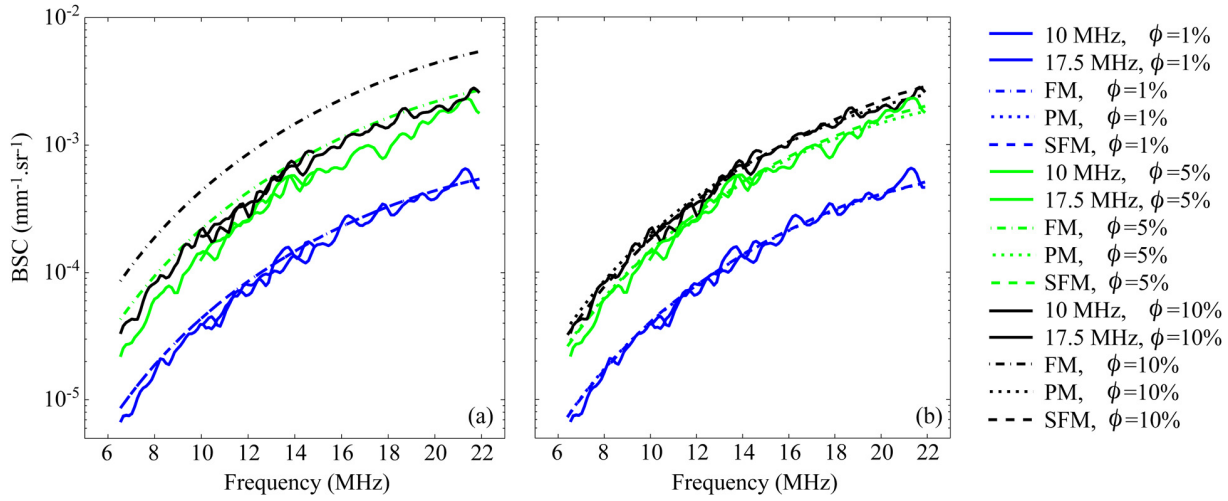

FIG. 6. (Color online) BSCs at scatterer concentrations of 1%, 5%, and 10%. (a) Comparison between the measured BSCs and the FM predictions. (b) Comparison between the measured BSCs and the SFM and PM predictions.

microspheres with a radius of 2.5 μm (orgasol 2001 UD NAT1, Arkema, France) present at a low concentration of 0.5% and gently stirred in water. The sample is easy to prepare and to handle, and the scattering process occurring in an ensemble of identical solid microspheres at a very low concentration (dilute medium) has been well documented using the FM.[18,27] Note that a small scatterer size of 2.5 μm was chosen so that the reference scattering medium would be in the Rayleigh scattering regime ($ka \ll 1$) and to avoid the resonant peaks that occur with higher scatterer sizes. Echoes from the reference scattering medium were windowed as with the tissue-mimicking phantoms at the same depth, and 60 echoes were also averaged to obtain $\overline{P_{\text{ref}}}$. The measured BSC was thus computed as follows:[25,26]

$$BSC_{\text{exp}}(k) = BSC_{ref}(k)\frac{\overline{P_{meas}(k)}}{\overline{P_{ref}(k)}}e^{(4/8.68)(\alpha_{ph}d)k(c/2\pi)} = BSC_{ref}(k)\frac{\overline{P_{meas}(k)}}{\overline{P_{ref}(k)}}e^{(4/8.68)(\alpha_{ph}d)f}, \quad (9)$$

where f is the frequency in MHz and the theoretical BSC of the reference sample BSC_{ref} is given by Eq. (2) using the FM. Note that the last term in Eq. (9) compensates the measured BSC_{exp} for the predetermined phantom attenuation values α_{ph} (in dB/cm/MHz). The coefficient 8.68 expresses unit conversion from dB to Neper: α_{ph}[Neper/cm/MHz] = α_{ph}[dB/cm/MHz]/8.68.

IV. RESULTS

A. Forward problem: Comparison between theoretical and experimental results

Figures 6 and 7 give the measured BSC_{exp} versus the frequency at scatterer concentrations of 1%, 5%, 10%, 15%, and 25%. The solid lines give the BSC_{exp} values based on measurements performed with the 10-MHz center frequency transducer in the 6–15 MHz frequency bandwidth and with the 17.5-MHz center frequency transducer in the 10–22 MHz frequency bandwidth. At all the concentrations tested, the BSC_{exp} measured with the two transducers in the 10–15 MHz

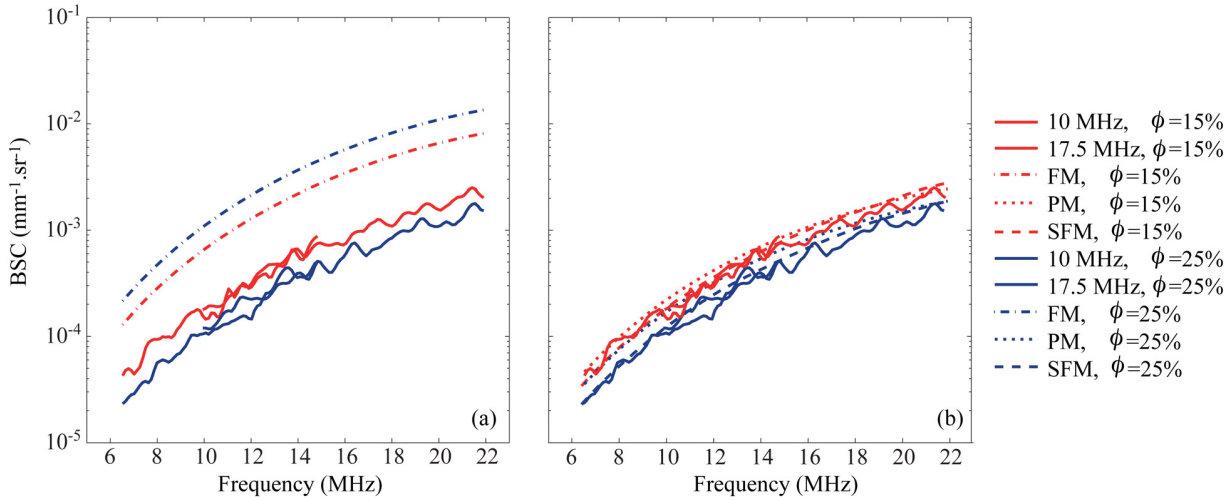

FIG. 7. (Color online) BSCs at scatterer concentrations of 15% and 25%. (a) Comparison between the measured BSCs and the FM predictions. (b) Comparison between the measured BSCs and the SFM and PM predictions.

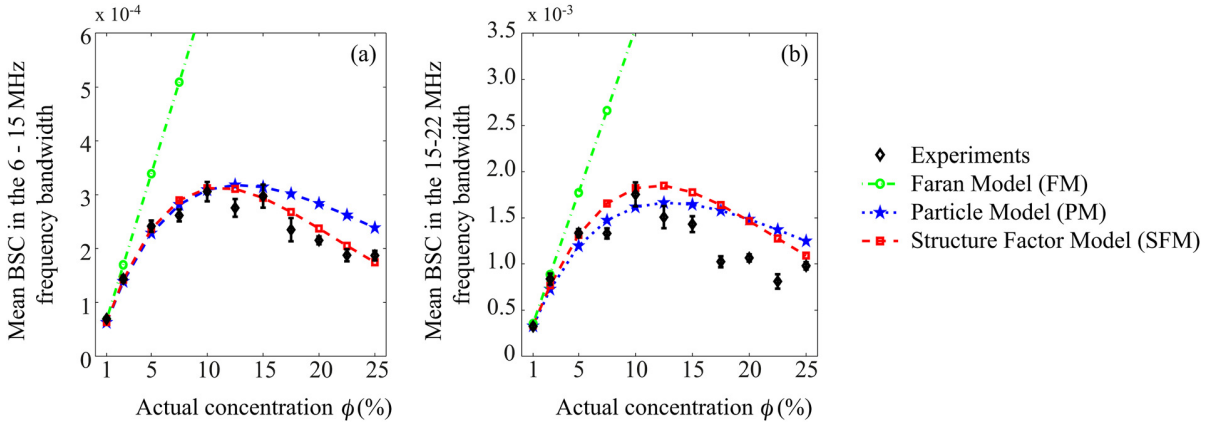

FIG. 8. (Color online) Comparison between the measured and theoretical mean BSC versus the scatterer concentration (a) in the 6–15 MHz frequency range and (b) in the 15-22 MHz frequency range.

frequency bandwidth were similar. This means that the results were not influenced by the system's transfer function. Figures 6(a) and 7(a) also give the theoretical BSC predictions based on the FM, and Figs. 6(b) and 7(b) give the theoretical BSC predictions based on the SFM and PM. At all the scatterer concentrations tested, the best agreement between the experimental BSC_{exp} and theoretical BSCs was obtained with the SFM in the 6–15 MHz frequency bandwidth, whereas the results obtained with the FM were only satisfactory at the 1% scatterer concentration, and those obtained with the PM were satisfactory at concentrations of 1%, 5%, 10%, and 15%. Note that the results obtained with the GM were not presented in the forward problem study because the GM does not include shear wave in the modeling. The GM therefore gave less satisfactory results that the FM (data not shown), even at the lowest concentration of 1%.

To enhance the lecture of these results, Fig. 8 shows the measured BSC_{exp} magnitude averaged in the frequency bandwidth from 6 to 15 MHz and in the frequency bandwidth from 15 to 22 MHz as a function of the scatterer concentration. The standard deviation plotted in Fig. 8 was computed as described in the following text. The power spectra of 10 backscattered RF echoes were averaged to obtain $\overline{P'_{\text{meas}}}$. Six power spectra $\overline{P'_{\text{meas}}}$ were thus obtained from all 60 RF echoes acquired, and the six corresponding BSC'_{exp} were calculated using Eq. (9). The standard deviation of the BSC'_{exp} averaged over the frequency bandwidth was then computed. Note that the BSC_{exp} magnitude changed with the concentration: The BSC_{exp} magnitude increased with increasing concentration between 1% and 10%, then decreased with increasing concentration between 10% and 25%. Also plotted in Fig. 8 are the theoretical BSC values predicted with the FM, SFM, and PM. Good agreement was obtained at a low scatterer concentration of 1% and 2.5% for all models. The FM and the PM overestimated the BSC amplitude at $\phi > 2.5\%$ and for $\phi > 10\%$, respectively. The SFM was the model showing the best agreement with the experimental data, especially in the 6–15 MHz frequency bandwidth. The SFM slightly overestimates the BSC magnitude at $\phi > 10\%$ in the 15–22 MHz frequency bandwidth.

A quantitative ultrasonic parameter that has often been used for tissue characterization is the spectral slope (SS). The SS is the linear slope of the BSC as a function of the frequency on a log–log scale. The changes in the SS in the 6–22 MHz frequency bandwidth with the actual concentration are shown in Fig. 9. The experimental data did not show the occurrence of any significant changes in the frequency dependence of the BSC_{exp} at the various scatterer concentrations tested because the SS varies randomly between 3.4 and 3.7. The SSs obtained with the three scatterings models were all in the same range of values. The SSs of the FM and the PM were equal to a constant value of 3.44 at all the concentrations tested, whereas the SS of the SFM slightly increased from 3.46 to 3.75 with increasing concentrations.

B. Inverse problem: Radius and concentration estimates

In what follows, the relative errors for parameters a^* and ϕ^* correspond to

$$\epsilon_{a*} = \frac{a^* - a}{a}, \quad \epsilon_{\phi*} = \frac{\phi^* - \phi}{\phi}. \tag{10}$$

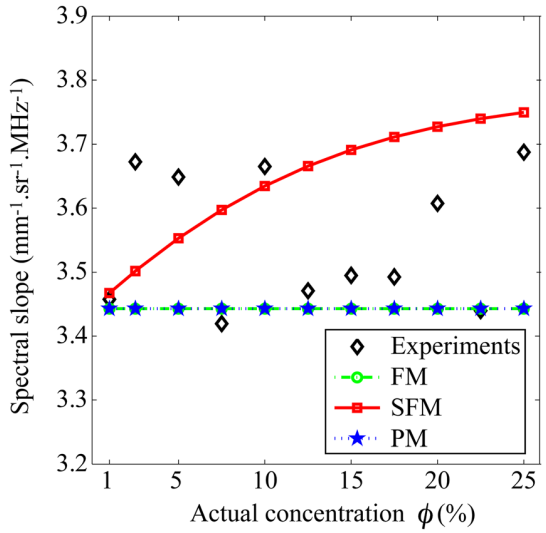

FIG. 9. (Color online) Spectral slopes obtained in the 6–22 MHz frequency bandwidth as a function of the actual concentration in the experiments and with the three theoretical scattering models (FM, SFM, and PM).

1. Radius and concentration estimates using the GM and FM

The estimated values a^* and ϕ^* using the GM and the FM and the corresponding relative errors are given in Fig. 10. The results obtained with the GM are presented in the inverse problem framework because that model has been widely used in previous studies.[3–9] Because the impedance difference γ_z between the microspheres and the water is known *a priori*, the estimated concentration $\phi* = (n_z^*(4/3)\pi a^{*3})/\gamma_z^2$ with the GM is given here instead of the estimated acoustic concentration n_z^* usually given in previous studies.[5,6] The GM overestimated the microsphere radii: The average effective radii estimated at all the concentrations was found equal to $10.43 \pm 1.65\,\mu$m, corresponding to a relative error of $74\% \pm 27\%$. The GM therefore underestimated the scatterer concentrations, giving relative errors between 88% and 100% (average relative errors $90\% \pm 9\%$) at all the actual concentrations tested. The results obtained with the GM were somewhat anticipated because this model is well adapted for fluid spheres in a dilute medium and is therefore not very suitable for modeling solid spheres in a dense medium.

The radii estimated using the FM were quantitatively satisfactory at all the actual concentrations tested because relative absolute errors of less than 22% were obtained except for the actual concentration of 5% at which a relative error of approximately 38% occurred (see Fig. 10). At concentrations of 1%, 2.5%, 7.5%, 10%, and 12.5%, the estimated concentrations given by the FM were qualitatively consistent with a significant correlation with r^2 of 0.96 between the true and estimated concentrations (data not shown). The estimated concentrations were quantitatively satisfactory for the actual concentrations 7.5%, 10%, and 12.5% with relative errors inferior to 23%. Note that at the actual concentration of 5%, underestimating the radius resulted in overestimating the concentration. The FM concentrations were underestimated at the highest actual concentrations, i.e., those greater than 12.5%, as it was expected.

2. Radius and concentration estimates using the SFM and PM

The results obtained using the SFM are shown in Fig. 11. The triangular symbols (and the diamond-shaped symbols) represent the possible solutions (a_1^*, ϕ_1^*) [and the possible solutions (a_2^*, ϕ_2^*), respectively] given by the SFM with an initial concentration of $\phi^{\text{init}} = 0.001$ (and $\phi^{\text{init}} = 0.74$, respectively) at the beginning of the minimization routine. The SFM gave quantitatively satisfactory radius estimates a_1^* and a_2^* at the concentrations studied with relative absolute errors of less than 20%. The estimated concentrations ϕ_1^* obtained with a low initial concentration $\phi^{\text{init}} = 0.001$ were quantitatively satisfactory, giving relative absolute errors of less than 31% at actual concentrations ranging from 5% to 15%, and were qualitatively consistent at the two lowest concentrations of 1% and 2.5%, giving relative absolute errors of 77% and 58%, respectively [see the triangular symbols in Figs. 11(a2) and 11(b2)]. The estimated concentrations ϕ_2^* obtained with a high initial concentration $\phi^{\text{init}} = 0.74$ were quantitatively satisfactory giving relative absolute errors of less than 38% at actual concentrations ranging from 10% to 25% [see the diamond-shaped symbols in Figs. 11(a2) and 11(b2)]. The circular symbols in Fig. 11 give the final solution (a^*,ϕ^*) corresponding to the global minimum of the cost function studied. Note that the global minimum (a^*,ϕ^*) did not always correspond to the actual parameters, whereas the value of one of the two local minima (a_1^*, ϕ_1^*) or (a_2^*, ϕ_2^*) is closed from the actual parameters.

Figure 12 presents the results obtained using the PM. These results were fairly similar to those obtained using the SFM. Note that the PM yielded less satisfactory concentrations ϕ_2^* with relative errors of up to 105% at the highest concentrations, i.e., those greater than 15% [see the diamond-shaped symbols in Figs. 12(a2) and 12(b2)]. But the estimated concentrations ϕ_1^* were more accurate at the low concentrations 1% and 2.5%, giving relative absolute errors of less than 32%.

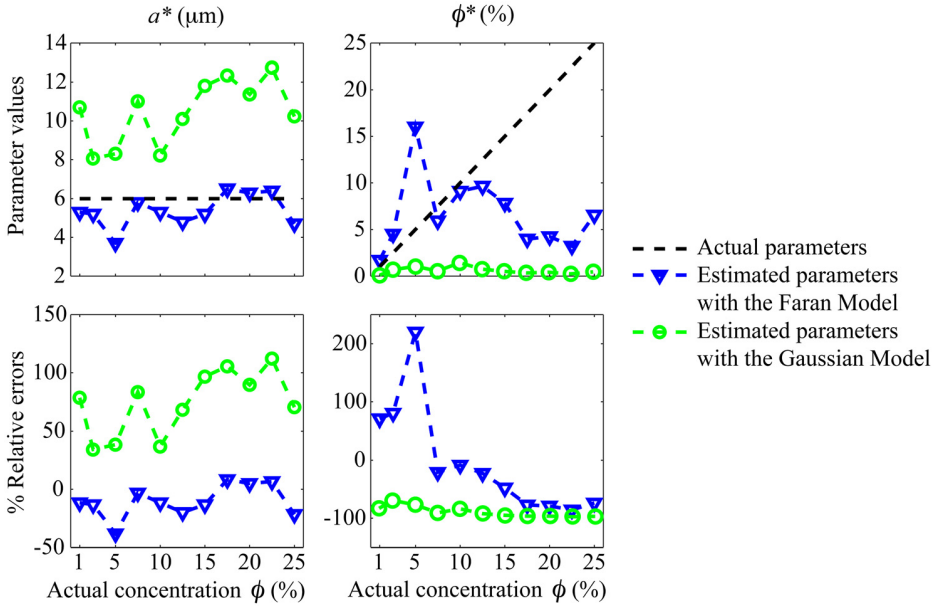

FIG. 10. (Color online) (a) Values of a^* and ϕ^* estimated by the GM and the FM versus the actual concentration. Also represented are actual values of a and ϕ. (b) Corresponding relative errors of a^* and ϕ^*.

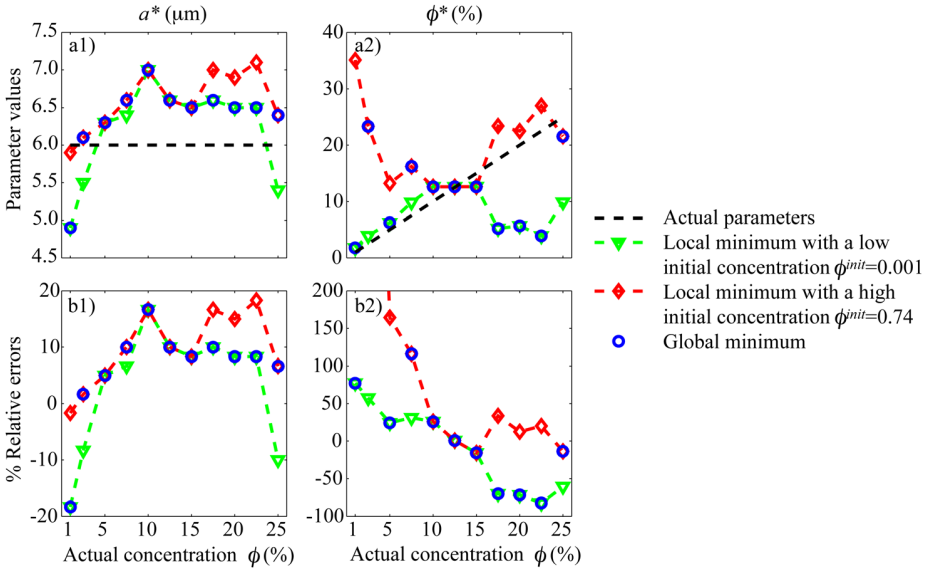

FIG. 11. (Color online) (a) Parameter estimates using the SFM versus the actual concentration. The triangular and the diamond-shaped symbols represent the possible solutions (a_1^*, ϕ_1^*) and (a_2^*, ϕ_2^*), respectively, with an initial value of the concentration $\phi^{init} = 0.001$ and $\phi^{init} = 0.74$, respectively, at the beginning of the minimization routine. The circular symbols give the global minimum, i.e., the solution (a^*, ϕ^*). Also represented in dashed lines are actual values of a and ϕ. (b) Corresponding relative errors.

V. DISCUSSION

A. Forward problem: Discussion

BSCs in the 6–22 MHz frequency range were measured using tissue-mimicking phantoms at scatterer concentrations ranging from 1% to 25%. The experimental data thus obtained were compared with the predictions of three ultrasound scattering models, namely, the FM, PM, and SFM, in the framework of a forward problem study. This study is in line with that performed by Chen and Zagzebski[28] using Sephadex spheres immersed in gel. In the latter study, qualitative comparison were made between the experimental and theoretical BSC behavior as a function of the scatterer concentration (see Figs. 1 and 8 in Ref. 28 using a continuum scattering model). In the present study, the relationship between the BSC magnitude and scatterer concentration was studied quantitatively. The observed BSC magnitude versus concentration relationship was satisfactorily predicted by the SFM and the PM, whereas the FM predicted that the BSC increases with increasing concentrations.

With the FM, the assumption that the scatterers were randomly distributed failed due to the spatial correlation among the scatterers at high scatterer concentrations. The FM therefore failed to predict the BSC magnitude at scatterer concentrations above 2.5%. The BSC_{PM} curves were in good agreement with the BSC_{exp} curves up to concentrations of 15% (see Fig. 8). But the best agreement between the theoretical and experimental BSC curves in scattering magnitude was obtained with the SFM, even at the highest concentration of more than 15%, especially in the 6–15 MHz frequency bandwidth [see Fig. 8(a)]. To conclude, the SFM was found to be more suitable than the PM and the FM for modeling high scatterer concentrations.

Concerning the frequency dependence of the BSC, the relationship between the SS and the scatterer concentration was also studied. Because the SS values obtained on the basis of the experimental data varied randomly around 3.55 at the various concentrations tested, there is no clear variation of the SS with the concentration. The experimental SSs did not match the theoretical SSs given by the FM, SFM, and

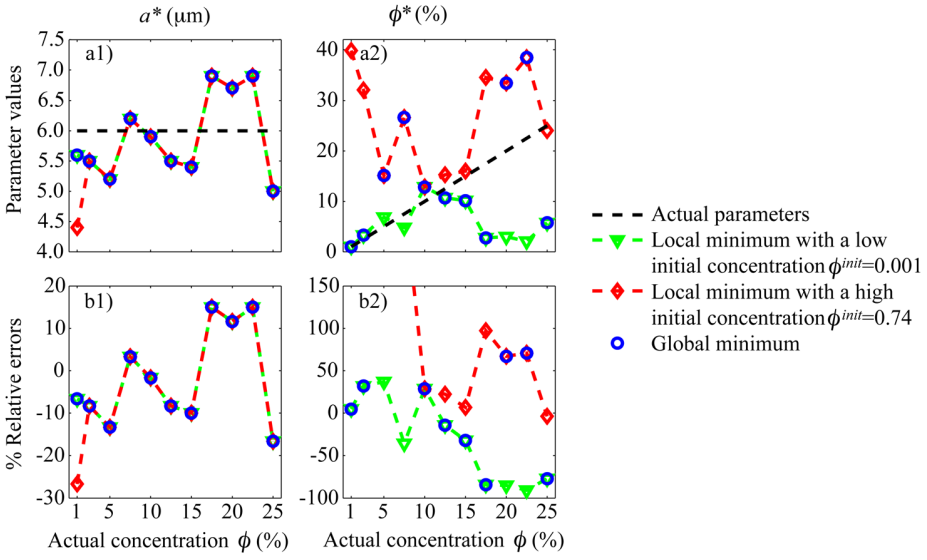

FIG. 12. (Color online) (a) Parameter estimates using the PM versus the actual concentration. The triangular and the diamond-shaped symbols represent the possible solutions (a_1^*, ϕ_1^*) and (a_2^*, ϕ_2^*), respectively, with an initial value of the concentration $\phi^{\mathrm{init}} = 0.001$ and $\phi^{\mathrm{init}} = 0.74$, respectively, at the beginning of the minimization routine. The circular symbols give the global minimum, i.e., the solution (a^*, ϕ^*). Also represented in dashed lines are actual values of a and ϕ. (b) Corresponding relative errors.

PM. Contrary to what occurred with the experimental values, the theoretical SSs obtained with the FM and PM are constant as a function of the concentration because the BSC frequency dependence with these models is determined only by the frequency dependence of σ_b [see Eqs. (2) and (7)]. Note that σ_b depends on the scatterer size and not on the concentration. With the SFM, the SS was predicted to increase with the concentration because of the structure factor. Indeed, according to Eq. (4), the BSC_{SFM} frequency dependence is determined by the frequency dependences of σ_b and S. Note that S depends on the scatterers' radius and their concentration. However, the experimental and theoretical SSs values obtained ranged between 3.4 and 3.75 with all three models.

B. On the use of polyamide microspheres to make cell-mimicking phantoms

In the present study, experiments were performed at the cell scale using solid polyamide microspheres with a radius of 6 μm, having similar acoustic parameters to those of isolated nuclei (see Table I). However, the suitability of models for describing scattering by cells has given rise to some debate. Cells have also been modeled as fluid media. Two other approaches have been used so far to modeling a cell: Using a single FFSM[29] or modeling two concentric fluid spheres[30] with impedances of around 1.6 Mrayl. However, weakly scattering fluid phantoms (i.e., with impedances of around 1.6 Mrayl) consisting of small microspheres are difficult to manufacture. The smallest weakly scattering fluid microspheres found in the literature were around 90–212 μm in size.[31] This means that only large scale experiments (using low frequencies) can be performed with these weakly scattering fluid microspheres.

Besides the choice of an elastic or fluid medium for modeling cells, another disadvantage of these tissue-mimicking phantoms is the large impedance contrast involved: That between polyamide microspheres and water is around 58% versus 30% between cell nuclei and cytoplasm/extracellular matrix (taking $c = 1570$ m/s, $\rho = 1.06$, and $z = 1.66$ Mrayl for the cytoplasm and the extracellular matrix and $z = 2.15$ Mrayl for nuclei as given in Table I). Although the wave propagation distance was quite short in our experiments ($d = 1.3$ mm), multiple scattering can occur at high scatterer concentrations; this may explain the discrepancies observed between the measured BSC_{exp} and theoretical BSC_{SFM} in the 15 – 22 MHz range [see Fig. 8(b)].

C. Inverse problem

In the forward problem study, it was established that the SFM was the model giving the best match with the experiments at all the concentrations tested. However, the best model for use with inverse problems should not only give a good fit with the data but also should be associated with a highly variable cost function in the ROI. It is worth noting that the cost function of the SFM has a higher gradient than the FM in the ROI and that the area in which the gradient is small is larger in the case of the FM [see Figs. 1(c) and 2(c)]. In addition, at a given value of the radius, the FM cost function minima all have similar values, whereas the SFM cost function minima are extremely variable [see Figs. 1(b) and 2(b)]. The behavior of the cost functions shows that the SFM is more sensitive than the FM to the unknown parameters, which could be an important point when dealing with the noisy data obtained in the case of real tissue.

The accuracy of the FM to estimate the scatterer size and concentration was first examined. As can be seen from Fig. 10, the FM does not give accurate scatterer concentrations at $\phi > 12.5\%$. However, good correlations between the scatterer concentration predicted by the FM and the actual concentration were found at actual concentrations ranging between 1% and 12.5% (apart from 5%). We did not actually expect to obtain such good results up to 12.5% because the FM overestimates the BSC amplitude for $\phi > 2.5\%$ as shown in the forward problem study. It is worth noting that the concentration estimates obtained at actual concentrations ranging between 7.5% and 12.5% were associated with a slight underestimation of the scatterer radius; this may explain why such accurate results were obtained at these actual concentrations.

The accuracy of the SFM and the PM to estimate the scatterer size and concentration was then examined in the case of high scatterer concentration because the PM and the SFM are more suitable than the FM for modeling dense media. To our knowledge, neither the PM nor the SFM have been tested so far in blood characterization studies as means of predicting the scatterer concentration because the hematocrit is assumed to be known *a priori*.[26] However, our study showed that the estimation of the scatterer concentration is not straightforward using the PM or the SFM. The following discussion intends to explain why the concentration estimates cannot be obtained directly using standard minimization procedures in the 6–22 MHz frequency bandwidth studied here.

As can be seen in Fig. 8(a), when the value of the radius is fixed, the BSC magnitude can be the same at both small and large scatterer concentrations (for example, at the concentrations 5% and 20% in the 6–15 MHz frequency bandwidth), apart from the maximum BSC magnitude at which the concentration is unique (herein, 10%). The BSC_{SFM} magnitudes computed with the SFM versus the concentration are plotted in Fig. 13(a) at several radius sizes (ranging from 5 to 7 μm). It can be observed here that several pairs of parameters (a, ϕ) can have the same BSC magnitude. This explains why the cost functions of the SFM and the PM had several local minima as shown in Fig. 2. In Figs. 11 and 12, one can notice that the global minimum (a^*,ϕ^*) did not always correspond to the actual parameters. However, one of the two local minima (a_1^*, ϕ_1^*) or (a_2^*, ϕ_2^*) corresponded to the actual parameters. To better understand what happened in these special cases, Fig. 13(b) gives the experimental BSC_{exp} at a concentration of 20% and two fitted curves BSC_{SFM} corresponding to the two local minima. Although the curves fitted with the SFM were similar, the concentration estimates were very different: $(a_1^* = 6.5\mu\text{m}, \phi_1^* = 5.69\%)$ and $(a_2^* = 6.9\mu\text{m}, \phi_2^* = 22.50\%)$. In this example, the global minimum was obtained with the smallest concentration (i.e., $\phi* = \phi_1^* = 5.69\%$), whereas the actual concentration was equal to 20%. This means that the information used to solve the inverse problem did not suffice

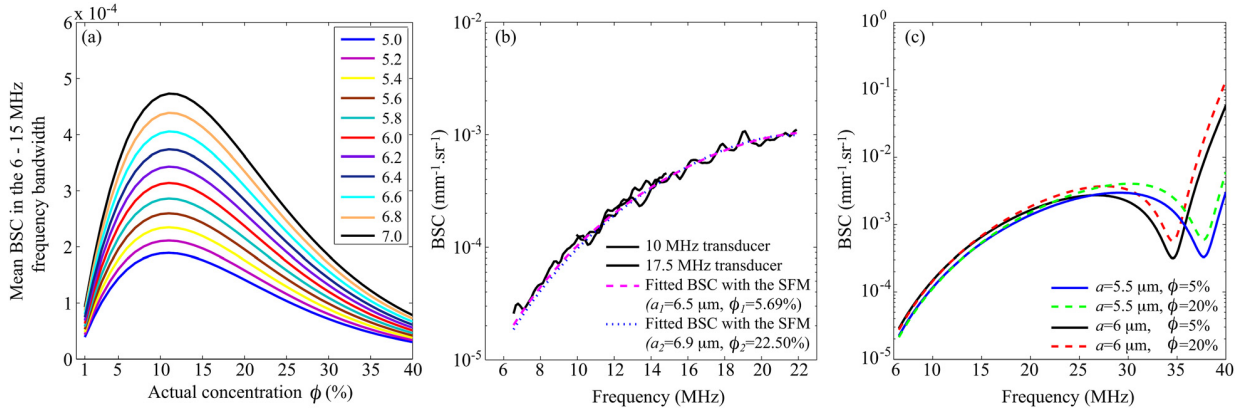

FIG. 13. (Color online) (a) BSC_{SFM} magnitude versus the concentration computed with the SFM for several fixed microsphere radii ranging from 5 to 7 μm. (b) Experimental BSC_{exp} at a scatterer concentration of 20% and the theoretical BSC_{SFM} computed with two possible solutions ($a_1^* = 6.5\,\mu\mathrm{m}, \phi_1^* = 5.69\%$) and ($a_2^* = 6.9\mu\mathrm{m}, \phi_2^* = 22.50\%$). (c) Theoretical BSC_{SFM} computed with the SFM for two scatterer concentrations of 5% and 20% with microsphere radii of 5.5 and 6 μm.

to be able to determine the concentration. The discussion next considers some possible solutions to this problem.

One solution might be to increase the information available by using higher frequencies. Figure 13(c) shows the theoretical BSC_{SFM} in the 6–40 MHz frequency bandwidth at concentrations of 5% and 20% with radii of 5.5 and 6 μm. With the same fixed radius, the BSC_{SFM} versus frequency curves obtained at both scatterer concentrations share a similar pattern because the peaks and dips occur at the same frequencies. In addition, at the same fixed radius, the BSC_{SFM} amplitudes are practically identical at low frequencies (<20 MHz), whereas the BSC_{SFM} amplitude is larger at high frequencies (>20 MHz) for the highest concentration of 20%. The use of higher frequencies may thus (1) improve the radius estimates because the BSC peaks and dips could be captured in the 25–40 MHz frequency bandwidth and (2) increase the ability to differentiate between low and high concentrations because the BSC amplitude differs between low and high concentrations at higher frequencies. The use of high frequencies with QUS techniques could be envisaged when working with subcutaneous or excised tissues as in the study performed by Mamou *et al.*[9] on cancer patients' freshly dissected lymph nodes. However, if one keeps a low frequency bandwidth (6–22 MHz as performed in our *in vitro* study or even less) with a view to develop *in vivo* SFM applications, the microstructure (i.e., the scatterer size and concentration) estimations based on the SFM might be associated with another quantitative parameter, such as the attenuation. In the tissue-mimicking phantom study presented here, the attenuation was found to increase with the concentration as shown in Fig. 5, and this information could be used to choose a solution between the two local minima. This means that if the attenuation is high, one can expect to have high scatterer concentrations. Moreover, in the case of some tissues such as liver or most cancer tissues, the cells are known to be densely packed. Structural parameter estimations based on the SFM could be possibly limited to a high initial concentration value of $\phi^{\mathrm{init}} = 0.74$ at the beginning of the minimization routine. It is worth emphasizing that by combining the structural estimates with the attenuation or by assuming *a priori* that the medium is dense, the SFM yielded satisfactory concentration estimates with relative errors of less than 38% at actual concentrations ranging from 10% to 25%.

VI. CONCLUSION

Four scattering models were examined for characterizing biological tissues with high scatterer concentrations. The GM has been previously used in various tissue studies;[3–9] whereas the FM has been mainly used for tissue-mimicking phantoms composed of solid particles.[10,28] Both of these models assume randomly distributed scatterers such that the theoretical BSC magnitude increases with scatterer concentration. These models are therefore most suitable for dealing with dilute media. The SFM and PM have been developed for modeling dense blood medium[13–16] to consider the interference effects caused by the correlation in the spatial disposition of individual scatterers.

The FM, SFM, and PM were first studied in the forward problem framework to compare the theoretical and experimental BSCs. The relationship between BSC magnitude and scatterer concentration was addressed. The BSC_{exp} magnitude was found to increase with the concentration at low scatterer concentrations and then decreased at concentrations greater than 10%. This pattern of BSC behavior versus the concentration was satisfactorily predicted by the SFM and the PM but not by the FM. The SFM was the model that better matched the experiments at all the scatterer concentrations studied especially in the 6–15 MHz frequency bandwidth.

The four scattering models were then examined to estimate the scatterer size and concentration from the experimentally measured BSC_{exp}. The GM did not yield accurate structural parameters because it gave relative errors of approximately 74% in the radius and 90% in the concentration. The FM provided significant correlations between the estimated and true concentrations with r^2 around 0.96 at actual concentrations ranging from 1% and 12.5% (apart from the actual concentration of 5%). However, the FM did not predict the concentration accurately at $\phi > 12.5\%$. The minimization routines used with the SFM and the PM were more complex than with the GM and FM because the cost

functions associated with these models often exhibited two local minima, corresponding to low and high scatterer concentration estimates. The global minimum did not always correspond to the actual parameters, but one of the two local minima corresponded to the actual parameter. To solve this problem, it is possible to either (1) assume the medium to be dense *a priori* or (2) associate the structural estimates with another quantitative parameter, such as the attenuation. With additional information of this kind, the SFM gave satisfactory concentration estimates with relative errors of less than 38% at actual concentrations ranging from 10% to 25%. Future works should focus on the combination of the SFM with other quantitative parameters (attenuation, signal envelope statistics[32] and on the use of higher frequencies.

ACKNOWLEDGMENTS

This work was supported by the CNRS and by the French Agence Nationale de la Recherche (ANR) under Grant No. ANR Tecsan 11-008-01. The authors would like to thank the anonymous reviewers for their valuable suggestions and Alain Busso, Eric Debieu, and Stephan Devic at the Laboratory of Mechanics and Acoustics (LMA–CNRS) for their technical assistance.

APPENDIX: ANALYTICAL EXPRESSION FOR THE STRUCTURE FACTOR

The analytical expression for the structure factor can be obtained from the article of Wertheim[21] giving the analytical expression of the direct correlation function $c(r)$. Indeed, Percus–Yevick equation[33] relates the pair correlation function (i.e., the radial distribution function) to the direct correlation function. Wertheim developed the analytical solution of the Percus–Yevick equation for hard spheres leading to[21]

$$-c(r) = \begin{cases} c_0 + c_1 \dfrac{r}{d} + c_3 \left(\dfrac{r}{d}\right)^3 & \text{for} \quad r \le d \\ 0 & \text{for} \quad r > d, \end{cases} \tag{A1}$$

where d is the hard-sphere diameter. The coefficients c_0, c_1, and c_3 are given by[21]

$$c_0 = \frac{(1+2\phi)^2}{(1-\phi)^4},$$

$$c_1 = -\frac{6\phi(1+\phi/2)^2}{(1-\phi)^4},$$

$$c_3 = \frac{\phi}{2} c_0 = \frac{\phi(1+2\phi)^2}{2(1-\phi)^4}. \tag{A2}$$

Note that the expression of c_0 is related to the inverse of the three-dimensional expression of the packing factor W_{PY} given in Eq. (6).

The Fourier transform of the structure factor S is linked to the Fourier transform of the direct correlation function C as follows:[34]

$$S(k) = \frac{1}{1 - mC(k)} \tag{A3}$$

with

$$C(k) = 4\pi d^3 \int_0^1 r^2 \frac{\sin(2kr)}{2kr} c(r) dr. \tag{A4}$$

The structure factor S was also calculated by computing the Fourier transform of a three-dimensional random distribution of particles as performed in Ref. 35 and was compared with the analytical expression of the structure factor [see Fig. 14(a)]. The two curves show good agreement at large $ka > 1$. To improve the analytical expression for small ka, we slightly modified the coefficient c_0 empirically as follows:

$$c_0' = \frac{(1+3\phi)^2}{(1-\phi)^4}. \tag{A5}$$

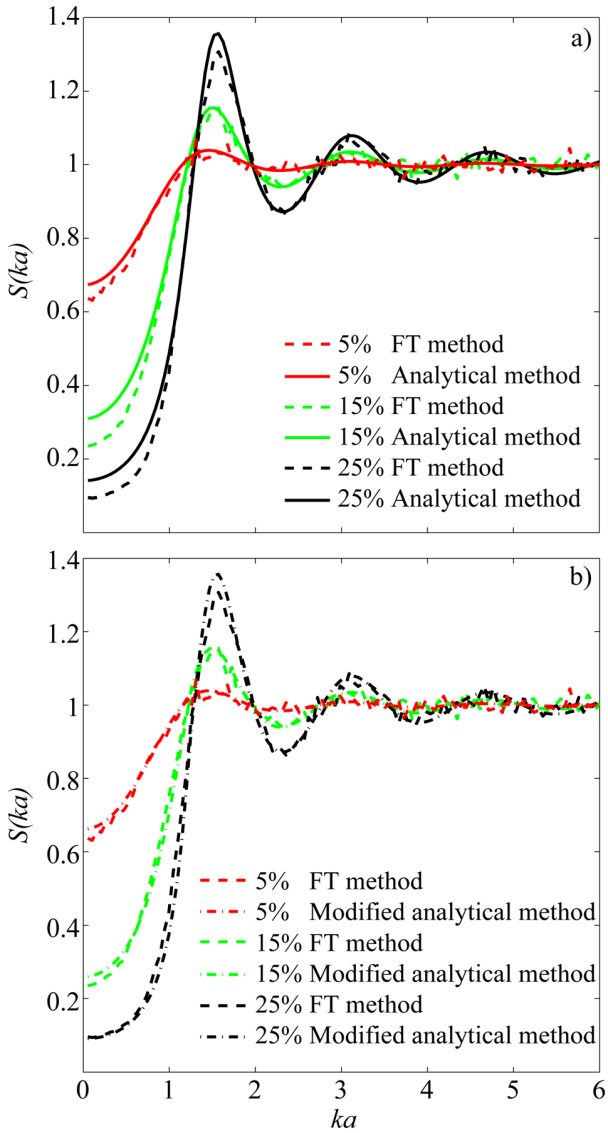

FIG. 14. (Color online) Comparison between structure factors at three different concentrations 5%, 15%, and 25%, computed by the Fourier transform (FT) of a three-dimensional random distribution of particles (Ref. 34) and computed by two analytical methods based on the article of Wertheim (Ref. 21) (a) using the coefficients given in Eq. (A2) and (b) using the coefficients given in Eqs. (A5) and (A6).

The inverse of c'_0 corresponds to the modified packing factor expression proposed by Twersky[36] with the variance parameter equals to 0 and with the shape parameter equals to 4. Because the new coefficients c'_0, c'_1, and c'_3 verify the following equations: $c'_3 = (\phi/2)c'_0$ and $-c(d) = c_0 + c_1 + c_3 = c'_0 + c'_1 + c'_3$, we obtained the following expressions:

$$c'_1 = -\frac{8\phi(1+\phi/2)(1+\phi)}{(1-\phi)^4},$$
$$c'_3 = \frac{\phi}{2}c'_0 = \frac{\phi(1+3\phi)^2}{2(1-\phi)^4}. \quad \text{(A6)}$$

Figure 14(b) represents the comparison of the structure factors computed by the Fourier transform of a three-dimensional random distribution of particles and computed by the modified analytical methods based on the article of Wertheim[21] using the coefficients given in Eqs. (A5) and (A6). The two curves agree well for high scatterer concentration even for small *ka*.

[1]F. L. Lizzi, M. Greenebaum, E. J. Feleppa, and M. Elbaum, "Theoretical framework for spectrum analysis in ultrasonic tissue characterization," J. Acoust. Soc. Am. **73**, 1366–1373 (1983).
[2]F. L. Lizzi, M. Ostromogilsky, E. J. Feleppa, M. C. Rorke, and M. M. Yaremko, "Relationship of ultrasonic spectral parameters to features of tissue microstructure," IEEE Trans. Ultrason. Ferroelectr. Freq. Control **33**, 319–329 (1986).
[3]E. J. Feleppa, F. L. Lizzi, D. J. Coleman, and M. M. Yaremko, "Diagnostic spectrum analysis in ophthalmology: A physical perspective," Ultrasound Med. Biol. **12**, 623–631 (1986).
[4]E. J. Feleppa, T. Liu, A. Kalisz, M. C. Shao, N. Fleshner, and V. Reuter, "Ultrasonic spectral-parameter imaging of the prostate," Int. J. Imaging Syst. Technol. **8**, 11–25 (1997).
[5]M. L. Oelze, J. F. Zachary, and W. D. O'Brien, "Characterization of tissue microstructure using ultrasonic backscatter: Theory and technique for optimization using a Gaussian form factor," J. Acoust. Soc. Am. **112**, 1202–1211 (2002).
[6]M. L. Oelze, W. D. O'Brien, J. P. Blue, and J. F. Zachary, "Differentiation and characterization of rat mammary fibroadenomas and 4T1 mouse carcinomas using quantitative ultrasound imaging," IEEE Trans. Med. Imaging **23**, 764–771 (2004).
[7]M. L. Oelze and W. D. O'Brien, "Application of three scattering models to characterization of solid tumors in mice," Ultrason. Imaging **28**, 83–96 (2006).
[8]M. C. Kolios, G. J. Czarnota, M. Lee, J. W. Hunt, and M. D. Sherar, "Ultrasonic spectral parameter characterization of apoptosis," Ultrasound Med. Biol. **28**, 589–597 (2002).
[9]J. Mamou, A. Coron, M. Hata, J. Machi, E. Yanagihara, P. Laugier, and E. Feleppa, "Three-dimensional high-frequency characterization of cancerous lymph nodes," Ultrasound Med. Biol. **36**, 361–375 (2010).
[10]M. F. Insana, R. F. Wagner, D. G. Brown, and T. J. Hall, "Describing small-scale structure in random media using pulse-echo ultrasound," J. Acoust. Soc. Am. **87**, 179–192 (1990).
[11]R. M. Vlad, R. K. Saha, N. M. Alajez, S. Ranieari, G. J. Czarnota, and M. C. Kolios, "An increase in cellular size variance contributes to the increase in ultrasound backscatter during cell death," Ultrasound Med. Biol. **9**, 1546–1558 (2010).
[12]L. Y. L. Mo and R. S. C. Cobbold, "Theoretical models of ultrasonic scattering in blood," in *Ultrasonic Scattering in Biological Tissues*, edited by K. K. Shung and G. A. Thieme (CRC, Boca Raton, FL, 1993), Chap. 5, pp. 125–170.
[13]V. Twersky, "Low-frequency scattering by correlated distributions of randomly oriented particles," J. Acoust. Soc. Am. **81**, 1609–1618 (1987).
[14]K. K. Shung, "On the ultrasound scattering from blood as a function of hematocrit," IEEE Trans. Ultrason. Ferroelectr. Freq. Control **SU-26**, 327–331 (1982).
[15]D. Savery and G. Cloutier, "A point process approach to assess the frequency dependence of ultrasound backscattering by aggregating red blood cells," J. Acoust. Soc. Am. **110**(6), 3252–3262 (2001).
[16]I. Fontaine, D. Savery, and G. Cloutier, "Simulation of ultrasound backscattering by red blood cell aggregates: Effect of shear rate and anisotropy," Biophys. J. **82**, 1696–1710 (2002).
[17]M. F. Insana and D. G. Brown, "Acoustic scattering theory applied to soft biological tissues," in *Ultrasonic Scattering in Biological Tissues*, edited by K. K. Shung and G. A. Thieme (CRC, Boca Raton, FL, 1993), Chap. 4, pp. 76–124.
[18]J. J. Faran, "Sound scattering by solid cylinders and spheres," J. Acoust. Soc. Am. **121**, 405–418 (1951).
[19]E. Franceschini, B. Metzger, and G. Cloutier, "Forward problem study of an effective medium model for ultrasound blood characterization," IEEE Trans. Ultrason. Ferroelectr. Freq. Control **58**, 2668–2679 (2011).
[20]I. Fontaine, M. Bertrand, and G. Cloutier, "A system-based approach to modeling the ultrasound signal backscattered by red blood cells," Biophys. J. **77**, 2387–2399 (1999).
[21]M. S. Wertheim, "Exact solution of the Percus–Yevick integral equation for hard spheres," Phys. Rev. Lett. **10**, 321–323 (1963).
[22]R. E. Baddour and M. C. Kolios, "The fluid and elastic nature of nucleated cells: Implications from the cellular backscatter response," J. Acoust. Soc. Am. **121**, EL16–EL22 (2007).
[23]T. E. Doyle, K. H. Warnick, and B. L. Carruth, "Histology-based simulations for the ultrasonic detection of microscopic cancer in vivo," J. Acoust. Soc. Am. **122**, EL210–EL216 (2007).
[24]R. Kuc and M. Schwartz, "Estimating the acoustic attenuation coefficient slope for liver from reflected ultrasound signals," IEEE Trans. Son. Ultrason. **SU-26**, 353–362 (1979).
[25]S. H. Wang and K. K. Shung, "An approach for measuring ultrasonic backscattering from biological tissues with focused transducers," IEEE Trans. Biomed. Eng. **44**, 549554 (1997).
[26]E. Franceschini, F. T. H. Yu, F. Destrempes, and G. Cloutier, "Ultrasound characterization of red blood cell aggregation with intervening attenuating tissue-mimicking phantoms," J. Acoust. Soc. Am. **127**, 1104–1115 (2010).
[27]J. J. Anderson, M. T. Herd, M. R. King, A. Haak, Z. T. Hafez, J. Song, M. L. Oelze, E. L. Madsen, J. A. Zagzebski, W. D. O'Brien, and T. J. Hall, "Interlaboratory comparison of backscatter coefficient estimates for tissue-mimicking phantoms," Ultrason. Imaging **32**, 48–64 (2010).
[28]J.-F. Chen and J. A. Zagzebski, "Frequency dependence of backscatterer coefficient versus scatterer volume fraction," IEEE Trans. Ultrason. Ferroelectr. Freq. Control **43**, 345–353 (1996).
[29]O. Falou, M. Rui, A. E. Kaffas, J. C. Kumaradas, and M. C. Kolios, "The measurement of ultrasound scattering from individual micron-sized objects and its application in single cell scattering," J. Acoust. Soc. Am. **128**, 894–902 (2010).
[30]M. Teisseire, A. Han, R. Abuhabsah, J. P. Blue, Jr., S. Sarwate, and W. D. O'Brien, "Ultrasonic backscatter coefficient quantitative estimates from chinese hamster ovary cell pellet biophantoms," J. Acoust. Soc. Am. **128**, 3175–3180 (2010).
[31]M. R. King, J. J. Anderson, M.-T. Herd, D. Ma, A. Haak, L. A. Wirtzfeld, E. L. Madsen, J. A. Zagzebski, M. L. Oelze, T. J. Hall, and W. D. O'Brien, "Ultrasonic backscatterer coefficients for weakly scattering, agar spheres in agar phantoms," J. Acoust. Soc. Am. **128**, 903–908 (2010).
[32]R. K. Saha and M. C. Kolios, "Effects of cell spatial organization and size distribution on ultrasound backscattering," IEEE Trans. Ultrason. Ferroelectr. Freq. Control **58**, 2118–2131 (2011).
[33]J. K. Percus and G. J. Yevick, "Analysis of classical statistical mechanics by means of collective coordinates," Phys. Rev. **110**, 1–13 (1958).
[34]N. W. Ashcroft, "Structure and resistivity of liquid metals," Phys. Rev. **145**, 83–90 (1966).
[35]R. K. Saha, E. Franceschini, and G. Cloutier, "Assessment of accuracy of the structure-factor-size-estimator method in determining red blood cell aggregate size from ultrasound spectral backscatter coefficient," J. Acoust. Soc. Am. **129**, 2269–2277 (2011).
[36]V. Twersky, "Low-frequency scattering by mixtures of correlated nonspherical particles," J. Acoust. Soc. Am. **84**, 409–415 (1988).

Structure factor model for understanding the measured backscatter coefficients from concentrated cell pellet biophantoms

Emilie Franceschini,[a] Régine Guillermin, and Franck Tourniaire
Laboratoire de Mécanique et d'Acoustique LMA - CNRS UPR 7051, Aix-Marseille Université, Centrale Marseille, 13402 Marseille Cedex 20, France

Sandrine Roffino
Laboratoire Motricité Humaine Education Sport Santé LAMHESS, Université de Nice Sophia-Antipolis, Nice, France

Edouard Lamy
Laboratoire de Biochimie, Faculté de Pharmacie, Aix-Marseille Université, Marseille, France

Jean-François Landrier
Nutrition, Obésité et Risque Thrombotique, UMR INSERM 1062/INRA 1260, Aix-Marseille Université, Marseille, France

(Received 4 December 2013; revised 23 March 2014; accepted 1 May 2014)

Ultrasonic backscatter coefficient (BSC) measurements were performed on K562 cell pellet biophantoms with cell concentrations ranging from 0.006 to 0.30 in the 10–42 MHz frequency bandwidth. Three scattering models, namely, the fluid-filled sphere model (FFSM), the particle model (PM), and the structure factor model (SFM), were compared for modeling the scattering from an ensemble of concentrated cells. A parameter estimation procedure was developed in order to estimate the scatterer size and relative impedance contrast that could explain the measured BSCs from all the studied cell concentrations. This procedure was applied to the BSC data from K562 cell pellet biophantoms in the 10–42 MHz frequency bandwidth and to the BSC data from Chinese hamster ovary cell pellet biophantoms in the 26–105 MHz frequency bandwidth given in Han, Abuhabsah, Blue, Sarwate, and O'Brien [J. Acoust. Soc. Am. **130**, 4139–4147 (2011)]. The data fitting quality and the scatterer size estimates show that the SFM was more suitable than the PM and the FFSM for modeling the responses from concentrated cell pellet biophantoms. © *2014 Acoustical Society of America.*
 [http://dx.doi.org/10.1121/1.4876375]

PACS number(s): 43.80.Cs, 43.80.Qf, 43.35.Bf [KAW] Pages: 3620–3631

I. INTRODUCTION

Quantitative ultrasound (QUS) techniques for determining the tissue microstructure are based on the frequency-based analysis of the signals backscattered from biological tissues. One approach consists in fitting the measured backscatter coefficient (BSC) from biological tissues to a theoretical BSC derived using an appropriate scattering model. The most frequently used theoretical scattering model is the spherical Gaussian model developed by Lizzi[1,2] that describes the tissue as a random inhomogeneous continuum with impedance fluctuations. The spherical Gaussian model yields two tissue properties: the average scatterer size and the acoustic concentration (i.e., the product of the scatterer number density by the square of the relative impedance difference between the scatterers and the surrounding medium). This approach has been used to assess the response to therapy[3] and to differentiate between diseased and healthy tissue or to detect cancer tumors for the eye,[4] the prostate,[5] the breast,[6,7] and cancerous lymph nodes.[8] Another class of theoretical scattering model describes the tissue as randomly distributed discrete scatterers using the fluid-filled sphere model[9–11] (FFSM) or the concentric sphere model.[10–14] In the aforementioned models (spherical Gaussian model, FFSM, and concentric sphere model), the scatterers are assumed to be independently and randomly distributed (i.e., to have a low scatterer concentration) and multiple scattering is neglected (in line with the Born approximation). Under these hypotheses, the power of the backscattered signals increases linearly with the scatterer concentration and depends on the size and acoustic properties of the tissue scattering structures. This linear relationship has been used to monitor the scatterer size and concentration. However, the assumption of randomly distributed scatterers may not hold in tumors with densely packed cells.[15] A model adapted to dense medium is the structure factor model (SFM) used in blood characterization.[16,17] The SFM is based on the assumption that at high scatterer concentrations, interference effects are mainly caused by correlations between the spatial positions of individual scatterers, i.e., caused by coherent scattering. The SFM sums the contributions from individual cells and models the cellular interaction by a statistical mechanics structure factor, which is defined as the Fourier transform of the spatial distribution of the cells.[16,17] The low frequency limit of the SFM is the particle model (PM) using the low frequency limit of the structure factor, which is by definition the packing

[a]Author to whom correspondence should be addressed. Electronic mail: franceschini@lma.cnrs-mrs.fr

factor.[18] The packing factor is a measure of orderliness in the spatial arrangement of cells. It depends only on the cell concentration (but not on the frequency). Experiments on tissue-mimicking phantoms were recently performed by our group[19] to compare the SFM with other classical scattering models (spherical Gaussian model, elastic sphere,[20] and PM). This study showed that the SFM was the most suitable theoretical scattering model for dealing with concentrated media such as densely packed cells in tumors.

In parallel with this work on QUS techniques, experimental studies were also conducted to understand and identify the cellular scattering sources. Identifying the scattering sites will lead to the improvement of the theoretical scattering models. Baddour *et al.*[21,22] and Falou *et al.*[23] performed measurements of high frequency (12–57 MHz) ultrasound BSC responses from individual cells and modeled a cell as a single spherical scatterer with uniform acoustic properties. The BSC measurements were compared to theoretical BSC predictions from a fluid sphere model[9] or from an elastic sphere model.[20] It was found that the BSC from an isolated cell was best modeled as a fluid sphere having the whole cell size.[23] Taggart *et al.*[24] conducted high frequency ultrasound measurements on cell pellets (i.e., highly packed cells) made up of mono- and multi-nucleated cells or isolated nuclei. This study suggests that the integrated BSCs were correlated with the size of the nuclei. Teisseire *et al.*[13] and Han *et al.*[14] developed cell pellet biophantoms that consist of identical cells embedded in a plasma-thrombin supportive background with various cell concentrations ranging from 0.0017 to 0.63. The concentrated biophantoms mimic densely packed cells with controlled cell volume fractions and are simplified versions of real tissue since only a single cell line is considered. The BSC estimates from the biophantoms were fitted with the concentric sphere model[12] in the 26–105 MHz frequency bandwidth. At low cell concentrations ($\leq$0.026), the estimated whole cell radii agree well with the true whole cell radii, but not at high cell concentrations (>0.096).[14] A nonlinear relationship between the BSC amplitude and the cell concentration was also observed below 50 MHz, which might be attributed to the coherent scattering.[14] This work on concentrated cell pellet biophantoms suggests that the concentric sphere model becomes less reliable as the cell concentration increases.[14]

The aim of this study was to use the SFM to go further in the understanding of the measured BSCs from cell pellet biophantoms. The SFM was modified to introduce the polydispersity by using a *local monodisperse approximation*.[25,26] The FFSM and the PM were also examined in both monodisperse and polydisperse modeling cases for the comparison with the SFM. Ultrasonic backscatter measurements were performed at frequencies ranging from 10 to 42 MHz on biophantoms. These biophantoms consisted of human leukemia K562 cells trapped in a mixture of plasma and thrombin with different cell concentrations ranging from 0.006 to 0.30. A parameter estimation procedure was developed in order to estimate the scatterer size and relative impedance contrast that could explain the measured $\mathrm{BSC}_{\mathrm{meas}}$ from all the studied cell concentrations using the FFSM, PM, and SFM. This procedure was applied to our BSC data from K562 cell pellet biophantoms in the 10–42 MHz frequency bandwidth and to the BSC data from Chinese hamster ovary (CHO) cell pellet biophantoms in the 26–105 MHz frequency bandwidth given in Ref. 14. The scatterer sizes estimated using our parameter estimation procedure were compared to the true cellular features to identify the scattering sites. The ability of the FFSM, PM, and SFM to model the measured BSCs from concentrated cell pellet biophantoms with a single set of structural and acoustic parameters was discussed.

II. ULTRASOUND SCATTERING THEORY

In the following, it is assumed that shear wave propagation and wave mode conversion are neglected so that only compressional waves are taken into account. The surrounding medium is acoustically described as a homogeneous fluid medium, characterized by a sound speed c_0 and a density ρ_0. This section presents the BSC modeling for an ensemble of cells using the FFSM, SFM, and PM. For all three models, the formulations were written for monodisperse and polydisperse spheres.

A. The fluid-filled sphere model (FFSM)

An isolated cell was modeled as a fluid-filled sphere representing the whole cell or the nucleus. The exact solution for the scattering of a plane wave of wave number k by a fluid-filled sphere of radius r, sound speed c, and density ρ embedded in a fluid medium can be calculated using the Anderson model.[9] In this study, we assumed weak scattering contrast such that the differential backscattering cross section from a single fluid-filled sphere σ_b was calculated using the following expression:

$$\sigma_b(k,r) = \frac{k^4 V_s^2 \gamma_z^2}{4\pi^2}\left(3\frac{\sin(2kr) - 2kr\,\cos(2kr)}{(2kr)^3}\right)^2, \quad (1)$$

where V_s is the sphere volume and γ_z is the relative impedance difference between the cells and the surrounding medium $\gamma_z = (c\rho - c_0\rho_0)/c_0\rho_0$. By considering an ensemble of identical fluid spheres independently and randomly distributed, the theoretical BSC using the FFSM can be written as

$$\mathrm{BSC}_{\mathrm{FFSM}}^{\mathrm{monod}}(k) = m\sigma_b(k,\ r), \quad (2)$$

where m is the number density related to the sphere concentration ϕ as $m = \phi/V_s$.

However, even if the same cell line is used in the biophantom, the cells are not identical in size and the BSC is affected by the scatterer size distribution. By considering a mixture of spheres differing only in size, the theoretical BSC using the FFSM can be expressed as

$$\mathrm{BSC}_{\mathrm{FFSM}}^{\mathrm{polyd}}(k) = m\int_0^\infty p(r)\,\sigma_b(k,\ r)\,dr, \quad (3)$$

where $p(r)$ is the sphere radius probability distribution function (i.e., the probability that the sphere radius takes the value r). The number density m is related to the total sphere concentration ϕ as

$$m = \frac{\phi}{(4/3)\pi \int_0^\infty p(r) r^3 dr}. \quad (4)$$

Note that the dependence of σ_b on r in Eq. (2) is usually not written; this dependence is necessary here for understanding the mathematical integration operation in Eq. (3). Figure 1(a) shows examples of theoretical BSCs computed with the FFSM in both monodiperse and polydiperse cases. We considered a monodisperse distribution of sphere radius 6.5 μm and a polydisperse distribution with a Gaussian size distribution of 6.5 $\pm$ 1.5 μm. In both monodisperse and polydisperse cases, the relative impedance contrast of the spheres was equal to $\gamma_z = 0.05$ and three sphere concentrations of 0.006, 0.06, and 0.3 were studied. One can notice from Fig. 1(a) that the size variance influences mainly the amplitude of the first BSC dip (in the example given at the frequency around 87 MHz). Whatever the sphere concentrations of 0.006, 0.06, and 0.3 in the monodisperse case (or in the polydisperse case), the frequency dependence of the BSC curves is identical for a given scatterer size r. It is due to the fact that the BSC frequency dependence for the FFSM depends only on $\sigma_b(k, r)$.

B. The structure factor model (SFM) and the particle model (PM)

1. Monodisperse case

The SFM (Ref. 16) is based on the assumption that at high scatterer concentrations, interference effects are mainly caused by correlations between the spatial positions of individual scatterers. In comparison with the FFSM described in Eq. (2), the SFM considers the interference effects relatively easily by replacing the single-particle backscattering contribution $\sigma_b(k, r)$ by the product $\sigma_b(k, r)\, S(k, r)$, where $S(k, r)$ is the structure factor depending on the scatterer concentration ϕ and the pattern of the spatial arrangement of the scatterers. By considering an ensemble of identical fluid spheres of radius r, the theoretical BSC for the SFM formulation is given by

$$\mathrm{BSC}_{\mathrm{SFM}}^{\mathrm{monod}}(k) = m \sigma_b(k, r)\, S(k, r, \phi), \quad (5)$$

where the differential backscattering cross section σ_b is calculated using Eq. (1). Note that there is no simple analytical expression of the structure factor for a complex spatial positioning of particles as occurs in the case of aggregates of particles. However, for an ensemble of identical hard (i.e., nondeformable) spheres that are homogeneously distributed, the structure factor depends on the sphere radius and the sphere concentration, and its analytical expression can be obtained as established by Wertheim.[27] The analytical expression of the structure factor used here was computed from Eqs. (A1)–(A4) in Ref. 19. The structure factor has an influence on the BSC frequency dependency and amplitude, as observed by plotting the structure factor versus the product kr, where r is the sphere radius [see Fig. 14(a) of Ref. 19]. For example, in the case of a sphere concentration of 0.15, the structure factor ranges between 0.30 and 0.77 for kr ranging between 0 and 1 [see the green solid line in Fig. 14(a) of Ref. 19].

In the low frequency limit, the structure factor tends toward a constant value $S(k) \to S(0) = W$ called the packing factor.[18] The most commonly used expression for the packing factor is based on the Percus-Yevick pair-correlation function for identical, hard (i.e., nondeformable) and radially symmetric particles. The Perkus-Yevick packing factor W_{PY} is linked to the scatterer concentration ϕ as[18]

$$W_{\mathrm{PY}} = \frac{(1-\phi)^4}{(1+2\phi)^2}. \quad (6)$$

Thus, in the low frequency limit, by considering an ensemble of identical fluid spheres of radius r, the theoretical BSC for the PM formulation is given by

$$\mathrm{BSC}_{\mathrm{PM}}^{\mathrm{monod}}(k) = m \frac{(1-\phi)^4}{(1+2\phi)^2} \sigma_b(k, r). \quad (7)$$

2. Polydisperse case

By considering a mixture of hard spheres differing only in size, the SFM expression involves the partial structure factor, as in Pedersen[25,26] in the field of small-angle scattering or

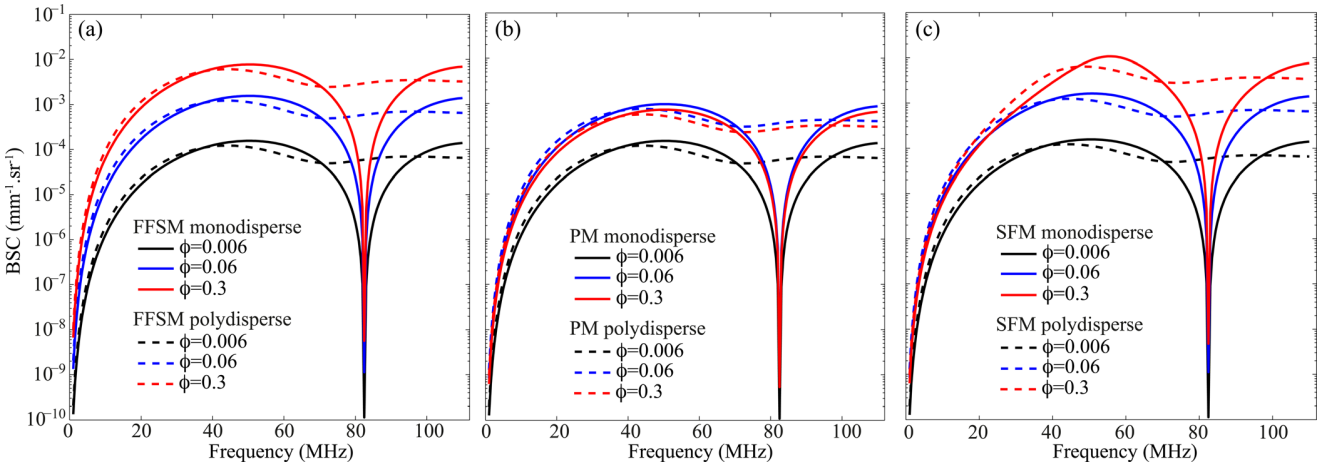

FIG. 1. (Color online) Theoretical BSCs computed with the FFSM, PM, and SFM considering a monodisperse distribution of sphere radius 6.5 μm or a polydisperse distribution with a Gaussian size distribution of 6.5 $\pm$ 1.5 μm with an impedance contrast $\gamma_z = 0.05$, for three sphere concentrations of 0.006, 0.06, and 0.3.

in Berger *et al.*[28] in the field of ultrasound. Since the computation of the partial structure factor is not straightforward,[25,26,28] approximations for polydisperse systems are often used to fit the scattering data. In this study, we used a *local monodisperse approximation*.[25,26] It is assumed that a scatterer of a certain size is always surrounded by scatterers of the same size. Under this hypothesis, the polydisperse system is approximated by many subsystems in which the particles are monodisperse. The scattering of the polydisperse medium is calculated as the sum of the scattering from the monodisperse subsystems weighted by the sphere radius probability distribution function $p(r)$. The theoretical BSC for a mixture of spheres differing only in size is thus given by

$$\mathrm{BSC}_{\mathrm{SFM}}^{\mathrm{polyd}}(k) = m\int_0^{\infty} p(r)\sigma_b(k,\, r)\, S(k,\, r,\, \phi)\, dr, \tag{8}$$

where $S(k, r, \phi)$ is the monodisperse structure factor for an equivalent system, consisting only of particles of radius r with a fixed total concentration ϕ.

In the low frequency limit, the theoretical BSC for the PM formulation in the polydisperse case is given by

$$\mathrm{BSC}_{\mathrm{PM}}^{\mathrm{polyd}}(k) = m\frac{(1-\phi)^4}{(1+2\phi)^2}\int_0^{\infty} p(r)\, \sigma_b(k,\, r)\, dr. \tag{9}$$

Figures 1(b) and 1(c) shows examples of theoretical BSCs computed with the SFM and the PM in both monodisperse and polydisperse cases with the same sphere configuration presented as the one presented in Sec. II A. One can notice from Figs. 1(b) and 1(c) that the BSC amplitude and frequency dependence computed with the PM and the SFM differ for the higher concentrations of 0.06 and 0.3. Indeed, the BSC frequency dependence computed with the PM (or with the SFM, respectively) depends on $\sigma_b(k,r)$ [on $\sigma_b(k,r)$ and $S(k,r,\phi)$, respectively]. That is why the frequency dependence of the BSC curves is identical with the PM (and is different with the SFM) for the sphere concentrations of 0.006, 0.06, and 0.3.

III. METHODS

A. Preparation of the K562 cell pellet biophantoms

The preparation of the cell pellet biophantoms was adapted from Teisseire *et al.*[13] and is presented here.

Human leukemia K562 cells were obtained from the European Collection of Cell Cultures (Salisbury, UK). K562 cells were grown in Roswell Park Memorial Institute 1640 medium (Life Technologies, Saint Aubin, France) supplemented with 10% fetal calf serum (PAA, Velizy-Villacoublay, France), 25 mM HEPES and 100 units of penicillin and 100 μg of streptomycin (Life Technologies). Cells were maintained at 37 °C in a humidified atmosphere of 5% CO_2 and 95% air.

The size distributions of K-562 nuclei were estimated from optical microscopy images of extracted nuclei. Nuclei were extracted using the protocol of Greenberg and Bender,[29] which is briefly recalled in the following: 10^7 cells were washed twice with 50 mL of ice-cold PBS and pelleted by centrifugation for 5 min at 4 °C and 500 g. The cell pellet was then gently vortexed and 4 mL of lysis buffer [10 mM Tris-HCl *p*H 7.4, 10 mM NaCl, 3 mM $MgCl_2$, 0.5% NP-40 (v/v)] were added under constant vortexing. After the whole volume of lysis had been dispensed, the cells were vortexed at maximum speed for 10 s and then incubated on ice for 5 min. At this stage, a few microliters of the lysate were placed on a hemocytometer and observed under microscope to check whether nuclei have been released and are free of cytoplasmic material. The cells were then centrifuged again as previously and the supernatant was discarded. Four milliliter of ice-cold lysis buffer were added under gentle vortexing as described before, and the nuclei were spun for 5 min at 4 °C and 500 g. The pellet was then resuspended in 100–300 μL of ice-cold glycerol buffer [50 mM Tris-HCl *p*H 8.3, 5 mM $MgCl_2$, 0.1 mM EDTA, 40% (v/v) glycerol], and diluted 20 times with ice-cold PBS.

The radius probability distribution functions estimated for extracted nuclei and whole cells are given in Fig. 2. Measurements were made using a calibrated optical microscope on 200 extracted nuclei and 120 whole cells randomly selected. The radius probability distribution functions for nuclei and whole cells were well approximated by Gaussian distributions. The mean nuclear and whole cell radii were found to be equal to 4.18 ± 0.43 and 6.34 ± 0.94 μm, respectively. Because of the polydispersity in the cell radius, the whole cell volume was calculated using a corrected sphere radius r_c^{cor} of 6.48 μm, which is determined by the expression $[\mathrm{mean}\ (r_c^3)]^{1/3}$, where r_c is the measured cell radius by optical microscopy.[14]

Biophantoms with different cell concentrations of 0.006, 0.03, 0.06, 0.12, 0.18, 0.24, and 0.30 were studied. For each biophantom concentration studied, three samples of 100 μL of the cell culture were withdrawn from the cell medium in order to estimate the mean cell concentration using the Scepter™ 2.0 cell counter (Millipore, Molsheim, France). A known number of cells were then suspended in a 1.5 mL plastic tube in a mixture consisting of 272 μL of human plasma (obtained after collection of blood from volunteers in citrated tubes), 3 μL of 1 M $CaCl_2$ and 25 μL of thrombin (6 U/ mL in bi-distilled water, Sigma-Aldrich, Saint Quentin Fallavier, France) to reach the desired concentration of the cell pellet biophantoms. After homogenization with a pipette tip, the suspension was transferred into a well of an 8-well Nunc Lab-Tek II Chamber Slide System (Dominique Dutscher, Brumath, France) and plasma was allowed to coagulate for 1 h at room temperature under agitation (70 rpm) on a Stuart™ Scientific Gyro rocker. The chamber slide was then placed in a plastic dish and immerged in PBS to allow ultrasound measurement. All the cell pellet preparation procedure was repeated twice.

After the ultrasound measurement, cell pellet biophantoms were fixed in a 10% (wt./vol) formalin solution for 48 h. The cell pellets were then removed from the chamber slide and embedded in paraffin to be sectioned. The sections were then stained with hematoxylin and eosin (HE) to verify that the cell spatial distribution was homogeneous (see Fig. 3).

B. Ultrasound data acquisition

US measurements were acquired using a Vevo 770 high frequency ultrasound system (Visualsonics Inc, Toronto,

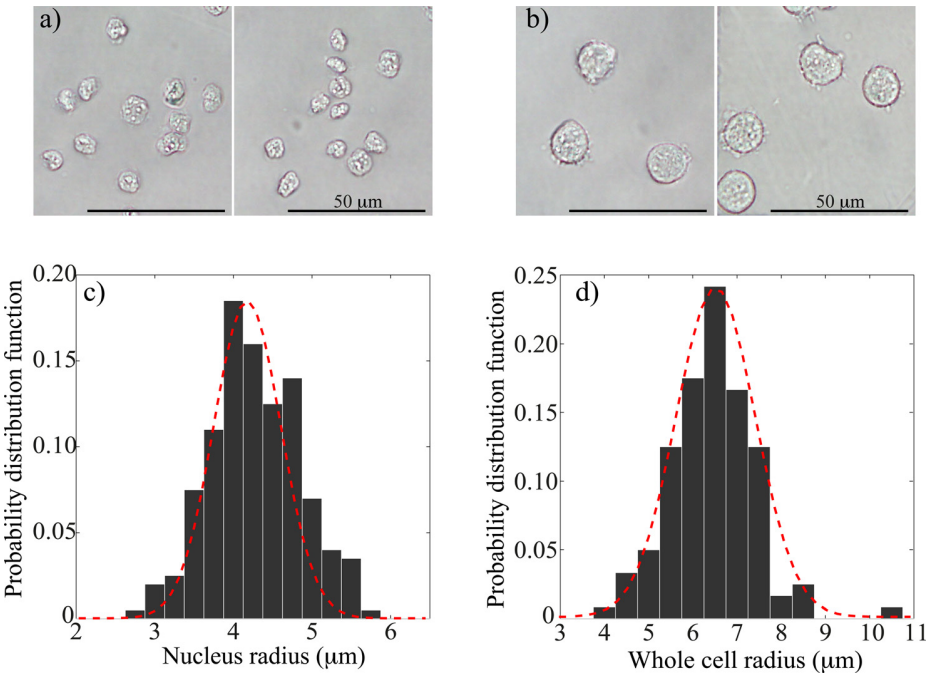

FIG. 2. (Color online) (a) and (b) Optical microscopy of isolated K-562 nuclei and whole K-562 cells. Scale bars represent 50 μm. (c) and (d) Radius distribution of isolated K-562 nuclei and whole K-562 cells. The dashed lines represent the Gaussian distribution curves that approximate the nuclear and whole cell radius distribution, respectively.

Canada). Two RMV 710 and RMV 703 probes were used in B-mode. For the RMV 710 and the RMV 703 probes, the oscillating single-element focused circular transducers had center frequencies of 20 and 30 MHz with −6 dB bandwidths of 10–32 and 18–42 MHz, focuses of 15 and 10 mm and f-numbers of 2.1 and 2.5, respectively. We acquired RF data from this scanner at a sampling frequency of 500 MHz with 8 bit resolution with a Gagescope model CS11G8 acquisition board.

The probe focus was positioned at a distance of 1 mm below the PBS/cell pellet biophantom interface. A translation stage (Physik Instrumente, model M-403.4PD, Karlsruhe, Germany) controlled the probe motion. Six B-mode images were constructed from acquired RF echoes by translating the probe every 600 μm. Examples of US B-mode scans obtained with the 20-MHz center frequency probe are provided in Fig. 4. For around 140 vertical lines at the center of each B-mode image, echoes were selected in the focal zone with a rectangular window of $d = 0.75$ mm, and the power spectra of the backscattered RF echoes were then averaged to provide P_{meas}. This procedure was repeated

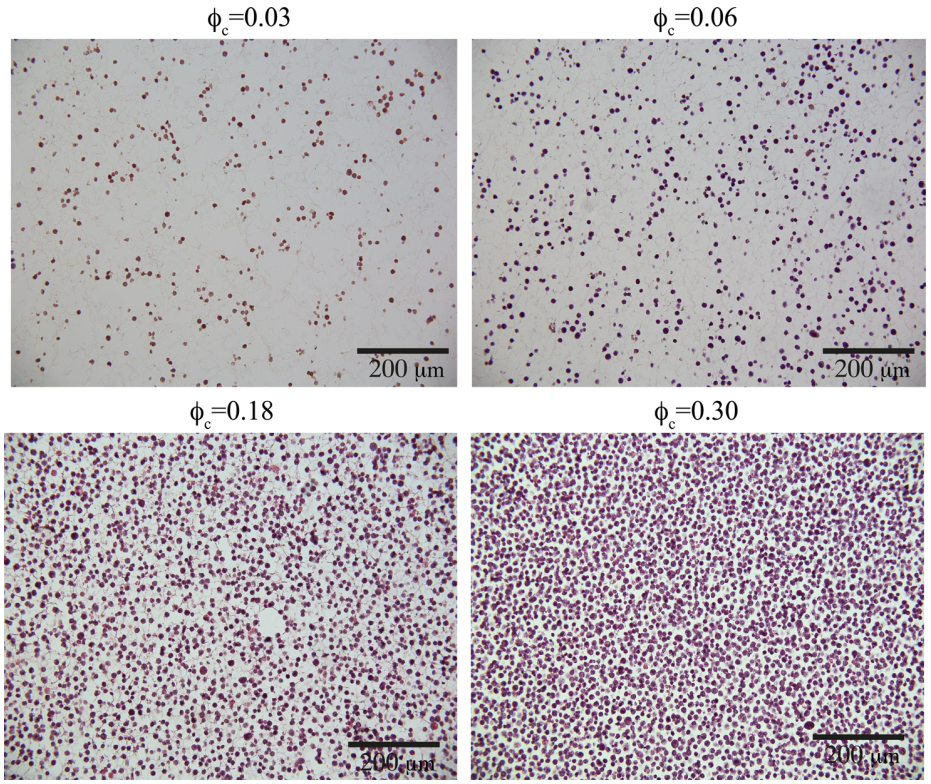

FIG. 3. (Color online) Representative HE stained sections of cell pellet biophantoms at several concentrations of 0.03, 0.06, 0.18, and 0.30.

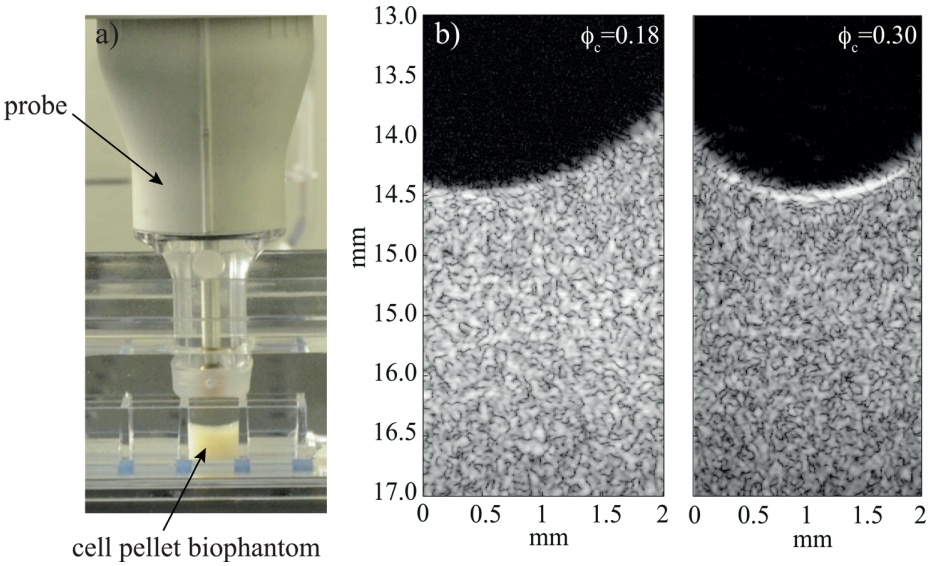

FIG. 4. (Color online) (a) US probe and cell pellet biophantom in a well immersed in PBS. (b) B-mode images of the cell pellet biophantoms obtained with the 20-MHz center frequency probe for two cell concentrations of 0.18 and 0.30.

twice with the two probes at each biophantom concentration studied.

C. Attenuation and BSC measurements

The attenuation coefficients of the cell pellet biophantoms were determined by using a standard substitution method. The Vevo 770 US scanner equipped with the 20-MHz center frequency probe was used in M-mode for reflection measurements. The measured cell pellet attenuation α_{ph} (in dB/mm) was computed as

$$\alpha_{\mathrm{ph}}(f) = \alpha_{\mathrm{PBS}}(f) + \frac{20}{2D}\log_{10}\left(\frac{S_{\mathrm{ref}}(f)}{S_{\mathrm{ph}}(f)}\right), \tag{10}$$

where α_{PBS} is the frequency-dependent attenuation of the PBS, which was taken to be similar to water, 2.1715×10^{-4} dB MHz^{-2} mm^{-1} at 20 °C.[30] f is the frequency and D is the thickness of the cell pellet. S_{ph} and S_{ref} are the amplitude spectra of the reflected signals from the well base surface with and without the presence of the cell pellet. Assuming that the cell pellet attenuation increases linearly with the frequency $[\alpha_{\mathrm{ph}}(f) = \alpha_{\mathrm{ph}_0} f]$ a linear regression analysis provided the attenuation coefficient α_{ph_0} in dB MHz^{-1} mm^{-1}. Averaged values obtained for 10 locations in the pellet well were 0.0098, 0.0184, 0.0215, 0.0202, and 0.0280 dB MHz^{-1} mm^{-1} for cell pellet concentrations of 0.06, 0.12, 0.18, 0.24, and 0.30, respectively.

The measured BSC values reported in this study were computed using the reference phantom technique.[31,32] This technique consists in using a reference scattering medium instead of a perfect flat reflector, on condition that the BSC of the reference scattering medium is known or can be determined. The reference scattering medium makes it possible to compensate the measured backscattered power spectrum $\overline{P_{\mathrm{meas}}}$ for the electromechanical system response and the depth-dependent diffraction and focusing effects caused by the ultrasound beam. The reference scattering medium used was a mixture of distilled water, 2% (w/w) agar powder (A9799, Sigma Aldrich, France), and 1% (w/w) of polyamide microspheres with a radius of 2.5 μm (orgasol 2001 UD NAT1, Arkema, France). The sample is easy to prepare and to handle, and the scattering process occurring in an ensemble of identical solid microspheres at a very low concentration of 1% (dilute medium) has been well documented using the Faran model.[20] Echoes from the reference scattering medium were acquired and windowed as with the cell pellet biophantoms, and their power spectra were averaged to obtain $\overline{P_{\mathrm{ref}}}$. The measured BSC was thus computed as follows:[31,32]

$$\mathrm{BSC}_{\mathrm{meas}}(k) = \mathrm{BSC}_{\mathrm{ref}}(k)\frac{\overline{P_{\mathrm{meas}}(k)}}{\overline{P_{\mathrm{ref}}(k)}}e^{4d(\alpha_{\mathrm{ph}_0}-\alpha_{\mathrm{ph}_{\mathrm{ref}}})k(c/2\pi)}, \tag{11}$$

where $\mathrm{BSC}_{\mathrm{ref}}$ is the theoretical BSC of the reference sample given by Eq. (2) in Ref. 19 using the Faran model,[20] and α_{ph_0} and $\alpha_{\mathrm{ph}_{\mathrm{ref}}}$ are the predetermined attenuation coefficients of the cell pellet biophantoms and of the reference phantoms. The value of $\alpha_{\mathrm{ph}_{\mathrm{ref}}}$ was equal to 0.004 dB MHz^{-1} mm^{-1}.

D. Parameter estimation

The objective of this study was to identify the cell structures responsible for scattering. In that aim, we estimated the scatterer radius r and its relative impedance contrast γ_z that could explain the measured $\mathrm{BSC}_{\mathrm{meas}}$ from all the studied cell concentrations. Indeed, if a unique scattering model can explain the frequency dependence and magnitude of the $\mathrm{BSC}_{\mathrm{meas}}$ data for all the cell concentrations, one could expect to identify the cell structures responsible for scattering. In the following, we will assume that the true cell radius mean (measured by optical microscopy) $r_c^{\mathrm{cor}} = 6.48\,\mu$m and the cell concentrations $\phi_c = (0.006, 0.03, 0.06, 0.12, 0.18, 0.24, 0.3)$ are known *a priori*. By considering that the cell number density is equal to the sphere number density, the fluid sphere concentration ϕ was calculated in the monodisperse case as $\phi = (r/r_c^{\mathrm{cor}})^3\phi_c$ and in the polydisperse case as

$$\phi = \phi_c\frac{\int p(r)\,r^3 dr}{r_c^{\mathrm{cor}3}}. \tag{12}$$

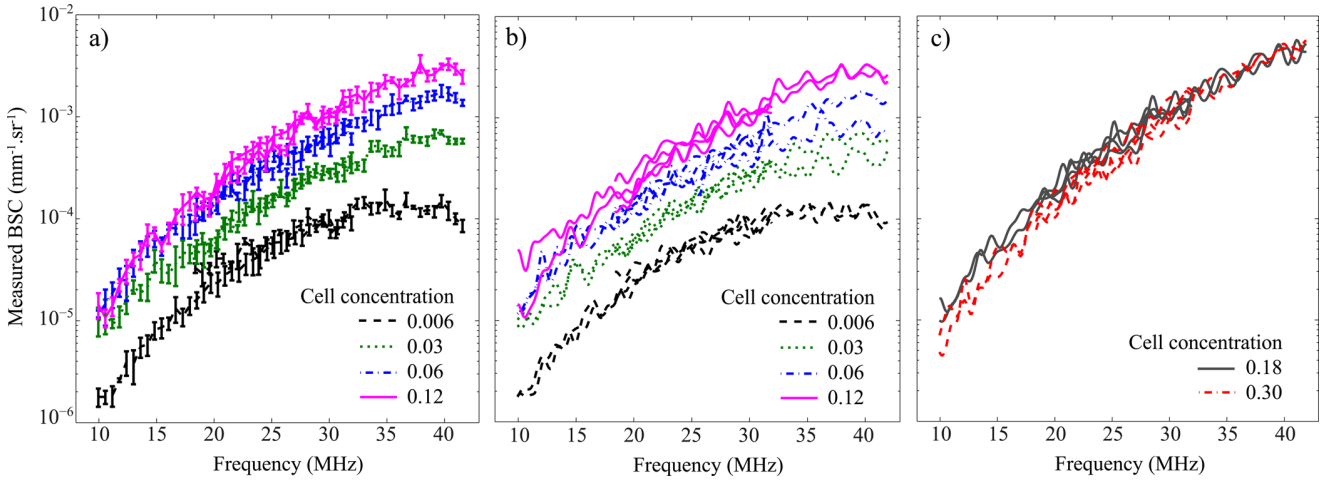

FIG. 5. (Color online) (a) Measured BSCs averaged over six measurements performed with the 20 - and 30-MHz center frequency probes for cell concentrations of 0.006, 0.03, 0.06, and 0.12. There is one experimental study. (b) and (c) Measured BSCs averaged over six measurements performed with the 20 - and 30-MHz center frequency probes for different cell concentrations. For each concentration, the two curves correspond to two different experimental studies (i.e., the preparation of the cell pellet biophantoms as well as the corresponding US acquisition). Standard deviations are not shown to enhance reading.

In the monodisperse case, the unknown parameters were r and γ_z. In the polydisperse case, the sphere radii were assumed to have a Gaussian distribution $p(r)$ with a mean radius $\bar{r}$ and a standard deviation μ. The unknown parameters were thus $\bar{r}$, μ, and γ_z. For the FFSM, PM, and SFM in both monodisperse and polydisperse cases, the unknown parameters were determined by minimizing the cost function F, which synthesizes the seven measurements with the seven biophantom concentrations ($\phi_{c_{i=1\cdots7}} = 0.006$, 0.03, 0.06, 0.12, 0.18, 0.24, and 0.3) over the wavenumbers k_j ($j = 1 \cdots M$) in the frequency bandwidth studied:

$$F = \frac{1}{N}\sum_{i=1}^{N} \frac{\Sigma_j \|\mathrm{BSC}_{\mathrm{meas}}(k_j, \phi_{c_i}) - \mathrm{BSC}_{\mathrm{theo}}(k_j,\ \phi_{c_i}\ \|^2}{\Sigma_j \|\mathrm{BSC}_{\mathrm{meas}}(k_j,\ \phi_{c_i})\|^2}, \tag{13}$$

where N is the number of studied cell concentrations (here $N = 7$). Note that the dependence of BSC on ϕ_{c_i} is usually not written; this dependence is necessary here for understanding the summation over i. In the monodisperse case, we employed a routine *fminsearch* in MATLAB (The Mathworks Inc., Natick, MA), i.e., a Nelder-Mead simplex method, to minimize the cost function F, whereas in the polydisperse case, we used a routine *fmincon* in MATLAB, with the constraint conditions that $0 \le \bar{r} \le 60\mu$m, $0 \le \mu \le 1$, $0 \le \gamma_z \le 1$, and that the minimum value of r was positive.

IV. SCATTERING FROM THE K562 CELL PELLET BIOPHANTOMS

A. Results

Figure 5(a) gives examples of the $\mathrm{BSC}_{\mathrm{meas}}$ versus frequency curves measured with the 20- and 30-MHz center frequency probes and averaged over the six measurements (corresponding to the six acquired B-mode images as described in Sec. III B). The experimental study (i.e., the preparation of the cell pellet biophantoms as well as the corresponding US acquisition) was repeated twice at each biophantom concentration to verify the measurement repeatability. The $\mathrm{BSC}_{\mathrm{meas}}$ averaged over the six measurements for the two studies are shown in Figs. 5(b) and 5(c). Standard deviations are not shown to enhance reading. The averaged $\mathrm{BSC}_{\mathrm{meas}}$ measured in the two studies have similar frequency dependence and magnitude, showing good repeatability. At all the studied concentrations, the $\mathrm{BSC}_{\mathrm{meas}}$ measured with the two probes in the 18–32 MHz frequency bandwidth were similar. This means that the results were not influenced by the system transfer function.

Tables I and II (see lines 1–3) report the scatterer radius r^* and the relative impedance contrast γ_z^* estimated by the three models FFSM, PM, and SFM in the monodisperse and the polydisperse cases, respectively. Also given in Tables I and II are the corresponding normalized errors to quantify the goodness of fit. The normalized errors were calculated by evaluating the cost function [given by Eq. (13)] at the values r^* (or $\bar{r}^* \pm \mu^*$) and γ_z^*. The standard deviation μ^* estimated with the polydisperse FFSM was equal to 0 so that the estimated sphere radius and impedance contrast were identical in the monodisperse and polydisperse cases. Normalized errors were smaller with the polydisperse SFM and larger with the FFSM. Figure 6 displays $\mathrm{BSC}_{\mathrm{meas}}$ measured for different cell concentrations, as well as the BSCs results with

TABLE I. Summary of the estimated parameters given by the FFSM, PM, and SFM in the monodisperse case.

	Cell line	Frequency bandwidth	Models	r^*	$\lvert\gamma_z^*\rvert$	Normalized errors
1	K562	10–42 MHz	FFSM	4.48	0.112	0.116
2	K562	10–42 MHz	PM	4.31	0.152	0.054
3	K562	10–42 MHz	SFM	5.88	0.070	0.039
4	CHO	26–105 MHz	FFSM	5.32	0.066	0.180
5	CHO	26–105 MHz	PM	4.96	0.079	0.292
6	CHO	26–105 MHz	SFM	5.78	0.062	0.157
7	CHO	26–56 MHz	FFSM	5.27	0.062	0.196
8	CHO	26–56 MHz	PM	4.09	0.136	0.102
9	CHO	26–56 MHz	SFM	5.67	0.064	0.072

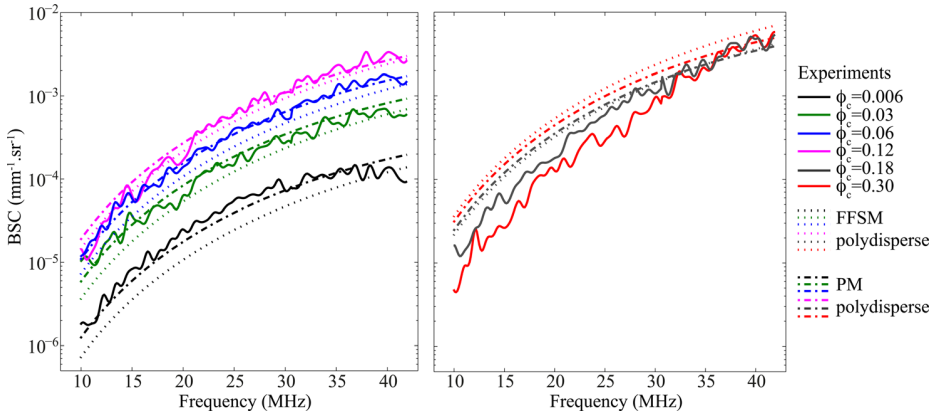

FIG. 6. (Color online) Measured BSCs (in solid lines) and BSCs computed with the polydisperse FFSM and the polydisperse PM (in dashed lines) by assuming the estimated scatterer size $\bar{r}^* \pm \mu^*$ and impedance contrast γ_z^* (see values in Table II lines 1–2).

the polydisperse FFSM and the polydisperse PM calculated by assuming the estimated scatterer size $\bar{r}^* \pm \mu^*$ and impedance contrast γ_z^* (see values in Table II lines 1–2). One can notice large differences between measured BSC_{meas} and estimated FFSM curves, even at low concentrations $\phi_c \leq 0.12$. So the FFSM cannot model the BSC_{meas} amplitude behavior for all concentrations. The PM provides satisfactory fittings of the BSC_{meas} for cell concentrations $\phi_c < 0.18$. As the cell concentration increases, the PM is not able to model the BSC_{meas} amplitude and frequency dependency. Figure 7 shows the BSCs curves with the SFM in both monodisperse and polydisperse cases calculated by assuming the estimated scatterer size $\bar{r}^* \pm \mu^*$ and impedance contrast γ_z^* (see values in Tables I and II lines 3). It is clear from these figures that the polydisperse SFM provides the best fits of the BSC_{meas} for all cell concentrations.

To make the reading of these results easier, Fig. 8 shows the measured BSCs magnitude averaged in the frequency bandwidth (from 10 to 28 MHz and from 10 to 42 MHz) as a function of the cell concentration. The standard deviations are calculated based on the six measurements (performed every 600 μm) on the same cell pellet biophantoms. Note that the BSC_{meas} is not linearly proportional to concentration. For the averaged BSC_{meas} in the 10–28 MHz frequency bandwidth shown in Fig. 8(a), the BSC_{meas} magnitude increases with increasing concentration between 0.006 and 0.12, then decreases with increasing concentration between 0.12 and 0.30. The averaged BSC_{meas} in the 10–42 MHz frequency bandwidth are in the same range of values for concentrations between 0.18 and 0.30 [see Fig. 8(b)]. Also plotted in Fig. 8 are the averaged BSCs computed with the FFSM, PM, and SFM using the estimated parameters given in Tables I and II (lines 1–3). The FFSM showed no agreement with the experimental data. Good agreement was obtained at low cell concentrations $\phi_c \leq 0.12$ but not for the higher concentrations of 0.24 and 0.30, for the PM in both monodisperse and polydisperse cases and for the monodisperse SFM, in both 10–28 MHz and 10–42 MHz frequency ranges. The polydisperse SFM was the model showing the best agreement with the experimental data.

TABLE II. Summary of the estimated parameters given by the FFSM, PM, and SFM in the polydisperse case.

	Cell line	Frequency bandwidth	Models	$\bar{r}^* \pm \mu^*$ (μm)	$\lvert\gamma_z^*\rvert$	Normalized errors
1	K562	10–42 MHz	FFSM	4.48 ± 0.00	0.112	0.116
2	K562	10–42 MHz	PM	4.03 ± 1.15	0.137	0.053
3	K562	10–42 MHz	SFM	6.40 ± 1.44	0.051	0.029
4	CHO	26–105 MHz	FFSM	5.04 ± 1.18	0.073	0.108
5	CHO	26–105 MHz	PM	4.02 ± 1.67	0.101	0.183
6	CHO	26–105 MHz	SFM	5.47 ± 1.07	0.068	0.077
7	CHO	26–56 MHz	FFSM	3.83 ± 1.39	0.094	0.196
8	CHO	26–56 MHz	PM	3.67 ± 1.56	0.124	0.069
9	CHO	26–56 MHz	SFM	6.04 ± 1.11	0.057	0.054

B. Discussion

For the polydisperse SFM giving the smallest normalized errors, the estimated radius of the fluid sphere was found equal to 6.40 μm and agrees well with the true measured radius of the K562 whole cells, with a relative error around 1.2%. Concerning the acoustic parameters, the surrounding medium was assumed to be plasma-like, with $c_0 = 1547$ m/s and $\rho_0 = 1.021$ g/mL.[33] By assuming that the cytoplasm occupies 71% of the K562 cell volume and that the cytoplasm contains 80%–90% of water,[34] the cell was thus expected to have water-like acoustic parameters, i.e., $c \approx 1500$ m/s, $\rho \approx 1$, and $\gamma_z \approx 0.05$. A good match was thus obtained between the estimated and expected relative impedances using the polydisperse SFM (see Table II line 3).

The nonlinear relationship between the BSC amplitude and the cell concentration observed in Fig. 8 was correctly modeled with the SFM but not with the FFSM and PM. Since the FFSM assumes that the BSC is linearly proportional to scatterer concentration, it was expected that the FFSM would give the largest errors. Even if the PM can model a nonlinear relationship between the BSC magnitude and the concentration, it was insufficient to explain the BSC_{meas} behaviors, as shown in Fig. 8. The main explanation for this lack of consistency is that the PM is only effective at low frequencies and loses its applicability in the large frequency range of 10–42 MHz.[19] To confirm this hypothesis, the estimation procedure was performed with the PM in a low and narrow frequency bandwidth of 10–15 MHz. The estimated parameters were equal to $r^* = 6.67$ μm and $\gamma_z^* = 0.060$ in the monodisperse case, and $\bar{r}^* = 6.66$ μm, $\mu^* = 0.059$ μm, and $\gamma_z^* = 0.059$ in the polydisperse case. Both radius and relative impedance contrast estimated in the low 10–15 MHz frequency

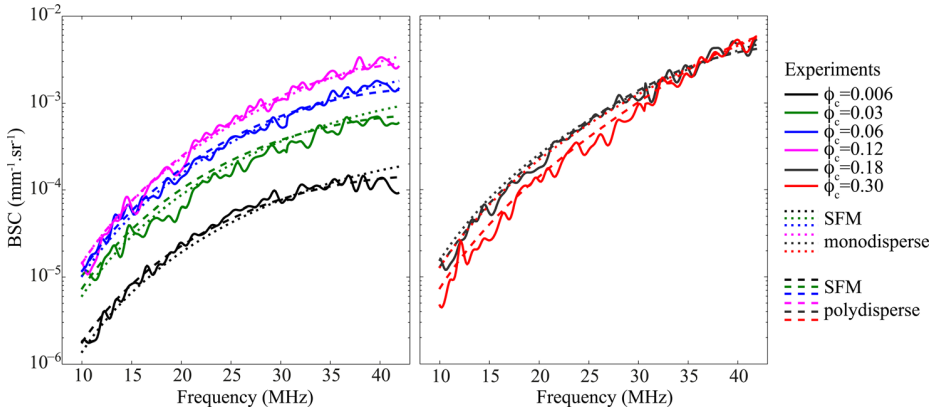

FIG. 7. (Color online) Measured BSCs (in solid lines) and BSCs computed with the SFM in both monodisperse and polydisperse cases (in dashed lines) by assuming the estimated scatterer size (r^* or $\bar{r}^* \pm \mu^*$, respectively) and impedance contrast γ_z^* (see values in Table I line 3 and Table II line 3, respectively).

bandwidth gave better results than those estimated in the 10–42 MHz frequency bandwidth (see Tables I and II lines 2). In the low 10–15 MHz frequency range, the relative error for the radius estimated with the PM was around 2.7% (against a relative error around 37.8% in the 10–42 MHz frequency bandwidth). Figure 9 represents the averaged BSC_{meas} in the 10–15 MHz frequency bandwidth versus cell concentrations. The PM provided good agreement with the experimental data in this case.

The good quality of the fitted BSC curves (see Fig. 7) as well as the good agreement between the estimated scatterer radius and the true whole cell radius reveals that the polydisperse SFM was more relevant that the FFSM and PM for modeling the responses from concentrated biophantoms in the studied 10–42 MHz frequency bandwidth. This finding also implies that a fluid sphere with the size of the whole cell and uniform acoustic properties is sufficient to model an isolated cell in this frequency range.

V. SCATTERING FROM CHINESE HAMSTER OVARY (CHO) CELL PELLET BIOPHANTOMS

A. Results

Han *et al.*[14] performed high frequency (26–105 MHz) ultrasound BSC measurements on CHO cell pellet biophantoms. The actual radii of nuclear and whole CHO cells are 3.32 ± 0.63 and 6.71 ± 0.86 μm, respectively.[14] The solid curves in Fig. 10(a) represent some BSC raw data that were extracted from Figs. 9 and 10 of Ref. 14 using DataThief III

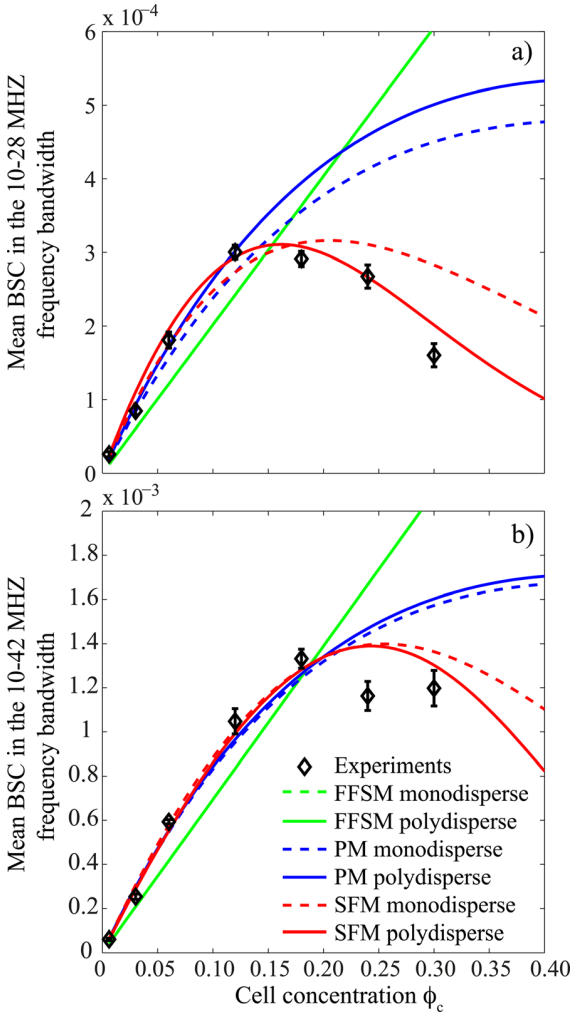

FIG. 8. (Color online) Comparison between the measured and predicted mean BSCs versus the K562 cell concentration for the FFSM, PM, and SFM. Note that the procedure of parameter estimation was performed in the 10–42 MHz frequency bandwidth.

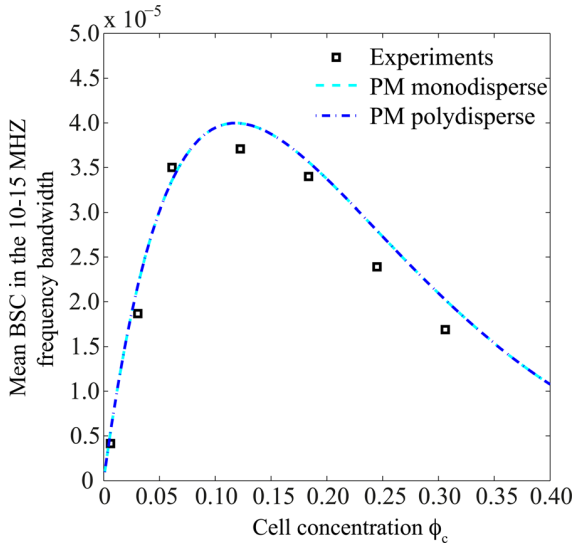

FIG. 9. (Color online) Comparison between the measured and predicted mean BSCs versus the K562 cell concentration for the PM. Note that the procedure of parameter estimation was performed in the 10–15 MHz frequency bandwidth.

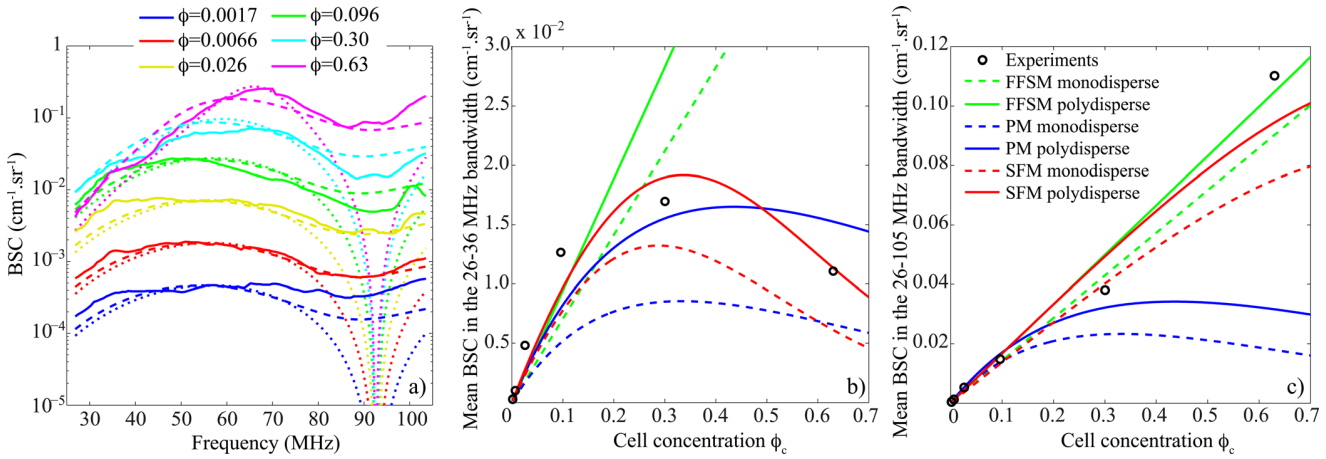

FIG. 10. (Color online) (a) Experimental BSCs of CHO cell pellet biophantoms from Ref. 14 (in solid lines) and BSCs computed with the monodisperse SFM (in dotted lines) and with the polydisperse SFM (in dashed lines) by assuming the estimated scatterer size $\bar{r}^* \pm \mu^*$ and impedance contrast γ_z^* (see values in Table I line 9 and Table II line 9). (b) and (c) Comparison between the measured and predicted mean BSCs versus the cell concentration. Note that the procedure of parameter estimation was performed in the 26–105 MHz frequency bandwidth.

software. The same procedure of parameter estimation presented in Sec. III D was applied to these data, except that we used different values for some known parameters: the true cell radius mean $\bar{r}_c = 6.71$ μm, the studied cell concentrations $\phi_c = (0.0017, 0.0066, 0.026, 0.096, 0.3, 0.63)$ and the number of studied cell concentrations $N = 6$.

The estimated parameters and the corresponding normalized errors computed with the three models FFSM, PM, and SFM are summarized in Tables I and II (lines 4–6). Normalized errors were smaller with the polydisperse SFM and larger with the monodisperse PM. Figure 10(a) represents the BSCs results with the SFM in both monodisperse and polydisperse cases calculated by assuming the estimated scatterer size $\bar{r}^* \pm \mu^*$ and impedance contrast γ_z^* given in Table II line 6. Figures 10(b) and 10(c) show the experimental and theoretical BSCs magnitude averaged in the frequency bandwidth (from 26 to 36 and from 26 to 105 MHz) versus cell concentration. The CHO cell experiments present a complex BSC_{meas} versus concentration relationship, which is nonlinear at low frequencies [Fig. 10(b)] and linear at high frequencies [Fig. 10(c)]. The polydisperse SFM was the model that better explained the BSC_{meas} behaviors.

B. Discussion

The CHO cell experiments showed BSC smooth curves, which could not be modeled by a monodisperse model especially at high frequencies larger than 70 MHz [see Figs. 1 and 10(a)]. That is why the errors obtained with the monodisperse modeling for the three models were about twice as large as those obtained with the polydisperse modeling [see Tables I and II lines 3–6].

It is interesting to observe that the error obtained with the FFSM was smaller than the error obtained with the PM in both monodiperse and polydisperse modeling cases (see Tables I and II lines 4 and 5). This is due to the linear relationship between the averaged BSC_{meas} and the cell concentration at high frequency [see Fig. 10(c)], which can be easily reproduced with the FFSM. However, the observed BSC_{meas} versus concentration relationship at low frequency cannot be modeled with the FFSM [see Fig. 10(b)]. The SFM was satisfactory to explain the BSC amplitude versus cell concentration whatever the frequency range studied. Indeed, the structure factor tends toward the packing factor in the low frequency range $(kr \to 0)$ and then oscillates around 1 for $kr \geq 1.5$ [see the solid lines in Fig. 14(a) in Ref. 19]. That is why the SFM can display a nonlinear relationship for the BSCs averaged in the low 26–36 MHz frequency range and a linear relationship in the higher 26–105 MHz frequency range [see the solid red lines in Figs. 10(b) and 10(c)].

For the polydisperse SFM giving the smallest errors, the estimated impedance contrast $\gamma_z^* = 0.068$ agreed quite well with the expected value. The estimated radius of the fluid sphere was found equal to 5.47 μm, which is close to the true whole cell radius of 6.71 μm, i.e., relative error of 18%. However, the correspondence between the true CHO cellular structures and the estimated radii was less accurate than the correspondence obtained with the K562 cells. The fluid-filled sphere might be less reliable for modeling a single cell in terms of shape and structure at high frequencies. Indeed, the product kr_c was less than 1 ($0.26 \leq kr_c \leq 1.11$ in the 10–42 MHz frequency range) for the K562 cell experiments against $0.73 \leq kr_c \leq 2.95$ in the 26–105 MHz frequency range for the CHO cell experiments. To confirm this hypothesis, the procedure of parameter estimation was applied in a reduced frequency bandwidth of 26–56 MHz. The upper frequency limit of 56 MHz corresponds to the average of BSC peaks and to a product $k\overline{r_c} = 1.5$. Tables I and II lines 7–9 give the estimated parameters and Fig. 11 represents the corresponding averaged BSCs versus the cell concentration for the estimation procedure performed in the 26–56 MHz frequency bandwidth. Normalized errors were smaller with the polydisperse SFM and larger with the FFSM, as previously obtained with the K562 cell study. For the polydisperse SFM giving the smallest errors, the radius of the fluid sphere was found equal to 6.04 μm and match better the true CHO whole cell radius with a relative error of 10%.

It is important to emphasize that cell pellet biophantoms mimic tumors only for high cellular concentration $(\phi_c \geq 0.3)$.

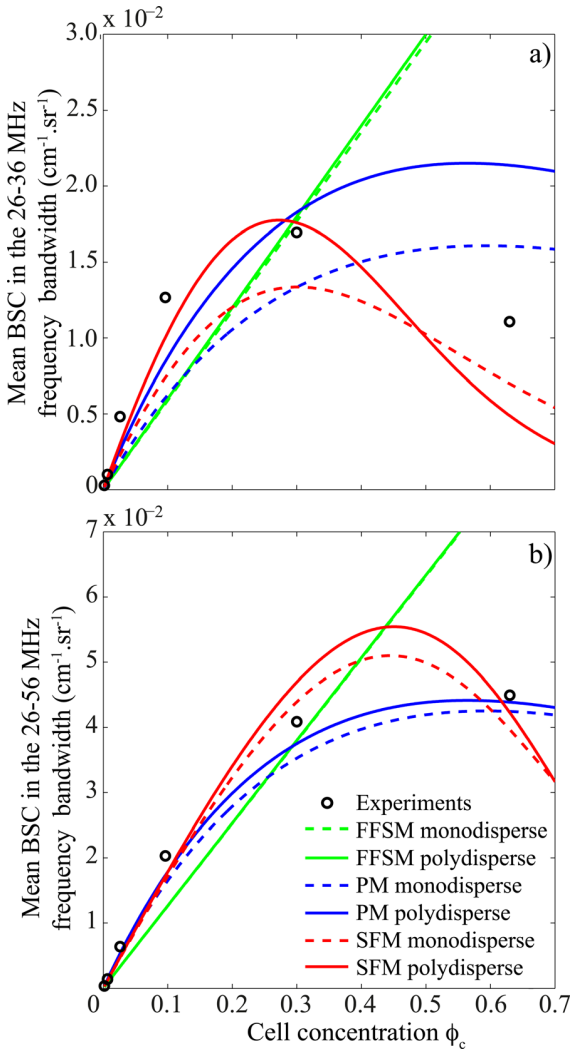

FIG. 11. (Color online) Comparison between the measured and predicted mean BSCs versus the cell concentration for the FFSM, PM, and SFM. Note that the procedure of parameter estimation was performed in the 26–56 MHz frequency bandwidth.

Frequency dependent BSC from dense cell pellets exhibit similar frequency dependent BSC as xenograft tumors from the same cell line (see for example Fig. 5.3 in Ref. 35). So concentrated cell pellet biophantoms allow the investigation of the basics of the biophysical mechanisms of scattering, since a dense cell pellet constitutes a simplified version of a real tumor. The results obtained with the K562 cells (in the 10–42 MHz frequency bandwidth) and with the CHO cells (in the 26–56 MHz frequency bandwidth) suggest that the polydisperse SFM is an adequate model for QUS characterization of tumors with high cellular content. However, further study should be conducted on *in vivo* tumors to confirm the added value of the SFM. Indeed, tumors have more complex structures than cell pellets. The extracellular matrix, the blood microvessels and the tumor heterogeneity (with proliferating and necrotic cell type regions) may play a role in tumor backscatter, as shown by Han *et al.*[11] At the moment, the SFM is an improvement over the FFSM for modeling high cellular content in simple tumor composed of a single cell line. Future work should focus on taking into account the heterogeneity of cell types as well as other structures such as blood microvessels.

VI. CONCLUSION

Three scattering models were examined in view of explaining the experimental BSCs from cell pellet biophantoms at different cell concentrations with a single set of structural and acoustic parameters. Both K562 and CHO cell studies revealed that the FFSM and PM are insufficient to model the complex behavior of the BSC_{meas} and that the polydisperse SFM is the model that better explains the behavior of BSC_{meas}. The impedance and size estimated with the polydisperse SFM are satisfactory: the relative impedance contrast estimates seem to be in a reasonable range of values and the fluid sphere radii match the true whole cell radii for both K562 and CHO cell studies. This finding shows that the whole cell plays a major role in the BSC behavior for the K562 and CHO cells studied. Note that, for these two cell lines, most of the cell volume is occupied by the cytoplasm (71% for the K562 cell and 88% for the CHO cell). Future studies should focus on similar experiments with different kinds of cells with different nucleus to cell volume ratios.

ACKNOWLEDGMENTS

This work was supported by the French Agence Nationale de la Recherche (ANR) under grant ANR Tecsan 11-008-01, Cancéropole PACA, and CNRS. The author would like to thank Eric Debieu and Stephan Devic from the Laboratory of Mechanics and Acoustics (LMA-CNRS) for their technical assistance.

[1]F. L. Lizzi, M. Greenebaum, E. J. Feleppa, and M. Elbaum, "Theoretical framework for spectrum analysis in ultrasonic tissue characterization," J. Acoust. Soc. Am. **73**, 1366–1373 (1983).
[2]F. L. Lizzi, M. Ostromogilsky, E. J. Feleppa, M. C. Rorke, and M. M. Yaremko, "Relationship of ultrasonic spectral parameters to features of tissue microstructure," IEEE Trans. Ultrason. Ferroelectr. Freq. Control **33**, 319–329 (1986).
[3]M. C. Kolios, G. J. Czarnota, M. Lee, J. W. Hunt, and M. D. Sherar, "Ultrasonic spectral parameter characterization of apoptosis," Ultrasound Med. Biol. **28**, 589–597 (2002).
[4]E. J. Feleppa, F. L. Lizzi, D. J. Coleman, and M. M. Yaremko, "Diagnostic spectrum analysis in ophthalmology: a physical perspective," Ultrasound Med. Biol. **12**, 623–631 (1986).
[5]E. J. Feleppa, T. Liu, A. Kalisz, M. C. Shao, N. Fleshner, and V. Reuter, "Ultrasonic spectral-parameter imaging of the prostate," Int. J. Imag. Syst. Technol. **8**, 11–25 (1997).
[6]M. L. Oelze, J. F. Zachary, and W. D. O'Brien, "Characterization of tissue microstructure using ultrasonic backscatter: Theory and technique for optimization using a Gaussian form factor," J. Acoust. Soc. Am. **112**, 1202–1211 (2002)
[7]M. L. Oelze, W. D. O'Brien, J. P. Blue, and J. F. Zachary, "Differentiation and characterization of rat mammary fibroadenomas and 4T1 mouse carcinomas using quantitative ultrasound imaging," IEEE Trans. Med. Imag. **23**, 764–771 (2004).
[8]J. Mamou, A. Coron, M. Hata, J. Machi, E. Yanagihara, P. Laugier, and E. Feleppa, "Three-dimensional high-frequency characterization of cancerous lymph nodes," Ultrasound Med. Biol. **36**, 361–375 (2010).
[9]V. C. Anderson, "Sound scattering from a fluid sphere," J. Acoust. Soc. Am. **22**, 426–431 (1950).
[10]M. L. Oelze and W. D. O'Brien, "Application of three scattering models to characterization of solid tumors in mice," Ultrason. Imag. **28**, 83–96 (2006).
[11]A. Han, R. Abuhabsah, J. P. Blue, S. Sarwate, and W. D. O'Brien, "The measurement of ultrasound backscattering from cell pellet biophantoms and tumors *ex vivo*," J. Acoust. Soc. Am. **134**, 686–693 (2013).

[12]J. McNew, R. Lavarello, and W. D. OBrien, "Sound scattering from two concentric fluid spheres (L)," J. Acoust. Soc. Am. **125**, 1–4 (2009).
[13]M. Teisseire, A. Han, R. Abuhabsah, J. P. Blue, Jr., S. Sarwate, and W. D. O'Brien, "Ultrasonic backscatter coefficient quantitative estimates from Chinese hamster ovary cell pellet biophantoms," J. Acoust. Soc. Am. **128**, 3175–3180 (2010).
[14]A. Han, R. Abuhabsah, J. P. Blue, S. Sarwate, and W. D. O'Brien, "Ultrasonic backscatter coefficient quantitative estimates from high-concentration Chinese hamster ovary cell pellet biophantoms," J. Acoust. Soc. Am. **130**, 4139–4147 (2011).
[15]R. M. Vlad, R. K. Saha, N. M. Alajez, S. Ranieari, G. J. Czarnota, and M. C. Kolios, "An increase in cellular size variance contributes to the increase in ultrasound backscatter during cell death," Ultrasound Med. Biol. **9**, 1546–1558 (2010).
[16]D. Savery and G. Cloutier, "A point process approach to assess the frequency dependence of ultrasound backscattering by aggregating red blood cells," J. Acoust. Soc. Am. **110**, 3252–3262 (2001).
[17]I. Fontaine, D. Savery, and G. Cloutier, "Simulation of ultrasound backscattering by red blood cell aggregates: effect of shear rate and anisotropy," Biophys. J. **82**, 1696–1710 (2002).
[18]V. Twersky, "Low-frequency scattering by correlated distributions of randomly oriented particles," J. Acoust. Soc. Am. **81** 1609–1618 (1987).
[19]E. Franceschini and R. Guillermin, "Experimental assessment of four ultrasound scattering models for characterizing concentrated tissue-mimicking phantoms," J. Acoust. Soc. Am. **132**, 3735–3747 (2012).
[20]J. J. Faran, "Sound scattering by solid cylinders and spheres," J. Acoust. Soc. Am. **23**, 405–418 (1951).
[21]R. E. Baddour, M. D. Sherar, M. D. J. W. Hunt, G. J. Czarnota, and M. C. Kolios, "High-frequency ultrasound scattering from microspheres and single cells," J. Acoust. Soc. Am. **117**, 934–943 (2005).
[22]R. E. Baddour and M. C. Kolios, "The fluid and elastic nature of nucleated cells: implications from the cellular backscatter response," J. Acoust. Soc. Am. **121**, EL16–EL22 (2007).
[23]O. Falou, M. Rui, A. E. Kaffas, J. C. Kumaradas, and M. C. Kolios, "The measurement of ultrasound scattering from individual micron-sized objects and its application in single cell scattering," J. Acoust. Soc. Am. **128**, 894–902 (2010).
[24]L. R. Taggart, R. E. Baddour, A. Giles, G. J. Czarnota, and M. C. Kolios, "Ultrasonic characterization of whole cells and isolated nuclei," Ultrasound Med. Biol. **33**, 389–401 (2007).
[25]J. S. Pedersen, "Determination of size distributions from small-angle scattering data for systems with effective hard-sphere interactions," J. Appl. Crystallogr. **27**, 595–608 (1994).
[26]J. S. Pedersen, "Analysis of small-angle scattering data from colloids and polymer solutions: modeling and lest-squares fitting," Adv. Colloid Interface Sci. **70**, 171–210 (1997).
[27]M. S. Wertheim, "Exact solution of the Percus-Yevick integral equation for hard spheres," Phys. Rev. Lett. **10**, 321–323 (1963).
[28]N. E. Berger, R. J. Lucas, and V. Twersky, "Polydisperse scattering theory and comparisons with data for red blood cells," J. Acoust. Soc. Am. **89**, 1394–1401 (1991).
[29]M. E. Greenberg and T. P. Bender, "Identification of newly transcribed RNA," in *Current Protocols in Molecular Biology* (Wiley Online Library, 2007), Chap. 4: Unit 4.10. doi: 10.1002/0471142727.mb0410s78.
[30]F. A. Duck, *Physical Properties of Tissue: A Comprehensive Reference Book* (Academic, London, 1990), Chap. 4, p. 95.
[31]L. X. Yao, J. A. Zagzebski, and E. L. Madsen, "Backscatter coefficient measurements using a reference phantom to extract depth-dependent instrumentation factors," Ultrason. Imag. **12**, 58–70 (1990).
[32]S. H. Wang and K. K. Shung, "An approach for measuring ultrasonic backscattering from biological tissues with focused transducers," IEEE Trans. Biomed. Eng. **44**, 549–554 (1997).
[33]E. Franceschini, B. Metzger, and G. Cloutier, "Forward problem study of an effective medium model for ultrasound blood characterization," IEEE Trans. Ultrason., Ferroelectr., Freq. Control **58**, 2668–2679 (2011).
[34]J. Bereither-Hahn, "Computer assisted microscope interferometry by image analysis of living cells," Proc. Clin. Biol. Res. **196**, 27–44 (1985).
[35]O. Falou, A. Sadeghi-Naini, A. Al-Mahrouki, M. C. Kolios, and G. Czarnota, "Quantitative ultrasound and cell death," in *Quantitative Ultrasound in Soft Tissues*, edited by J. Mamou and M. L. Oelze (Springer, Dordrecht, 2013), Chap. 5, pp. 95–115.